공학박사 학위논문

# Development of GPU-Based SPH-DEM Code for Hydrodynamic Interactions between Multi-Phase Flow and Solid Debris

## 다상유동 및 고체 파편물의 수력학적 거동 해석을 위한 GPU 기반의 SPH-DEM 연계해석 코드 개발

**2020 년 8 월**

서울대학교 대학원

에너지시스템공학부

조 영 범

# Development of GPU-Based SPH-DEM Code for Hydrodynamic Interactions Between Multi-Phase Flow and Solid Debris

다상유동 및 고체 파편물의 수력학적 거동 해석을 위한 GPU 기반의 SPH-DEM 연계해석 코드 개발

지도교수 김 응 수

이 논문을 공학박사 학위논문으로 제출함
2020 년 8 월

서울대학교 대학원
에너지시스템공학부
조 영 범

조영범의 박사 학위논문을 인준함
2020 년 8 월

위 원 장 조 형 규 (인)

부위원장 김 응 수 (인)

위 원 심 형 진 (인)

위 원 박 현 선 (인)

위 원 이 병 진 (인)

# Abstract

# Development of GPU-based SPH-DEM Code for Hydrodynamic Interactions between Multi-Phase Flow and Solid Debris

Young Beom Jo

Department of Energy System Engineering

The Graduate School

Seoul National University

In the late phase severe accident of LWR, the massive corium releases out of the reactor pressure vessel (RPV) and falls to the coolant if the In-Vessel Retention (IVR) strategy fails. The melt jet can be fragmented into debris particles based on the assumption that the ex-vessel pool is sufficiently deep. It is known that there are various three-phase flow issues associated with the fragmented debris particles under the influence of phase change of cavity coolant. In such cases, the vapor phase forms a sharp and dynamic interface with the liquid phase while the transient relocation behavior of debris particles is the main concern. Thus, coupling Lagrangian-based multi-phase CFD techniques and Discrete Element Method (DEM) can be an effective approach in terms of

numerical modeling of such behaviors. In this respect, an integrated numerical code for incompressible 3-phase flow has been developed in this study by two-way phase coupling of multi-phase Smoothed Particle Hydrodynamics (SPH) and DEM model.

Smoothed Particle Hydrodynamics (SPH) is one of the best-known meshless CFD methods in which the fluid system is represented as the finite number of Lagrangian particles. The SPH code developed in this study proposes a new density estimation model and improves the surface tension model for accurate simulation of incompressible two-phase flow behavior. The demonstration of its applicability has been performed through several V&V simulations including multi-phase dam-break and sloshing simulations.

Discrete Element Method (DEM) is a direct simulation method for a rigid body that can analyze the translation, rotation, and collision behavior of solid particles in detail. The soft-sphere collision model with Hertz-Mindlin contact force equations is adopted for developed DEM code in this study. To precisely estimate the wall boundary interactions of bed-formed debris particles, a versatile wall boundary model is newly proposed in this study that also covers the sliding and rolling behavior of solid particles. The inter-particle collision behavior and sliding & rolling motion of particles are well proven in several V&V cases.

The numerical code system for incompressible 3-phase flow is newly developed by two-way phase coupling of the above two models (SPH-DEM). The unresolved coupling approach between two methods was adopted for the analysis

of the overall behavior of particulate solid debris. The fundamental validation of the phase coupled model was performed for both single-particle behavior and particulate granular flow such as dam-breaking motion of particle-fluid.

The SPH-DEM coupled code in this study has been parallelized based on Graphical Process Unit (GPU) in order to overcome the inherent efficiency problem of the Lagrangian-based numerical method. Parallel mapping and reduction are applied for solving discretized summation equations of each SPH particle, solving contact force equations for each DEM particle, and also for solving coupling equations between SPH and DEM particles. The efficiency of code parallelization was evaluated through the scalability analysis based on the benchmark calculation.

Finally, the simulation of the vapor-driven leveling behavior of spherical solids was performed as a case study to demonstrate the applicability of the developed code. The time-variant surface shape of solid particles was compared with the benchmark experiments both qualitatively and quantitatively. The effect of gas flow rate on the tendency of leveling behavior also has been analyzed.

The developed numerical system in this study is expected to be a good alternative for the simulation of such phenomena that were difficult to handle with traditional numerical methods since the numerical schemes used in the code have a high potential for simulation of complicated physics with highly deformable geometry. In addition, this validated code system can contribute to hydrodynamic modeling studies for severe accident technology by performing

numerical experiments on conditions that hard to be conducted on a laboratory scale.

**Keywords**

**Smoothed Particle Hydrodynamics, Discrete Element Method, Two-Way Coupling, GPU Parallelization, Debris Bed, Self-Leveling**

**Student Number: 2014-21417**

# List of Contents

**Abstract** ..... **ii**

**List of Contents** ..... **vi**

**Chapter 1 Introduction** ..... **1**

1.1 Background and Motivation ..... 1

1.2 Previous Studies ..... 3

1.2.1 Numerical Studies on Particulate Debris Bed ..... 3

1.2.2 SPH-DEM Phase Coupling ..... 4

1.3 Objectives and Scope ..... 5

**Chapter 2 Fluid Phase: Smoothed Particle Hydrodynamics** ..... **8**

2.1 Smoothed Particle Hydrodynamics (SPH) ..... 9

2.1.1 SPH Particle Approximation ..... 9

2.1.2 SPH Particle Approximation of Derivatives ..... 10

2.1.3 Kernel Function ..... 11

2.1.4 Accuracy of SPH Approximation ..... 12

2.1.5 Governing Equations for Incompressible Flow ..... 14

2.2 Multi-phase SPH Governing Equations ..... 16

2.2.1 Treatment of Multi-Phase Flow ..... 16

2.2.2 Normalized Density Model ..... 18

2.2.3 Continuum Surface Force (CSF) Model ..... 19

2.3 Implementation of SPH Model ..... 21

2.3.1 Algorithm of SPH Code ..... 21

2.3.2 Nearest Neighboring Particles Searching (NNPS) ..... 22

2.3.3 Time Integration ..... 23

2.4 V&V Simulations ..... 24

2.4.1 Rayleigh-Taylor Instability ..... 25

2.4.2 Bubble Terminal Velocity ..... 25

2.4.3 Dam-Break Simulation ..... 25

2.4.4 Centralized Sloshing Simulation ..... 26

**Chapter 3 Solid Phase: Discrete Element Method** ..... **45**

3.1 Discrete Element Method (DEM) ..... 46
3.2 DEM Contact Force ..... 47
3.2.1 Soft-sphere Contact Model ..... 47
3.2.2 Contact Force Model ..... 48
3.2.3 Hertz-Mindlin Contact Force Model ..... 49
3.3 Wall Boundary Conditions ..... 52
3.3.1 Versatile Wall Boundary Model ..... 52
3.3.2 Particle Collision with the Wall ..... 54
3.3.3 Sliding and Rolling on the Wall Boundary ..... 56
3.4 DEM Implementation Algorithm ..... 57
3.4.1 Contact Detection ..... 58
3.4.2 Estimation of Relative Velocity ..... 59
3.4.3 Calculation of Contact Force ..... 60
3.4.4 Wall Boundary Conditions and Time Integration ..... 60
3.5 V&V and Simulations ..... 61
3.5.1 Conservation of Momentum and Angular Momentum ..... 62
3.5.2 Conservation of Energy in Elastic Collision ..... 63
3.5.3 V&V Simulations for Wall Boundary Model ..... 63
3.5.4 Granular Collapse of Spherical Particles ..... 64
**Chapter 4 Two-way Phase Coupling of SPH and DEM ..... 76**
4.1 Unresolved Coupling of SPH and DEM ..... 76
4.2 Governing Equations ..... 78
4.2.1 SPH Particles: Locally Averaged N-S Equations ..... 78
4.2.2 DEM Particles: Coupling Forces Acting on Solid Particles ..... 80
4.2.3 SPH Particles: Reaction Force from Momentum Exchange ..... 82
4.3 Algorithm of SPH-DEM Coupled Model ..... 83
4.4 V&V Simulations for SPH-DEM Coupled Model ..... 84
4.4.1 Single DEM Particle Behavior ..... 85
4.4.2 Pressure Drop through Packed Bed ..... 87
4.4.3 Granular Flow in Liquid: 3D Dam-Break ..... 89
**Chapter 5 GPU Parallelization of Coupled SPH-DEM Code ..... 103**
5.1 Parallelization of Governing Equations ..... 104
5.1.1 GPU-based Parallelization ..... 104
5.1.2 Parallelization of SPH-DEM Governing Equations ..... 104
5.2 Parallelization of NNPS and Contact Detection ..... 105

5.3 Results of GPU Parallelization.....107
5.3.1 Speedup in Computation Time.....107
5.3.2 Parallelization Factors.....107
**Chapter 6 Code Application to Vapor-Driven Leveling Behavior of Spherical Debris.....113**
6.1 Self-Leveling Behavior of Debris Bed.....114
6.1.1 Self-Leveling Issue in LWR.....114
6.1.2 Self-Leveling Behavior in Terms of Debris Coolability.....114
6.2 Benchmark Experiment.....116
6.3 SPH-DEM Simulation Setup.....118
6.3.1 Properties and Simulation Conditions.....118
6.3.2 Sequence of SPH-DEM Leveling Simulation.....120
6.3.3 Determination of Inclined Angle.....121
6.4 Validation Results and Discussions.....121
6.4.1 SPH-DEM Simulation Results.....121
6.4.2 Validation Result.....122
6.4.3 Effect of Gas Flow Rate.....122
**Chapter 7 Summary.....129**
7.1 Summary.....129
7.2 Recommendations.....131
**References.....134**
**국문 초록.....142**

# List of Tables

Table 1.1. Previous 3-Phase Modeling Studies of Solid Debris .....6
Table 1.2. Previous Studies on SPH-DEM Phase Coupling .....6

Table 2.1. SPH Differential Operators .....30
Table 2.2. Conditions for Kernel Approximation Function .....30
Table 2.3 SPH Governing Equations .....31
Table 2.4 V&V Simulation Cases for Developed SPH Code .....32
Table 2.5 Comparison of Simulation Results with Benchmark Experient .....33

Table 3.1 DEM Contact Force Model .....66
Table 3.2 Hertz-Mindlin Contact Force Model .....66
Table 3.3 V&V Simulation Cases for Implemented DEM Model .....67

Table 5.1 Parallelization Factors for the Code .....109

# List of Figures

Figure 1.1. Incorporated Physical Models and Scope of This Study.....7

Figure 2.1. Particle System of Smoothed Particle Hydrodynamics (SPH).....34
Figure 2.2. Kernel Weighting Function in SPH Method.....34
Figure 2.3. Normalized Density Approach for Density Estimation.....35
Figure 2.4. Density and Pressure Results for Two-Fluid Hydrostatic Problem.....35
Figure 2.5. Improvement of CSF Model for Calculation of Curvature .....36
Figure 2.6. Structure and Simplified Algorithm of Developed SPH Code.....36
Figure 2.7. Grid-based Nearest Neighboring Particles Searching (NNPS) .....37
Figure 2.8. 2D SPH Simulation Results of Dam-Break Behavior.....37
Figure 2.9. SPH Results on Dam-Break Simulation in Various Conditions (Single/Two Phase) and Scales .....38
Figure 2.10. Snapshots for 3D Single Phase Dam-Break Simulation .....38
Figure 2.11. Results of Rayleigh-Taylor Instability Simulation .....39
Figure 2.12. SPH Simulation Results for Bubble Terminal Velocity.....39
Figure 2.13. Validation Results of SPH Method for Multi-D, Multi-Phase Dam-Break Simulation .....40
Figure 2.14. Geometry and Conditions for 3D SPH Sloshing Simulation .....40
Figure 2.15. Qualitative Comparison of SPH Result with Benchmark Exp.....41
Figure 2.16. 3D Simulation Results of Developed SPH Code for Single-Phase Centralized Sloshing Behavior .....41
Figure 2.17. 3D Simulation Results of Developed SPH Code for 12 Vertical Rods Sloshing .....42
Figure 2.18. 3D Simulation Results of Developed SPH Code for Asymmetric Sloshing Condition .....42
Figure 2.19. 3D Comparison Results for Two-Phase Centralized Sloshing Simulation.....43
Figure 2.20. Effect of Particle Resolution in SPH Sloshing Simulation .....43
Figure 2.21. Convergence of Results for Particle Resolution.....44
Figure 2.22. Difference between Single and Two Phase Simulation.....44

Figure 3.1. Spring-Dashpot System of Soft-Sphere Collision Model .....68

Figure 3.2. Inter-particle Collision in Soft-Sphere Model ..... 68
Figure 3.3. Versatile Wall Boundary Treatment Model in This Study ..... 69
Figure 3.4. Implicit Primitive Object for DEM Wall Boundary Condition ..... 69
Figure 3.5. Particle Collision with Wall Boundary ..... 70
Figure 3.6. Algorithm of Implemented DEM Model ..... 70
Figure 3.7. Grid-Based Contact Detection ..... 71
Figure 3.8. Conservation of Linear Momentum in Collision ..... 71
Figure 3.9. Conservation of Angular Momentum in Collision ..... 72
Figure 3.10. Conservation of Kinetic Energy in Elastic Collision ..... 72
Figure 3.11. Wall Collision of Rotating Sphere ..... 73
Figure 3.12. Sliding and Rolling of Spherical Particle on the Wall boundary ..... 73
Figure 3.13. Descending Behavior of the Sphere on Slope ..... 74
Figure 3.14. 3D Hopper Flow Simulation ..... 74
Figure 3.15. Benchmark Experimental Setup for Granular Collapse Behavior [Chou, 2012] ..... 75
Figure 3.16. DEM Validation Results for Granular Collapse Behavior ..... 75

Figure 4.1. Concept of SPH-DEM Unresolved Coupling ..... 92
Figure 4.2. Momentum Exchange b/w SPH and DEM Particles ..... 92
Figure 4.3. Algorithm of SPH-DEM Two-Way Coupled Model ..... 93
Figure 4.4. NNPS and Contact Detection in SPH-DEM Coupled Model ..... 94
Figure 4.5. Single DEM Particle Behavior without Drag Force ..... 94
Figure 4.6. DEM Particle Oscillation Due to Gravity and Buoyancy Force ..... 95
Figure 4.7. Single DEM Particle Freefall (Drag, Buoyancy Force) ..... 96
Figure 4.8. Damped Oscillation Due to Energy Dissipation ..... 96
Figure 4.9. Terminal Velocity Behavior of Single DEM Particle ..... 97
Figure 4.10. Sensitive Study on Coupling Length for Terminal Velocity Behavior ..... 97
Figure 4.11. Single Phase Pressure Drop through Packed Bed ..... 98
Figure 4.12. Pressure Data of SPH-DEM Phase Coupled Simulation ..... 98
Figure 4.13. Conditions for Solid-Liquid Dam-Break Experiment [Sun, 2013 ..... 99
Figure 4.14. Qualitative Results of Solid-Liquid Dam-Break Simulation ..... 100
Figure 4.15. Quantitative Validation Result of SPH-DEM Coupled Code ..... 101
Figure 4.16. Qualitative Comparison Results (decoupled, one-way, two-way) ..... 101

Figure 4.17. Quantitative Comparison Results in Time Variation of Normalized Leading Front (one-way, two-way coupled) ..... 102

Figure 5.1. Memory Structure of CUDA ..... 110
Figure 5.2. Conceptual Description of GPU-based Parallelization of Code ..... 110
Figure 5.3. Parallel Reduction for Solving Governing Equations of SPH ..... 111
Figure 5.4. Simplified Algorithm of Code in Terms of GPU Parallelization..... 111
Figure 5.5. Simplified Sorting and Parallelization Algorithm for SPH-DEM Coupled Code ..... 112
Figure 5.6. Speedup for GPU Parallelization of SPH-DEM Coupled Code..... 112

Figure 6.1. Mechanism of Debris Bed Self-Leveling ..... 124
Figure 6.2. Schematic View of Experimental Apparatus [Cheng, 2012]..... 124
Figure 6.3. Conditions for Benchmark Leveling Experiment ..... 125
Figure 6.4. Time Variation of Inclined Angle in Benchmark Experiment [Cheng, 2012] ..... 125
Figure 6.5. Geometry of SPH-DEM Coupled Leveling Simulation..... 126
Figure 6.6. Gas Injection in SPH-DEM Coupled Simulation..... 126
Figure 6.7. DEM Particles Used for Data (Height) Analysis..... 127
Figure 6.8. Snapshots Comparison b/w Experiment and SPH-DEM Simulation (a) $t' = 5s$, (b) $t' = 10s$, (c) $t' = 15s$..... 127
Figure 6.9. Validation Results for Time Variation of $R$ Value ..... 128
Figure 6.10. Effect of Gas Flow Rate on Self-Leveling Behavior..... 128

# Chapter 1

# Introduction

## 1.1 Background and Motivation

It is the cornerstone of the mitigation approach to ensure containment integrity even in the worst accident scenarios of a nuclear reactor. In-vessel retention (IVR) is one of a key mitigation strategy of LWR late-phase severe accident, which aims to retain the core melt in the reactor vessel through appropriate cooling including ex-vessel cavity flooding. If the IVR strategy fails, the massive corium releases out of the reactor pressure vessel (RPV) and falls to the ex-vessel coolant forming the melt jet. Various fuel behaviors occur during the melt jetting including fuel fragmentation, relocation, and dispersal. Based on the assumption that the ex-vessel pool is sufficiently deep, the melt jet can be fragmented into debris particles. It is known that there are various safety-related 3-phase issues associated with particulate solid debris such as melt jet breakup, melt spreading, agglomeration of solid debris, self-leveling, and so on. In this situation, the main concern of mitigation strategy is to effectively remove the decay heat from fragmented debris particles, since there is a possibility of debris cake formation, which is considered a potentially non-coolable state. Thus, it is required to

understand and evaluate the thermal-hydraulic behavior of particulate debris particles.

In terms of numerical modeling of such 3-phase behaviors, traditional studies on the 3-phase behavior of particulate debris solved all three phases as a continuous phase with appropriate conservative assumptions. In recent studies, there were some attempts to treat the solid debris as a discrete rigid body using Discrete Element Method (DEM), while adopting grid-based CFD methods for the fluid phase. Meanwhile, in many 3-phase phenomena associated with the severe accident, the vapor phase can act as the trigger of such behavior, which forms a sharp and dynamic interface with the liquid phase. Thus, the detailed CFD methods that can resolve the vapor and liquid phase can be effective for the above vapor-driven behaviors.

In this respect, this study was motivated by an idea that the coupling Discrete Element Method (DEM) with the Lagrangian-based CFD methods, which can completely resolve the interface between liquid and vapor without empirical correlation, can provide an effective numerical method to simulate vapor-driven 3-phase phenomena in detail. With this motivation, the in-house code was developed in this study through the coupling Lagrangian-based Smoothed Particle Hydrodynamics (SPH) method with Discrete Element Method (DEM).

Although the applicability of Lagrangian-based numerical code has been improved with the improvement of computation performance, there are still some limitations on time step and resolution which come from the explicit Lagrangian nature of SPH and DEM method. Thus, the code acceleration is essential in order to apply the Lagrangian numerical system to the analysis of real phenomena, especially for the multi-phase flow system. In this respect, the GPU-based code

parallelization was also performed in this study to overcome the inherent efficiency problem of the Lagrangian-based numerical method. Finally, the simulation of the vapor-driven leveling behavior of spherical solids was performed as a case study to demonstrate the applicability of the GPU-parallelized SPH-DEM coupled code developed in this study.

The developed numerical system in this study is expected to be a good alternative for the simulation of such phenomena that were difficult to handle with traditional numerical methods since the numerical schemes used in the code have a high potential for simulation of complicated physics with highly deformable geometry. In addition, this validated code system can contribute to hydrodynamic modeling studies for severe accident technology by performing numerical experiments on conditions that hard to be conducted on a laboratory scale.

## 1.2 Previous Studies

### 1.2.1 Numerical Studies on Particulate Debris Bed

Some previous modeling studies associated with the 3-phase flow including particulate solid debris are summarized in Table 1.1. The traditional coupling between the fluid and solid phase was achieved by a macroscopic approach based on the two-fluid models (TFM), which also treat the particulate debris as a continuous phase. Recently, the numerical coupling of the CFD method has been carried out through solving the momentum exchange with a Discrete Element

Method (DEM), which can analyze the collisions, translation, and rotation of each solid particle discretely, as shown in Table 1.1. The sedimentation behavior of solid particles was simulated in POSTECH [Hwang, 2019], and the self-leveling behavior of solid particle bed was covered in Kyushu university both in 2D and 3D [Guo, 2013]. The fluid phase of both studies was simulated using a grid-based CFD method. There was also a numerical study coupling the Lagrangian-based Finite Volume Particle (FVP) method with DEM to simulate the sloshing behavior of single-phase liquid, which is associated with the core disruptive accident of liquid metal reactor. However, there have been no studies on coupling a Lagrangian-based two-phase CFD method with the DEM model yet in terms of the behavior of fragmented fuel debris.

### 1.2.2 SPH-DEM Phase Coupling

The coupling studies of DEM and Smoothed Particle Hydrodynamics (SPH) method, which are used in this study, has recently been conducted in some other fields such as slurry transportation, wet screening, and so on. Some of the recent studies of SPH-DEM coupling are listed in Table 1.2. All of the studies in the table covered the coupling between single-phase fluid (SPH) and solid (DEM), with a various range in particle number depending on the parallelization methods. The total number of 14,704 particles were used in the study of Markauskas (2019), while more than 600M particles were used in the study of Xu (2019) using multi-GPU parallelized code. In this study, up to 300,000 Lagrangian particles were used, and it is considered to be sufficiently competitive compared to the recent study of Xu, which also performed a single GPU-based code acceleration.

## 1.3 Objectives and Scope

The purpose of this study is to develop a numerical analysis code that can handle the 3-phase hydrodynamic behavior of solid debris. An integrated numerical code for 3-phase flow has been developed by two-way phase coupling of multi-phase Smoothed Particle Hydrodynamics (SPH) model and solid particle Discrete Element Method (DEM) model. The developed SPH-DEM coupled code focuses on the detailed hydrodynamic behavior of three phases, as can be seen in the incorporated physical model in Figure 1.1.

Chapter 2 describes the implementation of the Smoothed Particle Hydrodynamics (SPH) model, which is applied for the simulation of liquid-vapor two-phase flow in this study. Chapter 3 covers the implementation of the Discrete Element Method (DEM) model for solid particles, while the algorithm and results for the two-way phase coupling of two models are summarized in Chapter 4. In Chapter 5, the strategies and results for GPU parallelization of developed code are discussed. Finally, the simulation results and discussions for the case study on debris particle self-leveling behavior are introduced in Chapter 6.

Table 1. Previous 3-Phase Modeling Studies of Solid Debris

| | phenomenon | Solid Phase Treatment | Liquid Phase Treatment | Phase # | Coupling Method | Dim |
|---|---|---|---|---|---|---|
| *Buck (2007) Yakush (2011)* | debris bed cooling | continuum | Eulerian | 3-phase | - | 2D |
| *Hwang (2019)* | debris bed sedimentation | Discrete (DEM) | Eulerian | 2-phase | two-way | 3D |
| *Guo (2013)* | self-leveling of debris bed | Discrete (DEM) | Eulerian | 3-phase | two-way | 2D |
| *Guo (2017)* | self-leveling of debris bed | Discrete (DEM) | Eulerian | 3-phase | two-way | 3D |
| *Guo (2013)* | sloshing with debris bed | Discrete (DEM) | Lagrangian (FVP) | 2-phase | one-way | 3D |

Table 2. Previous Studies on SPH-DEM Phase Coupling

| | Year | Field | Phase # | Max. SPH # | Max. DEM # | Parallelization |
|---|---|---|---|---|---|---|
| *Markauskas* | 2019 | Wet screening | Liquid, Solid | 12,104 | 2,600 | - |
| *He* | 2019 | Slurry transport | Liquid, Solid | ~10,000 | 7,755 | Single GPU |
| *Xu* | 2019 | granular aggregation | Liquid, Solid | 600 M | 27,030 | Multi GPU |

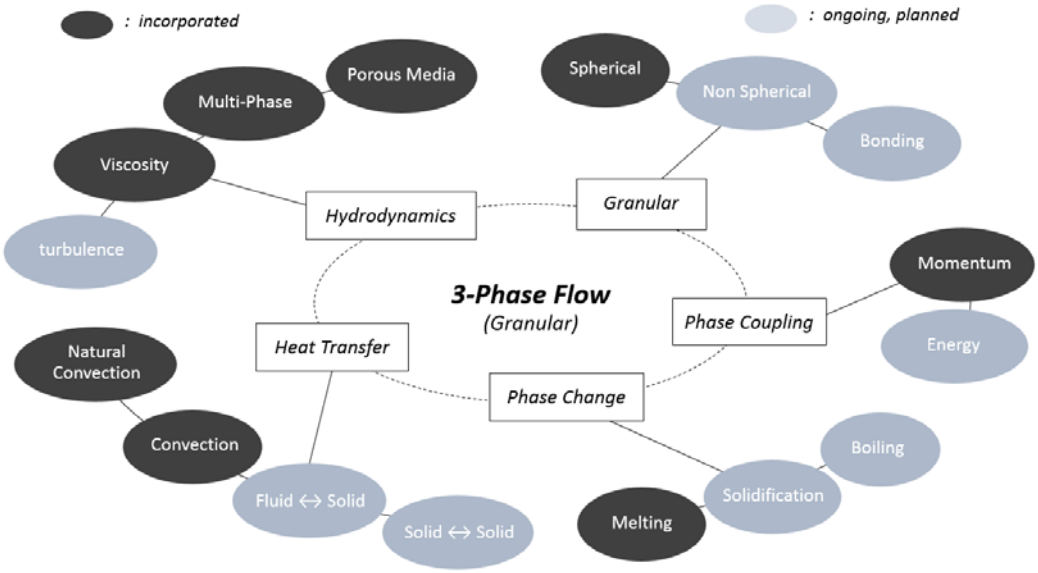


Figure 1.1. Incorporated Physical Models and Scope of This Study

# Chapter 2

# Fluid Phase: Smoothed Particle Hydrodynamics

Traditional hydrodynamic modeling studies for the multi-phase flow associated with severe accidents were conducted based on grid-based CFD methods. Many previous studies followed the statistical method based on two-fluid models (TFM) solving the averaged form of the governing equation for each phase. Some numerical techniques, including volume of fluid (VOF), and level set (LS) have been recently developed to apply grid-based methods for free surface flow. These methods are sufficiently mature and it is reported that the VOF model can effectively simulate the overall shape of multi-phase flow. However, there are still some difficulties in finding an exact interface for each phase, since the transport equation for phase interface function should be solved.

In the behavior of particulate sold debris such as debris sedimentation and self-leveling, the vapor phase acts as the driving force or trigger of overall motion, which forms a sharp and dynamic interface with the liquid phase. Thus, applying the Lagrangian-based detailed CFD methods that totally resolve the vapor and liquid area can be an effective modeling approach. In this respect, the Smoothed Particle Hydrodynamics (SPH) model, which is one of the best-known Lagrangian CFD methods, is implemented in this study for the numerical modeling of incompressible multi-phase flow.

## 2.1 Smoothed Particle Hydrodynamics (SPH)

Smoothed Particle Hydrodynamics (SPH hereafter) is a meshless Lagrangian method that was first developed in 1977 for astrophysical applications [Gingold, 1977]. In the SPH method, the fluid system is represented by a finite number of particles that carry individual properties, and the governing equations of each particle are solved in discretized smoothing formulation over the neighboring particles, as shown in Figure 2.1. The SPH method exhibits large advantages that come from Lagrangian nature in dealing with free surface liquid motion, highly deformable geometry, multiphase flow, and so on. Also, the convective term in the conservation equation is naturally reflected in the standard SPH without solving any nonlinear matrix, so that the convective flow and convective heat transfer can be implemented with simplicity. In addition, it is relatively easy to implement a wide range of physics in the existing framework.

In this section, the basic concept of the SPH method is described including particle approximation strategies of solving governing equations.

### 2.1.1 SPH Particle Approximation

The SPH is based on an interpolation method which is the theory of integral interpolants using delta function as follow,

$$f(x) = \int_{\Omega} f(x')\delta(x - x')dx' \tag{2.1}$$

where x variable x denotes the point in volume Ω, and δ denotes the Dirac delta function which has a value of zero everywhere except for at a certain point and whose integral over the entire region is equal to one. The SPH discretized formulation can be obtained by using the kernel functions that approximate a delta function as below.

$$f_i(r) = \sum_j f_j W(r_i - r_j, h) V_j \tag{2.2}$$

The variable $f_i$ is a function at the position $i$, subscript $j$ represents the adjacent particles of particle $i$, $V$ is the particle volume, and $W(r_i - r_j, h)$ stands for the kernel function, where $h$ denotes influencing area of the kernel weighting function. The kernel function is a symmetric weighting function of particle distance which should be normalized over its support domain. The particle system and kernel function are described in Figure 2.2.

### 2.1.2 SPH Particle Approximation of Derivatives

The SPH particle approximations of derivatives can be obtained by applying the Gauss integral formula to the above field approximation function (Equation 2.2) as follow.

$$\nabla \cdot f_i(r) \approx \int_{\Omega} \nabla \cdot \big(f(r)W(r-r',h)\big)dr' - \int_{\Omega} f(r)\nabla W(r-r',h)dr' \quad (2.3)$$

The first term on the right-hand side of the above equation can be replaced by the surface integral of the function $f(r)$ from the divergence theorem. Since the kernel weighting function has a non-zero value only within the smoothing radius, this surface integral value converges to zero. Finally, the first derivative of the field function $f(r)$ is expressed as a function of the kernel derivative, mass and density, as follow.

$$\nabla \cdot f_i(r) = \sum_j f_j \frac{m_j}{\rho_j} \nabla W\big(r_i - r_j, h\big) \quad (2.4)$$

From the above equation for kernel derivatives, various forms of the SPH differential operators can be derived including gradient, divergence, and Laplacian as summarized in Table 2.1.

### 2.1.3 Kernel Function

The kernel approximation functions are very important in the SPH method since they are closely related to the computational accuracy and stability of the SPH calculations. Because the kernel function is an approximation of the Dirac delta function, it should satisfy several conditions.

First, the integral value of kernel function over the support domain should have the value of 1. This so-called normalization condition of kernel function can be written as follow,

$$\int_{\Omega} W(x - x', h)dx' = 1 \tag{2.5}$$

where $\Omega$ is a computational domain, and $h$ is the smoothing length of the kernel function. Also, the kernel function should be defined only in the support domain. This compact condition can be expressed as below,

$$\mathrm{W}(r_i - r_j, h) = 0, \qquad where\ |r_i - r_j| > \kappa h \tag{2.6}$$

where $\kappa h$ is a support domain (searching range) in SPH calculation. The conditions for kernel approximation functions are summarized in Table 2.2 including the above unity condition and compact condition.

The SPH code developed in this study adopted Wendlend 6 kernel, which can inherently prevent particle clustering and improve the convergence of particle approximation.

### 2.1.4 Accuracy of SPH Approximation

The errors in SPH approximation can be estimated by using Taylor series expansion of field function $\mathrm{f(x')}$ around $\mathrm{x}$ as written below.

$$\langle f(x)\rangle = f(x)\int_{\Omega} W(x-x',h)dx' + f'(x)\int_{\Omega}(x'-x)\times W(x-x',h)dx' + r(h^2) \tag{2.7}$$

The integral of the first term on RHS unity, and the second term of RHS in above equation (9) vanishes since the kernel function satisfy the symmetry condition in interior region of calculation domain. Applying this conditions for kernel functions, the above equation (2.7) becomes,

$$\langle f(x)\rangle = f(x) + r(h^2) \tag{2.8}$$

The kernel approximation of a field function in SPH has second-order accuracy according to the above equation. However, the particle deficiency problem occurs when the support domain intersects with the computation domain (free surface open boundary). The unity condition and symmetry condition are no longer satisfied in the above equation (2.7) in this case. Thus, the kernel approximations are not of second-order accuracy anymore, and if the resolution of the particles is not sufficiently high, the numerical errors that occur in the boundary area can spread in the whole area in the form of pressure waves.

There have been many studies to restore the consistency of kernel approximation. In the SPH code developed in this study, the simple form of correction filter is applied to both kernel function and kernel gradient function in

order to ensure at least second-order accuracy in the whole computation domain. Instead of applying a better, but complex correction model, the accuracy of calculation was ensured through the code parallelization based on Graphical Process Unit (GPU) in this study. The results of GPU-based code acceleration are covered in Chapter 5.

### 2.1.5 Governing Equations for Incompressible Flow

The main equations describing the motion of an incompressible, Newtonian viscous fluid are the continuity equation and the Navier-Stokes equation which can be expressed in a Lagrangian frame as below,

$$\frac{d\rho}{dt} = -\rho\nabla \cdot \boldsymbol{u} \tag{2.9}$$

$$\rho\frac{\boldsymbol{du}}{dt} = -\nabla p + \mu\nabla^2\boldsymbol{u} + \rho\boldsymbol{g} \tag{2.10}$$

where $\rho$ and $\boldsymbol{u}$ are the density and velocity of the fluid, and $p$, $\mu$ and $\boldsymbol{g}$ denote pressure, dynamic viscosity, and the gravitational constant, respectively. The discretized SPH form of the continuity equation (2.9) for particle $i$ can be derived as below,

$$\left(\frac{d\rho}{dt}\right)_i = \rho_i \sum_j \frac{m_j}{\rho_j}\left(\boldsymbol{u_i} - \boldsymbol{u_j}\right) \cdot \nabla_i W_{ij} \tag{2.11}$$

where $j$ denotes the particles adjacent to the center particle $i$, and $m_j$, $\rho_j$, and $\boldsymbol{u_j}$ are the mass, density, and velocity vector of particle $j$, respectively. For incompressible flow, the LHS of the above equation (2.11) should always be zero. However, the general SPH model allows weak compressibility even for the incompressible fluids (Weakly-Compressible SPH, WCSPH hereafter). There are two methods to estimate density in the WCSPH model. One is to solve the above equation (2.11), and the other is to obtain the particle density based on the local particle distribution within the support domain as below, while the detailed derivation of the equation is summarized in Chapter 2.2.

$$\rho_i = \rho_{ref,i} \sum_j \frac{m_j}{(\rho_{ref})_j} W_{ij} \tag{2.12}$$

The first term on the RHS of the above momentum equation (2.10) represents the force because of the pressure gradient on the field. It can be discretized based on the SPH gradient operator equation as follow,

$$\left(\frac{1}{\rho}\nabla P\right)_i = -\sum_j m_j \left(\frac{p_i + p_j}{\rho_i \rho_j}\right) \nabla W_{ij} \tag{2.13}$$

where $p_j$ is the pressure of the nearby particle $j$. The second term on the RHS of the momentum equation (2.10) represents the viscous force of the fluid. The SPH discretized form of the laminar viscous force term is given below,

$$(\upsilon\nabla^2\boldsymbol{u})_i = \sum_j \frac{m_j\mu_{ij}\boldsymbol{r_{ij}}\cdot\nabla_i W_{ij}}{\rho_i\rho_j\left(\left|\boldsymbol{r_{ij}}\right|^2+\eta^2\right)}(\boldsymbol{u_i}-\boldsymbol{u_j}) \tag{2.14}$$

where $\mu_j$ and $\boldsymbol{r_{ij}}$ denote the dynamic viscosity and position vector of particle j. In the case of surface tension force, Continuum Surface Force (CSF) model is employed, which is covered in Chapter 2.2 in detail. The SPH formulations of each RHS term in the above equation (2.10) are summarized in Table 2.3.

In the WCSPH method, which is applied in the SPH code in this study, the pressure field is explicitly estimated as a function of local particle density using the Tait equation. The equation of state used in this study is as below,

$$p = \frac{{c_0}^2\rho_{ref}}{\gamma}\left[\left(\frac{\rho}{\rho_{ref}}\right)^{\gamma}-1\right] \tag{2.15}$$

where $\rho_{ref}$ is the standard reference density of the fluid, $\gamma$ is the polytrophic constant that determines the sensitivity of the pressure calculation, and $c_0 = c(\rho_0)$ is the reference speed of sound.

## 2.2 Multi-phase SPH Governing Equations

### 2.2.1 Treatment of Multi-Phase Flow

In solving multi-phase flow in SPH, several aspects should be considered, such

as interface tracking, discontinuous density field with high density ratio, surface tension, and so on. The interface tracking is an important issue for the Eulerian deterministic multi-phase model (ex. VOF), but the interface between two phases is naturally tracked due to the Lagrangian nature of each SPH particle.

In terms of handling discontinuous density field, the above governing equations (Equation 2.9, 2.10) should be discretized into volume-based form to prevent the unphysical contribution of particles with different density. In this reason, the above equation (2.13) and (2.14) were adopted for pressure gradient term and viscous term of N-S equation, respectively. In this respect, a new density estimation model is proposed in this study, which calculate the normalized density ($\rho/\rho_{ref}$) instead of local density. This normalized density model is introduced in next sub-section.

Besides, the surface tension model between two phases can play an important role depending on the scale of simulation. In this study, the surface tension based on Continuum Surface Force (CSF) model is adopted with some improvement in governing equations. This is summarized in chapter 2.2.3. In addition to physical surface tension force, an additional term for stabilizing the interface is also adopted, which is called the interface sharpness force [Grenier, 2009].

$$\left(\frac{d\boldsymbol{u}}{dt}\right)_i^{IS} = -\frac{\varepsilon}{m_i}\sum_j \left(|p_i|V_i^2 + |p_j|V_j^2\right)\nabla W_{ij}, \quad for\ f_i \neq f_j \qquad (2.16)$$

where $\varepsilon$ is a tuning parameter, which ranges between 0.01 and 0.1. This force is applied to the interface between two different phases. This force should be large enough to stabilize the interface between the phases, but it should be small

enough not to cause any unphysical behaviors.

### 2.2.2 Normalized Density Model

In general WCSPH method. The density of each fluid particle is estimated based on the mass summation equation as below,

$$\rho_i = \sum_j \rho_j \frac{m_j}{\rho_j} W_{ij} = \sum_j m_j W_{ij} \tag{2.17}$$

This standard SPH produces numerical pressure noise near the interface between the phases having different densities when it is directly applied. This problem is originated from handling the discontinuous density field in multi-phase flow as the continuous one. To simulate multi-phase flow with high-density ratio using the SPH, the normalized density, which is a continuous function on the interface, is suggested as the primary variable rather than the density in this study, as shown in Figure 2.3. In this approach, the normalized density is calculated as below.

$$\left(\frac{\rho}{\rho_{ref}}\right)_i = \sum_j \frac{m_j}{\rho_j} \cdot \left(\frac{\rho_j}{\rho_{ref,j}}\right) W_{ij} \tag{2.18}$$

Finally, the density of each particle can be calculated in simple form as below.

$$\rho_i = \rho_{ref,i} \sum_j \frac{m_j}{(\rho_{ref})_j} W_{ij} \tag{2.19}$$

When this normalized density approach is applied for density estimation, the physical discontinuity of density is fully ensured in the two-phase interface with a high density ratio, as shown in the simple validation simulation in Figure 2.4.

### 2.2.3 Continuum Surface Force (CSF) Model

In this study, the surface tension based on the Continuum Surface Force (CSF) model is adopted for handling two-phase interface interaction. The CSF model estimates the surface tension force on a macroscopic scale and is expressed as the product of the surface curvature and the surface normal. Based on the extensive review of the previous literature [Adami, 2010] [Morris, 2000], the following equations were used in this study,

$$\left(\frac{d\boldsymbol{u}}{dt}\right)_i^{CSF} = -\frac{\sigma_i}{\rho_i}\kappa_i \boldsymbol{n}_i \tag{2.20}$$

$$\boldsymbol{n}_i = \sum_j \frac{1}{V_i}\left(V_i^2 + V_j^2\right) c_{ij} \nabla W_{ij} \tag{2.21}$$

$$\kappa_i = -d \frac{\sum_j V_j \left(\hat{\boldsymbol{n}}_\iota - \varphi_{ij}\hat{\boldsymbol{n}}_j\right) \cdot \nabla W_{ij}}{\sum_j V_j |r_{ij}||\nabla W_{ij}|} \tag{2.22}$$

$$c_{ij} = \begin{cases} 0 & for\ f_i = f_j \\ \dfrac{\rho_i}{\rho_i + \rho_j} & for\ f_i \neq f_j \end{cases}, \quad \varphi_{ij} = \begin{cases} 1 & for\ f_i = f_j \\ -1 & for\ f_i \neq f_j \end{cases} \tag{2.23}$$

where $\sigma, \kappa, \boldsymbol{n}$ and $d$ denote a surface tension coefficient, the curvature, surface normal vector, and dimension $(d = 1,2,3)$. $\hat{\boldsymbol{n}}_\iota$ denotes the unit surface normal vector. In the above CSF model, however, the above curvature model of the interface can be calculated unphysically, especially for the second particle layer of the two-phase interface, as shown in Figure 2.5. When estimating the curvature of second layer particle, the unit normal vector of the surrounding particles is truncated (Figure 2.5, left), so that an unphysical curvature can be applied to the flat interface where the physical value should be calculated as zero.

In this respect, a new curvature model has been proposed in this study, which uses a non-truncated normal vector for curvature estimation instead of the above equation (2.21). This is possible since only the direction of the normal vector is important in curvature calculation rather than the exact magnitude of it. In this approach, the normal vector for curvature estimation ($\boldsymbol{n^c}$) is solved as below,

$$\psi_{ij} = \begin{cases} 0 & for\ f_i \neq f_j \\ 1 & for\ f_i = f_j \end{cases} \tag{2.24}$$

$$c_i^c = \frac{\sum_j \psi_{ij} W_{ij}}{\sum_j W_{ij}} \tag{2.25}$$

$$\boldsymbol{n_i^c} = \sum_j \frac{m_j}{\rho_j} \left(c_j^c - c_i^c\right) \nabla W_{ij} \tag{2.26}$$

Finally, the curvature in the above equation (2.22) is modified as below.

$$\kappa_i = -d\frac{\sum_j V_j\left(\widehat{\boldsymbol{n}_i^c} - \varphi_{ij}\widehat{\boldsymbol{n}_j^c}\right)\cdot\nabla W_{ij}}{\sum_j V_j|r_{ij}||\nabla W_{ij}|} \tag{2.27}$$

## 2.3 Implementation of SPH Model

### 2.3.1 Algorithm of SPH Code

Figure 2.6 shows a basic algorithm of the numerical model. First, the positions, properties, and conditions of each particle are initially prepared. Then, based on the given particle positions, the nearest-neighboring particle search (NNPS, hereafter) is conducted for each particle. Once the NNPS is completed, the density of each particle is estimated using the above equation (2.19). After that, the pressure is calculated for each particle explicitly by the equation-of-state (EOS) in Equation (2.15). After the pressure of each particle is calculated, the forces of each particle are estimated using the SPH force equations such as pressure, viscous, gravity, surface tension, surface sharpness force, and etc. Then, the velocity and position of each particle are updated using the calculated forces. If the particle positions are updated, the same calculation process is repeated from the NNPS. This iterative calculation is performed until the termination condition.

### 2.3.2 Nearest Neighboring Particles Searching (NNPS)

The SPH model solves the governing equations for each physics as a form of discretized summation for each neighboring particle; therefore, the nearest-neighboring particle search (NNPS) procedure for each particle should be performed before solving the governing equations. In general, the particles that are located within three times the initial particle distance are defined as neighboring particles of each center particle. In this case, there exist 25-30 neighboring particles within the smoothing radius in 2D geometry and 100-120 neighboring particles in 3D simulations. The NNPS is the most time-consuming part of the SPH calculation since it should be carried out for each neighboring particle for each targeted particle. Therefore, the performance of the whole SPH algorithm highly depends on the efficiency of the NNPS step.

The most intuitive NNPS algorithm is to go through the searching process for all particles in the computation domain. That is, it calculates the distance between the targeted particle and all the other particles to determine whether the particles are located within the support domain or not. In this case of the NNPS algorithm, the calculation time increases dramatically, in proportion to the square of the number of particles ($\sim N^2$). In recent studies, it is common to perform the uniform grid-based NNPS by assigning particles to grids. In this case, the NNPS can be carried out only for a few grids located near the center particle depending on the size of the grid; therefore, the calculation time can be considerably reduced ($\sim$ NlogN) [Xia, 2016]. The SPH code developed in this study also adopted the grid-based NNPS algorithm, as shown in Figure 2.7.

There are several ways to identify the neighboring particles among the particles

in each adjacent grid, depending on the data storage methods and the way to control the cache hit rate for memory performance. Typically, there are linked-list NNPS method and sorting-based methods. Since the SPH model in this study was implemented with parallelization in mind, the sorting-based NNPS algorithm was adopted rather than the former method. The specific algorithm and parallelization mechanism of NNPS is described in detail in Chapter 5.

### 2.3.3 Time Integration

In the SPH code developed in this study, a modified predictor-corrector scheme is applied [Gomez-Gesteira, 2012]. The predictor-corrector scheme divides the time integration into two steps. First, the prediction step extrapolates the physical variables as follows.

$$\begin{cases} \boldsymbol{u}^{p}_{t+\frac{\Delta t}{2}} = \boldsymbol{u}_t + \dfrac{\Delta t}{2}\left(\dfrac{d\boldsymbol{u}}{dt}\right)_{t-\frac{\Delta t}{2}} \\ \boldsymbol{r}^{p}_{t+\frac{\Delta t}{2}} = \boldsymbol{r}_t + \dfrac{\Delta t}{2}\left(\dfrac{d\boldsymbol{r}}{dt}\right)_{t-\frac{\Delta t}{2}} \\ \rho^{p}_{t+\frac{\Delta t}{2}} = \rho_t + \dfrac{\Delta t}{2}\left(\dfrac{d\rho}{dt}\right)_{t-\frac{\Delta t}{2}} \end{cases} \tag{2.28}$$

where $t$ and $\Delta t$ denote time and time step, respectively. The superscript *p* denotes ‘predictor’. The time derivatives of position, velocity, and density are newly evaluated by solving the discretized SPH formulations. After that, the field variables are re-integrated over the full-time step using the updated time derivatives in the correction step.

$$\begin{cases} \boldsymbol{u}^{c}_{t+\Delta t} = \boldsymbol{u}_t + \Delta t \left(\dfrac{d\boldsymbol{u}}{dt}\right)_{t+\frac{\Delta t}{2}} \\ \boldsymbol{r}^{c}_{t+\Delta t} = \boldsymbol{r}_t + \Delta t \left(\dfrac{d\boldsymbol{r}}{dt}\right)_{t+\frac{\Delta t}{2}} \\ \rho^{c}_{t+\Delta t} = \rho_t + \Delta t \left(\dfrac{d\rho}{dt}\right)_{t+\frac{\Delta t}{2}} \end{cases} \tag{2.29}$$

## 2.4 V&V Simulations

The demonstration of developed SPH code has been performed through several V&V simulations including some multi-phase cases. Table 2.4 shows the V&V simulation cases in progress for developed code. Among then, this section summarized the following four validation simulations that include some multi-phase flow issues.

- Rayleigh-Taylor Instability (2.4.1)
- Bubble Terminal Velocity (2.4.2)
- Dam-Break Simulation (2.4.3)
- Centralized Sloshing Simulation (2.4.4)

### 2.4.1 Rayleigh-Taylor Instability

In order to evaluate the normalized density approach proposed in this study (equation 2.19), Rayleigh-Taylor Instability simulation was performed in a two-fluid system with a density ratio of 1.8. As shown in Figure 2.8, the normalized density SPH model well simulates the interface between two fluids without any linearization of density both in qualitative and quantitative point of view, where the right-side graph in the figure shows the time-variant maximum height of lighter fluid, compared with the Layzer's theory.

### 2.4.2 Bubble Terminal Velocity

The SPH simulation for air bubble terminal velocity behavior in stagnant water (density ratio of 1,000) was conducted to demonstrate the capability of solving multi-phase flow. The terminal velocity of large bubbles increases with the equivalent diameter of the bubble since gravity is the dominant force in such a case, while the surface tension effect is dominant for smaller bubbles. As shown in Figure 2.9, the SPH results in this study well analyze the dominant force according to the size of the bubble, result in good prediction for terminal velocity value compared with the benchmark experiment [Clift, 1978]. The shape of the increasing bubble is also well simulated according to the bubble size.

### 2.4.3 Dam-Break Simulation

The dam-break simulation is a good benchmark problem for the Lagrangian-based numerical methods since it is associated with complex phenomena including surface break-up, high impact pressure, and other related effects. In this simulation, vertical square shape of the water column was collapsed with the beginning, as shown in Figure 2.10.

The simulation was conducted for 2D single-phase, 3D single-phase, and 2D multi-phase conditions, and the results of the simulation was compared with the experimental data of Martin and Moyce (1996) and also with the VOF results of Hirt (1981). The snapshots in Figure 2.10, Figure 2.11, and Figure 2.12 show that developed SPH code qualitatively well simulates the sharp surface of dam-breaking motion, while Figure 2.13 shows that the non-dimensional position of water in SPH simulation shows good agreement with the experimental data, especially for the multi-phase simulation.

Generally, the accuracy of SPH results are affected by the resolution of the particles and also the number density of neighboring particles since it solves the discretized governing equation through the weighted interaction with neighboring particles. In the multi-phase simulation above, it is free from the particle deficiency problems, and each targeted particle can interact with a sufficient number of neighboring particles. This inhibits the non-physical stream of front particles that can easily occur in the single-phase dam-break simulation.

### 2.4.4 Centralized Sloshing Simulation

The 3D single/two-phase simulations were performed on the centralized sloshing behavior, and the simulation results were compared with the benchmark

experiment data of Maschek et al. (1992). The experiments were composed of 5 series according to the geometry and initial conditions. The validation of developed code was performed in three out of five experimental cases listed below. The geometry and conditions for each case are summarized in Figure 2.14.

- Case 1: Centralized Sloshing (Perfect Symmetry)
- Case 2: Vertical Rods (Inner/Outer)
- Case 3: Asymmetric Sloshing

In each case above, the maximum sloshing height and arrival time were calculated and compared with the experimental data. In the case of centralized sloshing (Case 1), both single-phase and two-phase simulations were conducted in sufficiently high resolution. Up to 4,000,000 SPH particles were generated for single-phase simulation, while more than 10 million particles were used in the two-phase simulation. All of the SPH simulations qualitatively well reproduced the overall sloshing behavior as shown in Figures from 2.15 to 2.19.

In terms of quantitative validation, most of the results (maximum sloshing height, arrival time) are in good agreement with experiments especially for the high-resolution simulation, as summarized in Table 2.5. In detail, sloshing height on the wall is slightly over-estimated in the simulation compared to the experiments, which seems to be due to the perfect symmetry assumption in the simulation. The maximum sloshing height is calculated to be slightly lower than the experimental data, which is caused by the local particle resolution and numerical accuracy at the sloshing peak.

Thus the sensitivity on the particle size (resolution) has been conducted for the

maximum sloshing height. Generally, the lower resolution makes the lower number density of particles in center sloshing motion, finally result in a generation of fragmented particles that exhibits unphysical behavior. In other words, the bulk flow rate of piling up motion can be dropped significantly if the particle resolution gets poor. Thus, the sloshing height can be underestimated when the particle resolution is poor, and conversely, sufficient bulk flow can be ensured in the high-resolution simulation. As a result of the parametric study, the maximum sloshing height in SPH simulation converges to a certain value as the particle resolution increases as shown in Figure 2.20 and Figure 2.21.

Besides, the effect of multi-phase simulation has been analyzed through the centralized sloshing case (Case 1). As shown in the results of parametric studies on particle size (Figure 2.21), it can be seen that the multi-phase model predicts the sloshing height better than the single-phase model in the same particle resolution. This difference is due to the nature of the SPH method based on interaction with neighboring particles. In the two-phase SPH simulation, there are sufficient particles (including air particles) in the support domain regardless of the particle resolution in the sloshing peak, while serious particle deficiency occurs in low-resolution single-phase simulation. As a result of particle deficiency in single-phase simulation, an unphysical high-speed stream of solitary particles can be created with a high probability as shown on the right side of Figure 2.22. Likewise, the single-phase behavior near the gas trapping area may differ from two-phase simulation due to the particle deficiency issue. Since this small difference can be amplified as a large disturbance of a liquid wave, precise analysis based on the two-phase model is required for sloshing behavior.

The above results demonstrate that multi-phase simulation can produce better

results than single-phase analysis at the same particle spacing (resolution). However, it is better now to perform single-phase simulation with higher resolution, since many air particles should be considered in the multi-phase simulation. In order to achieve both accuracy and higher efficiency of simulation, it is necessary to further perform a kernel gradient correction in solving the governing equations (Equation 2.13, 2.14, 2.16, 2.27).

Table 2.1. SPH Differential Operators

| **Differential operator** | **SPH formulation** |
|---|---|
| Gradient | $\nabla \cdot f_i(r) = \rho_i \sum_j m_j \left( \frac{f_i}{{\rho_i}^2} + \frac{f_j}{{\rho_j}^2} \right) \nabla W(r_i - r_j, h)$ |
| Divergence | $\nabla \cdot \overrightarrow{f_i(r)} = \rho_i \sum_j m_j \left( \frac{\overrightarrow{f_i}}{{\rho_i}^2} + \frac{\overrightarrow{f_j}}{{\rho_j}^2} \right) \cdot \nabla W(r_i - r_j, h)$ |
| Laplacian | $\nabla^2 f_i(r) = \sum_j 2 \frac{m_i}{\rho_j} \left( \frac{f_i - f_j}{{\lvert r_{ij} \rvert}^2} \right) \underrightarrow{r_{ij}} \cdot \nabla W(r_i - r_j, h)$ |

Table 2.2. Conditions for Kernel Approximation Function

| **Conditions for Kernel Function** | |
|---|---|
| $\int_{-\infty}^{\infty} W(r_{ij},\ h)\ dr = 1$<br>Unity Condition | |
| $W(r_{ij}, h) = W(-r_{ij}, h)$<br>Symmetry Condition | $\lim_{h \to 0} W(r_{ij}, h) = \delta(r_{ij})$<br>Delta Function Property |
| $W(r_{ij}, h) = 0\ for\ \lvert r_{ij} \rvert > kh$<br>Compact Condition | $W(r_{ij}, \mathrm{h}) \geq 0\ for\ any\ r_{ij}$<br>Positive Condition |
| $\frac{\partial W(r,h)}{\partial r} < 0$<br>Monotonic Decrease | Sufficiently Smooth |

Table 2.3. SPH Governing Equations

| Governing Eq | SPH formulation |
|---|---|
| Mass Conservation | $\left(\frac{d\rho}{dt}\right)_i = \rho_i \sum_j \frac{m_j}{\rho_j}(\boldsymbol{u_i} - \boldsymbol{u_j}) \cdot \nabla_i W_{ij}$ |
| | $\rho_i = \rho_{ref,i} \sum_j \frac{m_j}{(\rho_{ref})_j} W_{ij}$ |
| Momentum Conservation | $\left(\frac{1}{\rho}\nabla P\right)_i = -\sum_j m_j \left(\frac{p_i + p_j}{\rho_i \rho_j}\right) \nabla W_{ij}$ |
| | $(\upsilon \nabla^2 \boldsymbol{u})_i = \sum_j \frac{m_j \mu_{ij} \boldsymbol{r_{ij}} \cdot \nabla_i W_{ij}}{\rho_i \rho_j \left(\lvert \boldsymbol{r_{ij}} \rvert^2 + \eta^2\right)} (\boldsymbol{u_i} - \boldsymbol{u_j})$ |
| Equation of State | $p = \frac{{c_0}^2 \rho_{ref}}{\gamma} \left[\left(\frac{\rho}{\rho_{ref}}\right)^{\gamma} - 1\right]$ |

Table 2.4. V&V Simulation Cases for Developed SPH Code

| **V&V Cases for developed SPH Model** | |
|---|---|
| **Single Phase SPH** | |
| N-S Equation (momentum conservation) | *Hydrostatic pressure*<br>*Poiseuille & Couette flow*<br>*Lid driven flow* |
| Multi-D Free-surface Hydrodynamics | *2D, 3D dam break*<br>*3D wave generation*<br>*3D liquid centralized sloshing* |
| Multi-fluid Flow | *Hydrostatic pressure (immiscible two-fluid)*<br>*Lock exchange problem*<br>*Rayleigh-Taylor instability* |
| **Multi-phase SPH** | |
| Large-scale Fluid Flow | *2D two-phase dam break*<br>*3D two-phase liquid centralized sloshing*<br>*Jet Breakup* |
| Meso-scale Multi-phase Hydrodynamics | *Bubble Terminal Velocity*<br>*Continuum based surface tension*<br>*Bubble lift behavior* |
| **Heat Transfer SPH** | |
| Heat Transfer | *Multi-D heat conduction*<br>*2D natural convection* |

Table 2.5. Comparison of Simulation Results with Benchmark Experient

| | | **Slosh at outer container wall** | | **Slosh at pool center** | |
|---|---|---|---|---|---|
| | | Time of max H [s] | Max H [cm] | Time of max H [s] | Max H [cm] |
| **Centralized Sloshing** | | | | | |
| Experiment [Maschek] | | 0.42 ± 0.02 | 16.0 ± 1.0 | 0.88 ± 0.04 | 40.0 ± 5.0 |
| SIMMER-Ⅳ [Pigny] | | 0.38 | 18.75 | - | >50 |
| SPH [Vorobyev] | | 0.40 ± 0.01 | 17.0 ± 0.6 | 0.87 ± 0.03 | 38.0 ± 6.0 |
| **This Study** high resolution | | 0.41 | 17.5 | 0.88 | 38.0 |
| **This Study** low resolution | | 0.40 | 17.0 | 0.86 | 36.3 |
| **This Study** two-phase, med | | 0.42 | 15.5 | 0.87 | 41 |
| **12 Vertical Rods (inner/outer)** | | | | | |
| Inner | Experiment [Maschek] | 0.44 ± 0.02 | 15.0 ± 1.0 | 0.90 ± 0.04 | 3.0 ± 2.0 |
| | SPH [Vorobyev] | 0.38 | 15.5 | 0.82 | 5.0 |
| | **This Study** | 0.43 | 16.0 | 0.88 | 3.5 |
| Outer | Experiment [Maschek] | 0.42 ± 0.02 | 15.0 ± 1.0 | 0.88 ± 0.04 | 15.0 ± 3.0 |
| | SPH [Vorobyev] | 0.41 | 08.5 | 0.84 | 15.5 |
| | **This Study** | 0.41 | 17.5 | 0.88 | 12.9 |
| **Asymmetric Sloshing** | | | | | |
| Experiment [Maschek] | | 0.36 ±0.02 | 14.0 ± 2.0 | 0.48 ± 0.02 | 24.0 ± 2.0 |
| **This Study** | | 0.36 | 16.5 | 0.47 | 21.0 |

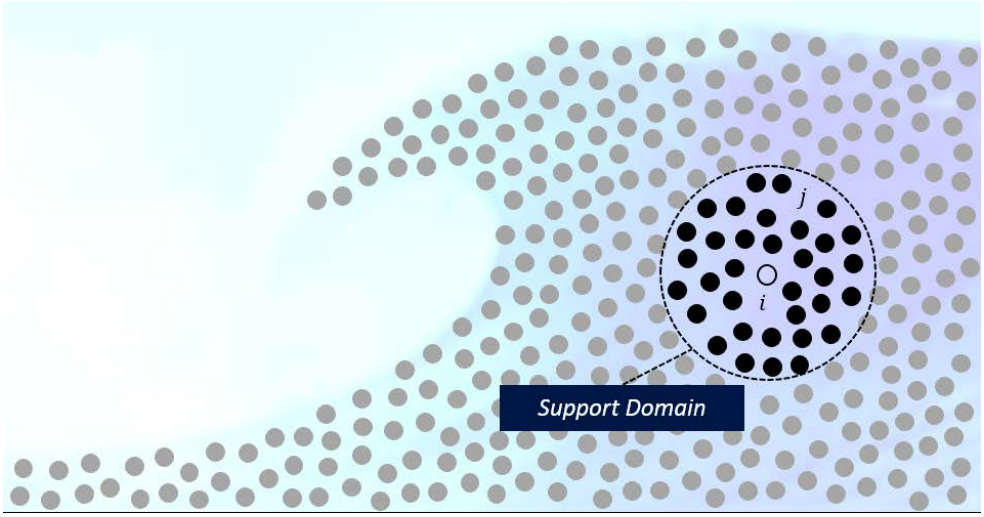


Figure 2.1. Particle System of Smoothed Particle Hydrodynamics (SPH)

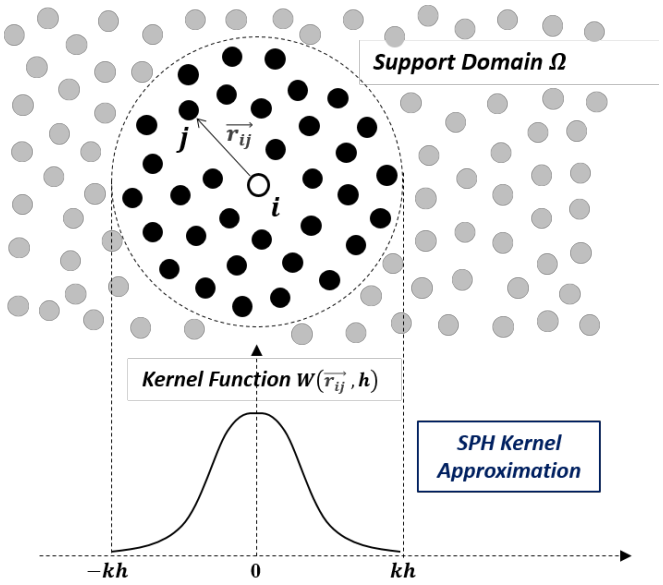


Figure 2.2. Kernel Weighting Function in SPH Method

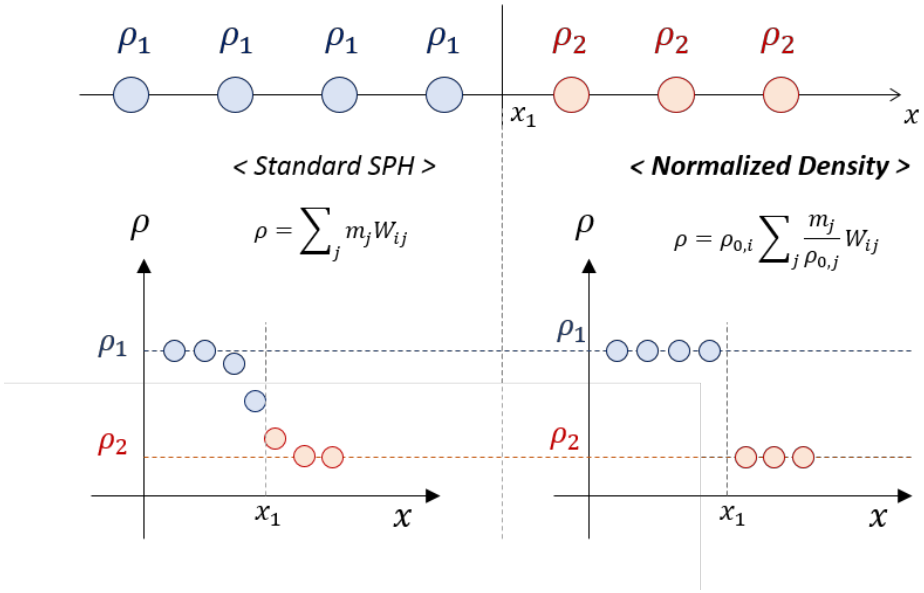


Figure 2.3. Normalized Density Approach for Density Estimation

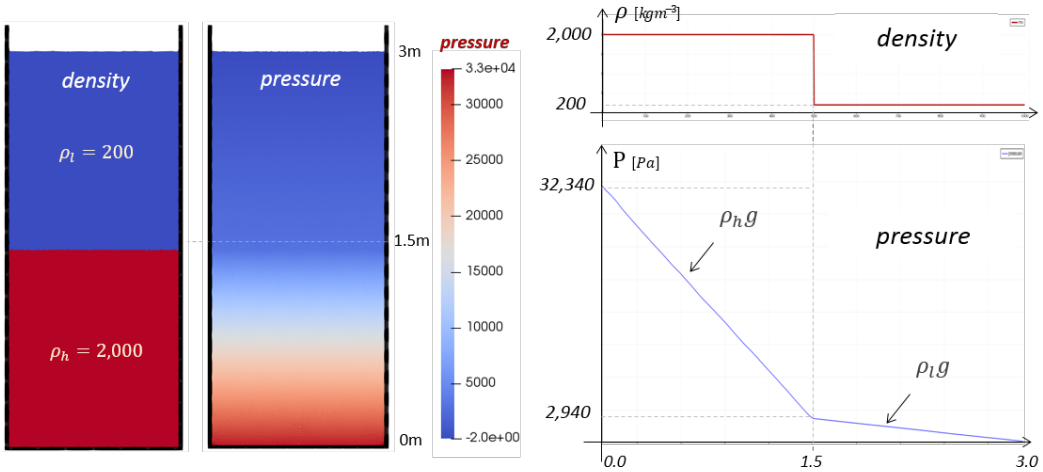


Figure 2.4. Density and Pressure Results for Two-Fluid Hydrostatic Problem

(With density ratio of 10)

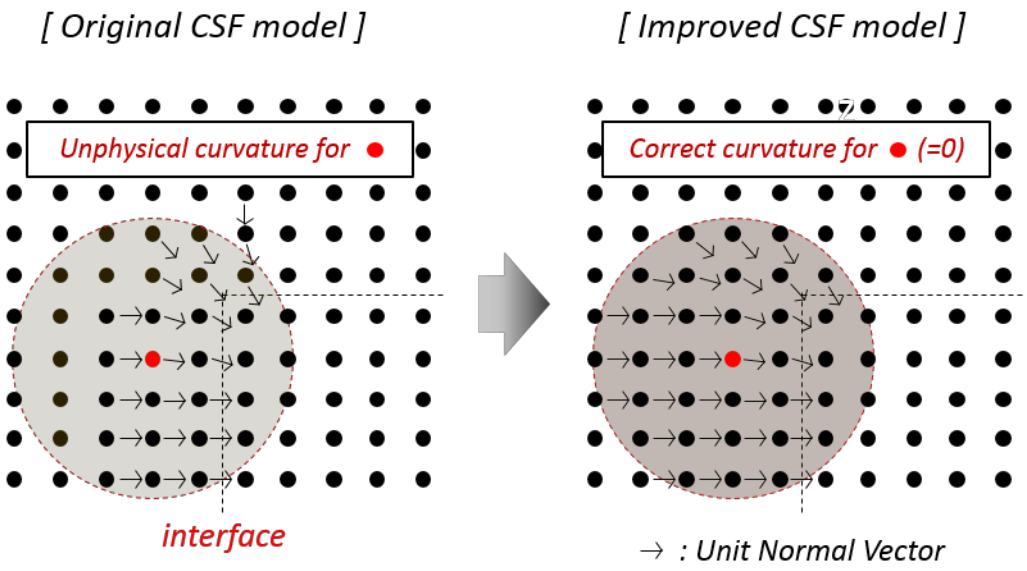


Figure 2.5. Improvement of CSF Model for Calculation of Curvature

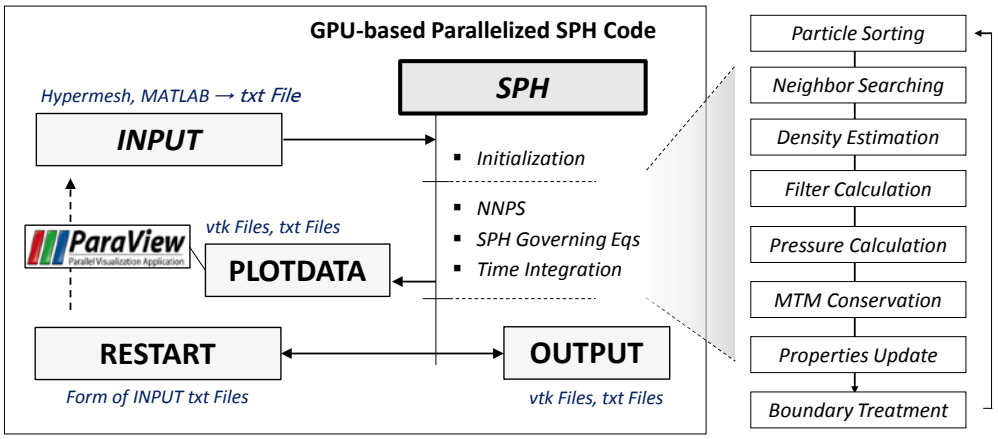


Figure 2.6. Structure and Simplified Algorithm of Developed SPH Code

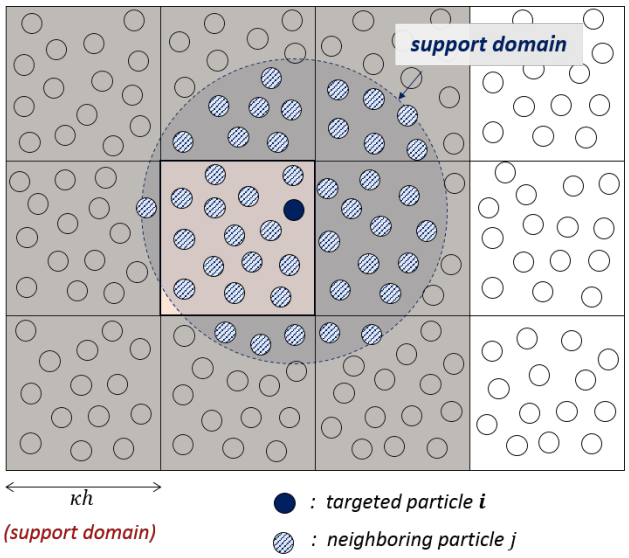


Figure 2.7. Grid-based Nearest Neighboring Particles Searching (NNPS)

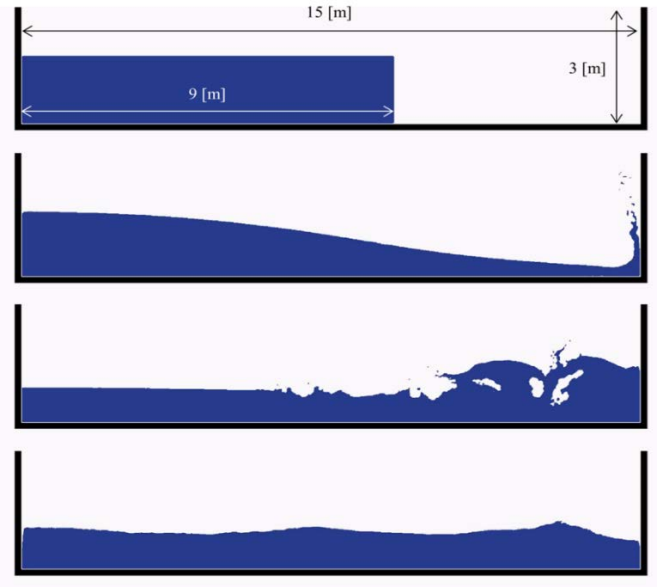


Figure 2.8. 2D SPH Simulation Results of Dam-Break Behavior

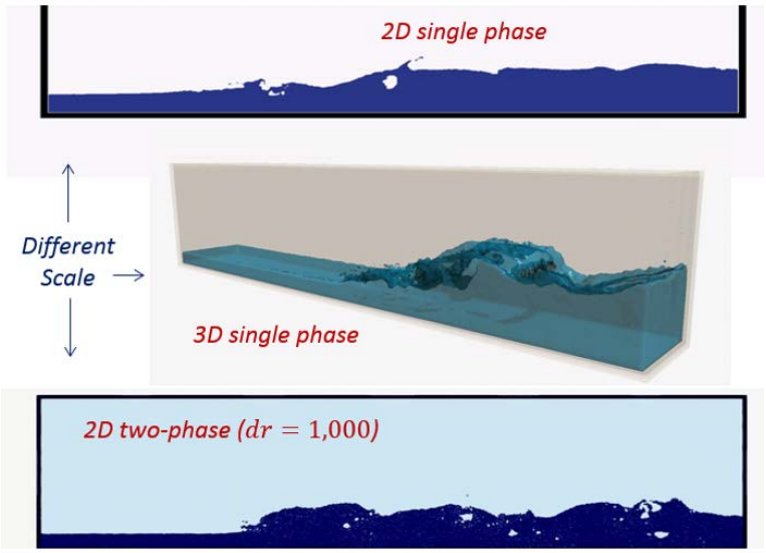


Figure 2.9. SPH Results on Dam-Break Simulation in Various Conditions (Single/Two Phase) and Scales

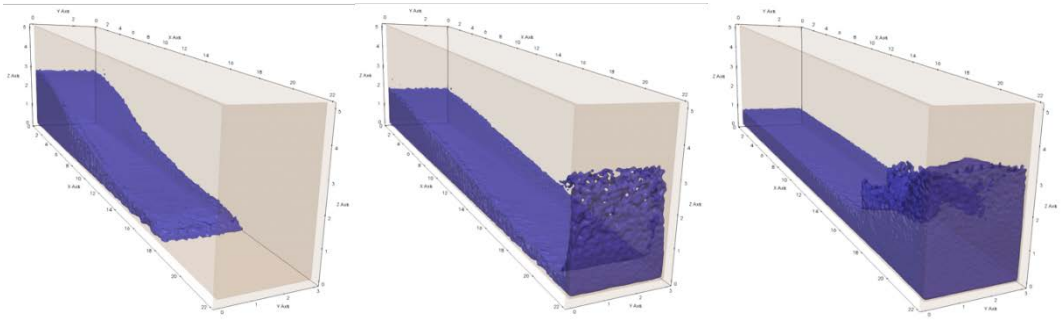

Figure 2.10. Snapshots for 3D Single Phase Dam-Break Simulation

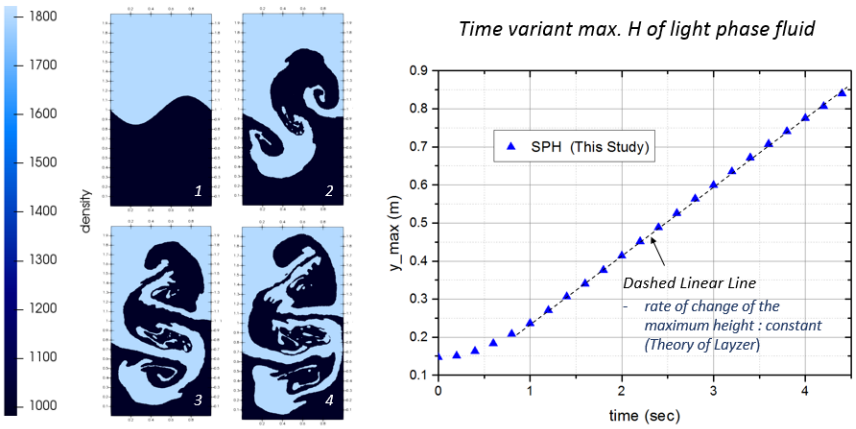


Figure 2.11. Results of Rayleigh-Taylor Instability Simulation

(Density Ratio: 1.8)

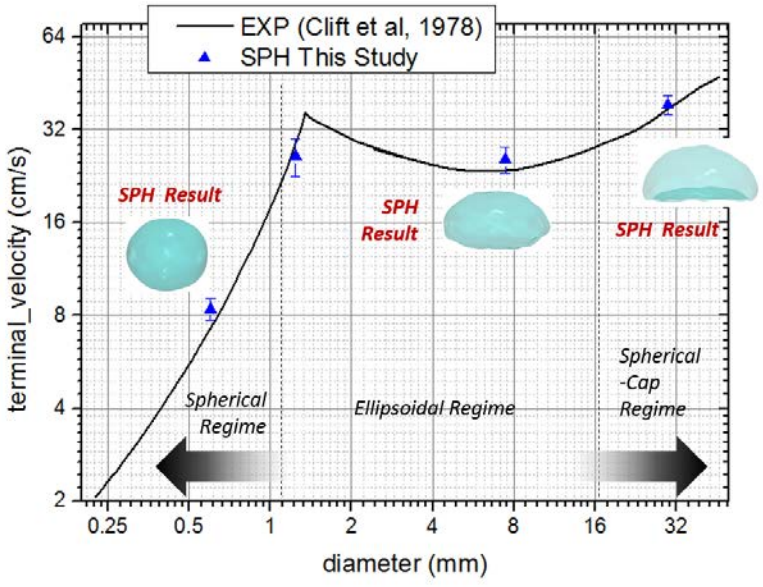


Figure 2.12. SPH Simulation Results for Bubble Terminal Velocity

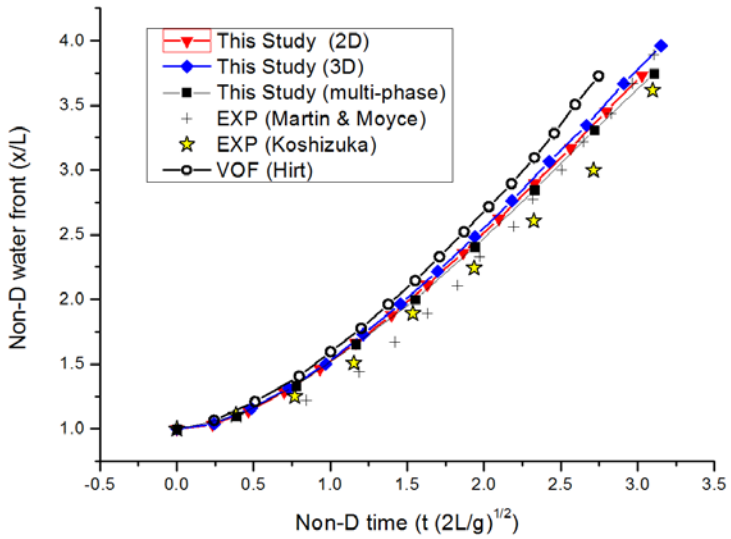


Figure 2.13. Validation Results of SPH Method for Multi-D, Multi-Phase Dam-Break Simulation

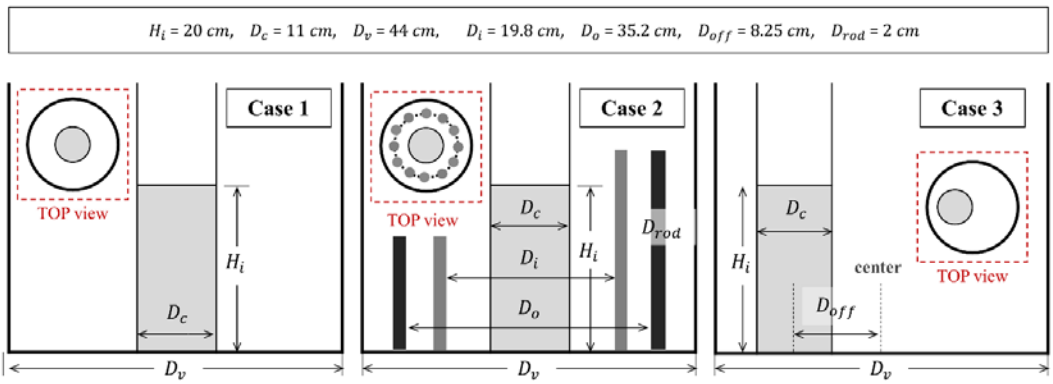


Figure 2.14. Geometry and Conditions for 3D SPH Sloshing Simulation

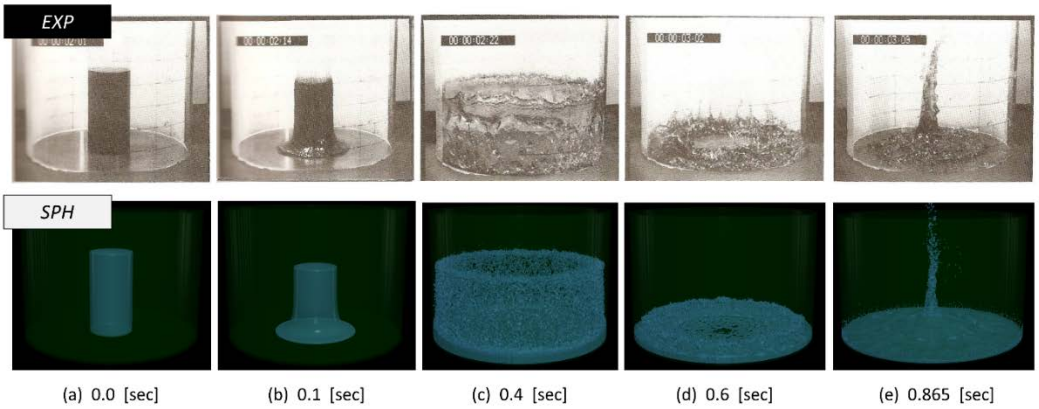


Figure 2.15. Qualitative Comparison of SPH Result with Benchmark Exp

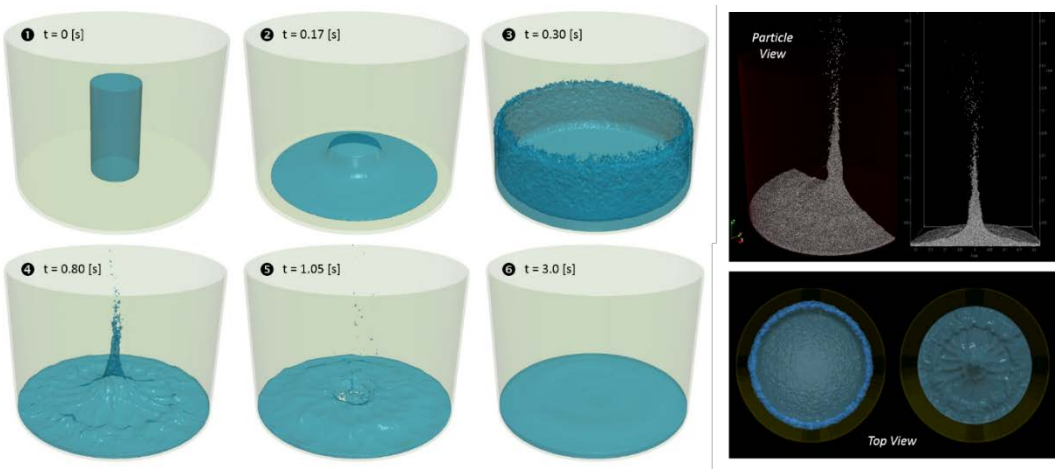


Figure 2.16. 3D Simulation Results of Developed SPH Code for Single-Phase Centralized Sloshing Behavior

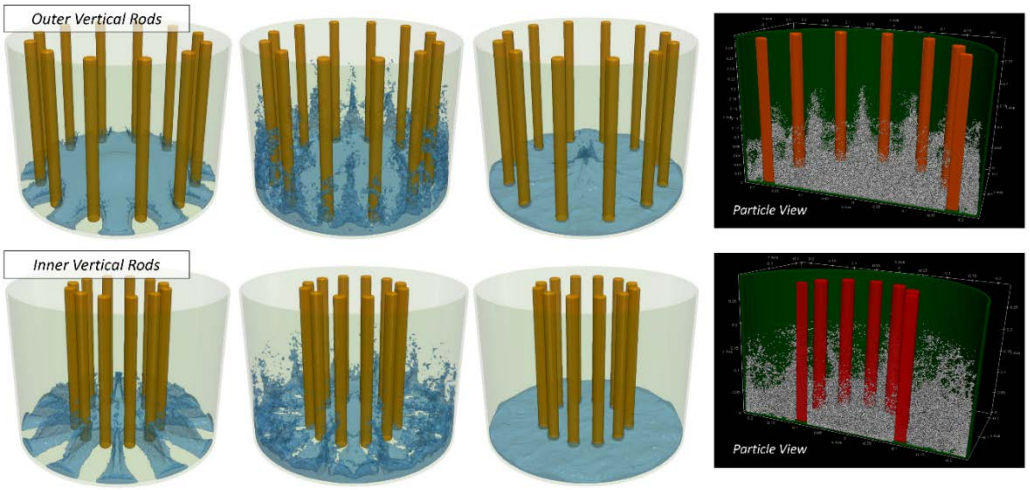


Figure 2.17. 3D Simulation Results of Developed SPH Code for 12 Vertical Rods Sloshing

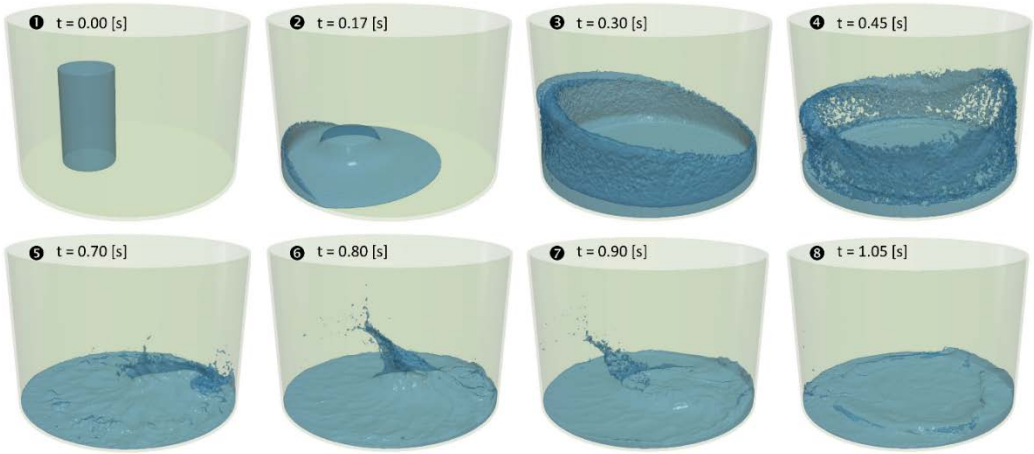


Figure 2.18. 3D Simulation Results of Developed SPH Code for Asymmetric Sloshing Condition

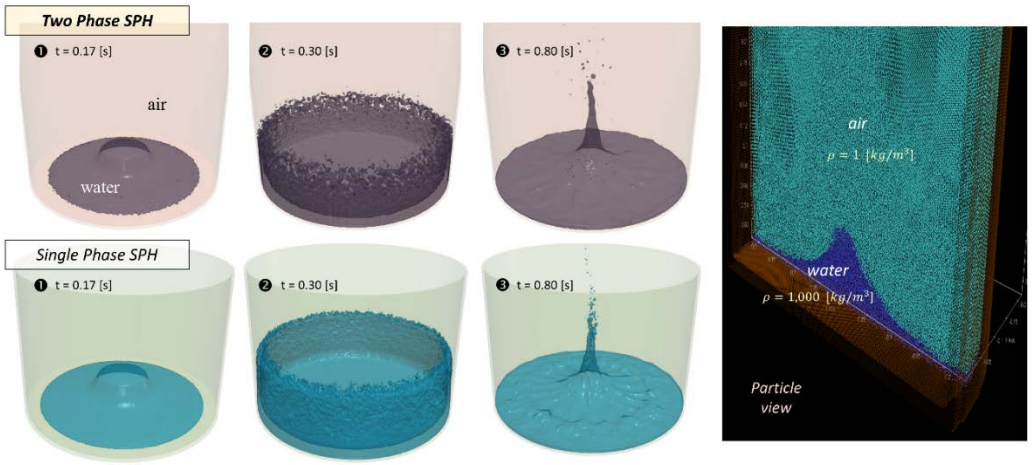


Figure 2.19. 3D Comparison Results for Two-Phase Centralized Sloshing Simulation

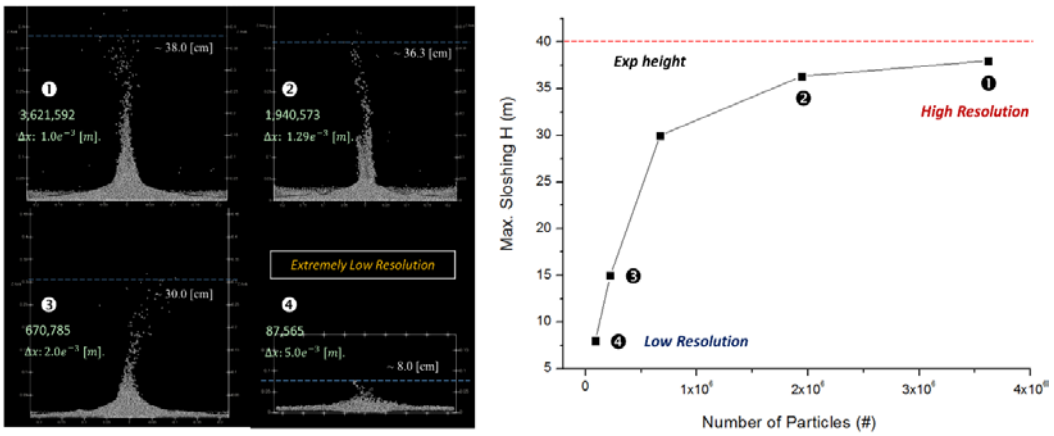


Figure 2.20. Effect of Particle Resolution in SPH Sloshing Simulation

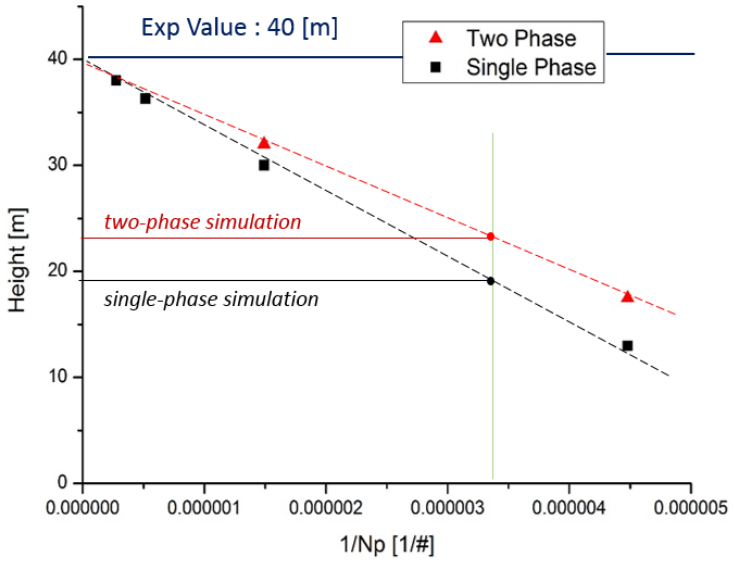


Figure 2.21. Convergence of Results for Particle Resolution (Single/Multi Phase)

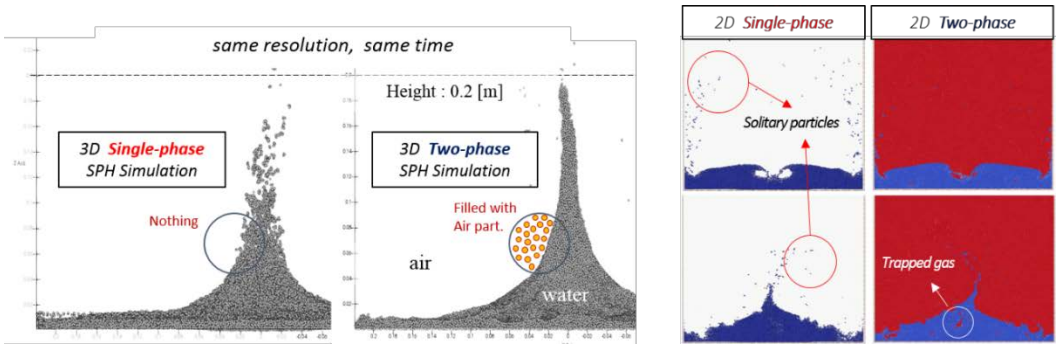


Figure 2.22. Difference between Single and Two Phase Simulation

# Chapter 3

# Solid Phase: Discrete Element Method

The numerical study of solid particle phase can be divided into the traditional continuum approach and discrete model based on the direct simulation method. The continuum approach treats the solid phase also as a continuous substance and ignores the specific behavior of each individual particle. The conservation of mass, momentum, and energy are solved in small regions of the solid material, while the interaction between solid particles depends on the empirical correlation. This continuum approach is effective when the average size of solid particles is much smaller than the characteristic length scale of the simulation.

However, in the case of the behavior of debris particles in this study, detailed interaction between solid particles should be considered since its own relocation behavior is an important parameter. Hence, in phenomena such as sedimentation and leveling of the solid debris bed, a numerical method based on a direct simulation that directly analyzes each collision between solid particles is suitable. A numerical model for the behavior of solid debris particles is constructed using the Discrete Element Method (DEM), which is the most mature and widely used direct simulation method. In this chapter, the DEM contact force model formulation, versatile wall boundary conditions, implementation algorithm, and simulation results including V&V cases are presented in order.

## 3.1 Discrete Element Method (DEM)

Discrete Element Method (DEM), which is firstly proposed by Cundall (1979), is the most widely used numerical method for describing the mechanical behavior of discrete rigid particles. DEM has been applied for the behavior of granular material such as material packing, heaping, hopper flow, and so on. In the DEM technique, the translation and rotation behavior of the particulate rigid body is analyzed by calculating the force and torque due to collision based on Newton's second law of motion. The simplified governing equations for the translational and rotational motion of each solid particle can be written as,

$$m_a \frac{d^2 \boldsymbol{r_a}}{dt^2} = \sum_b \boldsymbol{F_{ab}} + m_a \boldsymbol{g_a} \tag{3.1}$$

$$I_a \frac{d^2 \boldsymbol{\theta_a}}{dt^2} = \sum_b \left( \boldsymbol{r_{ac}} \times \boldsymbol{F_{ab}^t} \right) \tag{3.2}$$

where $m_a$ and $I_a$ are the mass and the moment of inertia of the particle a, $\boldsymbol{r_a}$ and $\boldsymbol{\theta_a}$ are the position vector and angular position vector of the particle a, respectively, and $\boldsymbol{r_{ac}}$ is the vector from the center of mass of particle a to contact point. Only the tangential component of the contact force $\boldsymbol{F_{ab}^t}$ is involved in rotational behavior.

The general DEM simulation sequence is as follows where a detailed DEM algorithm implemented in this study is summarized in section 3.4.

(1) Contact detection between particles

(2) Calculation of contact force ($F_{ab}$) and torque ($\tau_{ab}$)

(3) Calculation of wall condition (detection, collision, sliding, rolling)

(4) Calculation of new position

## 3.2 DEM Contact Force

### 3.2.1 Soft-sphere Contact Model

The DEM contact model can be classified into a hard-sphere model and a soft sphere model depending on the analytic perspective of inter-particle collision. In the hard sphere model, the momentum exchange between particles is solved just in a single collision. Hence, there is a difficulty in solving the collision matrix and there is a limitation that it can be only discussed for smooth spherical particles [Luding, 2008]. For this reason, the hard-sphere model is used within a limited range, while a soft-sphere based collision model is generally used to simulate the behavior of granular material including debris particles in this study.

In the soft sphere model, the collision between granular particles is solved in a spring-dashpot system which allows a thin overlap of contact particles (Figure. 3.1). As shown in Figure 3.1, the spring-dashpot system consists of a spring which provides the elasticity and a damper that corresponds to the energy dissipation in the collision. In the tangential direction, there is also the slider that analyzes rotation and energy dissipation due to the friction. Various contact force models for each of these components are known, which are summarized in the following sub-sections.

### 3.2.2 Contact Force Model

In the soft-sphere based spring-dashpot system, the collision between two particles is a continuous process in a short time period with a slight overlap between particles. It is inherently difficult to accurately describe the inter-particle contact physics over the contact area, as it is related to many geometrical and physical factors such as the shape, material properties, and also movement state of particles [Zhu, 2007]. Hence, the DEM generally adopts simplified equations to determine the contact forces and torques in order to be computationally efficient.

The contact force model can be classified on the basis of how the elastic force for the spring in Figure 3.1 is described. The simplest form of contact force is a linear model, which is proposed by Cundall (1979), where the linear spring is used for the elastic deformation. In addition, there is a nonlinear contact force model in which a nonlinear restoring force (proportional to $3/2$ power of overlap) acts according to Hertz's theory for elastic contact of spheres. Mindlin and Deresiewicz (1953) proposed a general tangential force model, and in combination with Hertz's theory, the most widely used Hertz-Mindlin contact force model was derived. There is also JKR model based on physical elastic collisions [Johnson, 1971], and the normal component formulation of each contact force is briefly summarized in Table 3.1.

In the DEM model implemented in this study, the Hertz-Mindlin contact force model is applied due to its accuracy and simplicity, which is described in detail in the following sub-section.

### 3.2.3 Hertz-Mindlin Contact Force Model

This sub-section describes the Hertz-Mindlin contact force model in detail, which is applied in the DEM model of this study. As described in the previous sub-sections and also shown in Figure 3.1, the collision force between particles is divided into the normal component and the tangential component first, and each is divided into the elastic spring term corresponding to the conservative force and damping term corresponding to dissipation term again. This can be expressed as the following equations.

$$\boldsymbol{F_{ab}} = f_{ab}^{n}\,\hat{\boldsymbol{n}} + f_{ab}^{t}\,\hat{\boldsymbol{t}} \tag{3.3}$$

$$f_{ab}^{n} = f_{spring}^{n} + f_{damper}^{n} \tag{3.4}$$

$$f_{ab}^{t} = f_{spring}^{t} + f_{damper}^{t} \tag{3.5}$$

The unit vector $\hat{\boldsymbol{n}}$ and $\hat{\boldsymbol{t}}$ respectively denote the normal and tangential component between particle a and particle b. $f_{ab}^{n}$ and $f_{ab}^{t}$ represent the magnitude of normal and tangential component of contact force, and each is divided into the elastic term($f_{spring}$) and damping term($f_{damper}$) again.

In the collision situation (Figure. 3.2) of particle a and b, the equivalent properties are defined as follows where $M$, $R$, $E$, $G$, and $\nu$ are mass, radius, Young's modulus, shear modulus, and Poisson's ratio of each particle, respectively.

$$M_{ab}{}^{*} = \left(\frac{1}{M_a} + \frac{1}{M_b}\right)^{-1} \tag{3.6}$$

$$R_{ab}{}^{*} = \left(\frac{1}{R_a} + \frac{1}{R_b}\right)^{-1} \tag{3.7}$$

$$E_{ab}{}^{*} = \left(\frac{1 - \nu_a{}^2}{E_a} + \frac{1 - \nu_b{}^2}{E_b}\right)^{-1} \tag{3.8}$$

$$G_{ab}{}^{*} = \left(\frac{2 - \nu_a}{G_a} + \frac{2 - \nu_b}{G_b}\right)^{-1} \tag{3.9}$$

According to the Hertz's theory of inter-particle elastic normal contact force, the maximum pressure ($P_{max}$) and elastic normal contact force ($f_{spring}^{n}$) in the collision between two spheres are written as follows where $\delta_c$ is contact radius in Figure 3.2.

$$P_{max} = \frac{3\, f_{spring}^{n}}{2\pi {\delta_c}^2} \tag{3.10}$$

$$f_{spring}^{n} = \frac{4E_{ab}{}^{*}}{3R_{ab}{}^{*}}{\delta_c}^3 = \frac{4E_{ab}{}^{*}}{3R_{ab}{}^{*}}\sqrt{R_{ab}{}^{*}\delta_n}^3 = \frac{4}{3}E_{ab}{}^{*}\sqrt{R_{ab}{}^{*}}\ {\delta_n}^{3/2} \tag{3.11}$$

The damping term ($f_{damper}^{n}$) in normal direction also can be derived in a nonlinear form as below:

$$f_{damper}^{n} = -\sqrt{\frac{10}{3}}\frac{\ln(e)}{\sqrt{ln(e)^2 + \pi^2}}\sqrt{M_{ab}{}^{*}K'_n}\, v_n \tag{3.12}$$

$$K'_n = 2E_{ab}{}^*\sqrt{R_{ab}{}^*\delta_n} \tag{3.13}$$

where $e$ is the restitution coefficient between two particles.

Similar to the normal force, the tangential force term, $f_{spring}^t$ and $f_{damper}^t$ are expressed as below.

$$f_{spring}^t = 8G_{ab}{}^*\sqrt{R_{ab}{}^*\delta_n}\,\delta_t = k_t\delta_t \tag{3.14}$$

$$f_{damper}^t = \sqrt{\frac{10}{3}}\frac{ln(e)}{\sqrt{ln(e)^2+\pi^2}}\sqrt{M_{ab}{}^*k_t} \tag{3.15}$$

Here, the overlap in the tangential direction $\delta_t$ is not a geometrically determined variable. $\delta_t$ can be obtained by accumulating the relative velocity between particles at the contact point during the collision period as follows where $v_t$ and $\mathrm{t}'$ are the relative velocity between particles and time, respectively.

$$\Delta\delta_t = v_t\Delta t' \tag{3.16}$$

On the other hand, the contact force in the tangential direction cannot be larger than the friction force acting on the contact surface. When the contact force exceeds the maximum friction force, sliding motion occurs between two contact particles. Therefore the contact force in the tangential direction can be written as below where $\mu_t$ is a friction coefficient between two contact particles.

$$f_{ab}^{t} = min\left(f_{spring}^{t} + f_{damper}^{t}, -\mu_t |f_{ab}^{n}\, \hat{\boldsymbol{n}}|\right) \tag{3.17}$$

The Hertz-Mindlin contact force in each direction corresponding to equations from (3.11) to (3.17) are summarized in Table 3.2.

## 3.3 Wall Boundary Conditions

### 3.3.1 Versatile Wall Boundary Model

The interaction between the solid particles and the wall boundary can be classified into two types. One is the collision with a sufficient normal velocity component, and the other is particle sliding (or rolling) on the boundary surface. In general, when the solid particle collides with a wall boundary, the particle velocity and its angular velocity are balanced within several collisions due to the friction of the wall surface, resulting in a quasi-rolling state. However, the collision behavior and sliding (or rolling) behavior are fundamentally different in physics. Hence, when the solid particle is initially placed on the wall boundary like billiard simulation, solving the solid particle behavior only based on a collision dynamics may cause abnormally large friction force, which can underestimate the particle motion. In addition, there is a limit to control this problem through the empirical modeling of the restitution coefficient, since the results can be influenced by the step size of time integration.

In the case of the self-leveling behavior of solid debris in the ex-vessel cooling,

granular debris particles are packed on the bottom concrete boundary as shown in Figure 1.2. When two-phase natural convection of the fluid occurs due to the decay heat generated from debris particles, solid particles move by drag force. Considering the velocity of the flow and the load due to the upper debris particles, the bottom particles may slide or roll on the boundary in continuous contact with the wall boundary. Therefore, the debris particle behavior can be estimated incorrectly if the interaction with the wall is considered only by the collision. Since the debris particle spreading and relocation behavior greatly affects the coolability of decay heat, a suitable model for the surface behavior of solid particles is required.

In order to overcome these limitations, a new versatile wall boundary model that considers both collision and sliding (or rolling) motion of solid particles is proposed as shown in Figure 3.3. In this boundary model, the collision equations are solved if the magnitude of the normal velocity component is sufficient while sliding and rolling behavior are solved if the magnitude is below a certain threshold. The implementation sequence of this wall boundary model is as follows.

(1) Determine if the solid particle contacts with the wall based on the primitive object function as shown in Figure 3.4.
(2) Calculate the surface normal vector at the contact point
(3) Calculate the surface tangential vector considering both transitional and rotational velocity of the particle
(4) Calculate the normal velocity component $\boldsymbol{v_n}$
(5) Solve the equations for collision dynamics if $|\boldsymbol{v_n}|$ is above the criteria

(6) Solve the physics for sliding & rolling if $|\boldsymbol{v_n}|$ is below the criteria

(7) Update particle position, velocity, angular velocity

The governing equations for each physics are described in the following sections as well as V&V simulations for this wall boundary model.

### 3.3.2 Particle Collision with the Wall

The collision dynamics are solved when a solid particle collides with a wall with sufficient normal velocity as shown in Figure 3.5. If the solid particle approaches the wall with velocity of $v_0$, and angular velocity of $\omega_0$, the velocity vectors at the contact point before and after the collision are calculated as follows,

$$\boldsymbol{v_{c0}} = \boldsymbol{v_0} - \boldsymbol{\omega_0} \times r\,\hat{\boldsymbol{n}} \tag{3.18}$$

$$\boldsymbol{v_{c1}} = \boldsymbol{v_1} - \boldsymbol{\omega_1} \times r\,\hat{\boldsymbol{n}} \tag{3.19}$$

where $\hat{\boldsymbol{n}}$ is the unit normal vector at the contact point $C$, and $\boldsymbol{v_1}$, $\boldsymbol{\omega_1}$ are the velocity and angular velocity vector after the collision, respectively. The unit tangential vector is also obtained by dot product of $\boldsymbol{v_{c0}}$ (Equation 3.18) with normal unit vector $\hat{\boldsymbol{n}}$.

$$\hat{\boldsymbol{t}} = \frac{\boldsymbol{v_{c0}} - (\boldsymbol{v_{c0}} \cdot \hat{\boldsymbol{n}})\hat{n}}{|\boldsymbol{v_{c0}} - (\boldsymbol{v_{c0}} \cdot \hat{\boldsymbol{n}})\hat{n}|} \tag{3.20}$$

In this case, the change of the momentum and angular momentum vector between the collisions are satisfy the equations below.

$$m\,(\boldsymbol{v_1} - \boldsymbol{v_0}) = \boldsymbol{J} \tag{3.21}$$

$$I\,(\boldsymbol{\omega_1} - \boldsymbol{\omega_0}) = -r\,\hat{\boldsymbol{n}} \times \boldsymbol{J} \tag{3.22}$$

Defining the restitution coefficient of the normal direction ($e_n$) and the tangential direction ($e_t$), the dot products of momentum vector in each direction are summarized as follows.

$$\boldsymbol{J} \cdot \hat{\boldsymbol{n}} = -m\,(1 + e_n)\,(\boldsymbol{v_{c0}} \cdot \hat{\boldsymbol{n}}) \tag{3.23}$$

$$\boldsymbol{J} \cdot \hat{\boldsymbol{t}} = -\left(\frac{1}{m} + \frac{r^2}{I}\right)^{-1} (1 + e_t)\,(\boldsymbol{v_{c0}} \cdot \hat{\boldsymbol{t}}) \tag{3.24}$$

Substituting these equations into the above equation (3.21) and (3.22), the final expressions for velocity and angular velocity after the collision are derived as below.

$$\boldsymbol{v_1} = \boldsymbol{v_0} - (1 + e_n)\,(\boldsymbol{v_{c0}} \cdot \hat{\boldsymbol{n}})\,\hat{\boldsymbol{n}} - \frac{1}{m}\left(\frac{1}{m} + \frac{r^2}{I}\right)^{-1} (1 + e_t)\,(\boldsymbol{v_{c0}} \cdot \hat{\boldsymbol{t}})\;\hat{\boldsymbol{t}} \tag{3.25}$$

$$\boldsymbol{\omega_1} = \boldsymbol{\omega_0} + \frac{r}{I}\left(\frac{1}{m} + \frac{r^2}{I}\right)^{-1} (1 + e_t)(\boldsymbol{v_{c0}} \cdot \hat{\boldsymbol{t}})\,(\hat{\boldsymbol{n}} \times \hat{\boldsymbol{t}}) \qquad (3.26)$$

### 3.3.3 Sliding and Rolling on the Wall Boundary

If the solid particle is in constant contact with the wall without sufficient normal velocity component, sliding and rolling occurs on the surface for the particle with curvature. In this situation, the velocity and angular velocity of particle over time ($t'$) are expressed in relation to the sliding friction coefficient ($\mu_s$) as follows,

$$\boldsymbol{v} = \boldsymbol{v_0} - \left(\mu_s g cos\alpha\, \hat{\boldsymbol{t}}\right) t' \qquad (3.27)$$

$$\boldsymbol{\omega} = \boldsymbol{\omega_0} - \left(\frac{\mu_s m g cos\alpha}{I}\, \boldsymbol{r} \times \hat{\boldsymbol{t}}\right) t' \qquad (3.28)$$

where $m$, $I$, and α are the mass, rotational inertia and surface slope, respectively. When solid particles roll (one-to-one contact between the particle surface and the boundary surface) over the wall boundary, the magnitude of velocity $|\boldsymbol{v}|$ is balanced with the magnitude of the cross product of $\boldsymbol{r}$ and $\boldsymbol{\omega}$. From this condition, the speed of rolling ($v_{roll}$) and the time taken to roll ($t_{roll}$) to be used for V&V simulation of wall boundary model, can be derived as follows.

$$v_{roll} = v_0 - (v_0 - r\omega_0)\left[1 + \frac{m\,r^{\,2}}{I}\right]^{-1} \tag{3.29}$$

$$t_{roll} = \frac{v_0 - r\omega_0}{\mu_s g cos\alpha}\left[1 + \frac{m\,r^{\,2}}{I}\right]^{-1} \tag{3.30}$$

When the spherical solid starts rolling, the relative velocity at the contact point is zero, so even if a non-conservative force acts, it does not work. In other words, a rolling rigid body can theoretically roll infinitely without any energy dissipation. However, in reality, there is resistive rolling friction ($\mu_r$) in the physical relationship between the wall boundary and the solid material that damping the rolling behavior such as the surface roughness. The velocity and acceleration considering rolling friction can be summarized as follows.

$$\boldsymbol{v} = \boldsymbol{v_0} - \left(\mu_s g cos\alpha\, \hat{\boldsymbol{t}}\right) t' \tag{3.31}$$

$$\boldsymbol{\omega} = \boldsymbol{\omega_0} - \left(\frac{(\mu_s + \mu_r) m g cos\alpha}{I}\, \boldsymbol{r} \times \hat{\boldsymbol{t}}\right) t' \tag{3.32}$$

## 3.4 DEM Implementation Algorithm

The detailed calculation sequence of the implemented DEM model is described in this section while the overall algorithm for DEM calculation is also summarized in Figure 3.6.

### 3.4.1 Contact Detection

Contact Detection with neighboring DEM particles is performed first in each time step. For the numerical efficiency, the entire computational domain is divided into grids as shown in Figure 3.7, and the contact detection is performed based on these girds rather than comparing the distance to all the other DEM particles. Each DEM particle is assigned to a specific grid according to the location, and the contact detection for each particle is conducted by comparing the distance with the particles within the neighboring grids. Since most simulation cases in this study require a uniform size of solid particles, the size of the grid is determined to be similar to the particle diameter. The contact detection equation for the particle a and the neighboring particle b can be written as below.

$$d_{ab} \leq r_a + r_b \tag{3.33}$$

$d_{ab}$ and r are the distance between particle a and particle b, and the radius of each particle, respectively. Then, the normal overlap ($\delta_n$), unit normal vector ($\hat{\boldsymbol{n}}$), and the position vector ($\boldsymbol{x_c}$) of the contact point are also determined as follows.

$$\delta_n = r_a + r_b - d_{ab} \tag{3.34}$$

$$\hat{\boldsymbol{n}} = (\boldsymbol{x_b} - \boldsymbol{x_a})/d_{ab} \tag{3.35}$$

$$\boldsymbol{x_c} = \boldsymbol{x_a} + \left(r_a - 0.5\,\delta_n\right) \cdot \hat{\boldsymbol{n}} \tag{3.36}$$

### 3.4.2 Estimation of Relative Velocity

The contact forces between the collision particles acting on the contact point are generally determined by the relative velocity between two particles as written in the above equations from (3.11) to (3.17). The relative velocity of the particle a and the particle b on the contact point is defined as,

$$\boldsymbol{v_{rel}} = \left(\boldsymbol{v_b} + \boldsymbol{\omega_b} \times (\boldsymbol{x_c} - \boldsymbol{x_b})\right) - \left(\boldsymbol{v_a} + \boldsymbol{\omega_a} \times (\boldsymbol{x_c} - \boldsymbol{x_a})\right) \tag{3.37}$$

where $\boldsymbol{v}$ and $\boldsymbol{\omega}$ are the velocity and angular velocity vector of each particle, respectively. This relative velocity can be divided into each direction (normal and tangential) by taking the dot product with a unit normal vector $\hat{\boldsymbol{n}}$.

$$\boldsymbol{v_n} = |\boldsymbol{v_{rel}} \cdot \hat{n}|\, \hat{\boldsymbol{n}} \tag{3.38}$$

$$\boldsymbol{v_t} = \boldsymbol{v_{rel}} - \boldsymbol{v_n} \tag{3.39}$$

The tangential overlap ($\delta_t$) is obtained from the above equation (3.16), and the unit tangential vector is also determined as follows, from the above equation

(3.24).

$$\hat{\boldsymbol{t}} = \boldsymbol{v_t} \,/\, |\boldsymbol{v_t}| \tag{3.40}$$

### 3.4.3 Calculation of Contact Force

When the relative velocity vector and the overlap in each direction are determined, the contact force based on the Hertz-Mindlin model is calculated. The detailed equations for the contact force model are summarized in the above equations from (3.11) to (3.17). From the calculated contact force, the particle acceleration ($\dot{\boldsymbol{v}}_{\boldsymbol{a}}$) and also the angular acceleration ($\dot{\boldsymbol{\omega}}_{\boldsymbol{b}}$) of the current time step are determined as follows,

$$\dot{\boldsymbol{v}}_{\boldsymbol{a}} = \boldsymbol{F_{ab}}/m_a \tag{3.41}$$

$$\dot{\boldsymbol{\omega}}_{\boldsymbol{a}} = (\boldsymbol{r_{ac}} \times \boldsymbol{F_{ab}^t})/I_a \tag{3.42}$$

Where $\boldsymbol{F_{ab}^t}$ is the tangential contact force, and $\boldsymbol{r_{ac}}$ is a position vector from the center of particle a to the contact point C.

### 3.4.4 Wall Boundary Conditions and Time Integration

From the particle acceleration calculated in the above equation (3.41) and

(3.42), the velocity, angular velocity, and the position of the next time step can be calculated as follows where $\Delta t'$ is a step size of time integration.

$$\boldsymbol{v_a} = \boldsymbol{v_a} + \frac{\boldsymbol{F_{ab}}}{m_a}\Delta t' \tag{3.43}$$

$$\boldsymbol{\omega_a} = \boldsymbol{\omega_a} + \frac{\boldsymbol{\tau_{ab}}}{I_a}\Delta t' \tag{3.44}$$

$$\boldsymbol{x_a} = \boldsymbol{x_a} + \boldsymbol{v_a}\Delta t' \tag{3.45}$$

Also, the interaction with the wall boundary is estimated according to the equations outlined in section 3.3 if the particle contacts with the wall. The time integration takes place after this step.

## 3.5 V&V and Simulations

Several collision simulations for the basic conservation laws (momentum, angular momentum, energy) are performed to verify the implemented DEM collision model. Also, some simulations for qualitative and quantitative V&V of the proposed particle-boundary interaction model were carried out. The simulation cases are listed in Table 3.3 and the main results are summarized in this section.

### 3.5.1 Conservation of Momentum and Angular Momentum

The momentum of solid particles in all collisions is conserved since all contact forces (including friction force and damping force) are internal forces acting between the colliding particles. If particle 1 and particle 2 collide with the velocity of $\boldsymbol{v_{10}}$ and $\boldsymbol{v_{20}}$ as shown in Figure 3.8, the conservation of momentum can be written as follow.

$$m_1\boldsymbol{v_{10}} + m_2\boldsymbol{v_{20}} = m_1\boldsymbol{v_1} + m_2\boldsymbol{v_2} \tag{3.46}$$

The angular momentum is also conserved in all collisions since the torque due to the tangential contact force is also the internal torque. However, since the angular momentum is defined based on a specific axis, a reference axis is required in order to compare it before and after the collision. Based on the axis on the contact point C, the conservation of angular momentum can be expressed as follows (Figure 3.9).

$$\begin{aligned} &m_1\boldsymbol{r_{c1}} \times \boldsymbol{v_{10}} + m_2\boldsymbol{r_{c2}} \times \boldsymbol{v_{20}} \\ &= I_1\boldsymbol{\omega_1} + m_1\boldsymbol{r_{c1}} \times \boldsymbol{v_1} + I_2\boldsymbol{\omega_2} + m_2\boldsymbol{r_{c2}} \times \boldsymbol{v_2} \end{aligned} \tag{3.47}$$

The momentum and angular momentum were calculated for various collision situations, and it was confirmed that both momentums are well conserved in all collisions.

### 3.5.2 Conservation of Energy in Elastic Collision

The kinetic energy, including both rotation and translation, is conserved in a situation where only the conservative force acts or the non-conservative force acts without any displacement (not work). In the general collision between the solid particles, the energy dissipation occurs since the friction or damping force acting on the contact point works for the specific displacement defined as overlap ($\delta_n$, $\delta_t$). Therefore, in order to confirm the conservation of kinetic energy, it is necessary to assume a hypothetical situation in which only an elastic force (which is the conservative force) acts on the contact point. In this situation, the kinetic energy before the collision is divided into the translational kinetic energy and the rotational kinetic energy after the collision, while the summation is conserved as follows (Figure 3.10).

$$\frac{1}{2}m_1{v_{10}}^2+\frac{1}{2}m_1{v_2}^2=\left(\frac{1}{2}m_1{v_1}^2+\frac{1}{2}m_2{v_2}^2\right)+\left(\frac{1}{2}I_1{\omega_1}^2+\frac{1}{2}I_2{\omega_2}^2\right) \quad (3.48)$$

When the collisions were simulated only with the elastic term of applied Hertz-Mindlin contact force model, it was confirmed that the kinetic energy is well conserved in an elastic collision.

### 3.5.3 V&V Simulations for Wall Boundary Model

The following simulations were performed for quantitative and qualitative

V&V of the wall boundary model proposed in this study. Quantitative results are also included in the figures corresponding to each simulation case.

a. Wall collision of rotating sphere (Figure 3.11)
b. Sliding and rolling of the spherical particles on the wall boundary (Figure 3.12)
c. Descending behavior of the sphere on a slope (Figure 3.13)
d. 3D hopper flow simulation (Figure 3.14)

Through the simulation a above, it can be confirmed that the restitution coefficients in the normal and tangential directions are well reflected in the rotation and translation behavior of the colliding particles. Simulation b was performed to verify the sliding and rolling motion on the boundary with the real physics represented by the above equation (3.29) and (3.30). Simulation c is a case to confirm if the newly proposed boundary model works well according to the established criteria. It has been found that a series of interaction behavior from collision to sliding and rolling is well simulated in accordance with real physics as shown in Figure 3.13. In addition, 3D hopper flow simulation (simulation d, Figure 3.14) was also carried out for qualitative validation of collisions between particles and also the interaction between DEM particles and wall boundary.

### 3.5.4 Granular Collapse of Spherical Particles

The granular collapse behavior of spherical particles was analyzed for validation of the overall DEM model including wall boundary conditions. The

falling test setup of the benchmark experiment is shown in Figure 3.15 [Chou, 2012]. The experimental system consisted of a rectangular cute ($60\text{cm} \times 40\text{cm} \times 5\text{cm}$) and a high-speed camera. The rectangular chute was made of transparent acrylic plates while the polystyrene beads are used for granular particles. In the benchmark experiment, the final static length and deposit angle (Figure 3.15) were analyzed, and it has been shown that the final granular surface has a linear slope. As shown in Figure 3.16, the DEM model in this study well simulates the time-variant granular flow and surface slope, where $t_c$ and $t_f$ are characteristic time ($\sqrt{h/g}$) and final state time, respectively.

Table 3.1. DEM Contact Force Model

| | | |
|---|---|---|
| Linear Contact Force Model | | |
| $f_{spring}^{n} = k_n \delta_n$ | $k_n = 0.094 {E_{ab}}^{*} {R_{ab}}^{*}$ | Misra (1999) |
| Hertz Mindlin Contact Force Model | | |
| $f_{spring}^{n} = k_n {\delta_n}^{3/2}$ | $k_n = \frac{4}{3} {E_{ab}}^{*} \sqrt{{R_{ab}}^{*}}$ | Zhu (2007) |
| JKR Contact Force Model | | |
| $f_{spring}^{n} = k_1 {\delta_n}^{3} - k_2 \sqrt{{\delta_n}^{3}}$ | $k_1 = 4 {E_{ab}}^{*} / (3 {R_{ab}}^{*})$ | Feng (2014) |

Table 3.2. Hertz-Mindlin Contact Force Model

| | |
|---|---|
| Normal Contact Force | |
| $f_{ab}^{n} = f_{spring}^{n} + f_{damper}^{n} = k_n \delta_n - c_n v_n$ | |
| $k_n = \frac{4}{3} E^{*} \sqrt{R^{*} \delta_n}$ | $c_n = \sqrt{\frac{10}{3}} \frac{\ln(e)}{\sqrt{ln(e)^2 + \pi^2}} \sqrt{M^{*} {K'}_n}$ |
| Tangential Contact Force | |
| $f_{ab}^{n} = f_{spring}^{n} + f_{damper}^{n} = k_n \delta_n - c_n v_n$<br>$f_{ab}^{t} = min\left(f_{spring}^{t} + f_{damper}^{t}, -\mu_t \lvert f_{ab}^{n} \hat{n} \rvert\right)$ | |
| $k_t = 8 G^{*} \sqrt{R^{*} \delta_n}$ | $c_s = \sqrt{\frac{10}{3}} \frac{ln(e)}{\sqrt{ln(e)^2 + \pi^2}} \sqrt{M^{*} k_s}$ |

Table 3.3. V&V Simulation Cases for Implemented DEM Model

| **V&V Cases for developed DEM Model** | **Notes** |
|---|---|
| **Single DEM Particle** | |
| Momentum Conservation<br>*Without damping*<br>*Without rotation*<br>*All physics included* | Figure 3.8 |
| Energy Conservation (elastic)<br>*Normal elastic force only*<br>*Tangential elastic force included*<br>*( with rotational energy)* | Figure 3.10 |
| Angular Momentum Conservation<br>*All physics included* | Figure 3.9 |
| **Wall Boundary Treatment** | |
| Wall Collision<br>*Without rotation*<br>*Rotation of DEM particle included* | Figure 3.10 |
| Sliding & Rolling on the Surface<br>*on the flat surface*<br>*on the inclined surface* | Figure 3.11<br>Figure 3.12 |
| 3D Hopper Flow | Figure 3.13 |
| **Granular Flow** | |
| Granular Collapse of Spherical Particles | Figure 3.16 |

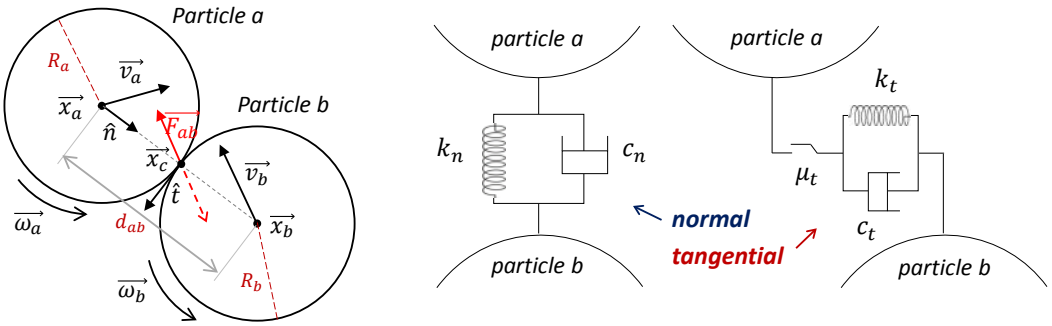


Figure 3.1. Spring-Dashpot System of Soft-Sphere Collision Model

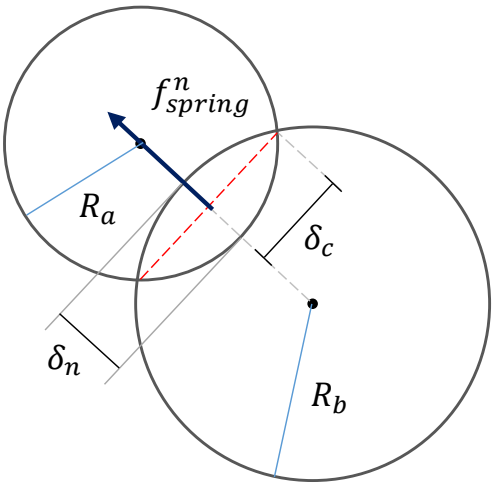


Figure 3.2. Inter-particle Collision in Soft-Sphere Model

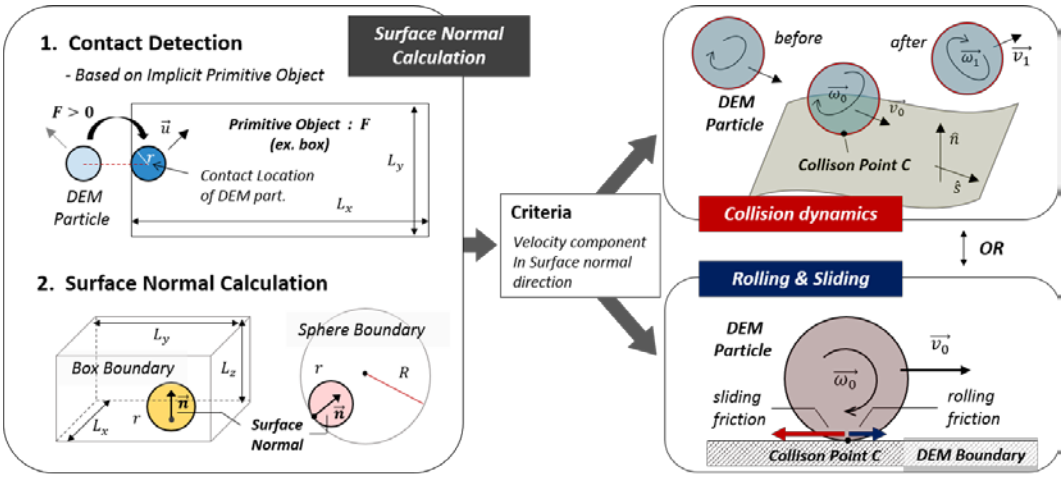


Figure 3.3. Versatile Wall Boundary Treatment Model in This Study

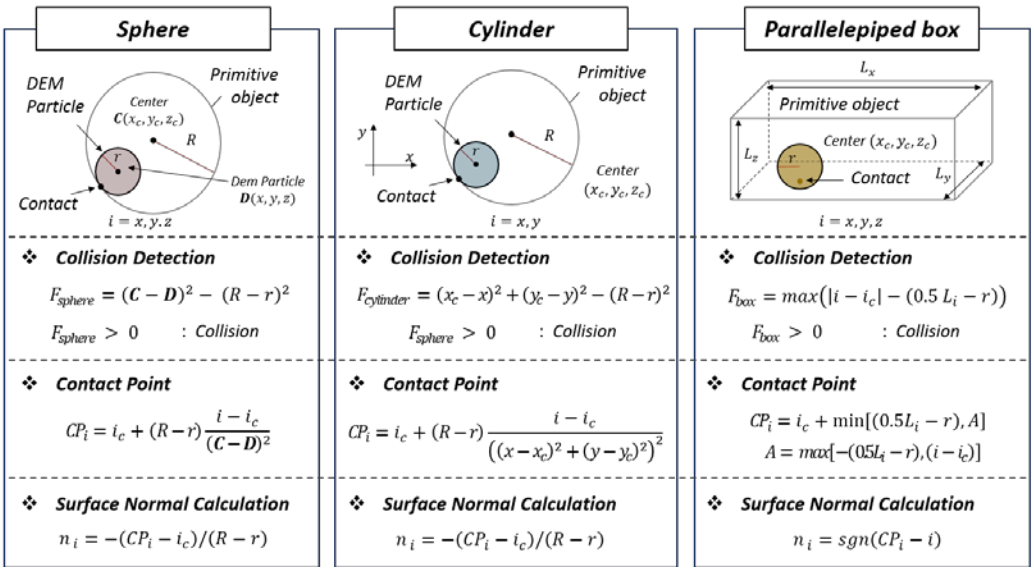


Figure 3.4. Implicit Primitive Object for DEM Wall Boundary Condition

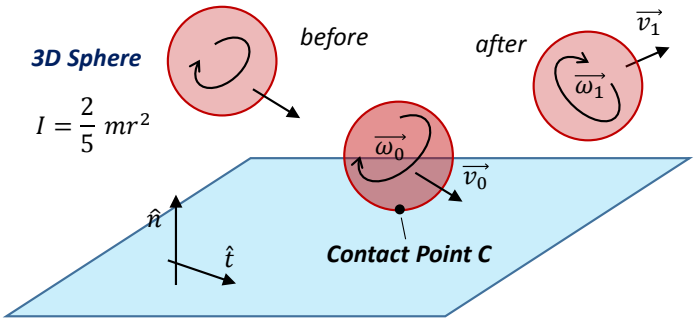


Figure 3.5. Particle Collision with Wall Boundary

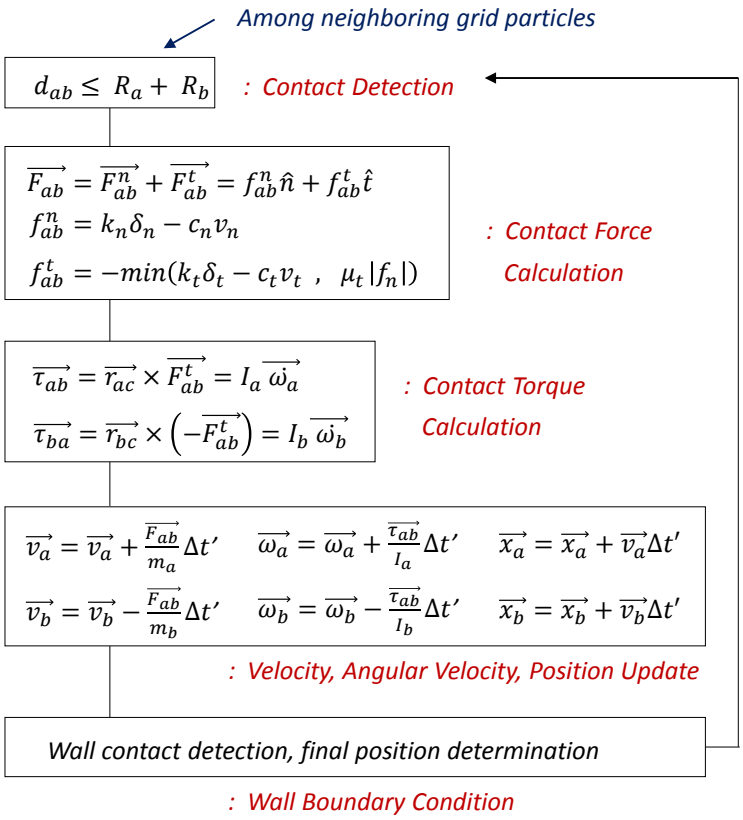


Figure 3.6. Algorithm of Implemented DEM Model

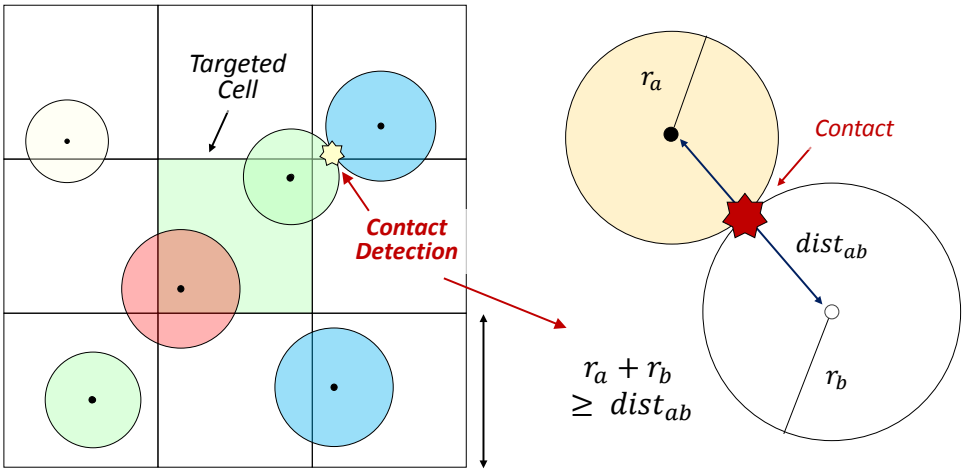


Figure 3.7. Grid-Based Contact Detection

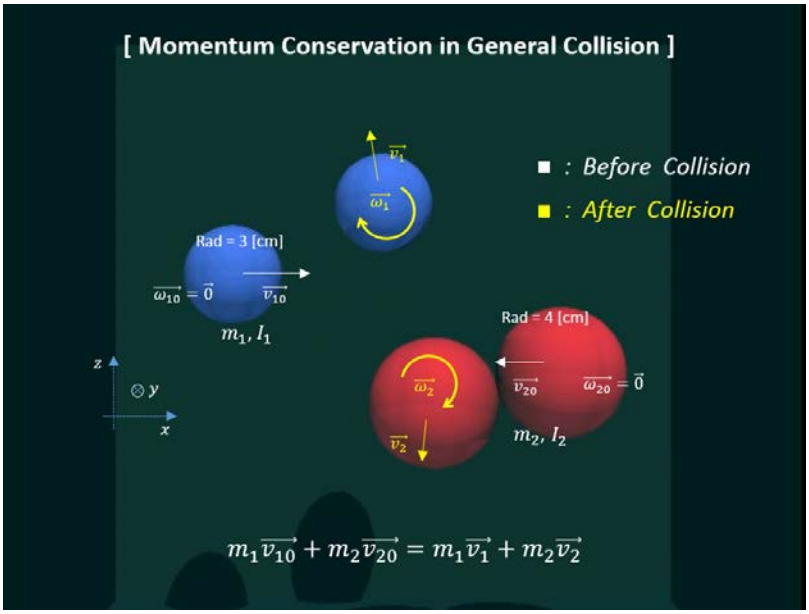


Figure 3.8. Conservation of Linear Momentum in Collision

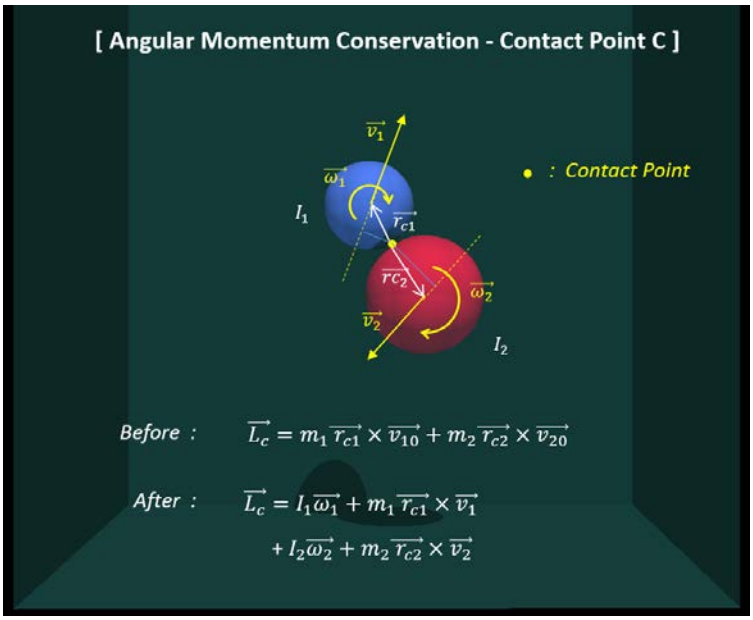


Figure 3.9. Conservation of Angular Momentum in Collision

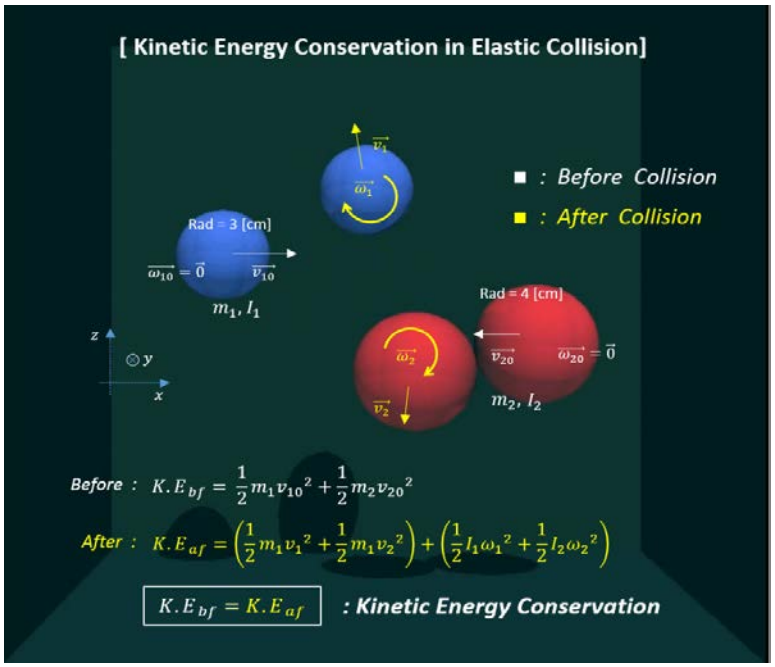


Figure 3.101. Conservation of Kinetic Energy in Elastic Collision

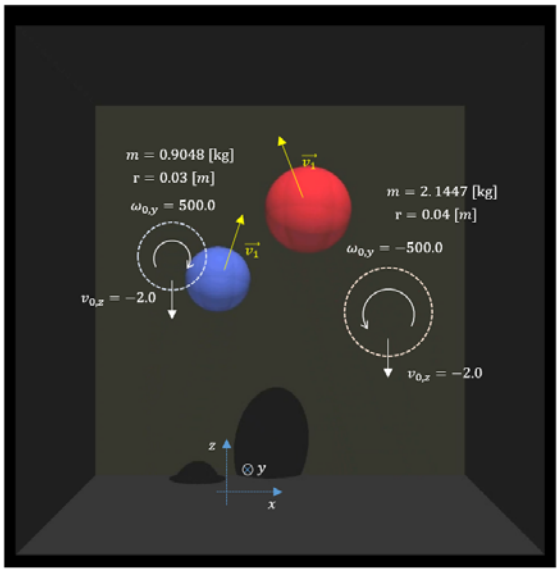


*Conservation of linear momentum, and angular momentum*

$$m\,(\vec{v_1} - \vec{v_0}) = \vec{J} \quad \cdots\cdots\ a$$

$$I\,(\vec{\omega_1} - \vec{\omega_0}) = -r\,\hat{n} \times \vec{J} \quad \cdots\cdots\ b$$

***[ Particle 1 ]*** *– first collision*

$\vec{v_0} = (0, 0, -2.0)$ $\quad \vec{v_1} = (0.4286, 0, 1.8)$

$\vec{\omega_0} = (0, 500.0, 0)$ $\quad \boxed{\vec{\omega_1} = (\mathbf{0, 464.586, 0})}$

*From eqn a,* $\vec{J} = m(\vec{v_1} - \vec{v_0}) = (0.3878, 0, 3.438)$

$\therefore\ \hat{n} \times \vec{J} = (0, 0.3878, 0)$

*Substitute to eqn b,*

$$\vec{\omega_1} = \vec{\omega_0} - \frac{r}{I}(\hat{n} \times \vec{J}) = \boxed{(\mathbf{0, 464.583, 0})}$$

Figure 3.11. Wall Collision of Rotating Sphere

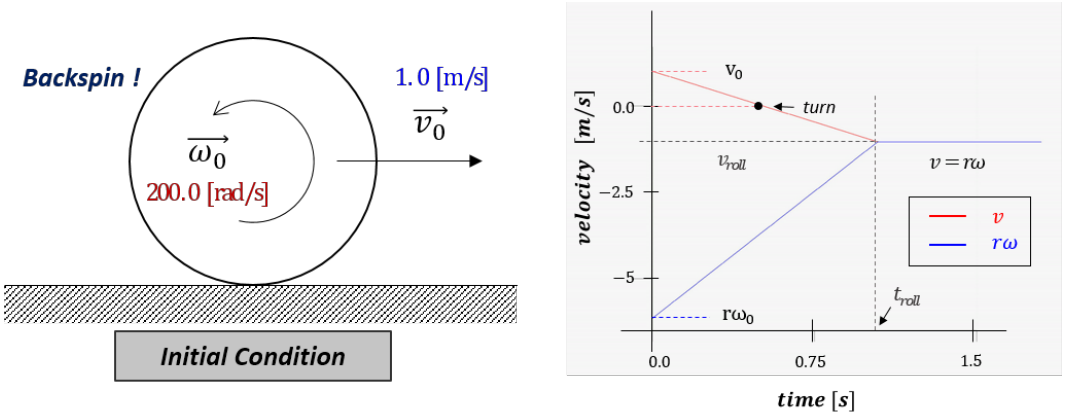


Figure 3.12. Sliding and Rolling of Spherical Particle on the Wall boundary

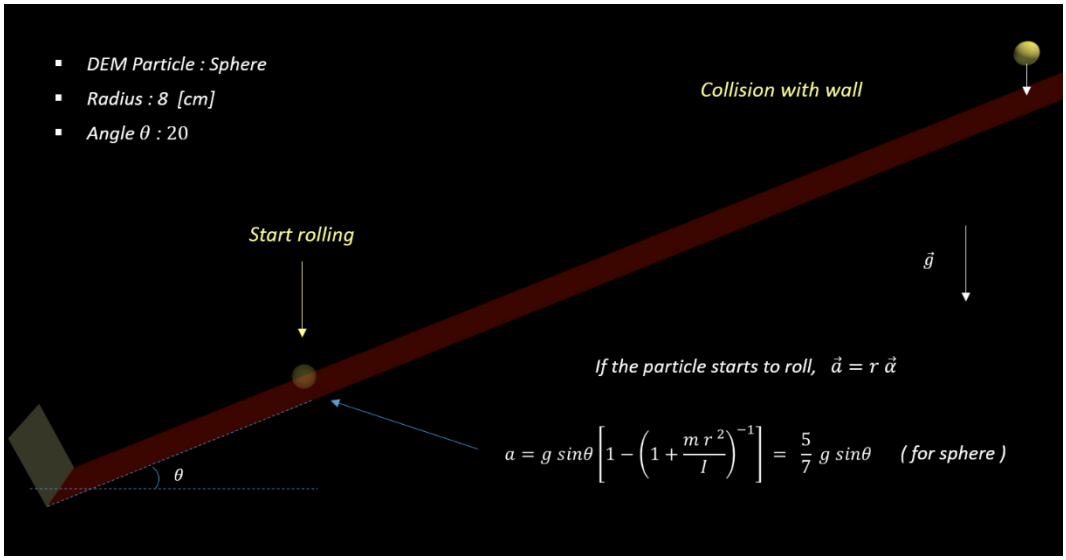


Figure 3.13. Descending Behavior of the Sphere on Slope

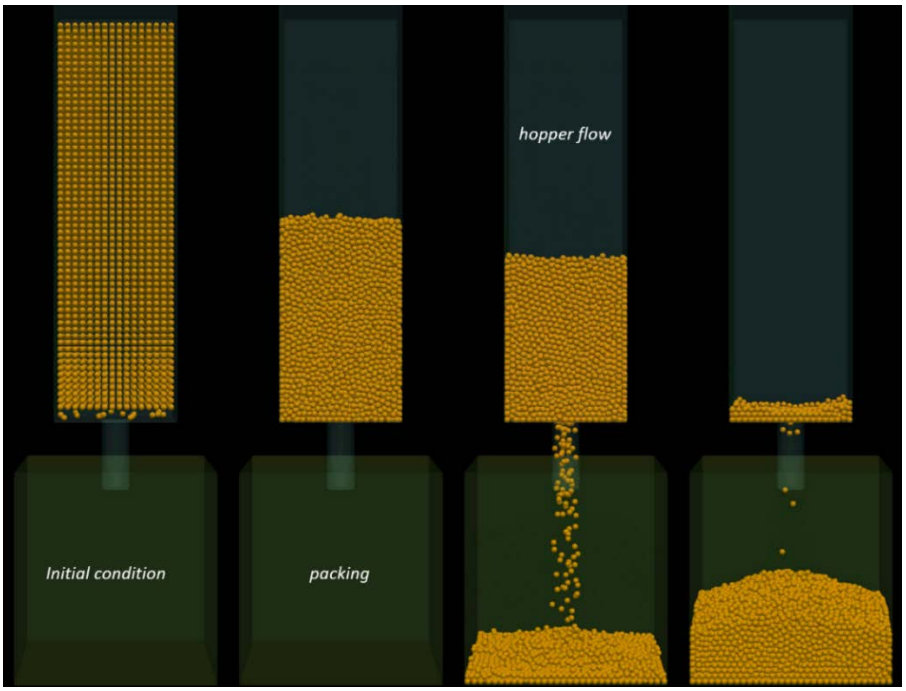


Figure 3.14. 3D Hopper Flow Simulation

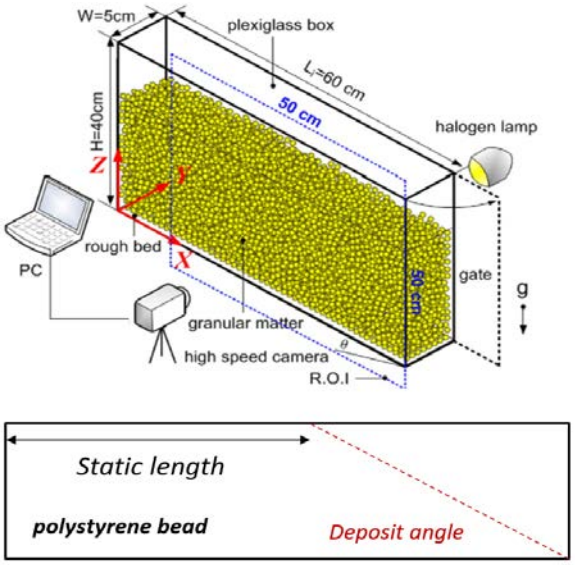


Figure 3.15. Benchmark Experimental Setup for Granular Collapse Behavior [Chou, 2012]

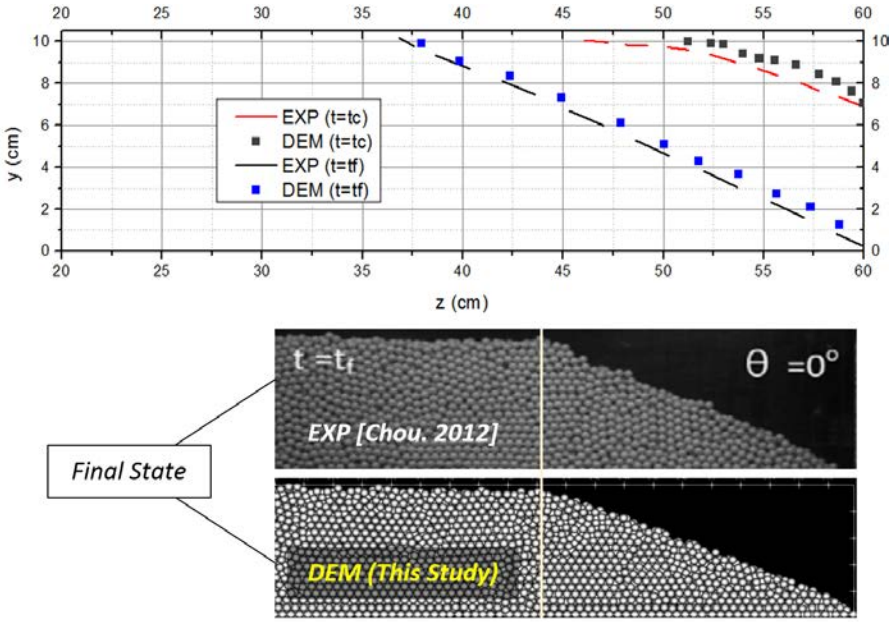


Figure 3.16. DEM Validation Results for Granular Collapse Behavior

# Chapter 4

# Two-Way Phase Coupling of SPH and DEM

In this study, the developed Lagrangian SPH model (Chapter 2) and DEM model (Chapter 3) were coupled in order to deal with the vapor-driven 3-phase behavior of particulate debris particles in the late phase of LWR severe accident. This chapter covers the coupling mechanism between SPH and DEM with the governing equations, the algorithm of the two-way coupled model, and several V&V simulation results as well.

## 4.1 Unresolved Coupling of SPH and DEM

Since the SPH and DEM are both fully Lagrangian-based numerical methods, there are many similarities in solving the governing equations. Thus, the potential in coupling two methods is higher than the coupling of DEM with Eulerian-based CFD methods.

Generally, the approaches for coupling the SPH and DEM can be classified into two groups. One is the resolved method that simulates the behavior of each phase by completely separating the computational domain, and the other is the unresolved method. In the resolved method, the SPH particles are significantly

smaller than the solid particles in order to analyze the flow (streamline) around the solid particles. Since SPH and DEM are based on the same methodology, the feasibility of resolved coupling is potentially high. However, this method is suitable when the behavior of each solid particle or the flow disturbance by a single solid particle is the main focus of simulation. In other words, there are limitations for the resolved coupling method in solving particulate flow, since it requires an extremely high-resolution for SPH particles.

In this respect, the unresolved coupling method of SPH and DEM is effective for particulate debris behavior (sedimentation, sloshing, self-leveling, etc.) where the overall behavior of debris particles is important. The SPH particles are of comparable size of the DEM solid particles, and the locally averaged Navier Stokes equation is solved for the fluid phase since the solid phase and fluid phase overlap the computational domain as shown in Figure 4.1. In addition, the empirical closure correlations (drag coefficient, lift coefficient, etc.) are used to capture the momentum transport between liquid and solid phase, since it is no longer a first principle numerical scheme. The main features of the unresolved coupling method of SPH and DEM are outlined below.

- Overlap b/w SPH and DEM Particles
- Locally Averaged N-S Equation (Two-Fluid Model)
- Empirical Closure Equations (ex. Drag Force)
- SPH Particle Size ~ DEM Particle Size
- Large Number of DEM Particles
- Efficient for Particulate Flow (Granular Flow)

## 4.2 Governing Equations

As described in the previous section, the locally averaged Navier-Stokes equation is solved for the fluid phase (SPH), which is slightly different from the SPH governing equations in Chapter 2. Considering this, the unresolved coupling sequence of SPH and DEM can be divided into the following three steps.

a. Solving locally averaged N-S equation
b. Solving coupling force acting on DEM particles
c. Solving the reaction force for SPH particles (Two-way Coupling)

The following sub-sections describe the governing equations for the above three steps.

### 4.2.1 SPH Particles: Locally Averaged N-S Equations

The fluid phase (SPH) is governed by a locally averaged Navier Stokes equation for an incompressible fluid. The corresponding momentum equation can be written in the Lagrangian description as below,

$$\rho_f \frac{\partial(\varepsilon \boldsymbol{u_f})}{\partial t} = -\varepsilon \nabla \mathrm{P} + \mu_f \nabla \cdot (\varepsilon \nabla \boldsymbol{u_f}) + \varepsilon \rho_f \boldsymbol{g} + \boldsymbol{S_f} \qquad (4.1)$$

where ε is the volume fraction of fluid f, $\rho_f$ and $\mu_f$ are the density and dynamic viscosity of a fluid, respectively. Also, the momentum exchange term $S_f$ is the reaction force by adjacent DEM particles, which is discussed in detail in a later section (Chapter 4.2.3).

Before discretization of the above equation (4.1) into the SPH form, the definition of the local porosity of SPH particles is required. The local porosity of fluid SPH particle $i$ is calculated by summation over neighboring DEM particles within a coupling length $h_c$. The detailed expression is as follow,

$$\varepsilon_i = 1 - \left( \sum_b W_{ib}(h_c) V_b \Big/ \sum_j W_{ij}(h_c) V_j \right) \tag{4.2}$$

where subscript i, j denote targeted SPH particle and neighboring SPH particles, respectively, while subscript b refers to the neighboring DEM particles. $W$ is the kernel weighting function between particles, and V is the volume of the particles. Taking the local porosity into account, the discretized summation form of the above governing equation (4.1) can be written as below,

$$\left(\frac{d\boldsymbol{u}}{dt}\right)_i = -\sum_j \overline{m_j} \left[ \frac{P_i}{\bar{\rho}_i^{\,2}} + \frac{P_j}{\bar{\rho}_j^{\,2}} \right] \nabla_i W_{ij} + \bar{\rho}_i \boldsymbol{g} + \boldsymbol{S_i} \tag{4.3}$$

where $\bar{\rho}$ denotes for the superficial fluid density, which is defined as $\bar{\rho} = \varepsilon\rho$, and $\overline{m}$ refers to the corresponding mass of the fluid particle. In the above equation (4.3), the volume of SPH particles is constant during simulation, since

the mass used in equation (4.3) is also changes as a function of local porosity. This approach is suitable when heavier DEM particles are submerged in the fluid throughout the simulation. However, if the DEM particles enter or exit the fluid area during the simulation, the above governing equation (4.3) should be modified as follow,

$$\left(\frac{d\boldsymbol{u}}{dt}\right)_i = -\sum_j m_j \left[\frac{P_i}{\bar{\rho}_i^{\,2}} + \frac{P_j}{\bar{\rho}_j^{\,2}}\right] \nabla_i W_{ij} + \bar{\rho}_i \boldsymbol{g} + \boldsymbol{S_i} \qquad (4.4)$$

Where constant mass is used instead of $\overline{m_j}$. In this case, SPH particles near DEM particles expand in volume according to their local porosity, and as a result, the total volume of the fluid region is increased by the volume of the submerged DEM particles. Since the volume of SPH particles is variable in this case, a conservative setting for coupling length ($h_c$), or an advanced model for adaptive smoothing length is required.

### 4.2.2 DEM Particles: Coupling Forces Acting on Solid Particles

There are various interaction forces acting on the solid phase including drag force, lift force, virtual mass force, and also non-contact force such as the Van der Waals force. However, in external flow without additional acceleration of the solid particle, the effects of lift force or added mass force are negligible. Thus, only drag force and pressure gradient force (buoyancy force) are taken into account in coupling interaction as dominant driving forces of solid particles.

The force acting on each solid particle by the fluid can be written as below,

$$\boldsymbol{F_a = F_a^P + F_a^D} \tag{4.5}$$

where superscript P and D denote for pressure-gradient and drag, respectively. The first term of the above equation models pressure gradient force, which reduces to the buoyancy force in hydrostatic equilibrium, while the second term in RHS refers to the drag force. The pressure gradient force is the interaction force that the solid particles receive from the pressure field developed by the fluid. Therefore, the pressure gradient force of the DEM particle is calculated by weight averaging the pressure gradient of the neighboring SPH particles ($\boldsymbol{\vartheta}$) as follows [He, 2018] [Robinson, 2013],

$$\boldsymbol{F_a^P} = V_i \sum_j \frac{m_j}{\rho_j} \boldsymbol{\vartheta_j} W_{aj} / \sum_j \frac{m_j}{\rho_j} W_{aj} \tag{4.6}$$

$$\boldsymbol{\vartheta_i} = -\bar{\rho}_i \sum_j \overline{m_J} \left[ \frac{P_i}{\bar{\rho}_i^{\,2}} + \frac{P_j}{\bar{\rho}_J^{\,2}} \right] \nabla_i W_{ij} \tag{4.7}$$

The drag force $\boldsymbol{F_a^D}$ in the above equation (4.5) depends on the local porosity and relative velocity between fluid and particle. Since the behavior of particulate solid debris (ex. Self-leveling) is a granular flow with low porosity, a suitable drag force model should be used for this kind of dense particulate flow. For the dense particulate flow with multiple particles, the drag law can be generalized to,

$$F_a^D = \frac{1}{8} C_d \rho_f \pi d^2 |\boldsymbol{u_{ja}}| \boldsymbol{u_{ja}} f(\varepsilon) \tag{4.8}$$

Where $C_d$ and $\boldsymbol{u_{ja}}$ denote for the general drag coefficient and relative velocity of solid particles, respectively, and $f(\varepsilon)$ is the correction factor taken from Di Felice (1994) which is used to account for the behavior of packed particles. The correction factor in the packed spheres can be written as follows [Di Felice, 1994] [Epstein, 2005],

$$f(\varepsilon) = \varepsilon^{2-\xi} \tag{4.9}$$

$$\xi = 4.7 - 0.65\ exp\left[-\frac{\left(1.5 - \log_{10} Re_p\right)^2}{2}\right] \tag{4.10}$$

where $Re_p$ is Reynolds number for the fluid flow through a bed where the superficial velocity $\varepsilon|\boldsymbol{u_{ja}}|$ is used for the calculation.

$$Re_p = \frac{\rho_f d_p \left(\varepsilon |\boldsymbol{u_{ja}}|\right)}{\mu_f} \tag{4.11}$$

### 4.2.3 SPH Particles: Reaction Force from Momentum Exchange

In a dense particulate flow with a sufficiently large number of solid particles, the reaction force should not be neglected since the presence of solid particles also greatly affects the fluid flow. The rate of momentum exchange ($\boldsymbol{S_i}$) in the

above equation (4.1) and (4.3) can be calculated by a weighted average of coupling force acting on the surrounding DEM particles, as shown in Figure 4.2. Specifically, the coupling force of DEM particle b is given to the SPH particles within the coupling length, and for each SPH particle, these interaction forces received from the DEM particles within the coupling length is added as follow,

$$\boldsymbol{S_i} = -\frac{1}{\bar{\rho}_i}\sum_b \frac{1}{\sum_{j'}\frac{m_{j'}}{\rho_{j'}}W_{bj'}}\boldsymbol{F_b}\,W_{ib} \tag{4.12}$$

where subscript $i, b,$ and $j'$ refer to targeted SPH particle, neighboring DEM particles, and neighboring SPH particles for DEM particle b, respectively. By applying the above equation to equations (4.1) and (4.3), Newton's third law of motion is satisfied. The importance of momentum exchange term is highlighted in the validation section of SPH-DEM phase coupled model (Chapter 4.4).

## 4.3 Algorithm of SPH-DEM Coupled Model

In general CFD-DEM coupling, the step size of time integration required in the DEM model is an order of $10^{-6}$, which is much smaller than that of the CFD model. Thus, the algorithms of CFD and DEM are separate, and the coupling of two models is performed based on the time step size of CFD calculation. However, since the SPH model implemented for the fluid phase in this study is a fully explicit Lagrangian-based CFD method, there is a limit on the step size of time integration. Besides, if the vapor phase is considered in coupled simulation, the required time step size in SPH calculation becomes similar to that of the DEM

model. For this reason, the SPH-DEM phase coupled model implemented in this study performs SPH calculation and DEM calculation within the same algorithm as shown in Figure 4.3. In addition, nearest neighboring particles searching (NNPS) in SPH and contact detection in DEM model are both performed in cell-based, and mutual search in the coupling step (within coupling length) is also conducted based on the grid, as shown in Figure 4.4. The simplified algorithm of theSPH-DEM coupled model is as follows, and also shown in Figure 4.3.

(1) Start & Initialization
(2) Nearest Neighboring Particles Searching (NNPS) – SPH
(3) Contact Detection – DEM
(4) Density, Pressure Estimation – SPH
(5) Momentum Equation – SPH
(6) Inter-particle Collision – DEM
(7) SPH-DEM Coupling Force 1 – DEM
(8) SPH-DEM Coupling Force 2 – SPH (reaction to (7))
(9) DEM Wall Boundary Condition
(10) Time Integration

## 4.4 V&V Simulations for SPH-DEM Coupled Model

The V&V of the implemented SPH-DEM coupled model has been conducted in the following three steps.

a. Single DEM particle behavior in liquid
b. Granular particle flow behavior in liquid
c. Granular particle flow behavior in multi-phase fluid (i.e. 3-phase)

This chapter only covers the simulations of liquid-solid two-phase (a and b above), and the validation for 3-phase flow including vapor phase (c) is described in detail in Chapter 6 (vapor-driven self-leveling behavior of particulate solid debris).

### 4.4.1 Single DEM Particle Behavior

The behavior of a single DEM particle was analyzed in order to verify the coupling forces acting on a DEM particle (above equation 4.6 and 4.8). First, for the verification of the pressure gradient force term (equation 4.6), the behavior of a single solid particle was simulated by assuming a hypothetical situation without drag force (Figure 4.5). The lighter DEM particle float under buoyancy force in the liquid region, and fall off again in the outer region by gravity force. Since both gravity force and pressure gradient force (buoyancy force) are conservative forces, the mechanical energy of the system is conserved, resulting in an oscillating behavior of the DEM particle. As shown in Figure 4.6, the physical properties of oscillation (gradient, amplitude, etc.) were quantitatively well verified.

When a DEM particle with the same physical properties is dropped on a liquid with a drag (Figure 4.7), the damped oscillation of DEM particle was observed due to the energy dissipation by drag force (Figure 4.8). In this case, the

penetration depth of the DEM particle well matched with the results calculated from the analytic equation below, as shown in Figure 4.8.

$$m_p\ddot{\boldsymbol{z}} = -m_p\boldsymbol{g} + m_p\frac{\rho_f}{\rho_p}\boldsymbol{g} - \frac{\rho_f|\dot{\boldsymbol{z}}|}{2}C_d\left(\frac{\pi {d_p}^2}{4}\right)\dot{\boldsymbol{z}} \tag{4.13}$$

In addition, the terminal velocity behavior of a single DEM particle was simulated for overall verification of the coupling force including pressure gradient force and drag force. The time variation of the velocity of the DEM particle was in good agreement with the results calculated from the theoretically derived equations (equation 4.13), as shown in Figure 4.9. In this case, the one-way phase coupling was applied, in which only a solid DEM particle receives the forces from neighboring SPH particles without momentum exchange.

However, the practical drag coefficient correlation is derived from the experimental results which essentially involves the momentum exchange, and the SPH-DEM phase coupling in this study should be also done in two-way in order to satisfy the momentum conservation law. Since the relative velocity between solid and fluid is determined from the velocity distribution of SPH particles within the coupling domain (equation (4.8)), it is necessary to evaluate the validity of the drag coefficient correlations depending on the coupling length($\Delta x_c$). In SPH-DEM two-way coupling in this study, coupling length $\Delta x_c$ is at least 6 times larger than the DEM particle diameter. In other words, the relative velocity between solid and fluid is calculated through the interaction with approximately 12 neighboring SPH particles in each dimension. According to the sensitivity study on coupling resolution for the single-particle terminal velocity

behavior (Figure 4.10), it was found that there was little difference in the simulation results between one-way coupling and two-way coupling when sufficient coupling length was guaranteed. On the other hand, if the coupling length is insufficient as shown in the right case in Figure 4.10, the application of the drag coefficient correlation is inappropriate, and a more fundamental coupling algorithm (resolved method) between SPH and DEM is required.

### 4.4.2 Pressure Drop through Packed Bed

In the late phase of PWR severe accident, the massive corium might release out of the reactor pressure vessel (RPV) and falls down to the ex-vessel coolant forming the melt jet if the In-Vessel Retention (IVR) strategy fails. Based on the assumption that the ex-vessel pool is sufficiently deep, the melt jet can be fragmented into debris particles and sediment on the concrete to form a debris bed. In order to demonstrate the feasibility of the SPH-DEM coupled model on debris bed cooling behavior, the basic pressure drop simulation the packed bed was performed as a validation case. In the SPH-DEM coupled model in this study, the flow resistance through the packed bed is estimated in two steps as follows.

a. DEM Particles: Calculate the drag force acting on each solid particle as a function of local porosity (voidage function, equation (4.8))
b. SPH Particles: Calculate the reaction force received by the neighboring solid particles (equation (4.12)).

Assuming that there are $N_{DEM}$ solid particles in the control volume of $V_{SPH}$,

the relationship between $N_{DEM}$ and $V_{SPH}$ can be described as follows,

$$N_{DEM} = \frac{V_{SPH}(1-\varepsilon)}{V_{DEM}} \tag{4.14}$$

where ε is the averaged local porosity in the packed bed region. In this case, total drag force acting on the DEM particles can be expressed as follows,

$$\overrightarrow{F_{Dp}} N_{DEM} = \frac{3}{4d} C_d \rho \left|\overrightarrow{u_{fp}}\right| \overrightarrow{u_{fp}} (1-\varepsilon)\varepsilon^{1-\chi} V_{SPH} \tag{4.15}$$

The above equation (4.15) can be summarized in pressure drop form as follows, where the vector $\boldsymbol{J}$ denotes the relative superficial velocity.

$$-\frac{dP}{dz} = \frac{3}{4d} C_d \rho |\boldsymbol{J}| \boldsymbol{J} (1-\varepsilon)\varepsilon^{-1-\chi} \tag{4.16}$$

Meanwhile, a great number of empirical models were developed for the prediction of single-phase pressure drop in a packed bed. The Ergun equation below is the most widely used semi-empirical model on the frictional pressure drop in porous media, which has been validated through the various type of flow experiments [Ergun, 1952].

$$-\frac{dP}{dz} = \frac{150(1-\varepsilon)^2 \mu}{d^2 \varepsilon^3} \boldsymbol{J} + \frac{1.75(1-\varepsilon)\rho}{d\varepsilon^3} |\boldsymbol{J}| \boldsymbol{J} \tag{4.17}$$

As shown in Figure 4.11, the above two equations (4.16 and 4.17) show similar trends for various solid particle diameters. In short, the drag force model in SPH-DEM coupled model in this study can be applied to various porosity ranges from the single solid particle to porous media, which shows the same tendency with the well-known Ergun equation for the case of paced bed.

Figure 4.12 shows the additional flow resistance in the packed bed region estimated in SPH-DEM coupled simulation, while the Figure 4.11 shows the comparison between the SPH-DEM simulation results and the analytic results of the above two equations (4.16 and 4.17). It can be seen that the pressure drops are increasing with the flowrates, while the pressure drops of 1.5 [mm] solids are higher than that of 6.0 [mm] spheres. The estimated pressure drops in SPH-DEM coupled simulation are well predicted by the analytic results of the Ergun equation.

### 4.4.3 Granular Flow in Liquid: 3D Dam-Break

To validate the SPH-DEM coupled model for granular particulate flow, a solid-liquid two-phase dam break simulation was conducted and compared with the experimental results reported by Sun (2013). This dam-break simulation is a general test case used for validation of CFD-DEM coupled code. The experiment was conducted by filling the water on one side of a rectangular shaped water tank, and removing the gate with a specific velocity, as shown in Figure 4.13. The conditions for the benchmark experiment are summarized below and also shown

in Figure 4.13.

- Tank overall dimensions: $200[\mathrm{mm}] \times 150[\mathrm{mm}] \times 150[\mathrm{mm}]$
- Size of water column: $50[\mathrm{mm}] \times 100[\mathrm{mm}] \times 100[\mathrm{mm}]$
- Moving gate velocity: $0.68\ [\mathrm{m/s}]$

For the solid particle phase, spherical particles are initially packed behind the moving gate. The physical properties and conditions for the particle phase are listed below.

- Density: $2{,}500\ [\mathrm{kg}/m^3]$
- Total mass of solid particles: $200$ [g]
- Young's modulus: $1.0 \times 10^8$ [Pa]
- Restitution coefficient: 0.9
- Friction coefficient: 0.2

In the SPH-DEM coupled simulation, a water column collapse was also triggered by removing the moving plate as in the benchmark experiment. The simulation conditions are summarized below.

- Time step size: $2 \times 10^{-6}$ [s]
- Number of DEM Particles: 7,762
- Number of SPH Particles (including moving gate): 182,716

The qualitative validation results with the experimental snapshots are shown

in Figure 4.14. The SPH-DEM coupled simulation results and experimental snapshots are compared at a time interval of 0.5[s]. The behaviors of both fluid and solid phase in the benchmark experiment are well reproduced in the SPH-DEM coupled simulation in this study.

In addition, for the quantitative validation of the simulation results, the extent of propagation of the leading front of both the fluid phase and solid particle phase is compared with the experimental data. The following non-dimension parameters are defined for the quantitative comparison.

$$x^* = \mathrm{x}/\mathrm{a} \tag{4.14}$$

$$t^* = t'(2g/a)^{0.5} \tag{4.15}$$

where a is the width of the initial water column as shown in Figure 4.10. It can be seen that the simulation results in this study match well with the benchmark experiment as shown in Figure 4.15.

Also, decoupled simulation and one-way coupled simulation were also performed in order to evaluate the effect of two-way coupling between SPH and DEM method. Here, the one-way coupling means that only the DEM particles move under the influence of fluid, while the SPH particles do not get any reaction forces. As shown in Figure 4.16, only the two-way phase coupled model well simulated the real physics, while the one-way coupled simulation over-estimated both the fluid and solid phases. The results of the decoupled simulation and one-way phase coupled simulation were in good agreement with the experimental results of the single fluid dam-breaking motion, as shown in Figure 4.17.

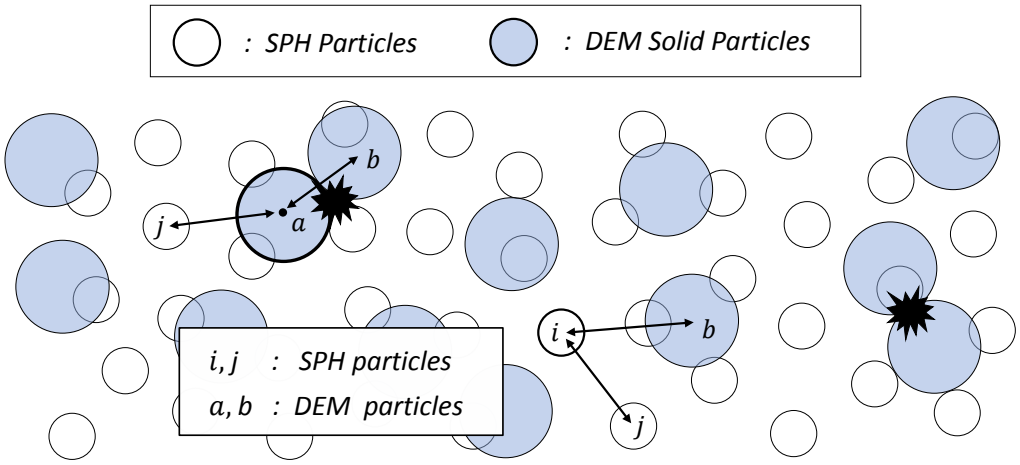


Figure 4.1. Concept of SPH-DEM Unresolved Coupling

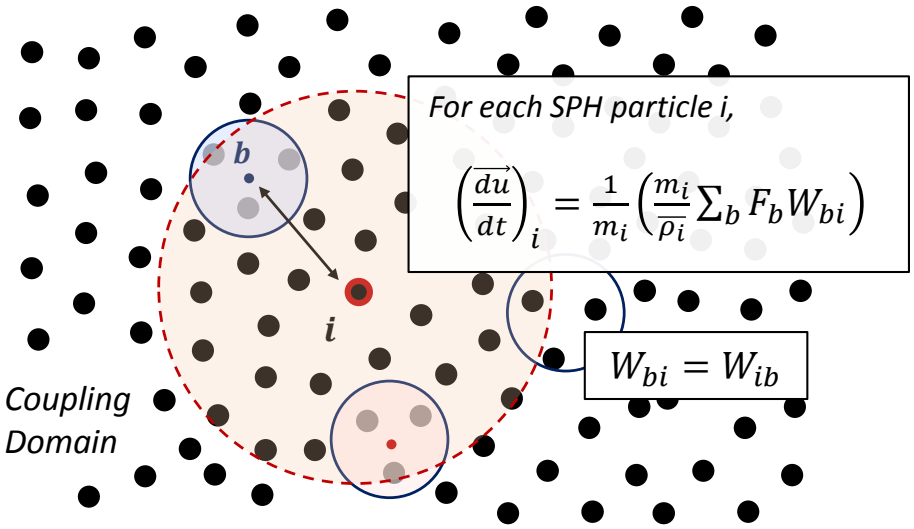


Figure 4.2. Momentum Exchange b/w SPH and DEM Particles

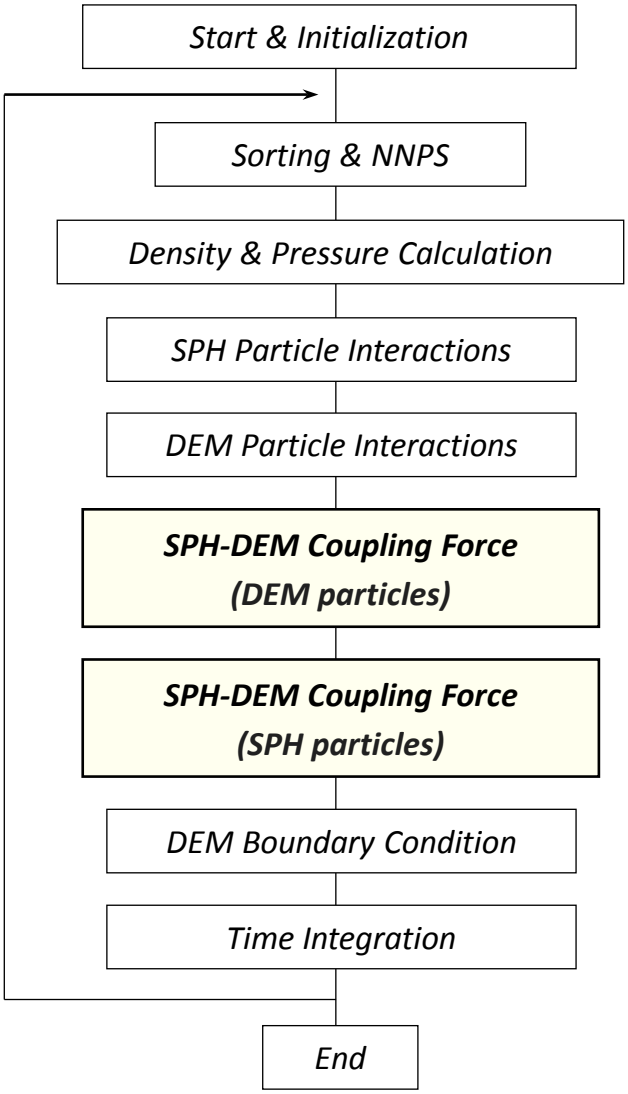


Figure 4.3. Algorithm of SPH-DEM Two-Way Coupled Model

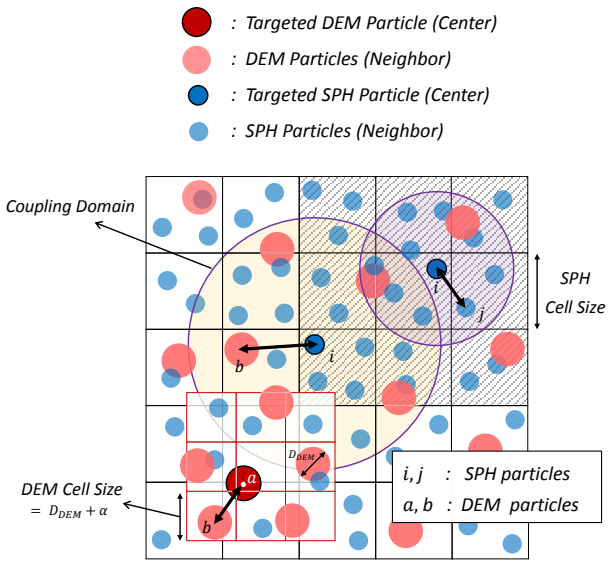


Figure 4.4. NNPS and Contact Detection in SPH-DEM Coupled Model

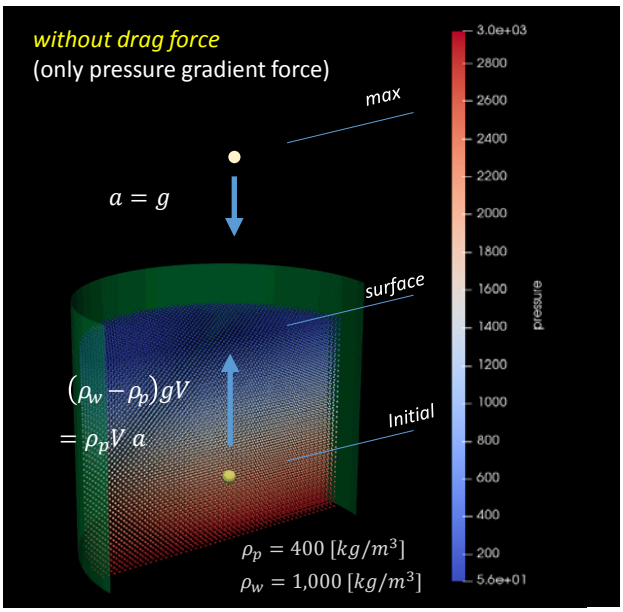


Figure 4.5. Single DEM Particle Behavior without Drag Force

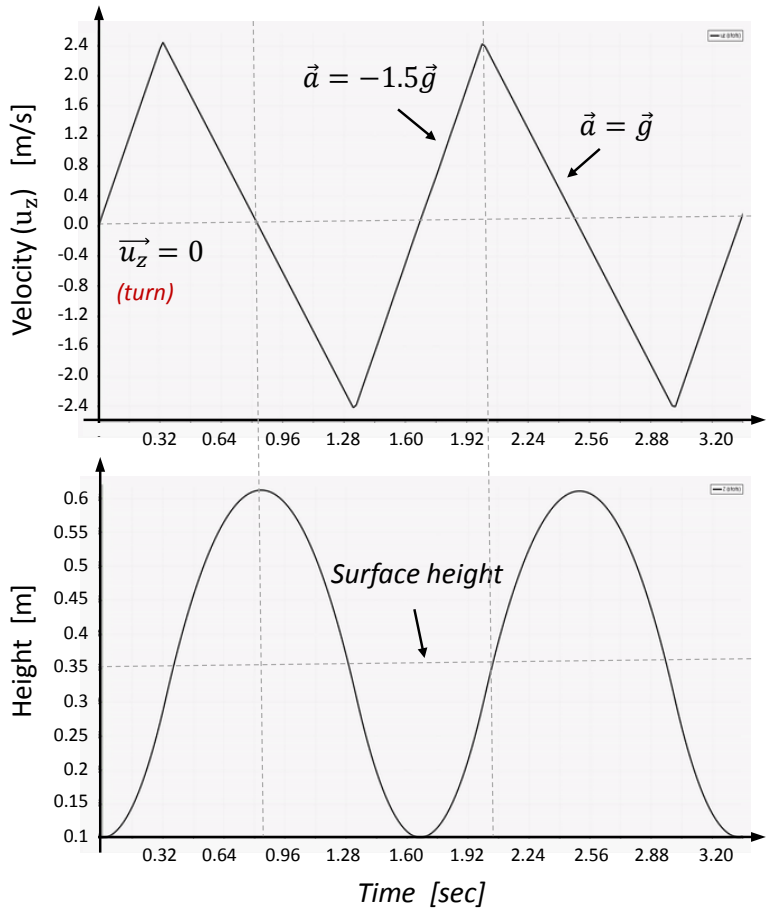


Figure 4.6. DEM Particle Oscillation Due to Gravity and Buoyancy Force

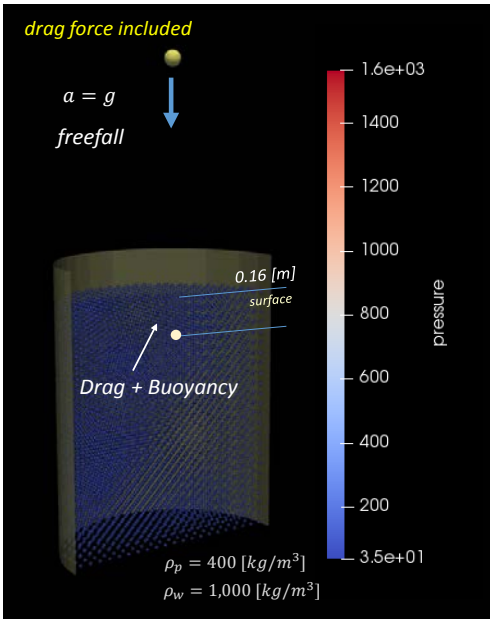


Figure 4.7. Single DEM Particle Freefall (Drag, Buoyancy Force)

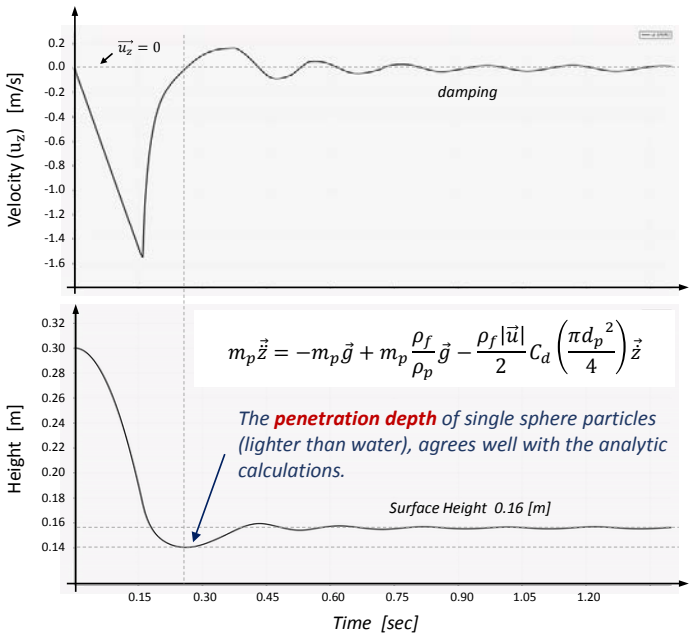


Figure 4.8. Damped Oscillation Due to Energy Dissipation

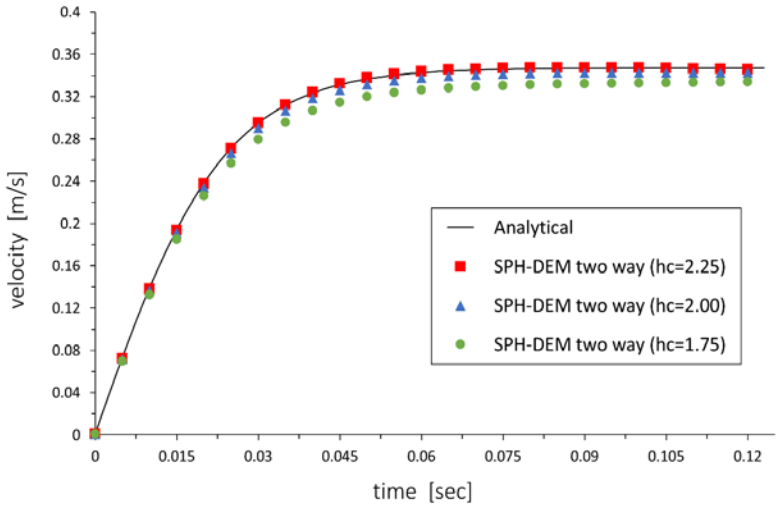


Figure 4.9. Terminal Velocity Behavior of Single DEM Particle

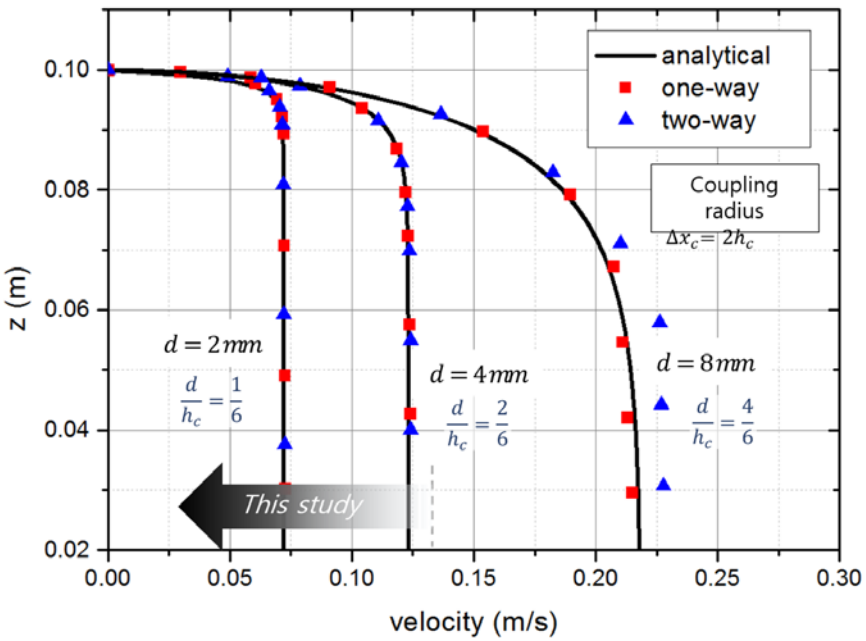


Figure 4.10. Sensitive Study on Coupling Length for Terminal Velocity Behavior

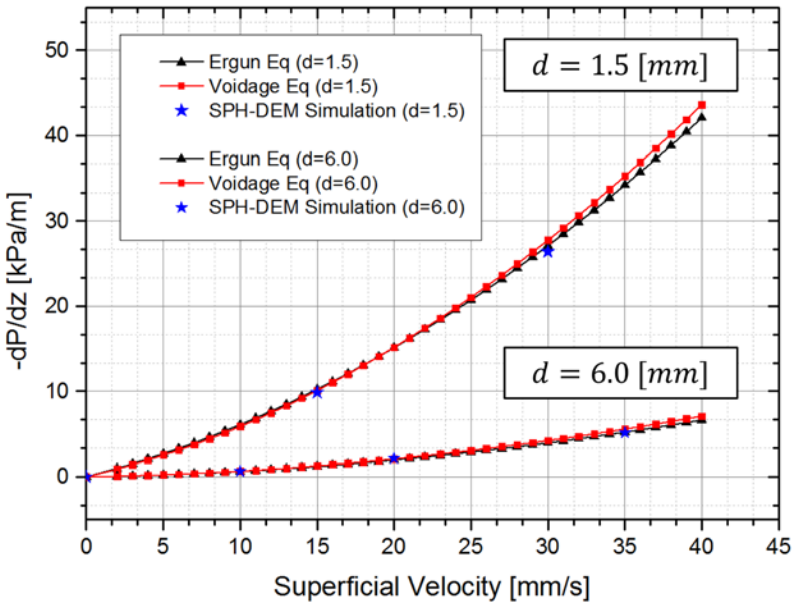


Figure 4.11. Single Phase Pressure Drop through Packed Bed

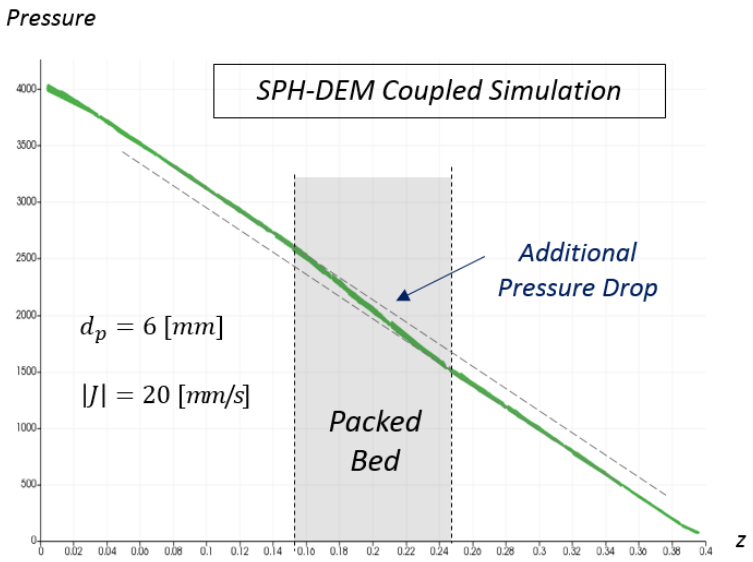


Figure 4.12. Pressure Data of SPH-DEM Phase Coupled Simulation

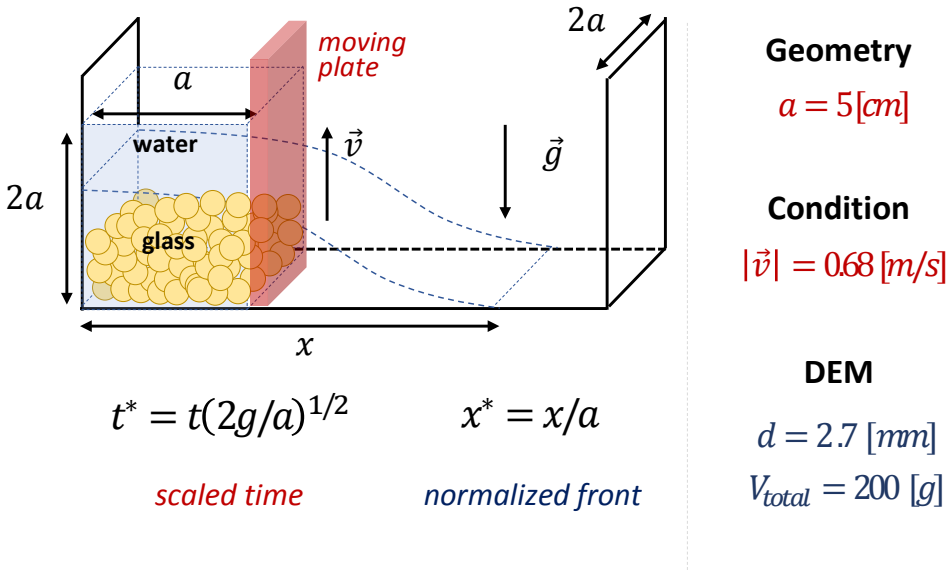


Figure 4.13. Conditions for Solid-Liquid Dam-Break Experiment [Sun, 2013

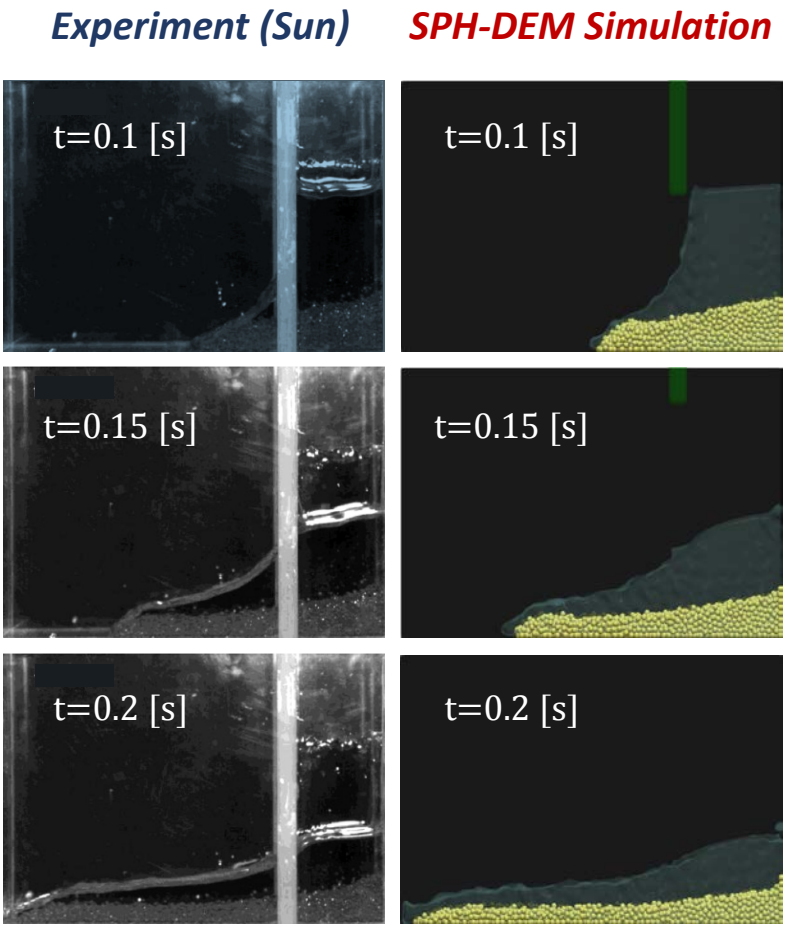


Figure 4.14. Qualitative Results of Solid-Liquid Dam-Break Simulation

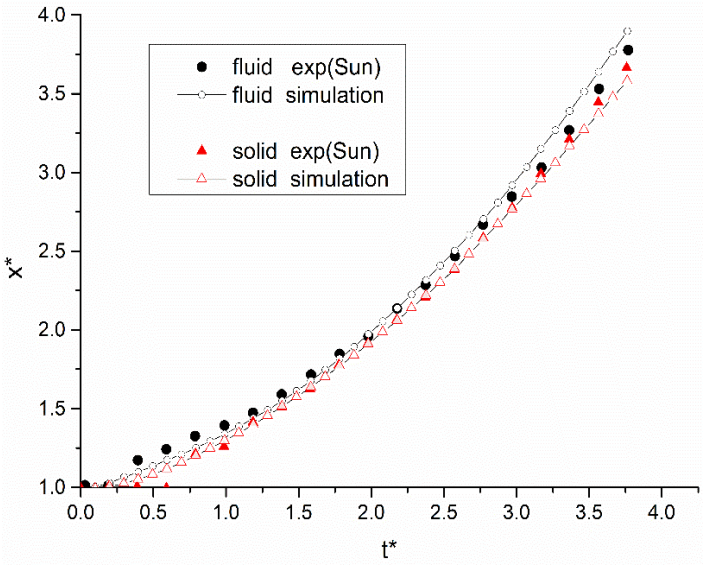


Figure 4.15. Quantitative Validation Result of SPH-DEM Coupled Code

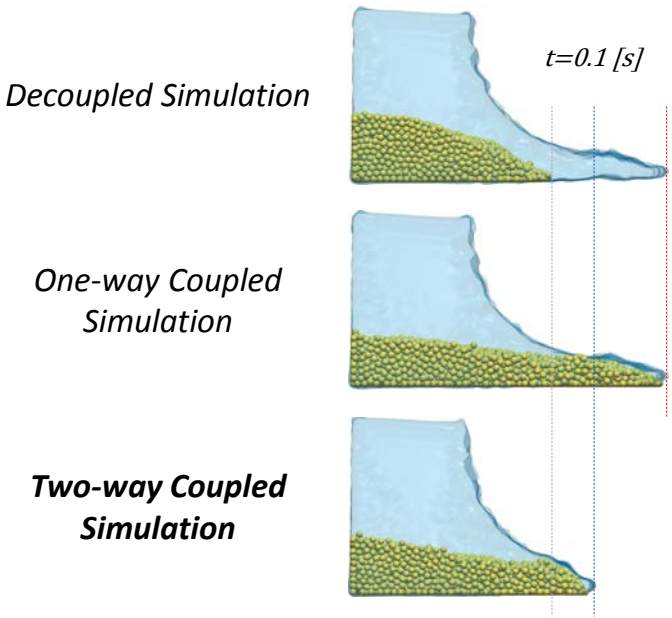


Figure 4.16. Qualitative Comparison Results (decoupled, one-way, two-way)

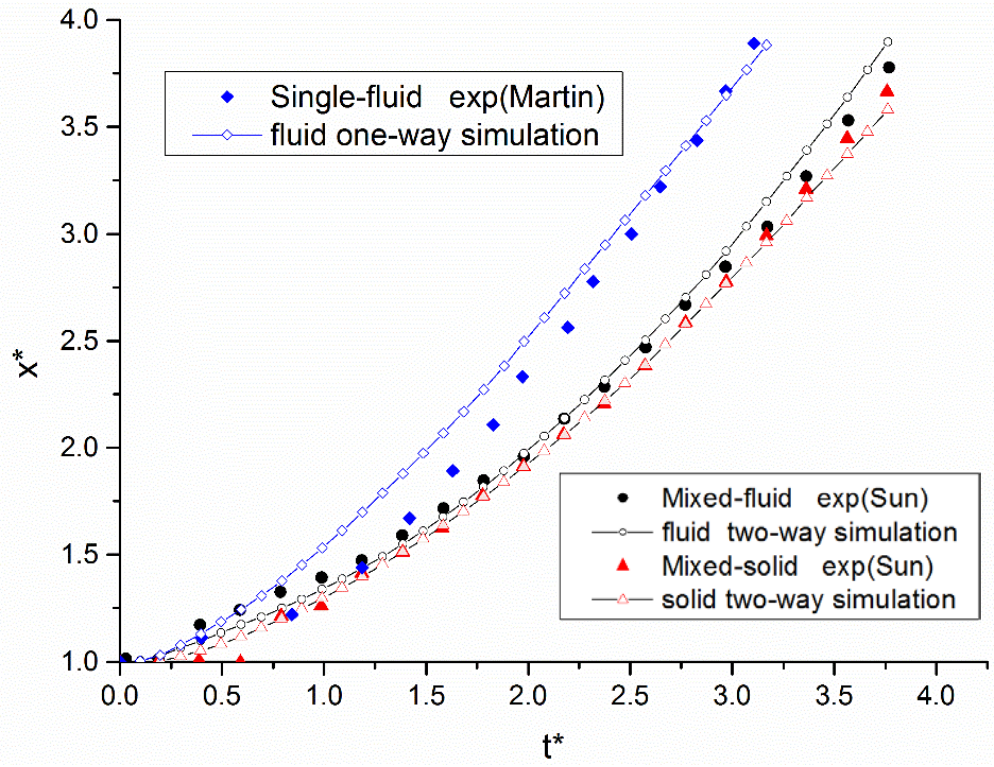


Figure 4.17. Quantitative Comparison Results in Time Variation of Normalized Leading Front (one-way, two-way coupled)

# Chapter 5

# GPU Parallelization of Coupled SPH-DEM Code

The developed SPH-DEM phase coupled model has an essential time step limitation since the SPH and DEM model in this study are both fully explicit numerical methods. Since the accuracy of the simulation in Lagrangian-based numerical methods can be highly affected by the particle resolution, some strategies are required to improve the efficiency of code calculation. Fortunately, solving the governing equations for each SPH particle and DEM particle is relatively easy to parallelize, and can thereby significantly improve the code efficiency through parallelization. (The weakly compressible approach in SPH and the Lagrangian-based governing equations makes parallelization relatively easy by not solving the complex matrix in the model calculation)

The acceleration of the SPH-DEM coupled model was achieved by Graphical Process Unit (GPU) to solve the governing equations of SPH and DEM in parallel for each SPH and DEM particle, rather than to divide the computational area (domain decomposition). The parallelization mechanism of SPH-DEM coupled code and the results of acceleration are described in the sections below.

## 5.1 Parallelization of Governing Equations

### 5.1.1 GPU-based Parallelization

The GPU is a graphic controller developed for large-scale data processing in the computer graphics field. Many commercial architectures, such as OpenCL, ATI Stream, and CUDA C, have been developed. The SPH-DEM coupled code in this study has been parallelized through NVDIA's CUDA architecture, which is the most widely used general-purpose GPU (GPGPU) programing language. Figure 5.1 is a simplified representation of the CUDA memory structure. A block is a unit that acts as a streaming multiprocessor in the GPU memory, and it is composed of shared memory, register, and threads. The shared memory is a space shared by threads in a block, and it is frequently used in data processing in which cooperation among threads is required

### 5.1.2 Parallelization of SPH-DEM Governing Equations

In the calculation of SPH and DEM physical models, one block in Figure 5.1 is mapped to each targeted particle $i$ (SPH) and particle $a$ (DEM), and the threads are assigned to each neighboring particles (SPH) and contact particles (DEM), respectively as shown in Figure 5.2. Similarly, in the calculation of the coupling force between SPH and DEM particles, the neighboring DEM particles for targeted SPH particles and the neighboring SPH particles for targeted DEM particles both are assigned to the treads of each block. Then, each thread stores

the calculated value associated with each neighboring particle (SPH) or contact particle (DEM) in the shared memory, and the summation of each term is performed in the shared memory. In this step, a parallel reduction is carried out, in which the values of the shared memory are summed in parallel while reducing the size of the data by half at every reduction step, as shown in Figure 5.3. Figure 5.4 shows the simplified algorithm of the SPH-DEM coupled code in this study. As shown in the figure, the parallel mapping is applied for most of the particle functions, and the parallel reduction using shared memory is performed in the part for solving the interaction equations with neighboring particles (SPH) or contact particles (DEM).

## 5.2 Parallelization of NNPS and Contact Detection

The SPH method solves the physical models as a form of discretized summation for each neighboring particle, and the DEM method solves the contact forces; therefore, the nearest-neighboring particles search (NNPS hereafter) procedure and contact detection for each SPH and DEM particle must be performed before solving the governing equations for physical models. Generally, the NNPS step and contact detection are the most time-consuming part of the SPH and DEM calculation, respectively, because these procedures should be carried out for each neighboring particle and each contact particle for the targeted center particle. Thus, the performance of the code algorithm highly depends on the efficiency of the NNPS and contact detection procedure.

The NNPS and contact detection of the SPH-DEM coupled code are carried

out based on the rectangular grids as described in Chapter 2 (SPH) and Chapter 3 (DEM). In the SPH-DEM coupled code in this study, a counting sort algorithm is implemented in which particles are rearranged based on the order of each grid index, as described in the previous chapter (Chapter 2). Various GPU parallelization algorithms, including inclusive scanning and atomic add, are applied to all the detailed process of particle sorting. The detailed sequences of the counting sort are as follows.

(1) SPH and DEM particles are assigned to each grid, and the grid index of each particle is determined based on the position, as shown in Figure 5.5(a) and Figure 5.5(b), respectively.
(2) The number of particles belonging to each grid is counted in parallel, using the atomic add function in the CUDA C architecture (Figure 5.5(c)).
(3) The cumulative number summation is carried out with the use of the parallel inclusive scanning method, as shown in Figure 5.5(d).
(4) The starting index at which the particle of each grid stars is obtained.
(5) All of the particles are sorted in grid order based on the starting index and the cell index of each particle, as shown in Figure 5.5(e).

After the above particle sorting is completed, the grid-based NNPS and contact detection are performed also in parallel. The targeted particle is assigned to a block of the CUDA memory, and the adjacent grids of the targeted particle are allocated to the threads of each block, as shown in Figure 5.5. Each thread follows the starting index of grid particles and compares the distance between the grid particles and the targeted particle. Then, each thread determines the neighboring

particles (SPH) or contact particles (DEM) of the targeted particle and saves the index of the particle into the list of neighboring particles of the targeted particle.

## 5.3 Results of GPU Parallelization

### 5.3.1 Speedup in Computation Time

The computation time in the simulation of 3D single-phase dam-break flow was compared before and after the parallelization of developed code. As shown in Figure 5.6, the calculation speed increases by up to 2 orders of magnitude compared to the previous CPU-based code. It can be seen that the effect of code parallelization increases as the number of total particles increases.

### 5.3.2 Parallelization Factors

The degree and efficiency of GPU parallelization were quantified by calculating reference factors such as speedup factor, relative efficiency, and parallelization factor. The speedup factor ($T_1/P_1$) is the ratio of an execution time before parallelization to the execution time after parallelization, which is also written in Figure 5.6 on each number of particles. Since the speedup factor is the function of particle numbers, other factors including relative efficiency, parallelization factor are also the function of particle numbers as summarized in Table 5.1. According to the table, the speedup factor is 157.9 in the case of a

million particles, which means it has been more than 150 times faster than single CPU calculations. In this case, the parallelization factor is also over 0.99, which is enough to expect sufficient performance improvement by parallelization. Also, it can be said that the GPU parallelization is efficient enough since the speedup factor for 3,854 GPU cores reaches 96.3% of the convergence value for the corresponding parallelization factor.

Table 53.1. Parallelization Factors for the Code

| Number of Particles | | $10^3$ | $10^4$ | $10^5$ | $10^6$ |
|---|---|---|---|---|---|
| Speedup Factor ($SF_p$) | $T_1/T_p$ | 36.85 | 77.18 | 117.5 | 157.9 |
| Relative Efficiency | $SF_p/p$ | 0.0103 | 0.0215 | 0.0328 | 0.0440 |
| Parallelization Factor (Amdahl's Law) | $\left(1-\frac{1}{SF_p}\right) * p/(p-1)$ | 0.9731 | 0.9873 | 0.9918 | 0.9939 |

- $T_1$: number of processors (3,584 CUDA cores for GeForce GTX 1080 Ti)
- $T_1$: execution time for one processor (one single CPU in this case)
- $T_p$: execution time for p processors (multi-core GPU)

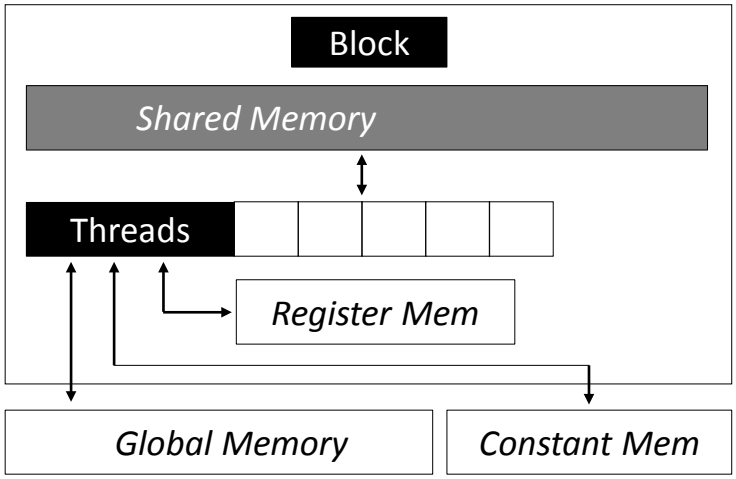


Figure 5.1. Memory Structure of CUDA

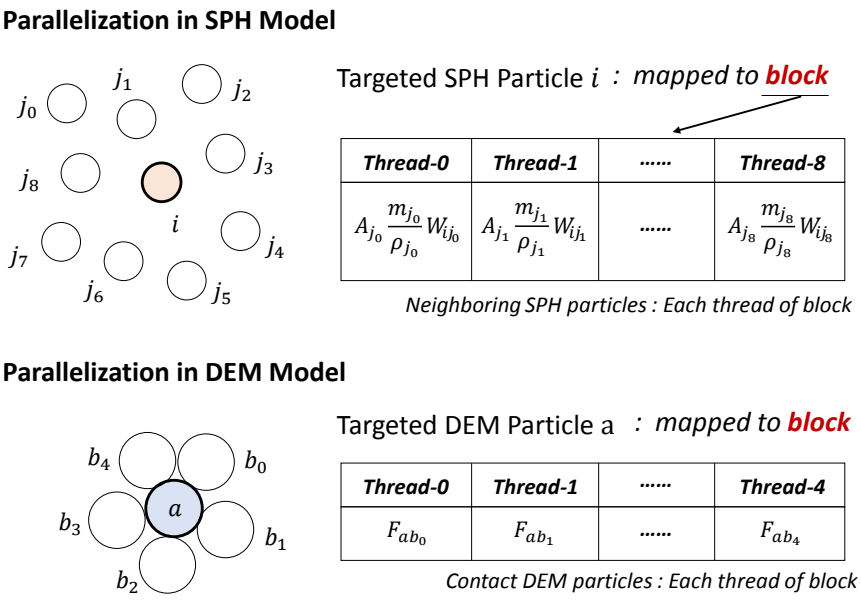


Figure 5.2. Conceptual Description of GPU-based Parallelization of Code

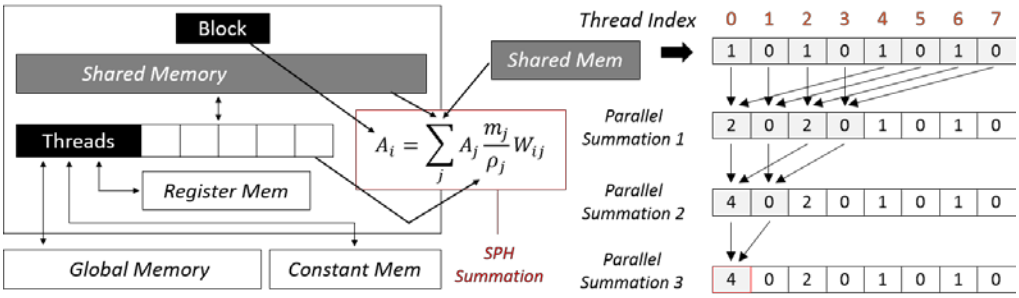


Figure 5.3. Parallel Reduction for Solving Governing Equations of SPH

| | |
|---|---|
| 1. Start Simulation<br>2. Input & Initialization | **Parallelization scheme used in SPH-DEM model** |
| 3. NNPS (SPH)<br>Contact Detection | Counting,<br>Cum sum, sorting |
| 4. Density Calculation | Mapping, Reduction |
| 5. Pressure Calculation | Mapping |
| 6. MTM Conservation | Mapping, Reduction |
| 7. Contact Force (DEM) | Mapping, Reduction |
| 8. MTM Exchange<br>(SPH-DEM Coupling) | Mapping, Reduction |
| 9. Update Properties | Mapping |

Figure 5.4. Simplified Algorithm of Code in Terms of GPU Parallelization

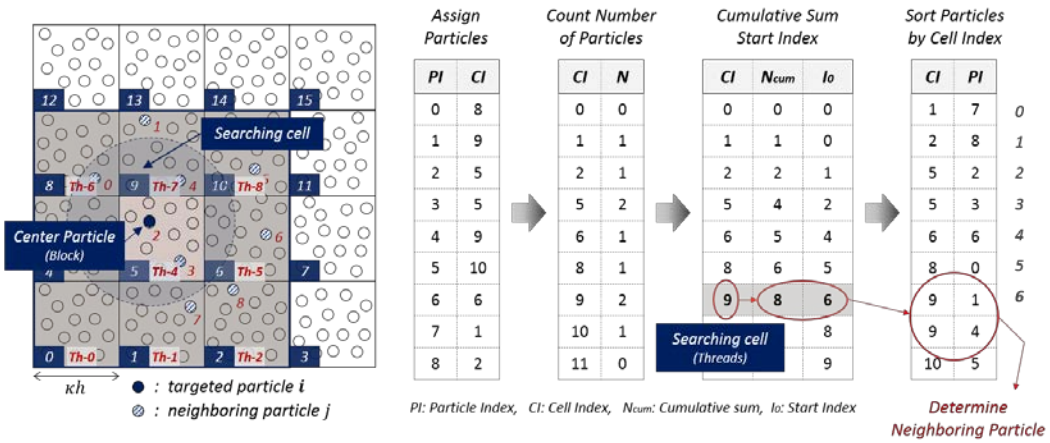


Figure 5.5. Simplified Sorting and Parallelization Algorithm for SPH-DEM Coupled Code

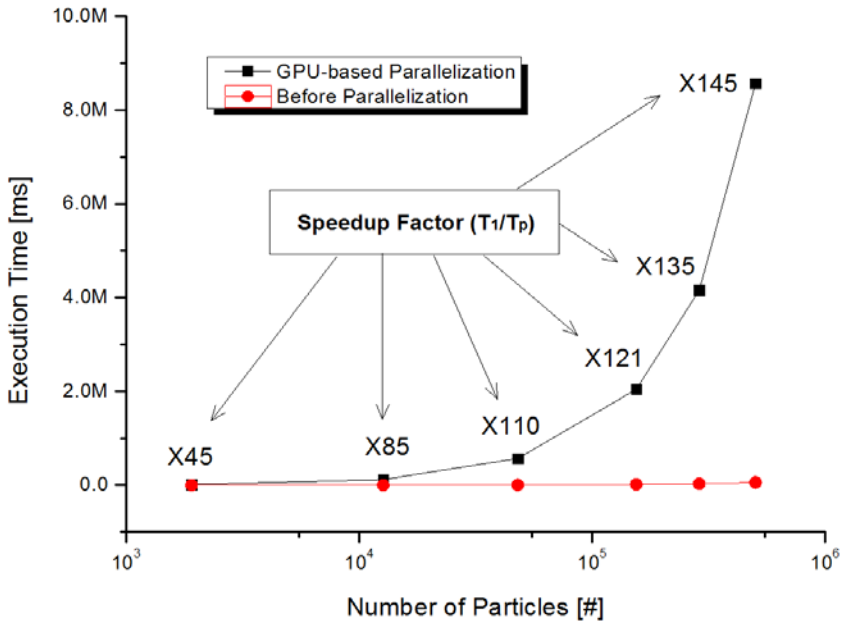


Figure 5.6. Speedup for GPU Parallelization of SPH-DEM Coupled Code

# Chapter 6

# Code Application to Vapor-Driven Leveling Behavior of Spherical Debris

In the late phase of the severe accident of reactor, there are many safety issues related to the 3-phase flow such as melt jet breakup, melt spreading, agglomeration of solid debris, sloshing, self-leveling, and so on. Among them, the vapor-driven self-leveling behavior of particulate solid debris is selected as an application case for demonstration of developed 3-phase flow analysis code in this study. There are some reasons for this.

a. It is suitable to demonstrating the hydrodynamic behavior of each phase.
b. Unresolved coupling of SPH and DEM is suitable for particulate flow.
c. Validation of the newly proposed boundary model is possible since the debris particles are packed on the bottom concrete surface.
d. There are enough benchmarking experiment data for comparison.

The following sections cover benchmarking experiments on self-leveling behavior and also the results of 3D SPH-DEM simulation as well as validation results.

## 6.1 Self-Leveling Behavior of Debris Bed

### 6.1.1 Self-Leveling Issue in LWR

In the late phase of PWR severe accident, failure of In-Vessel Retention strategy may lead to the release of core melt out of the vessel. In the wet cavity strategy with ex-vessel cooling, the core melt may be quenched and fragmented into the solid particles depending on the depth of the wet cavity. These particulate debris particles may spread by coolant drag and finally sediment into a mound shape. Two-phase natural convection occurs due to the decay heat generated from debris particles, which is the main heat removal mechanism of decay heat. In this situation, the steam flow escaping from the porous bed can be a source of mechanical energy, which can move the solid debris particles. Then, the conical shape of the particulate debris bed can change the geometry and be leveled due to the two-phase natural convection (Figure 6.1). This so-called self-leveling phenomenon of debris bed is an important issue in terms of mitigation of severe accident.

### 6.1.2 Self-Leveling Behavior in Terms of Debris Coolability

The wet cavity strategy (ex-vessel reactor cooling) succeeds only if the decay heat from debris particles is removed by two-phase natural convection of coolant (water). Otherwise, the debris bed can be re-melted due to dry out on the debris

particle surface, eventually attacking the containment (MCCI). Therefore, the coolability of the debris bed is a very important safety parameter in the late phase of a severe accident.

Generally, the coolability of the debris bed depends mainly on the properties of the bed including particle size, porosity, and also the overall shape of the debris bed. Especially, the maximum height of the bed is an important factor for debris bed coolability. According to the previous study, the same mass of debris bed can be cooled much easier if it is distributed uniformly over the basemat, rather than if it forms a tall mound-shaped debris bed [Basso, 2016]. A tall bed is hardly coolable since it is most prone to dry-out. Thus, the physical phenomena that can reduce the maximum height of the debris bed are of safety importance in a coolability analysis. In this respect, the self-leveling behavior is an important phenomenon since it may change the non-coolable shape to coolable geometry.

In order to be effective in establishing a coolable geometrical configuration of the bed, the characteristic time scale of the self-leveling should be smaller than the characteristic time scale for reaching dryout and re-melting of debris. If the former time scale (reaching coolable configuration) is shorter than the latter time scale (onset of re-melting), initially non-coolable debris bed becomes coolable due to self-leveling behavior. Therefore, it is necessary to analyze the leveling behavior over time in various conditions (particle size, steam flow rate, porosity, sphericity, etc.).

## 6.2 Benchmark Experiment

Several series of experiments were elaborately designed and conducted in Kyushu University to clarify the mechanisms underlying the self-leveling behavior of debris bed [Cheng, 2012]. The tendency of leveling behavior was analyzed from various experiment cases, and an empirical model was also developed to describe the transient variation in the bed inclination angle during the self-leveling process based on the experimental data. Besides, a parametric study was performed on various experiment factors including particle size, particle density, gas flow rate, and so on.

In these experiments, solid particles and water are contained in a tank, and various methods including gas injection, depressurized boiling, and bottom-heated boiling were employed o simulate the vapor-driven leveling behavior. The gas injection experiment in the rectangular viewing tank was selected as a benchmark experiment for code validation in this study.

A schematic diagram of the experimental setup is shown in Figure 6.2. A rectangular tank with $500mm$ height, $250mm$ width, $55mm$ gap thickness is filled with solid particles with a total volume of $2.5L$. Water and nitrogen gas were employed to simulate the coolant and steam, respectively. The depth of water was maintained at around $400\mathrm{mm}$, and the nitrogen gas was released into the tank from the bottom with a constant flow rate. Over the bottom of the viewing tank, a porous medium called airsotne served as a gas distributor ensuring a uniform percolation of gas. The main experimental conditions for the cases used in validation simulation are as below, and are also summarized in Figure 6.3.

- Particle Size : $6\ [mm]$
- Particle Sphericity : ~1.0 (Sphere)
- Porosity : ~0.42
- Total Volume of Particle : $2.5\ [L]$
- Particle Material : Glass (Glass bead)
- Liquid Material : Purified Water
- Gas Material : Nitrogen Gas ($100\ [kPa]$)
- Nitrogen Gas Flow Rate : $1.53,\ 3.43,\ 4.16\ [L/min]$
- Initial Inclined Angle : $20^{\circ}$~$27^{\circ}$

In this benchmark experiment, the ratio of the inclination angle at time $t'$ to initial angle ($t' = 0$) is defined as $R(t')$, and used to further quantify and anlyze the transient behavior of self-leveling. The simple expression of $R(t')$ is as below,

$$R(t') = \frac{Inclined\ Angle\ at\ t'\ \theta(t')}{Initial\ Inclined\ Angle\ \theta_0} \tag{6.1}$$

where $\theta$ *i*s an inclined angle of particle slope as shown in Figure 6.3, and the tangent of inclined angle is calculated as the ratio of the measured height of apex to the half-width of the rectangular tank in the experiment. In each experiment case, $R(t')$ was measured over time, and the experiment data are plotted as shown in Figure 6.4.

## 6.3 SPH-DEM Simulation Setup

For 3-phase flow validation of the developed SPH-DEM coupled code, the simulation was performed under the same conditions as the benchmarking experiment in the above section [Cheng, 2012]. The simulation was performed in exactly the same geometry and conditions with the benchmark experiment, as shown in Figure 6.5. The simulation conditions including the physical properties of DEM particles, the sequence of the SPH-DEM coupled simulation, and the determination method of inclined angle are covered in the following sub-sections.

### 6.3.1 Properties and Simulation Conditions

The physical properties of the fluid and solid used in this simulation were mostly referred to the real properties of purified water, nitrogen gas, and glass bead used in the benchmark experiment. For the properties that are not described in the benchmark experiment such as restitution coefficient and friction coefficient, the physical properties were obtained from the numerical analysis conducted in the same institution [Guo, 2013]. The physical properties of SPH and DEM particles used in the simulation are as follows.

1. Purified Water (SPH)

- Density: 1,000 [$kg/m^3$]
- Dynamic Viscosity: 0.001 [Pa · s]

2. Nitrogen Gas (SPH)

- Density: 1.126 [$kg/m^3$]

- Dynamic Viscosity: $1.789 \times 10^{-5}$ [Pa · s]

3. Glass Bead (DEM)

- Density: 2,590 [$kg/m^3$]
- Elasticity Modulus: $1.0 \times 10^{10}$ [Pa]
- Poisson's Ratio: 0.25
- Particle Diameter: 6 [mm]
- Restitution coefficient: 0.9
- Friction Coefficient: 0.3

As described in the previous chapter (Chapter 4), the unresolved coupling of SPH-DEM is effective when the SPH particle resolution is similar to the characteristic size (Diameter) of the DEM particle. Since the diameter of the DEM particles is fixed (6 mm) in this simulation, the applicable SPH resolution range is pre-determined. In the case of the time-step of the simulation, the step size required for the vapor phase SPH simulation is similar to that of DEM calculation ($\sim 10^{-6}$). Therefore, time integration was performed in the same algorithm. In addition, SPH particles corresponding to nitrogen gas are generated and injected at a constant rate that satisfies the volumetric gas flow rate given in the benchmark experiment. The conditions for SPH-DEM coupled leveling simulation are as follows.

- SPH Particle Spacing: 3.6 [mm]
- Coupling Length: 14.4 [mm]
- Time Step Size : $2.0 \times 10^{-6}$

- Nitrogen SPH Particles Velocity: $1.85, 4.16, 5.04\ [\mathrm{mm/s}]$
- Number of SPH Particles: $231{,}664$
- Number of DEM Particles: $12{,}480$

### 6.3.2 Sequence of SPH-DEM Leveling Simulation

The sequence for performing SPH-DEM simulation under the benchmark experiment conditions can be summarized as follows.

(1) SPH, DEM particle generation. In the case of DEM particles, the total volume of particles should be same as experiment condition ($2.5\mathrm{L}$) considering the packed porosity ($\sim 0.52$)
(2) DEM particle packing using DEM wall boundary condition. DEM particles should be packed in a mound shape by applying a wall boundary model inclined to around $25^{\circ}$ degree (Figure 6.5).
(3) Particles initialization. The DEM wall boundary that packed the DEM particles is removed and the particles are initialized to have a stable shape. The SPH particles are also coupled with DEM particles in this step.
(4) Nitrogen SPH particle injection. The nitrogen SPH particles are generated in a checkerboard shape in order to simulate the airstone (porous medium) in the benchmark experiment, as shown in Figure 6.6.
(5) Upper SPH boundary moving. The upper SPH boundary is raised in a constant velocity satisfy the incompressible condition in the computational domain.

### 6.3.3 Determination of Inclined Angle

In the benchmark experiment, the inclined angle of solid particles slope is defined based on the maximum height of solid particles. Specifically, the tangent of the inclined angle is calculated as the ratio of the measured height of apex to the half-width of the rectangular tank. The following definition of inclined angle is also applied in the simulation of this study,

$$\theta(t') = tan^{-1}\left(\frac{Height\ of\ Apex,\ H_{apex}(t')}{Half\ Width\ of\ Tank,\ W_{tank}}\right) \tag{6.2}$$

where $H_{apex}$ and $W_{tank}$ are the maximum height of apex and half-width of the rectangular tank, respectively. The maximum height of DEM particles was determined only for the particles within a specific area in order to exclude the effect of particles leaning on the sidewall, as shown in Figure 6.7.

## 6.4 Validation Results and Discussions

### 6.4.1 SPH-DEM Simulation Results

The SPH-DEM phase coupled simulation for self-leveling behavior was performed for three different gas inlet flow rate ($1.53,\ 3.43,\ 4.16\ [L/min]$). The simulation results for the case with a gas flow rate of $4.16\ [L/min]$ are

compared with the snapshots of the experimental result in Figure 6.8. From Figure 6.8, the self-leveling behavior of solid particle bed is clearly visible. The inclined angle, which was initially $20.5^{\circ}$, dropped to $15.1^{\circ}$ after 20 seconds under the influence of nitrogen gas-driven self-leveling behavior.

### 6.4.2 Validation Result

Figure 6.9 shows the comparison of $R(t')$ values, which is the ratio of the inclination angle at time $t'$ to initial angle, versus time $t'$ between experimental data and simulation results for the case with gas flow rate of $4.16\ [L/min]$. The data labeled SIMMER on Figure 6.9 are the results for the Eulerian-DEM coupled analysis performed in the same institution with the benchmark experiment [Guo, 2013], where SIMMER code is an Eulerian-based multiphase, multicomponent, multi-velocity field fluid dynamics code developed for the safety analysis of fast reactor.

As shown in Figure 6.9, the SPH-DEM coupled simulation results in this study well predict the long-term leveling behavior of solid particles in the benchmark experiment, showing better agreement than the results of Eulerian-DEM coupled simulation.

### 6.4.3 Effect of Gas Flow Rate

According to the previous experiments on self-leveling behavior, the equivalent power density appeared as a driving factor of leveling motion. Namely, the larger the equivalent power density, the faster the self-leveling proceeds

[Zhang, 2011]. In the gas injection experiment (benchmark experiment in this study), the gas flow rate can play an analogous role as shown in Figure 6.4. In this study, the self-leveling simulation was performed on three different gas velocities in order to analyze the effect of the gas flow rate. As shown in Figure 6.10, the inverse relation between $R(t')$ and gas inlet velocity can be clearly observed in simulation, which agrees well in the tendency with the results of experiments.

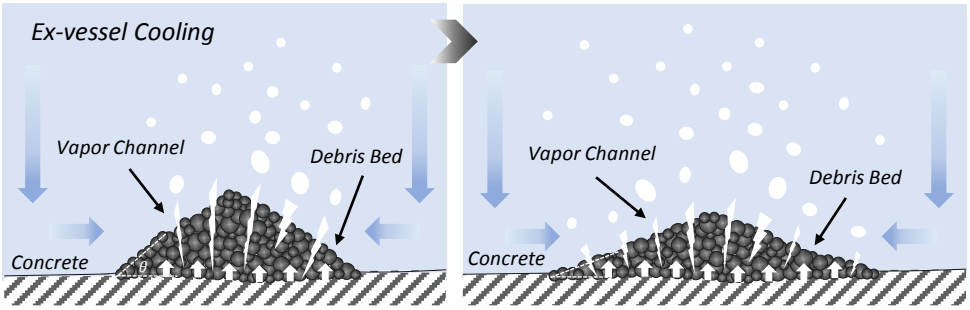


Figure 6.1. Mechanism of Debris Bed Self-Leveling

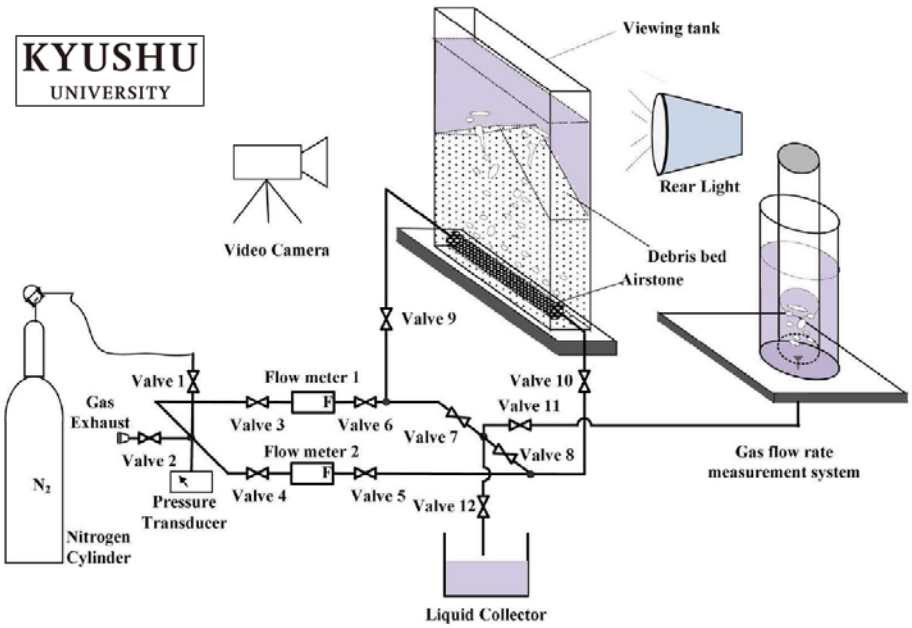


Figure 6.2. Schematic View of Experimental Apparatus [Cheng, 2012]

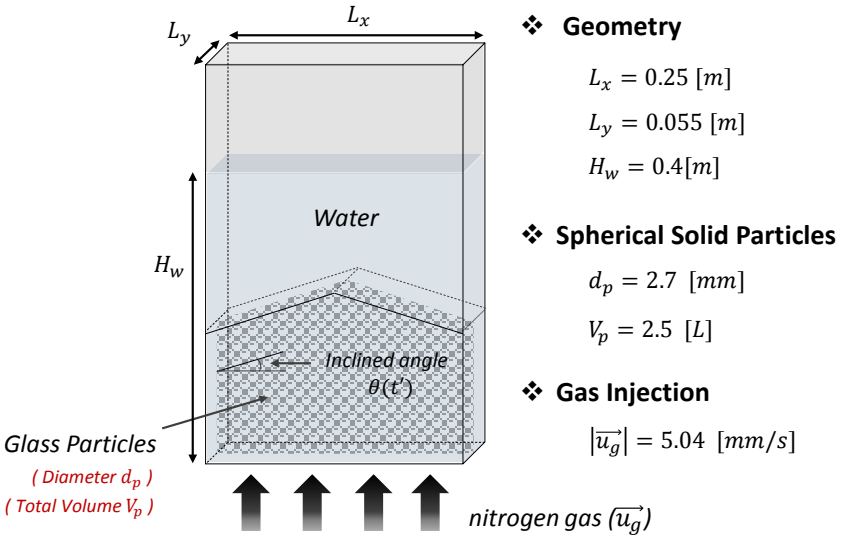


Figure 6.3. Conditions for Benchmark Leveling Experiment

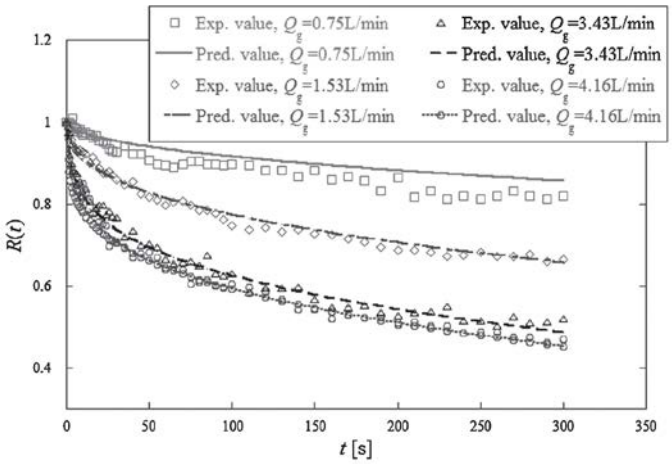


Figure 6.4. Time Variation of Inclined Angle in Benchmark Experiment [Cheng, 2012]

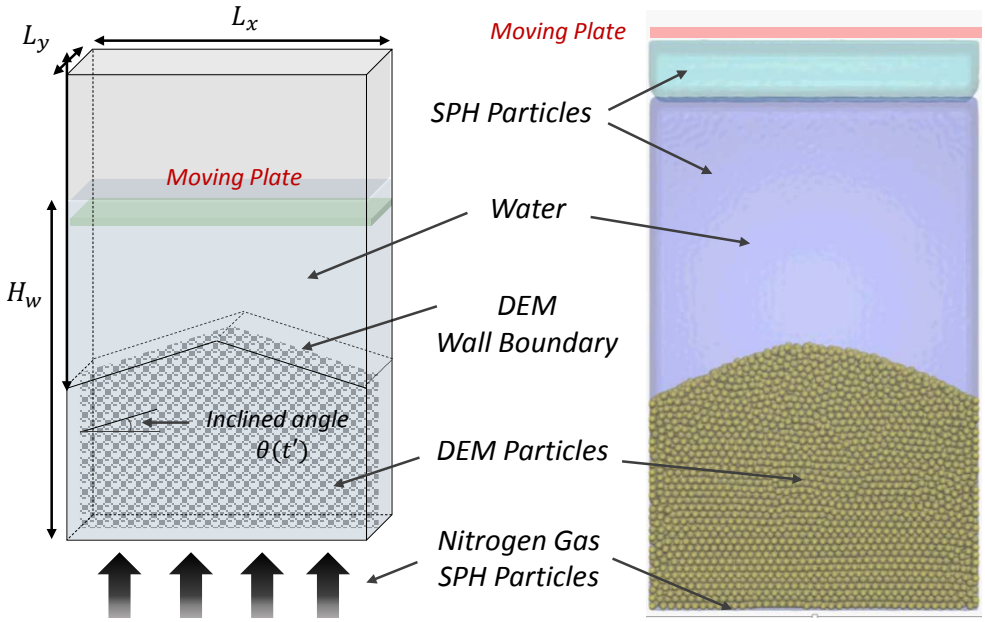


Figure 6.5. Geometry of SPH-DEM Coupled Leveling Simulation

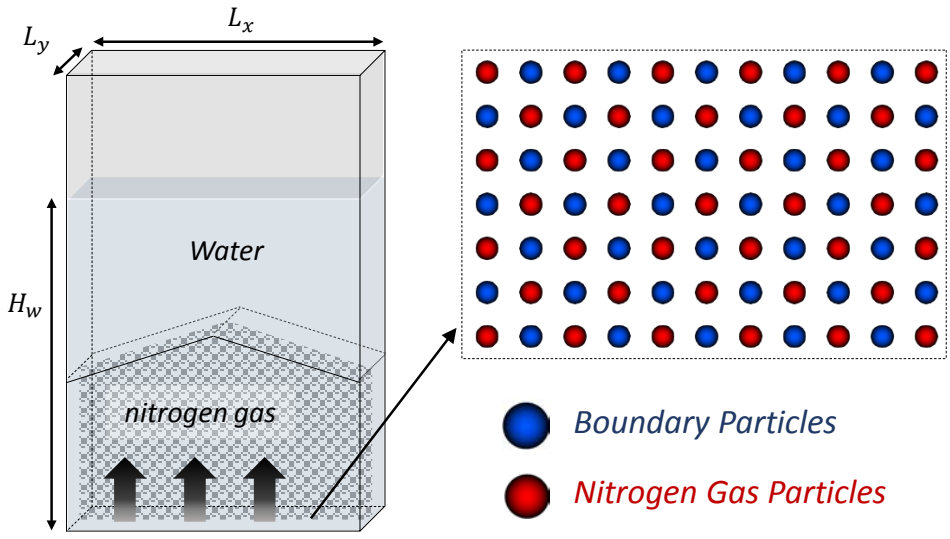


Figure 6.6. Gas Injection in SPH-DEM Coupled Simulation

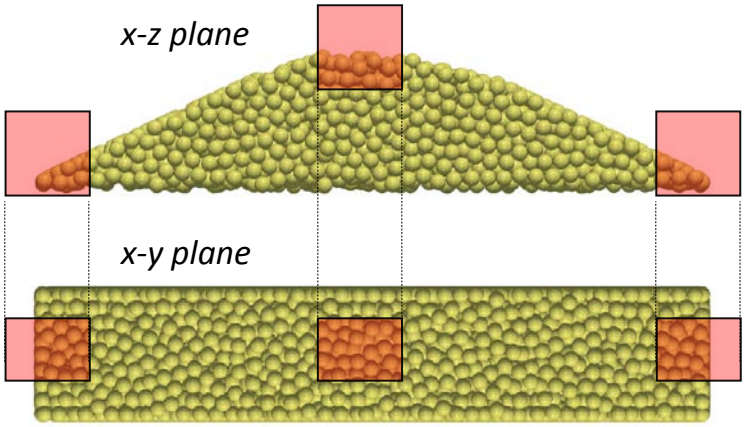


Figure 6.7. DEM Particles Used for Data (Height) Analysis

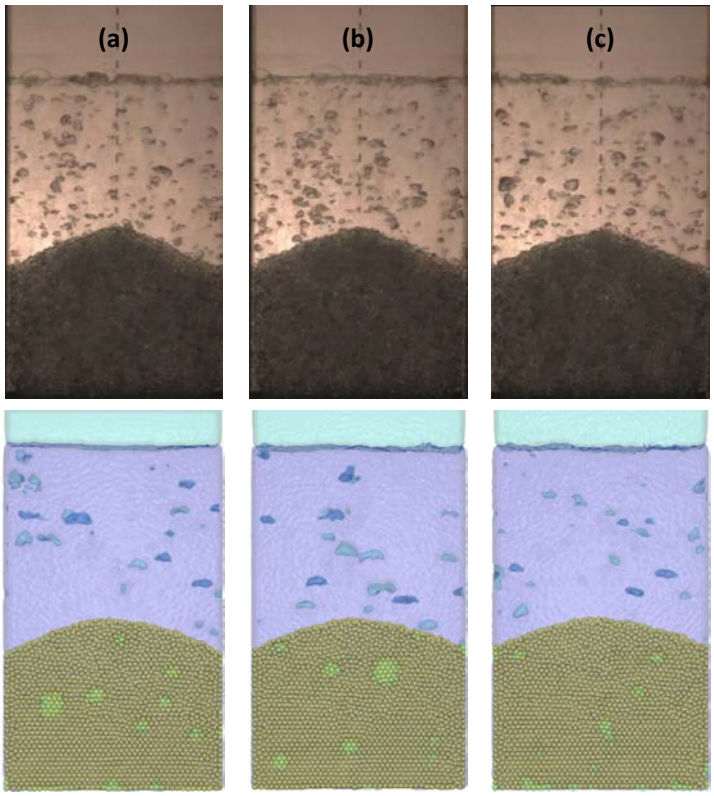


Figure 6.8. Snapshots Comparison b/w Experiment and SPH-DEM Simulation
(a) $t' = 5s$, (b) $t' = 10s$, (c) $t' = 15s$

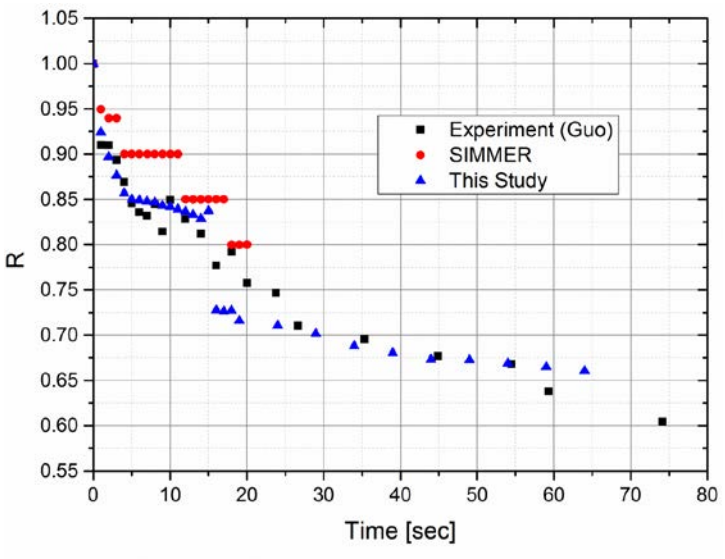


Figure 6.9. Validation Results for Time Variation of $R$ Value

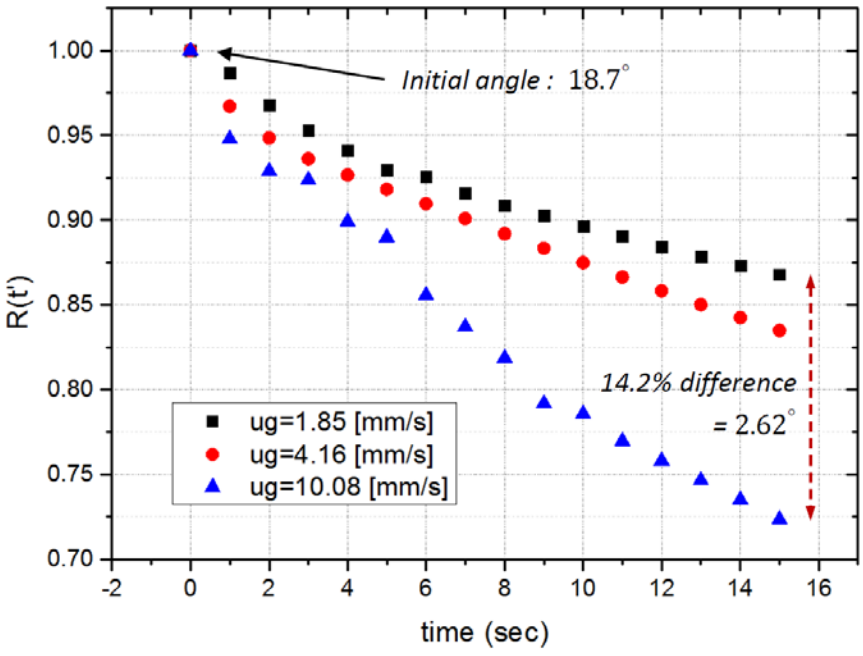


Figure 6.10. Effect of Gas Flow Rate on Self-Leveling Behavior

# Chapter 7

# Summary

## 7.1 Summary

In this study, the GPU-parallelized SPH-DEM phase coupled code was developed for the simulation of 3-phase hydrodynamic phenomena involving solid particles related to fuel debris in a reactor severe accident. The results, achievement, and findings of the study are summarized as follows.

1. Development of Multi-Phase SPH Code
    A. Lagrangian-based in-house SPH code has been developed for the analysis of incompressible multi-phase flow.
    B. An improved density estimation model and surface tension model was newly proposed for accurate tracking of the liquid-vapor interface.
    C. Qualitative and quantitative validations were carried out through various V&V cases including bubble terminal velocity behavior, multi-phase dam break, and multi-phase sloshing simulation. The results were well agreed with the benchmark data.
    D. It has been identified that the implemented two-phase SPH model well simulates the interface without any linearization of density, and also

better predicts the real free surface flow compared to the single-phase SPH.

2. Development of DEM Code
   A. A DEM code for solid particles was developed based on the soft-sphere collision model using Hertz-Mindlin contact force equations.
   B. A versatile wall boundary model incorporating both collision and sliding & rolling behavior was newly proposed in order to cover the wall interaction of packed solid particles.
   C. The momentum and angular moment were well conserved in all type of inter-particle collisions.
   D. A series of particle-boundary interaction behaviors including collision and also sliding and rolling were well proven in several V&V simulations.

3. Two-Way Phase Coupling of SPH-DEM
   A. The numerical code system for incompressible 3-phase flow is newly developed by a two-way phase coupling of SPH-DEM.
   B. An unresolved coupling approach between SPH and DEM was adopted for the analysis of particulate debris behavior.
   C. Validation of SPH-DEM coupled code was performed for solid-fluid pressure drop and dam-breaking behavior. The simulation results matched well with the result of the benchmark experiment.

4. GPU Parallelization of Coupled SPH-DEM Code

A. The SPH-DEM coupled code was parallelized based on Graphical Process Unit (GPU).
B. Various parallelization schemes were used for both solving governing equations of each SPH and DEM particle and finding the neighbor particles in SPH or contact particles in DEM.
C. Based on the benchmark calculation, the calculation speed increases by up to 2 orders of magnitude after code parallelization.
D. GPU parallelization in this study was efficient enough since the speedup factor reached 96.3% of the convergence value for the corresponding parallelization factor.

5. Code Application to Self-Leveling Simulation of Spherical Debris
   A. The simulation on vapor-driven debris bed self-leveling behavior was performed as a case study for the demonstration of developed SPH-DEM coupled code for 3-phase flow.
   B. The simulation results showed good agreement with the results of benchmark experiments both in qualitative and quantitative manners.
   C. The leveling behavior of solid particles in the simulation was suppressed in a lower gas flow rate, as also observed in the benchmark experiment.

## 7.2 Recommendations

The result of this research suggests following further studies.

1. The simulation and validation of the self-leveling behavior of solid particles in this study were carried out in a thin rectangular tank with cm scale. Since the benchmark experiments on self-leveling behavior were also carried out in relatively larger cylinder shaped tanks at Kyushu University and KTH, it is recommended to conduct the numerical simulations in cylindrical geometry based on a larger number of particles and higher particle resolution.
2. This study is focused on the hydrodynamic behavior of particulate solid within the incompressible multi-phase flow. However, in order to simulate the behavior of solid debris in actual reactor conditions, various advanced physics should be incorporated especially with regard to heat transfer and phase change, as shown in Figure 1.2. It is recommended to expand the scope of developed code through implementation and V&V of each physics listed in Figure 1.2.
3. If the validations of advanced physical models including turbulence, phase change, and non-spherical DEM particles are made, it is recommended to apply the code for actual reactor conditions. It is expected that the numerical experiments can be performed on the actual reactor conditions using developed SPH-DEM coupled code, which is hard to be conducted in laboratory-scale experiments.
4. The newly developed SPH-DEM coupled code used the unresolved coupling strategies between two methods. Thus it is suitable for particulate granular flow rather than single rigid body behavior. In this respect, the following numerical studies are recommended associated with the behavior of fragmented solid debris in addition to self-leveling phenomena.

A. Vapor-driven sloshing behavior of particulate debris (LMR)

B. Vapor entrainment in sedimentation behavior of solid particles (LWR)

# References

Adami, S., X. Y. Hu, and Nikolaus A. Adams. "A new surface-tension formulation for multi-phase SPH using a reproducing divergence approximation." *Journal of Computational Physics* 229.13 (2010): 5011-5021.

Basso, Simone, Alexander Konovalenko, and Pavel Kudinov. "Effectiveness of the debris bed self-leveling under severe accident conditions." *Annals of Nuclear Energy* 95 (2016): 75-85.

Brackbill, Jeremiah U., Douglas B. Kothe, and Charles Zemach. "A continuum method for modeling surface tension." Journal of computational physics 100.2 (1992): 335-354.

Breinlinger, Thomas, et al. "Surface tension and wetting effects with smoothed particle hydrodynamics." *Journal of Computational Physics* 243 (2013): 14-27.

Buck, Michael. "Modelling of the late phase of core degradation in light water reactors." (2007).

Buruchenko, Sergei K., and Alejandro JC Crespo. "Validation DualSPHysics Code for Liquid Sloshing Phenomena." 2014 22nd International Conference on Nuclear Engineering. American Society of Mechanical Engineers, 2014.

Cheng, Songbai, et al. "A two-dimensional experimental investigation on the sloshing behavior in a water pool." Annals of nuclear energy 114 (2018): 66-73.

Cheng, Songbai, et al. "An experimental study on pool sloshing behavior with

solid particles." *Nuclear Engineering and Technology* 51.1 (2019): 73-83.

Cheng, Songbai, et al. "Experimental studies and empirical models for the transient self-leveling behavior in debris bed." *Journal of nuclear science and technology* 48.10 (2011): 1327-1336.

Chou, H. T., et al. "Discrete element modelling and experimental validation for the falling process of dry granular steps." *Powder technology* 231 (2012): 122-134.

Cleary, Paul W. "Modelling confined multi-material heat and mass flows using SPH." *Applied Mathematical Modelling* 22.12 (1998): 981-993.

Clift, Roland, John R. Grace, and Martin E. Weber. *Bubbles, drops, and particles*. Courier Corporation, 2005.

Cossins, Peter J. *The Gravitational Instability and its Role in the Evolution of Protostellar and Protoplanetary Discs. Chapter 3: Smoothed Particle Hydrodynamics-Or: How I Learned to Stop Worrying and Love the Lagrangian*. Diss. PhD thesis, University of Leicester, 2010.

Cundall, Peter A., and Otto DL Strack. "A discrete numerical model for granular assemblies." *Geotechnique* 29.1 (1979): 47-65.

DEM Solutions Ltd. 2016. EDEM 2.6 Theory Reference Guide. Edinburgh: DEM Solutions Ltd.

Di Felice, Rosa. "The voidage function for fluid-particle interaction systems." *International journal of multiphase flow* 20.1 (1994): 153-159.

Gingold, Robert A., and Joseph J. Monaghan. "Smoothed particle hydrodynamics: theory and application to non-spherical stars." *Monthly notices of the royal astronomical society* 181.3 (1977): 375-389.

Gomez-Gesteira, Moncho, et al. "SPHysics–development of a free-surface fluid solver–Part 1: Theory and formulations." Computers & Geosciences 48 (2012): 289-299.

Grenier, Nicolas, et al. "An Hamiltonian interface SPH formulation for multi-fluid and free surface flows." Journal of Computational Physics 228.22 (2009): 8380-8393.

Guo, L., and Koji Morita. "Numerical simulation of 3D sloshing in a liquid–solid mixture using particle methods." *International journal for numerical methods in engineering* 95.9 (2013): 771-790.

Guo, Liancheng, et al. "Numerical simulation of self-leveling behavior in debris bed by a hybrid method." *2013 21st International Conference on Nuclear Engineering*. American Society of Mechanical Engineers Digital Collection, 2013.

Guo, Liancheng, Koji Morita, and Yoshiharu Tobita. "Numerical simulations on self-leveling behaviors with cylindrical debris bed." *Nuclear Engineering and Design* 315 (2017): 61-68.

Harada, Takahiro, Seiichi Koshizuka, and Yoichiro Kawaguchi. "Smoothed particle hydrodynamics on GPUs." Computer Graphics International. Petropolis: SBC, 2007.

He, Yi, et al. "A GPU-based coupled SPH-DEM method for particle-fluid flow with free surfaces." *Powder technology* 338 (2018): 548-562.

Hegeman, Kyle, Nathan A. Carr, and Gavin SP Miller. "Particle-based fluid simulation on the GPU."*International Conference on Computational Science*. Springer, Berlin, Heidelberg, 2006.

Hirt, Cyril W., and Billy D. Nichols. "Volume of fluid (VOF) method for the dynamics of free boundaries." *Journal of computational physics* 39.1 (1981): 201-225.

Hwang, Byoungcheol, et al. "Numerical validation and investigation for the sedimentation of solid particles in liquid pool using the CFD-DEM coupling algorithm." *Nuclear Engineering and Design* 355 (2019): 110364.

Kelager, Micky. "Lagrangian fluid dynamics using smoothed particle hydrodynamics." *University of Copenhagen: Department of Computer Science* 2 (2006).

Koshizuka, Seiichi, and Yoshiaki Oka. "Moving-particle semi-implicit method for fragmentation of incompressible fluid." *Nuclear science and engineering* 123.3 (1996): 421-434.

Li, Liangxing, et al. "Pressure losses and interfacial drag for two-phase flow in porous beds with coarse particles." *Annals of Nuclear Energy* 101 (2017): 481-488.

Liu, Gui-Rong, and Moubin B. Liu. *Smoothed particle hydrodynamics: a meshfree particle method*. World scientific, 2003.

Luebke, David, and M. Harris. "General-purpose computation on graphics hardware." Workshop, SIGGRAPH. 2004.

Markauskas, D., et al. "Comparative study on mesh-based and mesh-less coupled CFD-DEM methods to model particle-laden flow." *Powder Technology* 305 (2017): 78-88.

Markauskas, Darius, and Harald Kruggel-Emden. "Coupled DEM-SPH simulations of wet continuous screening." *Advanced Powder Technology* 30.12 (2019): 2997-3009.

Maschek, Werner, Claus Dieter Munz, and Leonhard Meyer. "Investigations of sloshing fluid motions in pools related to recriticalities in liquid-metal fast breeder reactor core meltdown accidents." *Nuclear technology* 98.1 (1992): 27-43.

Maschek, Werner, et al. "Investigation on upper bounds of recriticality energetics of hypothetical core disruptive accidents in sodium cooled fast reactors." Nuclear Engineering and Design326 (2018): 392-402.

Maschek, Werner, et al. "Simulation experiments for centralized liquid sloshing motions." KERNFORSCHUNGSZENTRUM KARLSRUHE-PUBLICATIONS-KFK (1992).

Mayrhofer, Arno, et al. "Combining Blender with SPHysics, an Introduction." (2010).

Monaghan, Joe J. "Simulating free surface flows with SPH." *Journal of computational physics* 110.2 (1994): 399-406.

Monaghan, Joe J. "Smoothed particle hydrodynamics." *Annual review of astronomy and astrophysics* 30.1 (1992): 543-574.

Monaghan, Joe J. "Smoothed particle hydrodynamics." *Reports on progress in physics* 68.8 (2005): 1703.

Monaghan, Joseph John, and Ashkan Rafiee. "A simple SPH algorithm for multi-fluid flow with high density ratios." *International Journal for Numerical Methods in Fluids* 71.5 (2013): 537-561.

Morris, Joseph P. "Simulating surface tension with smoothed particle hydrodynamics." International journal for numerical methods in fluids 33.3 (2000): 333-353.

Morrison, Faith A. *An introduction to fluid mechanics*. Cambridge University Press, 2013.

Nickolls, John, et al. "Scalable parallel programming with CUDA." Queue 6.2 (2008): 40-53.

Peng, Bo. *Discrete element method (DEM) contact models applied to pavement simulation*. Diss. Virginia Tech, 2014.

Pigny, Sylvain L. "Academic validation of multi-phase flow codes." Nuclear Engineering and Design 240.11 (2010): 3819-3829.

Raji, Abdulganiy Olayinka. "Discrete element modelling of the deformation of bulk agricultural particulates." (1999).

Roache, Patrick J. Verification and validation in computational science and

engineering. Vol. 895. Albuquerque, NM: Hermosa, 1998.

Robinson, Martin, Marco Ramaioli, and Stefan Luding. "Fluid-particle flow modelling and validation using two-way-coupled mesoscale SPH-DEM." *arXiv preprint arXiv:1301.0752* (2013).

Sanders, Jason, and Edward Kandrot. CUDA by Example: An Introduction to General-Purpose GPU Programming, Portable Documents. Addison-Wesley Professional, 2010.

Siegel, Jakob, Juergen Ributzka, and Xiaoming Li. "CUDA memory optimizations for large data-structures in the gravit simulator." *Journal of Algorithms & Computational Technology* 5.2 (2011): 341-362.

Suzuki, Tohru, et al. "A scenario of core disruptive accident for Japan sodium-cooled fast reactor to achieve in-vessel retention." Journal of Nuclear Science and Technology 51.4 (2014): 493-513.D.E.

Vorobyev, Alexander. *A Smoothed particle hydrodynamics method for the simulation of centralized sloshing experiments*. KIT Scientific Publishing, 2012.

Xia, Xilin, and Qiuhua Liang. "A GPU-accelerated smoothed particle hydrodynamics (SPH) model for the shallow water equations." Environmental Modelling & Software 75 (2016): 28-43.

Xu, Wen-Jie, Xue-Yang Dong, and Wen-Tao Ding. "Analysis of fluid-particle interaction in granular materials using coupled SPH-DEM method." *Powder Technology* 353 (2019): 459-472.

Yakush, Sergey, and Pavel Kudinov. "Effects of water pool subcooling on the debris bed spreading by coolant flow." *Proceedings of ICAPP 2011, Paper* 11416 (2011): 2-5.

Yamano H., Hosono S., Sugaya M Analysis of sloshing experiments // Proc. of 14th JAEA-FZK/CEA/IRSN/ENEA SIMMER-III/IV Review Meeting, Karlsruhe, Germany, September 9–12, 2008.

Zhang, Aman, Pengnan Sun, and Furen Ming. "An SPH modeling of bubble rising and coalescing in three dimensions." *Computer Methods in Applied Mechanics and Engineering* 294 (2015): 189-209.

Zhu, H. P., et al. "Discrete particle simulation of particulate systems: theoretical developments." *Chemical Engineering Science* 62.13 (2007): 3378-3396.

Ergun, Sabri. "Fluid flow through packed columns." *Chem. Eng. Prog.* 48 (1952): 89-94.

# 국문 초록

가압경수로 중대사고 후기 과정에서 핵연료 용융물 노내 억류 전략의 실패로 용융 핵연료가 용기 바깥쪽 침수 공동으로 재배치되면, 공동의 깊이나 제트의 속도 등의 조건에 따라 핵연료 파편화가 발생할 수 있다. 이러한 핵연료 파편물에서 발생하는 붕괴열에 의해 냉각재의 상변화가 이루어지면, 이상유동 자연대류와 고체 파편물이 공존하는 3상유동 시스템이 된다. 핵연료 용융물의 제트 파쇄, 하강 및 퇴적, 평탄화 등 일련의 과정에서 다양한 형태의 파편물 3상 냉각 거동이 발생할 수 있으며, 핵연료 파편물의 붕괴열이 충분히 제거되지 못하면 파편물의 응집 및 재용융이 발생할 수 있다. 중대사고 완화의 관점에서 이러한 3상 냉각 거동에 대한 상세한 이해가 필요하지만, 이상유동 자연대류, 이상유동 열전달, 고화, 용융, 비등, 유동-입자 상호작용 등을 포함하는 거동 자체의 복잡성으로 인해 관련 현상들의 예측 및 평가는 큰 불확실성을 내포하고 있다.

전통적인 핵연료 파편물을 포함한 3상 거동 해석은 다른 중대사고 해석과 마찬가지로 경험적 방법론에 의존한 보수적인 접근 방법이나 고체 입자와 이상 유체를 모두 연속체로 가정하는 다유체 모델을 기반으로 이루어졌다. 최근에는 이러한 방법론들이 가지는 본질적인 한계를 극복하고자 고체 입자들 사이의 충돌이나 회전을 별개로 다루는 이산요소법(Discrete Element Method, DEM)과 격자 기반의

오일러리안 전산유체해석(CFD) 기법을 연계하는 형태로 서로 간의 상호작용을 해석하는 연구들이 많이 이루어지고 있다.

한편, 최근에는 하드웨어 및 소프트웨어의 성능이 비약적으로 좋아지면서 격자(Grid)에 기반하지 않고 질점 하나하나의 움직임을 따라가면서 유동에 대한 지배방정식을 해석하는 라그랑지안 유체해석기법의 응용이 늘어나고 있다. 라그랑지안 해석 기법에서는 다상유동 해석 시에 액체와 기체 두 상을 완전히 별개의 영역으로 해상하여 지배방정식을 풀기 때문에 계면 마찰력이나 항력, 양력 등에 대한 별도의 상관식 없이 제 1 원리 기반으로 유동을 해석할 수 있어, 이상유동에 대한 보다 근본적인 해석이 가능하다.

핵연료 파편물의 생성 및 3상 냉각 거동과 관련된 현상들은 대부분 기체 상의 생성이나 이상유동 자연대류에 영향을 받는 현상들로 액체 기체 사이의 인터페이스가 복잡하고 역동적인 경향이 있기 때문에, 액체-기체 다상유동에 효과적인 라그랑지안 기반의 유체해석 기법과 강체 이산요소법(DEM)을 연계하면 효과적인 3상 유동 해석 체계를 구축할 수 있다. 하지만, 핵연료 파편물을 포함한 3상 냉각 거동과 관련하여 라그랑지안 입자 기반 유체해석 기법을 활용한 연구는 세계적으로도 아직 수행된 바가 없다.

이러한 필요성에 따라, 본 연구에서는 대표적인 입자 기반의

유체해석 방법론 중 하나인 완화입자유체동역학(Smoothed Particle Hydrodynamics, SPH) 기법과 강체의 충돌, 병진, 회전 운동을 직접적으로 다루는 이산요소법(DEM)의 연계를 통해 고체 입자를 포함한 3상 유동 해석을 위한 라그랑지안 해석 체계를 구축하였다. 고체 입자와 유체 사이의 연계는 mm 이하의 스케일을 가지는 핵연료 파편물의 형상적 특성을 고려하여 두 상 사이의 겹침을 허용하여 운동량 교환을 모델링하는 비해상(unresolved) 방식으로 이루어졌다. 또한, SPH 유체 모델, DEM 강체 모델, SPH-DEM 연계 모델 각각에 대한 검증을 다양한 스케일에서 다양한 실험 연구들과의 비교를 통해 수행하였다.

한편, 완화입자유체동역학(SPH) 기법과 이산요소법(DEM) 모델은 라그랑지안 해석 기법의 특성상 컴퓨터 성능의 비약적인 발전에도 불구하고 오일러리안 해석 기법에 비해 계산 효율 및 시간에 대한 상대적인 제약이 존재한다. 특히 액체-기체의 이상유동 해석을 다룰 경우 기체 상의 밀도가 작기 때문에 라그랑지안 유체해석 기법에서는 더 작은 시간 간격이 요구된다. 이에 본 연구에서는 그래픽 처리 장치 (Graphics Processing Unit, GPU)를 활용하여 SPH 해석, DEM 해석, SPH-DEM 연계 해석이 모두 각 라그랑지안 질점에 대해 동시에 수행될 수 있도록 GPU 기반의 연계코드 병렬화 및 가속화를 수행하였다.

마지막으로 개발한 라그랑지안 기반의 3상유동 해석 체계의 유용성 입증을 위해 원자로 중대사고 후기 과정에서 발생할 수 있는 핵연료 파편물 층(debris bed)의 평탄화(self-leveling) 거동에 대한 검증 해석을 수행하였다. 시간에 따른 파편물 층 표면의 형상 변화를 타 기관에서 수행된 기체주입 실험과 비교하는 형태로 검증이 이루어졌다. 분석 결과, 본 연구에서 개발한 SPH-DEM 연계해석 코드가 고체 입자 상을 포함한 수력학적 3상 거동을 정량적으로, 정성적으로 잘 해석하는 것을 확인하였다.

본 연구에서 개발한 라그랑지안 기반의 SPH-DEM 3상유동 해석 체계는 원자로 중대사고의 해석적 관점에서 기존의 수치해석 기법들이 다루기 어려웠던 현상들에 대한 대안 또는 상호 보완의 역할을 할 수 있다. 또한, 본 연구에서 개발한 코드는 제 1원리 기반의 물리 법칙을 기반으로 유동 및 강체의 거동을 해석하기 때문에 실험으로 구현하기 어려운 조건이나 스케일에 대한 수치적 재현이 가능하고, 이를 바탕으로 기존의 스케일링 법칙을 검증하거나 실험 결과가 없는 영역에서 수치 데이터를 생성하여 기존의 상관식을 개선하는데 활용할 수 있다. 이러한 점에서 본 연구는 원자로 중대사고의 해석이나 안전성 평가와 관련하여 불확실성을 저감하는데 기여한다.

**주요어**

완화입자유체동역학, 이산요소법, 양방향 연계, GPU 병렬화, 원자로 중대사고, 파편물 층, 파편층 평탄화

학번: 2014-21417

공학박사 학위논문

# Development of GPU-Based SPH-DEM Code for Hydrodynamic Interactions between Multi-Phase Flow and Solid Debris

## 다상유동 및 고체 파편물의 수력학적 거동 해석을 위한 GPU 기반의 SPH-DEM 연계해석 코드 개발

**2020 년 8 월**

서울대학교 대학원

에너지시스템공학부

조 영 범

# Development of GPU-Based SPH-DEM Code for Hydrodynamic Interactions Between Multi-Phase Flow and Solid Debris

다상유동 및 고체 파편물의 수력학적 거동 해석을 위한 GPU 기반의 SPH-DEM 연계해석 코드 개발

지도교수 김 응 수

이 논문을 공학박사 학위논문으로 제출함
2020 년 8 월

서울대학교 대학원
에너지시스템공학부
조 영 범

조영범의 박사 학위논문을 인준함
2020 년 8 월

위 원 장 조 형 규 (인)

부위원장 김 응 수 (인)

위 원 심 형 진 (인)

위 원 박 현 선 (인)

위 원 이 병 진 (인)

# Abstract

# Development of GPU-based SPH-DEM Code for Hydrodynamic Interactions between Multi-Phase Flow and Solid Debris

Young Beom Jo

Department of Energy System Engineering

The Graduate School

Seoul National University

In the late phase severe accident of LWR, the massive corium releases out of the reactor pressure vessel (RPV) and falls to the coolant if the In-Vessel Retention (IVR) strategy fails. The melt jet can be fragmented into debris particles based on the assumption that the ex-vessel pool is sufficiently deep. It is known that there are various three-phase flow issues associated with the fragmented debris particles under the influence of phase change of cavity coolant. In such cases, the vapor phase forms a sharp and dynamic interface with the liquid phase while the transient relocation behavior of debris particles is the main concern. Thus, coupling Lagrangian-based multi-phase CFD techniques and Discrete Element Method (DEM) can be an effective approach in terms of

numerical modeling of such behaviors. In this respect, an integrated numerical code for incompressible 3-phase flow has been developed in this study by two-way phase coupling of multi-phase Smoothed Particle Hydrodynamics (SPH) and DEM model.

Smoothed Particle Hydrodynamics (SPH) is one of the best-known meshless CFD methods in which the fluid system is represented as the finite number of Lagrangian particles. The SPH code developed in this study proposes a new density estimation model and improves the surface tension model for accurate simulation of incompressible two-phase flow behavior. The demonstration of its applicability has been performed through several V&V simulations including multi-phase dam-break and sloshing simulations.

Discrete Element Method (DEM) is a direct simulation method for a rigid body that can analyze the translation, rotation, and collision behavior of solid particles in detail. The soft-sphere collision model with Hertz-Mindlin contact force equations is adopted for developed DEM code in this study. To precisely estimate the wall boundary interactions of bed-formed debris particles, a versatile wall boundary model is newly proposed in this study that also covers the sliding and rolling behavior of solid particles. The inter-particle collision behavior and sliding & rolling motion of particles are well proven in several V&V cases.

The numerical code system for incompressible 3-phase flow is newly developed by two-way phase coupling of the above two models (SPH-DEM). The unresolved coupling approach between two methods was adopted for the analysis

of the overall behavior of particulate solid debris. The fundamental validation of the phase coupled model was performed for both single-particle behavior and particulate granular flow such as dam-breaking motion of particle-fluid.

The SPH-DEM coupled code in this study has been parallelized based on Graphical Process Unit (GPU) in order to overcome the inherent efficiency problem of the Lagrangian-based numerical method. Parallel mapping and reduction are applied for solving discretized summation equations of each SPH particle, solving contact force equations for each DEM particle, and also for solving coupling equations between SPH and DEM particles. The efficiency of code parallelization was evaluated through the scalability analysis based on the benchmark calculation.

Finally, the simulation of the vapor-driven leveling behavior of spherical solids was performed as a case study to demonstrate the applicability of the developed code. The time-variant surface shape of solid particles was compared with the benchmark experiments both qualitatively and quantitatively. The effect of gas flow rate on the tendency of leveling behavior also has been analyzed.

The developed numerical system in this study is expected to be a good alternative for the simulation of such phenomena that were difficult to handle with traditional numerical methods since the numerical schemes used in the code have a high potential for simulation of complicated physics with highly deformable geometry. In addition, this validated code system can contribute to hydrodynamic modeling studies for severe accident technology by performing

numerical experiments on conditions that hard to be conducted on a laboratory scale.

**Keywords**

**Smoothed Particle Hydrodynamics, Discrete Element Method, Two-Way Coupling, GPU Parallelization, Debris Bed, Self-Leveling**

**Student Number: 2014-21417**

# List of Contents

**Abstract** ..... **ii**

**List of Contents** ..... **vi**

**Chapter 1 Introduction** ..... **1**

1.1 Background and Motivation ..... 1

1.2 Previous Studies ..... 3

1.2.1 Numerical Studies on Particulate Debris Bed ..... 3

1.2.2 SPH-DEM Phase Coupling ..... 4

1.3 Objectives and Scope ..... 5

**Chapter 2 Fluid Phase: Smoothed Particle Hydrodynamics** ..... **8**

2.1 Smoothed Particle Hydrodynamics (SPH) ..... 9

2.1.1 SPH Particle Approximation ..... 9

2.1.2 SPH Particle Approximation of Derivatives ..... 10

2.1.3 Kernel Function ..... 11

2.1.4 Accuracy of SPH Approximation ..... 12

2.1.5 Governing Equations for Incompressible Flow ..... 14

2.2 Multi-phase SPH Governing Equations ..... 16

2.2.1 Treatment of Multi-Phase Flow ..... 16

2.2.2 Normalized Density Model ..... 18

2.2.3 Continuum Surface Force (CSF) Model ..... 19

2.3 Implementation of SPH Model ..... 21

2.3.1 Algorithm of SPH Code ..... 21

2.3.2 Nearest Neighboring Particles Searching (NNPS) ..... 22

2.3.3 Time Integration ..... 23

2.4 V&V Simulations ..... 24

2.4.1 Rayleigh-Taylor Instability ..... 25

2.4.2 Bubble Terminal Velocity ..... 25

2.4.3 Dam-Break Simulation ..... 25

2.4.4 Centralized Sloshing Simulation ..... 26

**Chapter 3 Solid Phase: Discrete Element Method** ..... **45**

3.1 Discrete Element Method (DEM) ..... 46
3.2 DEM Contact Force ..... 47
3.2.1 Soft-sphere Contact Model ..... 47
3.2.2 Contact Force Model ..... 48
3.2.3 Hertz-Mindlin Contact Force Model ..... 49
3.3 Wall Boundary Conditions ..... 52
3.3.1 Versatile Wall Boundary Model ..... 52
3.3.2 Particle Collision with the Wall ..... 54
3.3.3 Sliding and Rolling on the Wall Boundary ..... 56
3.4 DEM Implementation Algorithm ..... 57
3.4.1 Contact Detection ..... 58
3.4.2 Estimation of Relative Velocity ..... 59
3.4.3 Calculation of Contact Force ..... 60
3.4.4 Wall Boundary Conditions and Time Integration ..... 60
3.5 V&V and Simulations ..... 61
3.5.1 Conservation of Momentum and Angular Momentum ..... 62
3.5.2 Conservation of Energy in Elastic Collision ..... 63
3.5.3 V&V Simulations for Wall Boundary Model ..... 63
3.5.4 Granular Collapse of Spherical Particles ..... 64
**Chapter 4 Two-way Phase Coupling of SPH and DEM ..... 76**
4.1 Unresolved Coupling of SPH and DEM ..... 76
4.2 Governing Equations ..... 78
4.2.1 SPH Particles: Locally Averaged N-S Equations ..... 78
4.2.2 DEM Particles: Coupling Forces Acting on Solid Particles ..... 80
4.2.3 SPH Particles: Reaction Force from Momentum Exchange ..... 82
4.3 Algorithm of SPH-DEM Coupled Model ..... 83
4.4 V&V Simulations for SPH-DEM Coupled Model ..... 84
4.4.1 Single DEM Particle Behavior ..... 85
4.4.2 Pressure Drop through Packed Bed ..... 87
4.4.3 Granular Flow in Liquid: 3D Dam-Break ..... 89
**Chapter 5 GPU Parallelization of Coupled SPH-DEM Code ..... 103**
5.1 Parallelization of Governing Equations ..... 104
5.1.1 GPU-based Parallelization ..... 104
5.1.2 Parallelization of SPH-DEM Governing Equations ..... 104
5.2 Parallelization of NNPS and Contact Detection ..... 105

5.3 Results of GPU Parallelization.....107
5.3.1 Speedup in Computation Time.....107
5.3.2 Parallelization Factors.....107
**Chapter 6 Code Application to Vapor-Driven Leveling Behavior of Spherical Debris.....113**
6.1 Self-Leveling Behavior of Debris Bed.....114
6.1.1 Self-Leveling Issue in LWR.....114
6.1.2 Self-Leveling Behavior in Terms of Debris Coolability.....114
6.2 Benchmark Experiment.....116
6.3 SPH-DEM Simulation Setup.....118
6.3.1 Properties and Simulation Conditions.....118
6.3.2 Sequence of SPH-DEM Leveling Simulation.....120
6.3.3 Determination of Inclined Angle.....121
6.4 Validation Results and Discussions.....121
6.4.1 SPH-DEM Simulation Results.....121
6.4.2 Validation Result.....122
6.4.3 Effect of Gas Flow Rate.....122
**Chapter 7 Summary.....129**
7.1 Summary.....129
7.2 Recommendations.....131
**References.....134**
**국문 초록.....142**

# List of Tables

Table 1.1. Previous 3-Phase Modeling Studies of Solid Debris .....6
Table 1.2. Previous Studies on SPH-DEM Phase Coupling .....6

Table 2.1. SPH Differential Operators .....30
Table 2.2. Conditions for Kernel Approximation Function .....30
Table 2.3 SPH Governing Equations .....31
Table 2.4 V&V Simulation Cases for Developed SPH Code .....32
Table 2.5 Comparison of Simulation Results with Benchmark Experient .....33

Table 3.1 DEM Contact Force Model .....66
Table 3.2 Hertz-Mindlin Contact Force Model .....66
Table 3.3 V&V Simulation Cases for Implemented DEM Model .....67

Table 5.1 Parallelization Factors for the Code .....109

# List of Figures

Figure 1.1. Incorporated Physical Models and Scope of This Study.....7

Figure 2.1. Particle System of Smoothed Particle Hydrodynamics (SPH).....34
Figure 2.2. Kernel Weighting Function in SPH Method.....34
Figure 2.3. Normalized Density Approach for Density Estimation.....35
Figure 2.4. Density and Pressure Results for Two-Fluid Hydrostatic Problem.....35
Figure 2.5. Improvement of CSF Model for Calculation of Curvature .....36
Figure 2.6. Structure and Simplified Algorithm of Developed SPH Code.....36
Figure 2.7. Grid-based Nearest Neighboring Particles Searching (NNPS) .....37
Figure 2.8. 2D SPH Simulation Results of Dam-Break Behavior.....37
Figure 2.9. SPH Results on Dam-Break Simulation in Various Conditions (Single/Two Phase) and Scales .....38
Figure 2.10. Snapshots for 3D Single Phase Dam-Break Simulation .....38
Figure 2.11. Results of Rayleigh-Taylor Instability Simulation .....39
Figure 2.12. SPH Simulation Results for Bubble Terminal Velocity.....39
Figure 2.13. Validation Results of SPH Method for Multi-D, Multi-Phase Dam-Break Simulation .....40
Figure 2.14. Geometry and Conditions for 3D SPH Sloshing Simulation .....40
Figure 2.15. Qualitative Comparison of SPH Result with Benchmark Exp.....41
Figure 2.16. 3D Simulation Results of Developed SPH Code for Single-Phase Centralized Sloshing Behavior .....41
Figure 2.17. 3D Simulation Results of Developed SPH Code for 12 Vertical Rods Sloshing .....42
Figure 2.18. 3D Simulation Results of Developed SPH Code for Asymmetric Sloshing Condition .....42
Figure 2.19. 3D Comparison Results for Two-Phase Centralized Sloshing Simulation.....43
Figure 2.20. Effect of Particle Resolution in SPH Sloshing Simulation .....43
Figure 2.21. Convergence of Results for Particle Resolution.....44
Figure 2.22. Difference between Single and Two Phase Simulation.....44

Figure 3.1. Spring-Dashpot System of Soft-Sphere Collision Model .....68

Figure 3.2. Inter-particle Collision in Soft-Sphere Model ..... 68
Figure 3.3. Versatile Wall Boundary Treatment Model in This Study ..... 69
Figure 3.4. Implicit Primitive Object for DEM Wall Boundary Condition ..... 69
Figure 3.5. Particle Collision with Wall Boundary ..... 70
Figure 3.6. Algorithm of Implemented DEM Model ..... 70
Figure 3.7. Grid-Based Contact Detection ..... 71
Figure 3.8. Conservation of Linear Momentum in Collision ..... 71
Figure 3.9. Conservation of Angular Momentum in Collision ..... 72
Figure 3.10. Conservation of Kinetic Energy in Elastic Collision ..... 72
Figure 3.11. Wall Collision of Rotating Sphere ..... 73
Figure 3.12. Sliding and Rolling of Spherical Particle on the Wall boundary ..... 73
Figure 3.13. Descending Behavior of the Sphere on Slope ..... 74
Figure 3.14. 3D Hopper Flow Simulation ..... 74
Figure 3.15. Benchmark Experimental Setup for Granular Collapse Behavior [Chou, 2012] ..... 75
Figure 3.16. DEM Validation Results for Granular Collapse Behavior ..... 75

Figure 4.1. Concept of SPH-DEM Unresolved Coupling ..... 92
Figure 4.2. Momentum Exchange b/w SPH and DEM Particles ..... 92
Figure 4.3. Algorithm of SPH-DEM Two-Way Coupled Model ..... 93
Figure 4.4. NNPS and Contact Detection in SPH-DEM Coupled Model ..... 94
Figure 4.5. Single DEM Particle Behavior without Drag Force ..... 94
Figure 4.6. DEM Particle Oscillation Due to Gravity and Buoyancy Force ..... 95
Figure 4.7. Single DEM Particle Freefall (Drag, Buoyancy Force) ..... 96
Figure 4.8. Damped Oscillation Due to Energy Dissipation ..... 96
Figure 4.9. Terminal Velocity Behavior of Single DEM Particle ..... 97
Figure 4.10. Sensitive Study on Coupling Length for Terminal Velocity Behavior ..... 97
Figure 4.11. Single Phase Pressure Drop through Packed Bed ..... 98
Figure 4.12. Pressure Data of SPH-DEM Phase Coupled Simulation ..... 98
Figure 4.13. Conditions for Solid-Liquid Dam-Break Experiment [Sun, 2013 ..... 99
Figure 4.14. Qualitative Results of Solid-Liquid Dam-Break Simulation ..... 100
Figure 4.15. Quantitative Validation Result of SPH-DEM Coupled Code ..... 101
Figure 4.16. Qualitative Comparison Results (decoupled, one-way, two-way) ..... 101

Figure 4.17. Quantitative Comparison Results in Time Variation of Normalized Leading Front (one-way, two-way coupled) ..... 102

Figure 5.1. Memory Structure of CUDA ..... 110
Figure 5.2. Conceptual Description of GPU-based Parallelization of Code ..... 110
Figure 5.3. Parallel Reduction for Solving Governing Equations of SPH ..... 111
Figure 5.4. Simplified Algorithm of Code in Terms of GPU Parallelization..... 111
Figure 5.5. Simplified Sorting and Parallelization Algorithm for SPH-DEM Coupled Code ..... 112
Figure 5.6. Speedup for GPU Parallelization of SPH-DEM Coupled Code..... 112

Figure 6.1. Mechanism of Debris Bed Self-Leveling ..... 124
Figure 6.2. Schematic View of Experimental Apparatus [Cheng, 2012]..... 124
Figure 6.3. Conditions for Benchmark Leveling Experiment ..... 125
Figure 6.4. Time Variation of Inclined Angle in Benchmark Experiment [Cheng, 2012] ..... 125
Figure 6.5. Geometry of SPH-DEM Coupled Leveling Simulation..... 126
Figure 6.6. Gas Injection in SPH-DEM Coupled Simulation..... 126
Figure 6.7. DEM Particles Used for Data (Height) Analysis..... 127
Figure 6.8. Snapshots Comparison b/w Experiment and SPH-DEM Simulation (a) $t' = 5s$, (b) $t' = 10s$, (c) $t' = 15s$..... 127
Figure 6.9. Validation Results for Time Variation of $R$ Value ..... 128
Figure 6.10. Effect of Gas Flow Rate on Self-Leveling Behavior..... 128

# Chapter 1

# Introduction

## 1.1 Background and Motivation

It is the cornerstone of the mitigation approach to ensure containment integrity even in the worst accident scenarios of a nuclear reactor. In-vessel retention (IVR) is one of a key mitigation strategy of LWR late-phase severe accident, which aims to retain the core melt in the reactor vessel through appropriate cooling including ex-vessel cavity flooding. If the IVR strategy fails, the massive corium releases out of the reactor pressure vessel (RPV) and falls to the ex-vessel coolant forming the melt jet. Various fuel behaviors occur during the melt jetting including fuel fragmentation, relocation, and dispersal. Based on the assumption that the ex-vessel pool is sufficiently deep, the melt jet can be fragmented into debris particles. It is known that there are various safety-related 3-phase issues associated with particulate solid debris such as melt jet breakup, melt spreading, agglomeration of solid debris, self-leveling, and so on. In this situation, the main concern of mitigation strategy is to effectively remove the decay heat from fragmented debris particles, since there is a possibility of debris cake formation, which is considered a potentially non-coolable state. Thus, it is required to

understand and evaluate the thermal-hydraulic behavior of particulate debris particles.

In terms of numerical modeling of such 3-phase behaviors, traditional studies on the 3-phase behavior of particulate debris solved all three phases as a continuous phase with appropriate conservative assumptions. In recent studies, there were some attempts to treat the solid debris as a discrete rigid body using Discrete Element Method (DEM), while adopting grid-based CFD methods for the fluid phase. Meanwhile, in many 3-phase phenomena associated with the severe accident, the vapor phase can act as the trigger of such behavior, which forms a sharp and dynamic interface with the liquid phase. Thus, the detailed CFD methods that can resolve the vapor and liquid phase can be effective for the above vapor-driven behaviors.

In this respect, this study was motivated by an idea that the coupling Discrete Element Method (DEM) with the Lagrangian-based CFD methods, which can completely resolve the interface between liquid and vapor without empirical correlation, can provide an effective numerical method to simulate vapor-driven 3-phase phenomena in detail. With this motivation, the in-house code was developed in this study through the coupling Lagrangian-based Smoothed Particle Hydrodynamics (SPH) method with Discrete Element Method (DEM).

Although the applicability of Lagrangian-based numerical code has been improved with the improvement of computation performance, there are still some limitations on time step and resolution which come from the explicit Lagrangian nature of SPH and DEM method. Thus, the code acceleration is essential in order to apply the Lagrangian numerical system to the analysis of real phenomena, especially for the multi-phase flow system. In this respect, the GPU-based code

parallelization was also performed in this study to overcome the inherent efficiency problem of the Lagrangian-based numerical method. Finally, the simulation of the vapor-driven leveling behavior of spherical solids was performed as a case study to demonstrate the applicability of the GPU-parallelized SPH-DEM coupled code developed in this study.

The developed numerical system in this study is expected to be a good alternative for the simulation of such phenomena that were difficult to handle with traditional numerical methods since the numerical schemes used in the code have a high potential for simulation of complicated physics with highly deformable geometry. In addition, this validated code system can contribute to hydrodynamic modeling studies for severe accident technology by performing numerical experiments on conditions that hard to be conducted on a laboratory scale.

## 1.2 Previous Studies

### 1.2.1 Numerical Studies on Particulate Debris Bed

Some previous modeling studies associated with the 3-phase flow including particulate solid debris are summarized in Table 1.1. The traditional coupling between the fluid and solid phase was achieved by a macroscopic approach based on the two-fluid models (TFM), which also treat the particulate debris as a continuous phase. Recently, the numerical coupling of the CFD method has been carried out through solving the momentum exchange with a Discrete Element

Method (DEM), which can analyze the collisions, translation, and rotation of each solid particle discretely, as shown in Table 1.1. The sedimentation behavior of solid particles was simulated in POSTECH [Hwang, 2019], and the self-leveling behavior of solid particle bed was covered in Kyushu university both in 2D and 3D [Guo, 2013]. The fluid phase of both studies was simulated using a grid-based CFD method. There was also a numerical study coupling the Lagrangian-based Finite Volume Particle (FVP) method with DEM to simulate the sloshing behavior of single-phase liquid, which is associated with the core disruptive accident of liquid metal reactor. However, there have been no studies on coupling a Lagrangian-based two-phase CFD method with the DEM model yet in terms of the behavior of fragmented fuel debris.

### 1.2.2 SPH-DEM Phase Coupling

The coupling studies of DEM and Smoothed Particle Hydrodynamics (SPH) method, which are used in this study, has recently been conducted in some other fields such as slurry transportation, wet screening, and so on. Some of the recent studies of SPH-DEM coupling are listed in Table 1.2. All of the studies in the table covered the coupling between single-phase fluid (SPH) and solid (DEM), with a various range in particle number depending on the parallelization methods. The total number of 14,704 particles were used in the study of Markauskas (2019), while more than 600M particles were used in the study of Xu (2019) using multi-GPU parallelized code. In this study, up to 300,000 Lagrangian particles were used, and it is considered to be sufficiently competitive compared to the recent study of Xu, which also performed a single GPU-based code acceleration.

## 1.3 Objectives and Scope

The purpose of this study is to develop a numerical analysis code that can handle the 3-phase hydrodynamic behavior of solid debris. An integrated numerical code for 3-phase flow has been developed by two-way phase coupling of multi-phase Smoothed Particle Hydrodynamics (SPH) model and solid particle Discrete Element Method (DEM) model. The developed SPH-DEM coupled code focuses on the detailed hydrodynamic behavior of three phases, as can be seen in the incorporated physical model in Figure 1.1.

Chapter 2 describes the implementation of the Smoothed Particle Hydrodynamics (SPH) model, which is applied for the simulation of liquid-vapor two-phase flow in this study. Chapter 3 covers the implementation of the Discrete Element Method (DEM) model for solid particles, while the algorithm and results for the two-way phase coupling of two models are summarized in Chapter 4. In Chapter 5, the strategies and results for GPU parallelization of developed code are discussed. Finally, the simulation results and discussions for the case study on debris particle self-leveling behavior are introduced in Chapter 6.

Table 1. Previous 3-Phase Modeling Studies of Solid Debris

| | phenomenon | Solid Phase Treatment | Liquid Phase Treatment | Phase # | Coupling Method | Dim |
|---|---|---|---|---|---|---|
| *Buck (2007) Yakush (2011)* | debris bed cooling | continuum | Eulerian | 3-phase | - | 2D |
| *Hwang (2019)* | debris bed sedimentation | Discrete (DEM) | Eulerian | 2-phase | two-way | 3D |
| *Guo (2013)* | self-leveling of debris bed | Discrete (DEM) | Eulerian | 3-phase | two-way | 2D |
| *Guo (2017)* | self-leveling of debris bed | Discrete (DEM) | Eulerian | 3-phase | two-way | 3D |
| *Guo (2013)* | sloshing with debris bed | Discrete (DEM) | Lagrangian (FVP) | 2-phase | one-way | 3D |

Table 2. Previous Studies on SPH-DEM Phase Coupling

| | Year | Field | Phase # | Max. SPH # | Max. DEM # | Parallelization |
|---|---|---|---|---|---|---|
| *Markauskas* | 2019 | Wet screening | Liquid, Solid | 12,104 | 2,600 | - |
| *He* | 2019 | Slurry transport | Liquid, Solid | ~10,000 | 7,755 | Single GPU |
| *Xu* | 2019 | granular aggregation | Liquid, Solid | 600 M | 27,030 | Multi GPU |

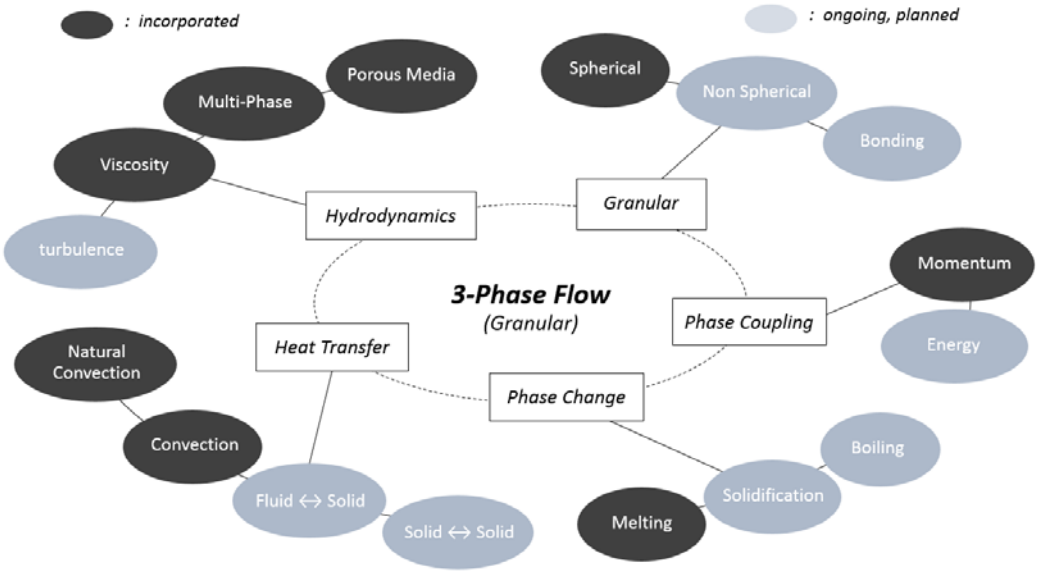


Figure 1.1. Incorporated Physical Models and Scope of This Study

# Chapter 2

# Fluid Phase: Smoothed Particle Hydrodynamics

Traditional hydrodynamic modeling studies for the multi-phase flow associated with severe accidents were conducted based on grid-based CFD methods. Many previous studies followed the statistical method based on two-fluid models (TFM) solving the averaged form of the governing equation for each phase. Some numerical techniques, including volume of fluid (VOF), and level set (LS) have been recently developed to apply grid-based methods for free surface flow. These methods are sufficiently mature and it is reported that the VOF model can effectively simulate the overall shape of multi-phase flow. However, there are still some difficulties in finding an exact interface for each phase, since the transport equation for phase interface function should be solved.

In the behavior of particulate sold debris such as debris sedimentation and self-leveling, the vapor phase acts as the driving force or trigger of overall motion, which forms a sharp and dynamic interface with the liquid phase. Thus, applying the Lagrangian-based detailed CFD methods that totally resolve the vapor and liquid area can be an effective modeling approach. In this respect, the Smoothed Particle Hydrodynamics (SPH) model, which is one of the best-known Lagrangian CFD methods, is implemented in this study for the numerical modeling of incompressible multi-phase flow.

## 2.1 Smoothed Particle Hydrodynamics (SPH)

Smoothed Particle Hydrodynamics (SPH hereafter) is a meshless Lagrangian method that was first developed in 1977 for astrophysical applications [Gingold, 1977]. In the SPH method, the fluid system is represented by a finite number of particles that carry individual properties, and the governing equations of each particle are solved in discretized smoothing formulation over the neighboring particles, as shown in Figure 2.1. The SPH method exhibits large advantages that come from Lagrangian nature in dealing with free surface liquid motion, highly deformable geometry, multiphase flow, and so on. Also, the convective term in the conservation equation is naturally reflected in the standard SPH without solving any nonlinear matrix, so that the convective flow and convective heat transfer can be implemented with simplicity. In addition, it is relatively easy to implement a wide range of physics in the existing framework.

In this section, the basic concept of the SPH method is described including particle approximation strategies of solving governing equations.

### 2.1.1 SPH Particle Approximation

The SPH is based on an interpolation method which is the theory of integral interpolants using delta function as follow,

$$f(x) = \int_{\Omega} f(x')\delta(x - x')dx' \tag{2.1}$$

where x variable x denotes the point in volume Ω, and δ denotes the Dirac delta function which has a value of zero everywhere except for at a certain point and whose integral over the entire region is equal to one. The SPH discretized formulation can be obtained by using the kernel functions that approximate a delta function as below.

$$f_i(r) = \sum_j f_j W(r_i - r_j, h) V_j \tag{2.2}$$

The variable $f_i$ is a function at the position $i$, subscript $j$ represents the adjacent particles of particle $i$, $V$ is the particle volume, and $W(r_i - r_j, h)$ stands for the kernel function, where $h$ denotes influencing area of the kernel weighting function. The kernel function is a symmetric weighting function of particle distance which should be normalized over its support domain. The particle system and kernel function are described in Figure 2.2.

### 2.1.2 SPH Particle Approximation of Derivatives

The SPH particle approximations of derivatives can be obtained by applying the Gauss integral formula to the above field approximation function (Equation 2.2) as follow.

$$\nabla \cdot f_i(r) \approx \int_{\Omega} \nabla \cdot \big(f(r)W(r-r',h)\big)dr' - \int_{\Omega} f(r)\nabla W(r-r',h)dr' \quad (2.3)$$

The first term on the right-hand side of the above equation can be replaced by the surface integral of the function $f(r)$ from the divergence theorem. Since the kernel weighting function has a non-zero value only within the smoothing radius, this surface integral value converges to zero. Finally, the first derivative of the field function $f(r)$ is expressed as a function of the kernel derivative, mass and density, as follow.

$$\nabla \cdot f_i(r) = \sum_j f_j \frac{m_j}{\rho_j} \nabla W\big(r_i - r_j, h\big) \quad (2.4)$$

From the above equation for kernel derivatives, various forms of the SPH differential operators can be derived including gradient, divergence, and Laplacian as summarized in Table 2.1.

### 2.1.3 Kernel Function

The kernel approximation functions are very important in the SPH method since they are closely related to the computational accuracy and stability of the SPH calculations. Because the kernel function is an approximation of the Dirac delta function, it should satisfy several conditions.

First, the integral value of kernel function over the support domain should have the value of 1. This so-called normalization condition of kernel function can be written as follow,

$$\int_{\Omega} W(x - x', h)dx' = 1 \tag{2.5}$$

where $\Omega$ is a computational domain, and $h$ is the smoothing length of the kernel function. Also, the kernel function should be defined only in the support domain. This compact condition can be expressed as below,

$$\mathrm{W}(r_i - r_j, h) = 0, \qquad where\ |r_i - r_j| > \kappa h \tag{2.6}$$

where $\kappa h$ is a support domain (searching range) in SPH calculation. The conditions for kernel approximation functions are summarized in Table 2.2 including the above unity condition and compact condition.

The SPH code developed in this study adopted Wendlend 6 kernel, which can inherently prevent particle clustering and improve the convergence of particle approximation.

### 2.1.4 Accuracy of SPH Approximation

The errors in SPH approximation can be estimated by using Taylor series expansion of field function $\mathrm{f(x')}$ around $\mathrm{x}$ as written below.

$$\langle f(x)\rangle = f(x)\int_{\Omega} W(x-x',h)dx' + f'(x)\int_{\Omega}(x'-x)\times W(x-x',h)dx' + r(h^2) \tag{2.7}$$

The integral of the first term on RHS unity, and the second term of RHS in above equation (9) vanishes since the kernel function satisfy the symmetry condition in interior region of calculation domain. Applying this conditions for kernel functions, the above equation (2.7) becomes,

$$\langle f(x)\rangle = f(x) + r(h^2) \tag{2.8}$$

The kernel approximation of a field function in SPH has second-order accuracy according to the above equation. However, the particle deficiency problem occurs when the support domain intersects with the computation domain (free surface open boundary). The unity condition and symmetry condition are no longer satisfied in the above equation (2.7) in this case. Thus, the kernel approximations are not of second-order accuracy anymore, and if the resolution of the particles is not sufficiently high, the numerical errors that occur in the boundary area can spread in the whole area in the form of pressure waves.

There have been many studies to restore the consistency of kernel approximation. In the SPH code developed in this study, the simple form of correction filter is applied to both kernel function and kernel gradient function in

order to ensure at least second-order accuracy in the whole computation domain. Instead of applying a better, but complex correction model, the accuracy of calculation was ensured through the code parallelization based on Graphical Process Unit (GPU) in this study. The results of GPU-based code acceleration are covered in Chapter 5.

### 2.1.5 Governing Equations for Incompressible Flow

The main equations describing the motion of an incompressible, Newtonian viscous fluid are the continuity equation and the Navier-Stokes equation which can be expressed in a Lagrangian frame as below,

$$\frac{d\rho}{dt} = -\rho\nabla \cdot \boldsymbol{u} \tag{2.9}$$

$$\rho\frac{\boldsymbol{du}}{dt} = -\nabla p + \mu\nabla^2\boldsymbol{u} + \rho\boldsymbol{g} \tag{2.10}$$

where $\rho$ and $\boldsymbol{u}$ are the density and velocity of the fluid, and $p$, $\mu$ and $\boldsymbol{g}$ denote pressure, dynamic viscosity, and the gravitational constant, respectively. The discretized SPH form of the continuity equation (2.9) for particle $i$ can be derived as below,

$$\left(\frac{d\rho}{dt}\right)_i = \rho_i \sum_j \frac{m_j}{\rho_j}(\boldsymbol{u_i} - \boldsymbol{u_j}) \cdot \nabla_i W_{ij} \tag{2.11}$$

where $j$ denotes the particles adjacent to the center particle $i$, and $m_j$, $\rho_j$, and $\boldsymbol{u_j}$ are the mass, density, and velocity vector of particle $j$, respectively. For incompressible flow, the LHS of the above equation (2.11) should always be zero. However, the general SPH model allows weak compressibility even for the incompressible fluids (Weakly-Compressible SPH, WCSPH hereafter). There are two methods to estimate density in the WCSPH model. One is to solve the above equation (2.11), and the other is to obtain the particle density based on the local particle distribution within the support domain as below, while the detailed derivation of the equation is summarized in Chapter 2.2.

$$\rho_i = \rho_{ref,i} \sum_j \frac{m_j}{(\rho_{ref})_j} W_{ij} \tag{2.12}$$

The first term on the RHS of the above momentum equation (2.10) represents the force because of the pressure gradient on the field. It can be discretized based on the SPH gradient operator equation as follow,

$$\left(\frac{1}{\rho}\nabla P\right)_i = -\sum_j m_j \left(\frac{p_i + p_j}{\rho_i \rho_j}\right) \nabla W_{ij} \tag{2.13}$$

where $p_j$ is the pressure of the nearby particle $j$. The second term on the RHS of the momentum equation (2.10) represents the viscous force of the fluid. The SPH discretized form of the laminar viscous force term is given below,

$$(\upsilon\nabla^2\boldsymbol{u})_i = \sum_j \frac{m_j\mu_{ij}\boldsymbol{r_{ij}}\cdot\nabla_i W_{ij}}{\rho_i\rho_j\left(\left|\boldsymbol{r_{ij}}\right|^2+\eta^2\right)}(\boldsymbol{u_i}-\boldsymbol{u_j}) \tag{2.14}$$

where $\mu_j$ and $\boldsymbol{r_{ij}}$ denote the dynamic viscosity and position vector of particle j. In the case of surface tension force, Continuum Surface Force (CSF) model is employed, which is covered in Chapter 2.2 in detail. The SPH formulations of each RHS term in the above equation (2.10) are summarized in Table 2.3.

In the WCSPH method, which is applied in the SPH code in this study, the pressure field is explicitly estimated as a function of local particle density using the Tait equation. The equation of state used in this study is as below,

$$p = \frac{{c_0}^2\rho_{ref}}{\gamma}\left[\left(\frac{\rho}{\rho_{ref}}\right)^{\gamma}-1\right] \tag{2.15}$$

where $\rho_{ref}$ is the standard reference density of the fluid, $\gamma$ is the polytrophic constant that determines the sensitivity of the pressure calculation, and $c_0 = c(\rho_0)$ is the reference speed of sound.

## 2.2 Multi-phase SPH Governing Equations

### 2.2.1 Treatment of Multi-Phase Flow

In solving multi-phase flow in SPH, several aspects should be considered, such

as interface tracking, discontinuous density field with high density ratio, surface tension, and so on. The interface tracking is an important issue for the Eulerian deterministic multi-phase model (ex. VOF), but the interface between two phases is naturally tracked due to the Lagrangian nature of each SPH particle.

In terms of handling discontinuous density field, the above governing equations (Equation 2.9, 2.10) should be discretized into volume-based form to prevent the unphysical contribution of particles with different density. In this reason, the above equation (2.13) and (2.14) were adopted for pressure gradient term and viscous term of N-S equation, respectively. In this respect, a new density estimation model is proposed in this study, which calculate the normalized density ($\rho/\rho_{ref}$) instead of local density. This normalized density model is introduced in next sub-section.

Besides, the surface tension model between two phases can play an important role depending on the scale of simulation. In this study, the surface tension based on Continuum Surface Force (CSF) model is adopted with some improvement in governing equations. This is summarized in chapter 2.2.3. In addition to physical surface tension force, an additional term for stabilizing the interface is also adopted, which is called the interface sharpness force [Grenier, 2009].

$$\left(\frac{d\boldsymbol{u}}{dt}\right)_i^{IS} = -\frac{\varepsilon}{m_i}\sum_j \left(|p_i|V_i^2 + |p_j|V_j^2\right)\nabla W_{ij}, \quad for\ f_i \neq f_j \qquad (2.16)$$

where $\varepsilon$ is a tuning parameter, which ranges between 0.01 and 0.1. This force is applied to the interface between two different phases. This force should be large enough to stabilize the interface between the phases, but it should be small

enough not to cause any unphysical behaviors.

### 2.2.2 Normalized Density Model

In general WCSPH method. The density of each fluid particle is estimated based on the mass summation equation as below,

$$\rho_i = \sum_j \rho_j \frac{m_j}{\rho_j} W_{ij} = \sum_j m_j W_{ij} \tag{2.17}$$

This standard SPH produces numerical pressure noise near the interface between the phases having different densities when it is directly applied. This problem is originated from handling the discontinuous density field in multi-phase flow as the continuous one. To simulate multi-phase flow with high-density ratio using the SPH, the normalized density, which is a continuous function on the interface, is suggested as the primary variable rather than the density in this study, as shown in Figure 2.3. In this approach, the normalized density is calculated as below.

$$\left(\frac{\rho}{\rho_{ref}}\right)_i = \sum_j \frac{m_j}{\rho_j} \cdot \left(\frac{\rho_j}{\rho_{ref,j}}\right) W_{ij} \tag{2.18}$$

Finally, the density of each particle can be calculated in simple form as below.

$$\rho_i = \rho_{ref,i} \sum_j \frac{m_j}{(\rho_{ref})_j} W_{ij} \tag{2.19}$$

When this normalized density approach is applied for density estimation, the physical discontinuity of density is fully ensured in the two-phase interface with a high density ratio, as shown in the simple validation simulation in Figure 2.4.

### 2.2.3 Continuum Surface Force (CSF) Model

In this study, the surface tension based on the Continuum Surface Force (CSF) model is adopted for handling two-phase interface interaction. The CSF model estimates the surface tension force on a macroscopic scale and is expressed as the product of the surface curvature and the surface normal. Based on the extensive review of the previous literature [Adami, 2010] [Morris, 2000], the following equations were used in this study,

$$\left(\frac{d\boldsymbol{u}}{dt}\right)_i^{CSF} = -\frac{\sigma_i}{\rho_i}\kappa_i \boldsymbol{n}_i \tag{2.20}$$

$$\boldsymbol{n}_i = \sum_j \frac{1}{V_i}\left(V_i^2 + V_j^2\right) c_{ij} \nabla W_{ij} \tag{2.21}$$

$$\kappa_i = -d \frac{\sum_j V_j \left(\hat{\boldsymbol{n}}_\iota - \varphi_{ij}\hat{\boldsymbol{n}}_j\right) \cdot \nabla W_{ij}}{\sum_j V_j |r_{ij}||\nabla W_{ij}|} \tag{2.22}$$

$$c_{ij} = \begin{cases} 0 & for\ f_i = f_j \\ \dfrac{\rho_i}{\rho_i + \rho_j} & for\ f_i \neq f_j \end{cases}, \quad \varphi_{ij} = \begin{cases} 1 & for\ f_i = f_j \\ -1 & for\ f_i \neq f_j \end{cases} \tag{2.23}$$

where $\sigma, \kappa, \boldsymbol{n}$ and $d$ denote a surface tension coefficient, the curvature, surface normal vector, and dimension $(d = 1,2,3)$. $\hat{\boldsymbol{n}}_\iota$ denotes the unit surface normal vector. In the above CSF model, however, the above curvature model of the interface can be calculated unphysically, especially for the second particle layer of the two-phase interface, as shown in Figure 2.5. When estimating the curvature of second layer particle, the unit normal vector of the surrounding particles is truncated (Figure 2.5, left), so that an unphysical curvature can be applied to the flat interface where the physical value should be calculated as zero.

In this respect, a new curvature model has been proposed in this study, which uses a non-truncated normal vector for curvature estimation instead of the above equation (2.21). This is possible since only the direction of the normal vector is important in curvature calculation rather than the exact magnitude of it. In this approach, the normal vector for curvature estimation ($\boldsymbol{n^c}$) is solved as below,

$$\psi_{ij} = \begin{cases} 0 & for\ f_i \neq f_j \\ 1 & for\ f_i = f_j \end{cases} \tag{2.24}$$

$$c_i^c = \frac{\sum_j \psi_{ij} W_{ij}}{\sum_j W_{ij}} \tag{2.25}$$

$$\boldsymbol{n_i^c} = \sum_j \frac{m_j}{\rho_j} \left(c_j^c - c_i^c\right) \nabla W_{ij} \tag{2.26}$$

Finally, the curvature in the above equation (2.22) is modified as below.

$$\kappa_i = -d\frac{\sum_j V_j\left(\widehat{\boldsymbol{n}_i^c} - \varphi_{ij}\widehat{\boldsymbol{n}_j^c}\right)\cdot\nabla W_{ij}}{\sum_j V_j|r_{ij}||\nabla W_{ij}|} \tag{2.27}$$

## 2.3 Implementation of SPH Model

### 2.3.1 Algorithm of SPH Code

Figure 2.6 shows a basic algorithm of the numerical model. First, the positions, properties, and conditions of each particle are initially prepared. Then, based on the given particle positions, the nearest-neighboring particle search (NNPS, hereafter) is conducted for each particle. Once the NNPS is completed, the density of each particle is estimated using the above equation (2.19). After that, the pressure is calculated for each particle explicitly by the equation-of-state (EOS) in Equation (2.15). After the pressure of each particle is calculated, the forces of each particle are estimated using the SPH force equations such as pressure, viscous, gravity, surface tension, surface sharpness force, and etc. Then, the velocity and position of each particle are updated using the calculated forces. If the particle positions are updated, the same calculation process is repeated from the NNPS. This iterative calculation is performed until the termination condition.

### 2.3.2 Nearest Neighboring Particles Searching (NNPS)

The SPH model solves the governing equations for each physics as a form of discretized summation for each neighboring particle; therefore, the nearest-neighboring particle search (NNPS) procedure for each particle should be performed before solving the governing equations. In general, the particles that are located within three times the initial particle distance are defined as neighboring particles of each center particle. In this case, there exist 25-30 neighboring particles within the smoothing radius in 2D geometry and 100-120 neighboring particles in 3D simulations. The NNPS is the most time-consuming part of the SPH calculation since it should be carried out for each neighboring particle for each targeted particle. Therefore, the performance of the whole SPH algorithm highly depends on the efficiency of the NNPS step.

The most intuitive NNPS algorithm is to go through the searching process for all particles in the computation domain. That is, it calculates the distance between the targeted particle and all the other particles to determine whether the particles are located within the support domain or not. In this case of the NNPS algorithm, the calculation time increases dramatically, in proportion to the square of the number of particles ($\sim N^2$). In recent studies, it is common to perform the uniform grid-based NNPS by assigning particles to grids. In this case, the NNPS can be carried out only for a few grids located near the center particle depending on the size of the grid; therefore, the calculation time can be considerably reduced ($\sim$ NlogN) [Xia, 2016]. The SPH code developed in this study also adopted the grid-based NNPS algorithm, as shown in Figure 2.7.

There are several ways to identify the neighboring particles among the particles

in each adjacent grid, depending on the data storage methods and the way to control the cache hit rate for memory performance. Typically, there are linked-list NNPS method and sorting-based methods. Since the SPH model in this study was implemented with parallelization in mind, the sorting-based NNPS algorithm was adopted rather than the former method. The specific algorithm and parallelization mechanism of NNPS is described in detail in Chapter 5.

### 2.3.3 Time Integration

In the SPH code developed in this study, a modified predictor-corrector scheme is applied [Gomez-Gesteira, 2012]. The predictor-corrector scheme divides the time integration into two steps. First, the prediction step extrapolates the physical variables as follows.

$$\begin{cases} \boldsymbol{u}^{p}_{t+\frac{\Delta t}{2}} = \boldsymbol{u}_t + \dfrac{\Delta t}{2}\left(\dfrac{d\boldsymbol{u}}{dt}\right)_{t-\frac{\Delta t}{2}} \\ \boldsymbol{r}^{p}_{t+\frac{\Delta t}{2}} = \boldsymbol{r}_t + \dfrac{\Delta t}{2}\left(\dfrac{d\boldsymbol{r}}{dt}\right)_{t-\frac{\Delta t}{2}} \\ \rho^{p}_{t+\frac{\Delta t}{2}} = \rho_t + \dfrac{\Delta t}{2}\left(\dfrac{d\rho}{dt}\right)_{t-\frac{\Delta t}{2}} \end{cases} \tag{2.28}$$

where $t$ and $\Delta t$ denote time and time step, respectively. The superscript *p* denotes ‘predictor’. The time derivatives of position, velocity, and density are newly evaluated by solving the discretized SPH formulations. After that, the field variables are re-integrated over the full-time step using the updated time derivatives in the correction step.

$$\begin{cases} \boldsymbol{u}^{c}_{t+\Delta t} = \boldsymbol{u}_t + \Delta t \left(\dfrac{d\boldsymbol{u}}{dt}\right)_{t+\frac{\Delta t}{2}} \\ \boldsymbol{r}^{c}_{t+\Delta t} = \boldsymbol{r}_t + \Delta t \left(\dfrac{d\boldsymbol{r}}{dt}\right)_{t+\frac{\Delta t}{2}} \\ \rho^{c}_{t+\Delta t} = \rho_t + \Delta t \left(\dfrac{d\rho}{dt}\right)_{t+\frac{\Delta t}{2}} \end{cases} \tag{2.29}$$

## 2.4 V&V Simulations

The demonstration of developed SPH code has been performed through several V&V simulations including some multi-phase cases. Table 2.4 shows the V&V simulation cases in progress for developed code. Among then, this section summarized the following four validation simulations that include some multi-phase flow issues.

- Rayleigh-Taylor Instability (2.4.1)
- Bubble Terminal Velocity (2.4.2)
- Dam-Break Simulation (2.4.3)
- Centralized Sloshing Simulation (2.4.4)

### 2.4.1 Rayleigh-Taylor Instability

In order to evaluate the normalized density approach proposed in this study (equation 2.19), Rayleigh-Taylor Instability simulation was performed in a two-fluid system with a density ratio of 1.8. As shown in Figure 2.8, the normalized density SPH model well simulates the interface between two fluids without any linearization of density both in qualitative and quantitative point of view, where the right-side graph in the figure shows the time-variant maximum height of lighter fluid, compared with the Layzer's theory.

### 2.4.2 Bubble Terminal Velocity

The SPH simulation for air bubble terminal velocity behavior in stagnant water (density ratio of 1,000) was conducted to demonstrate the capability of solving multi-phase flow. The terminal velocity of large bubbles increases with the equivalent diameter of the bubble since gravity is the dominant force in such a case, while the surface tension effect is dominant for smaller bubbles. As shown in Figure 2.9, the SPH results in this study well analyze the dominant force according to the size of the bubble, result in good prediction for terminal velocity value compared with the benchmark experiment [Clift, 1978]. The shape of the increasing bubble is also well simulated according to the bubble size.

### 2.4.3 Dam-Break Simulation

The dam-break simulation is a good benchmark problem for the Lagrangian-based numerical methods since it is associated with complex phenomena including surface break-up, high impact pressure, and other related effects. In this simulation, vertical square shape of the water column was collapsed with the beginning, as shown in Figure 2.10.

The simulation was conducted for 2D single-phase, 3D single-phase, and 2D multi-phase conditions, and the results of the simulation was compared with the experimental data of Martin and Moyce (1996) and also with the VOF results of Hirt (1981). The snapshots in Figure 2.10, Figure 2.11, and Figure 2.12 show that developed SPH code qualitatively well simulates the sharp surface of dam-breaking motion, while Figure 2.13 shows that the non-dimensional position of water in SPH simulation shows good agreement with the experimental data, especially for the multi-phase simulation.

Generally, the accuracy of SPH results are affected by the resolution of the particles and also the number density of neighboring particles since it solves the discretized governing equation through the weighted interaction with neighboring particles. In the multi-phase simulation above, it is free from the particle deficiency problems, and each targeted particle can interact with a sufficient number of neighboring particles. This inhibits the non-physical stream of front particles that can easily occur in the single-phase dam-break simulation.

### 2.4.4 Centralized Sloshing Simulation

The 3D single/two-phase simulations were performed on the centralized sloshing behavior, and the simulation results were compared with the benchmark

experiment data of Maschek et al. (1992). The experiments were composed of 5 series according to the geometry and initial conditions. The validation of developed code was performed in three out of five experimental cases listed below. The geometry and conditions for each case are summarized in Figure 2.14.

- Case 1: Centralized Sloshing (Perfect Symmetry)
- Case 2: Vertical Rods (Inner/Outer)
- Case 3: Asymmetric Sloshing

In each case above, the maximum sloshing height and arrival time were calculated and compared with the experimental data. In the case of centralized sloshing (Case 1), both single-phase and two-phase simulations were conducted in sufficiently high resolution. Up to 4,000,000 SPH particles were generated for single-phase simulation, while more than 10 million particles were used in the two-phase simulation. All of the SPH simulations qualitatively well reproduced the overall sloshing behavior as shown in Figures from 2.15 to 2.19.

In terms of quantitative validation, most of the results (maximum sloshing height, arrival time) are in good agreement with experiments especially for the high-resolution simulation, as summarized in Table 2.5. In detail, sloshing height on the wall is slightly over-estimated in the simulation compared to the experiments, which seems to be due to the perfect symmetry assumption in the simulation. The maximum sloshing height is calculated to be slightly lower than the experimental data, which is caused by the local particle resolution and numerical accuracy at the sloshing peak.

Thus the sensitivity on the particle size (resolution) has been conducted for the

maximum sloshing height. Generally, the lower resolution makes the lower number density of particles in center sloshing motion, finally result in a generation of fragmented particles that exhibits unphysical behavior. In other words, the bulk flow rate of piling up motion can be dropped significantly if the particle resolution gets poor. Thus, the sloshing height can be underestimated when the particle resolution is poor, and conversely, sufficient bulk flow can be ensured in the high-resolution simulation. As a result of the parametric study, the maximum sloshing height in SPH simulation converges to a certain value as the particle resolution increases as shown in Figure 2.20 and Figure 2.21.

Besides, the effect of multi-phase simulation has been analyzed through the centralized sloshing case (Case 1). As shown in the results of parametric studies on particle size (Figure 2.21), it can be seen that the multi-phase model predicts the sloshing height better than the single-phase model in the same particle resolution. This difference is due to the nature of the SPH method based on interaction with neighboring particles. In the two-phase SPH simulation, there are sufficient particles (including air particles) in the support domain regardless of the particle resolution in the sloshing peak, while serious particle deficiency occurs in low-resolution single-phase simulation. As a result of particle deficiency in single-phase simulation, an unphysical high-speed stream of solitary particles can be created with a high probability as shown on the right side of Figure 2.22. Likewise, the single-phase behavior near the gas trapping area may differ from two-phase simulation due to the particle deficiency issue. Since this small difference can be amplified as a large disturbance of a liquid wave, precise analysis based on the two-phase model is required for sloshing behavior.

The above results demonstrate that multi-phase simulation can produce better

results than single-phase analysis at the same particle spacing (resolution). However, it is better now to perform single-phase simulation with higher resolution, since many air particles should be considered in the multi-phase simulation. In order to achieve both accuracy and higher efficiency of simulation, it is necessary to further perform a kernel gradient correction in solving the governing equations (Equation 2.13, 2.14, 2.16, 2.27).

Table 2.1. SPH Differential Operators

| **Differential operator** | **SPH formulation** |
|---|---|
| Gradient | $\nabla \cdot f_i(r) = \rho_i \sum_j m_j \left( \frac{f_i}{{\rho_i}^2} + \frac{f_j}{{\rho_j}^2} \right) \nabla W(r_i - r_j, h)$ |
| Divergence | $\nabla \cdot \overrightarrow{f_i(r)} = \rho_i \sum_j m_j \left( \frac{\overrightarrow{f_i}}{{\rho_i}^2} + \frac{\overrightarrow{f_j}}{{\rho_j}^2} \right) \cdot \nabla W(r_i - r_j, h)$ |
| Laplacian | $\nabla^2 f_i(r) = \sum_j 2 \frac{m_i}{\rho_j} \left( \frac{f_i - f_j}{{\lvert r_{ij} \rvert}^2} \right) \underrightarrow{r_{ij}} \cdot \nabla W(r_i - r_j, h)$ |

Table 2.2. Conditions for Kernel Approximation Function

| **Conditions for Kernel Function** | |
|---|---|
| $\int_{-\infty}^{\infty} W(r_{ij},\ h)\ dr = 1$<br>Unity Condition | |
| $W(r_{ij}, h) = W(-r_{ij}, h)$<br>Symmetry Condition | $\lim_{h \to 0} W(r_{ij}, h) = \delta(r_{ij})$<br>Delta Function Property |
| $W(r_{ij}, h) = 0\ for\ \lvert r_{ij} \rvert > kh$<br>Compact Condition | $W(r_{ij}, \mathrm{h}) \geq 0\ for\ any\ r_{ij}$<br>Positive Condition |
| $\frac{\partial W(r,h)}{\partial r} < 0$<br>Monotonic Decrease | Sufficiently Smooth |

Table 2.3. SPH Governing Equations

| Governing Eq | SPH formulation |
|---|---|
| Mass Conservation | $\left(\frac{d\rho}{dt}\right)_i = \rho_i \sum_j \frac{m_j}{\rho_j}(\boldsymbol{u_i} - \boldsymbol{u_j}) \cdot \nabla_i W_{ij}$ |
| | $\rho_i = \rho_{ref,i} \sum_j \frac{m_j}{(\rho_{ref})_j} W_{ij}$ |
| Momentum Conservation | $\left(\frac{1}{\rho}\nabla P\right)_i = -\sum_j m_j \left(\frac{p_i + p_j}{\rho_i \rho_j}\right) \nabla W_{ij}$ |
| | $(\upsilon \nabla^2 \boldsymbol{u})_i = \sum_j \frac{m_j \mu_{ij} \boldsymbol{r_{ij}} \cdot \nabla_i W_{ij}}{\rho_i \rho_j \left(\lvert \boldsymbol{r_{ij}} \rvert^2 + \eta^2\right)} (\boldsymbol{u_i} - \boldsymbol{u_j})$ |
| Equation of State | $p = \frac{{c_0}^2 \rho_{ref}}{\gamma} \left[\left(\frac{\rho}{\rho_{ref}}\right)^{\gamma} - 1\right]$ |

Table 2.4. V&V Simulation Cases for Developed SPH Code

| **V&V Cases for developed SPH Model** | |
|---|---|
| **Single Phase SPH** | |
| N-S Equation (momentum conservation) | *Hydrostatic pressure*<br>*Poiseuille & Couette flow*<br>*Lid driven flow* |
| Multi-D Free-surface Hydrodynamics | *2D, 3D dam break*<br>*3D wave generation*<br>*3D liquid centralized sloshing* |
| Multi-fluid Flow | *Hydrostatic pressure (immiscible two-fluid)*<br>*Lock exchange problem*<br>*Rayleigh-Taylor instability* |
| **Multi-phase SPH** | |
| Large-scale Fluid Flow | *2D two-phase dam break*<br>*3D two-phase liquid centralized sloshing*<br>*Jet Breakup* |
| Meso-scale Multi-phase Hydrodynamics | *Bubble Terminal Velocity*<br>*Continuum based surface tension*<br>*Bubble lift behavior* |
| **Heat Transfer SPH** | |
| Heat Transfer | *Multi-D heat conduction*<br>*2D natural convection* |

Table 2.5. Comparison of Simulation Results with Benchmark Experient

| | | **Slosh at outer container wall** | | **Slosh at pool center** | |
|---|---|---|---|---|---|
| | | Time of max H [s] | Max H [cm] | Time of max H [s] | Max H [cm] |
| **Centralized Sloshing** | | | | | |
| Experiment [Maschek] | | 0.42 ± 0.02 | 16.0 ± 1.0 | 0.88 ± 0.04 | 40.0 ± 5.0 |
| SIMMER-Ⅳ [Pigny] | | 0.38 | 18.75 | - | >50 |
| SPH [Vorobyev] | | 0.40 ± 0.01 | 17.0 ± 0.6 | 0.87 ± 0.03 | 38.0 ± 6.0 |
| **This Study** high resolution | | 0.41 | 17.5 | 0.88 | 38.0 |
| **This Study** low resolution | | 0.40 | 17.0 | 0.86 | 36.3 |
| **This Study** two-phase, med | | 0.42 | 15.5 | 0.87 | 41 |
| **12 Vertical Rods (inner/outer)** | | | | | |
| Inner | Experiment [Maschek] | 0.44 ± 0.02 | 15.0 ± 1.0 | 0.90 ± 0.04 | 3.0 ± 2.0 |
| | SPH [Vorobyev] | 0.38 | 15.5 | 0.82 | 5.0 |
| | **This Study** | 0.43 | 16.0 | 0.88 | 3.5 |
| Outer | Experiment [Maschek] | 0.42 ± 0.02 | 15.0 ± 1.0 | 0.88 ± 0.04 | 15.0 ± 3.0 |
| | SPH [Vorobyev] | 0.41 | 08.5 | 0.84 | 15.5 |
| | **This Study** | 0.41 | 17.5 | 0.88 | 12.9 |
| **Asymmetric Sloshing** | | | | | |
| Experiment [Maschek] | | 0.36 ±0.02 | 14.0 ± 2.0 | 0.48 ± 0.02 | 24.0 ± 2.0 |
| **This Study** | | 0.36 | 16.5 | 0.47 | 21.0 |

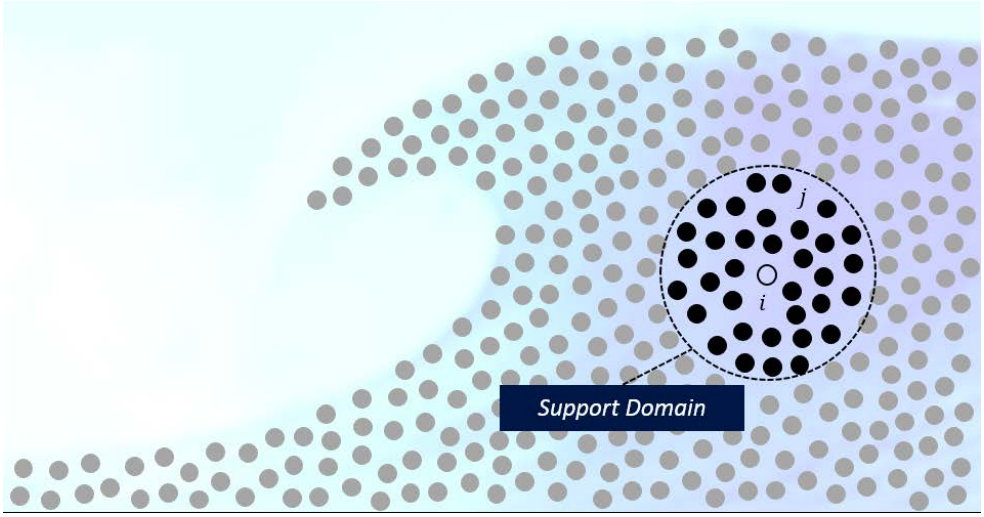


Figure 2.1. Particle System of Smoothed Particle Hydrodynamics (SPH)

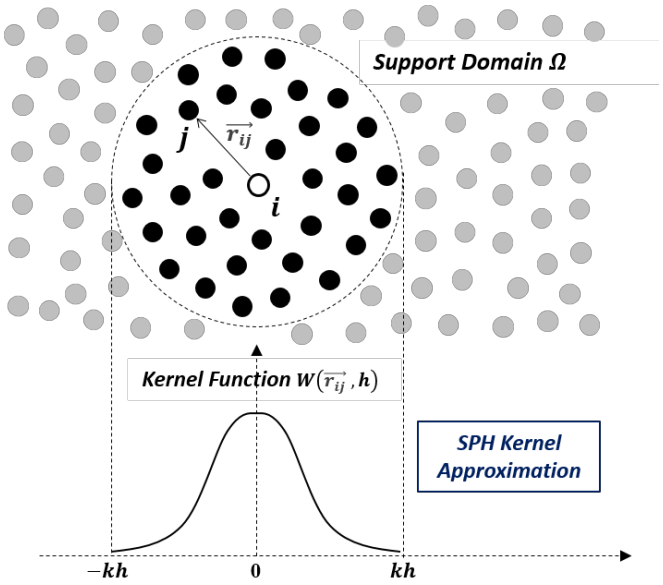


Figure 2.2. Kernel Weighting Function in SPH Method

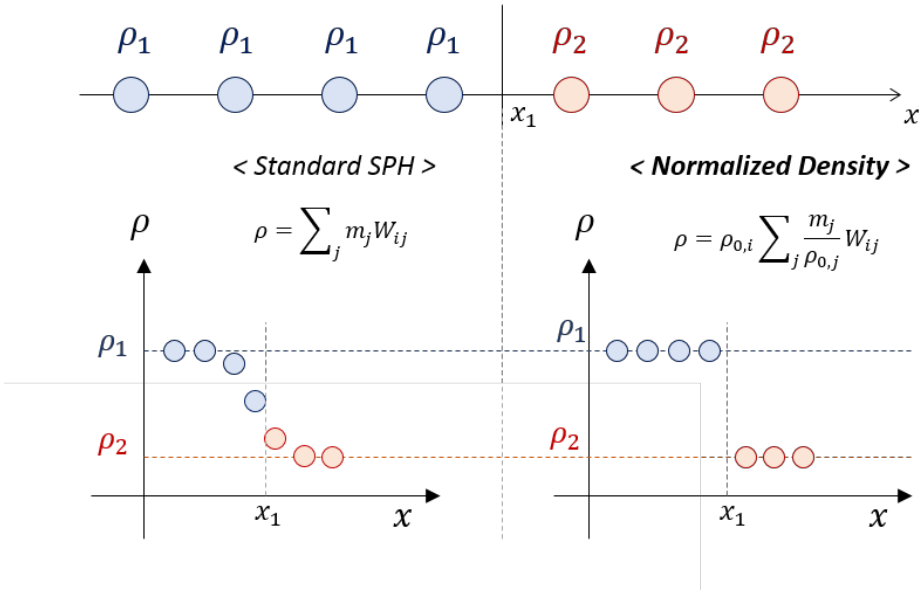


Figure 2.3. Normalized Density Approach for Density Estimation

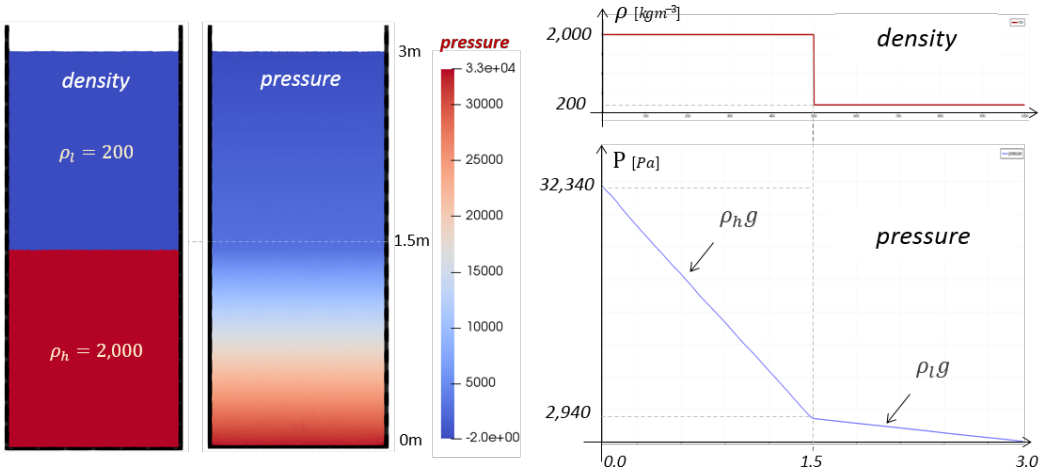


Figure 2.4. Density and Pressure Results for Two-Fluid Hydrostatic Problem

(With density ratio of 10)

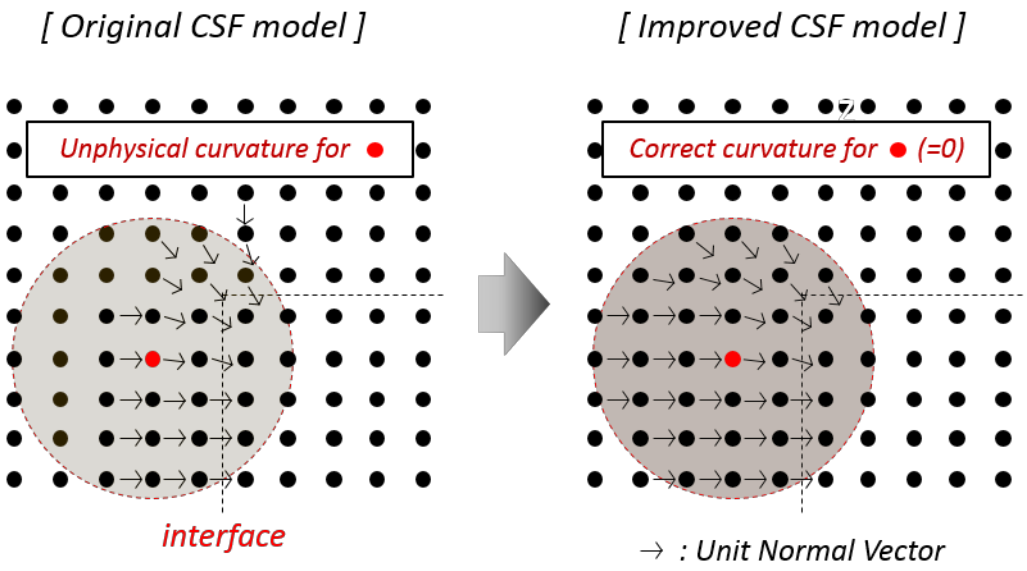


Figure 2.5. Improvement of CSF Model for Calculation of Curvature

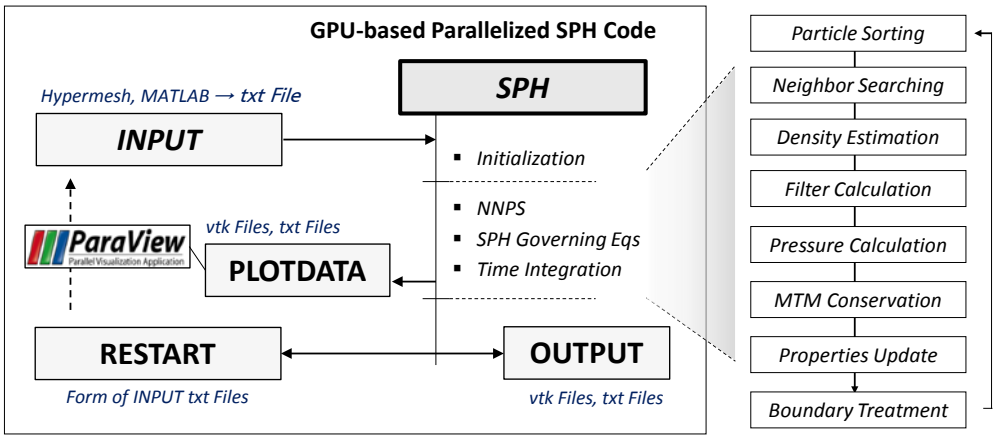


Figure 2.6. Structure and Simplified Algorithm of Developed SPH Code

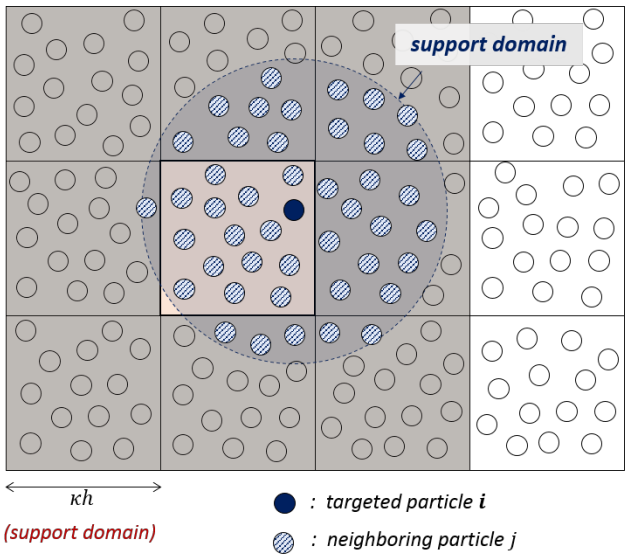


Figure 2.7. Grid-based Nearest Neighboring Particles Searching (NNPS)

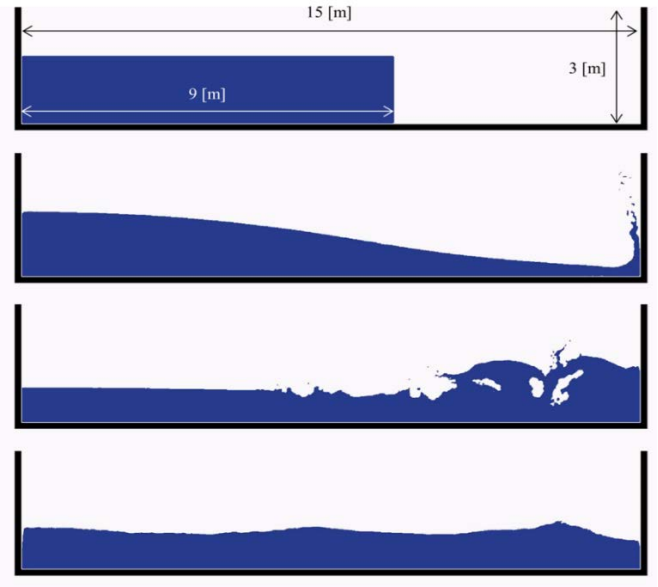


Figure 2.8. 2D SPH Simulation Results of Dam-Break Behavior

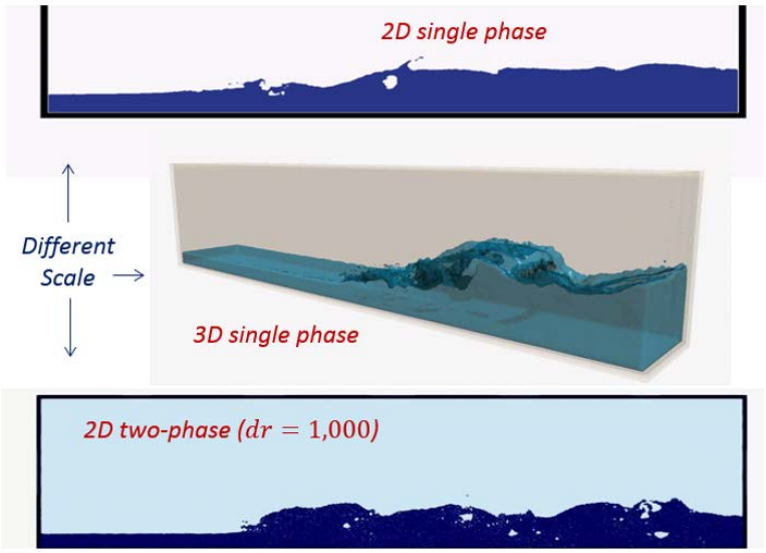


Figure 2.9. SPH Results on Dam-Break Simulation in Various Conditions (Single/Two Phase) and Scales

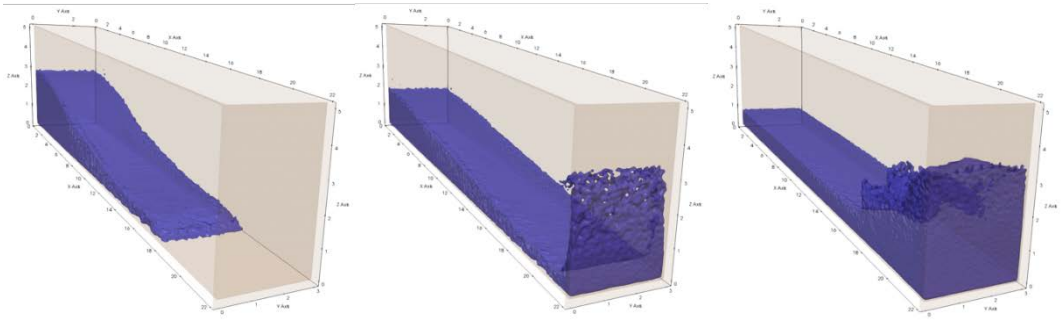

Figure 2.10. Snapshots for 3D Single Phase Dam-Break Simulation

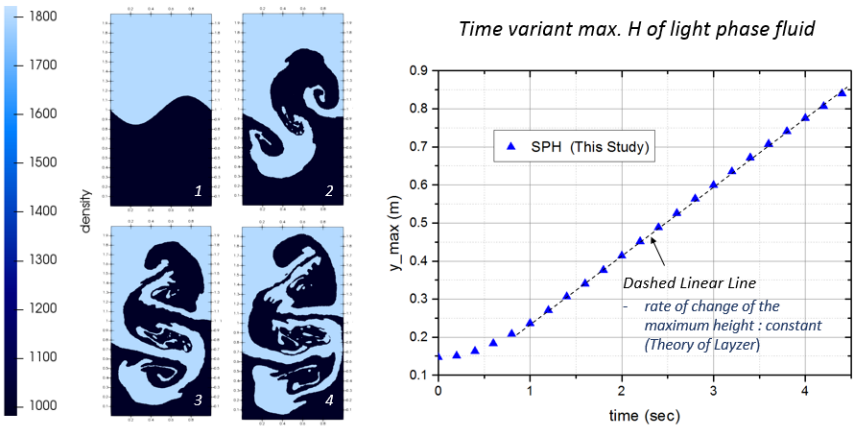


Figure 2.11. Results of Rayleigh-Taylor Instability Simulation

(Density Ratio: 1.8)

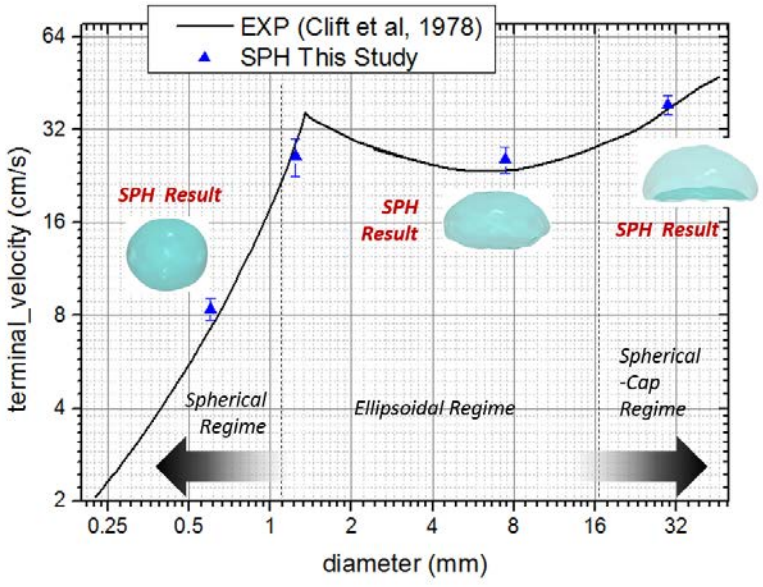


Figure 2.12. SPH Simulation Results for Bubble Terminal Velocity

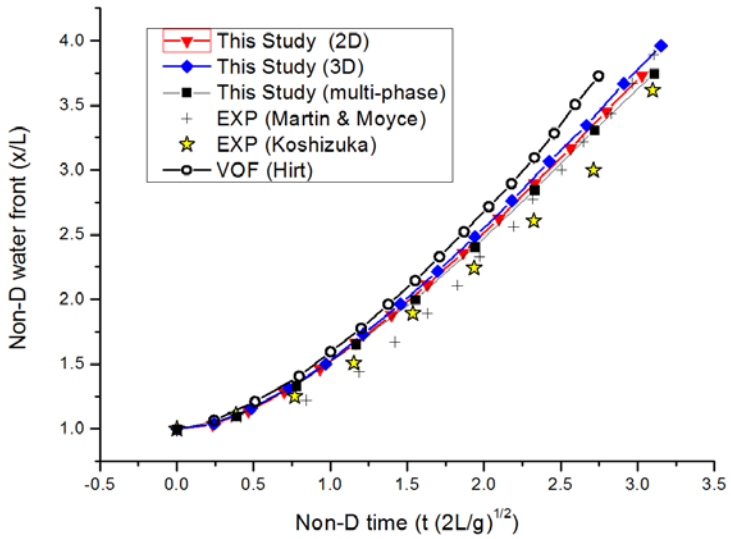


Figure 2.13. Validation Results of SPH Method for Multi-D, Multi-Phase Dam-Break Simulation

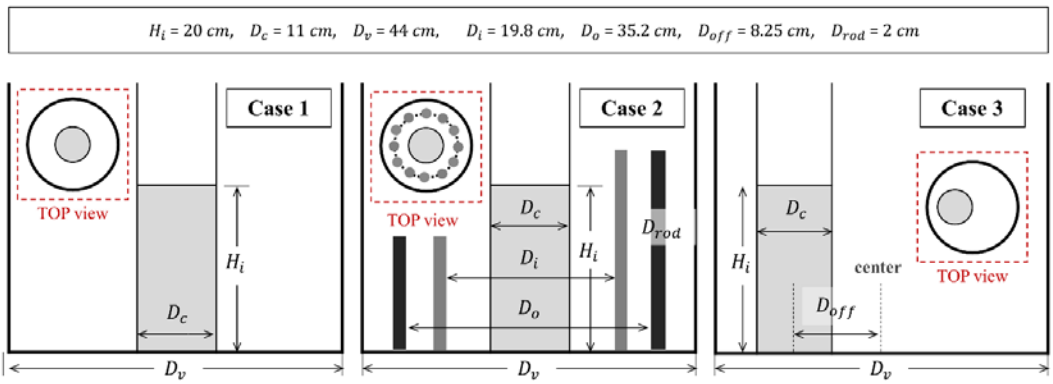


Figure 2.14. Geometry and Conditions for 3D SPH Sloshing Simulation

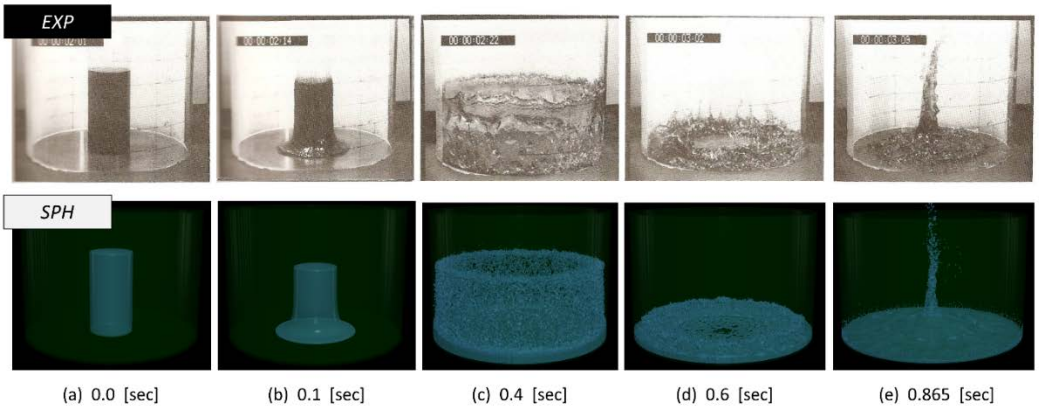


Figure 2.15. Qualitative Comparison of SPH Result with Benchmark Exp

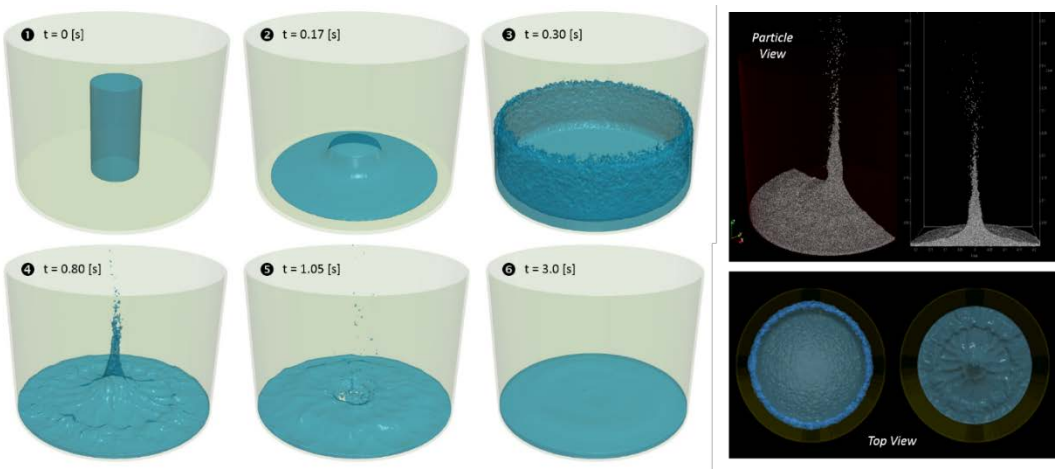


Figure 2.16. 3D Simulation Results of Developed SPH Code for Single-Phase Centralized Sloshing Behavior

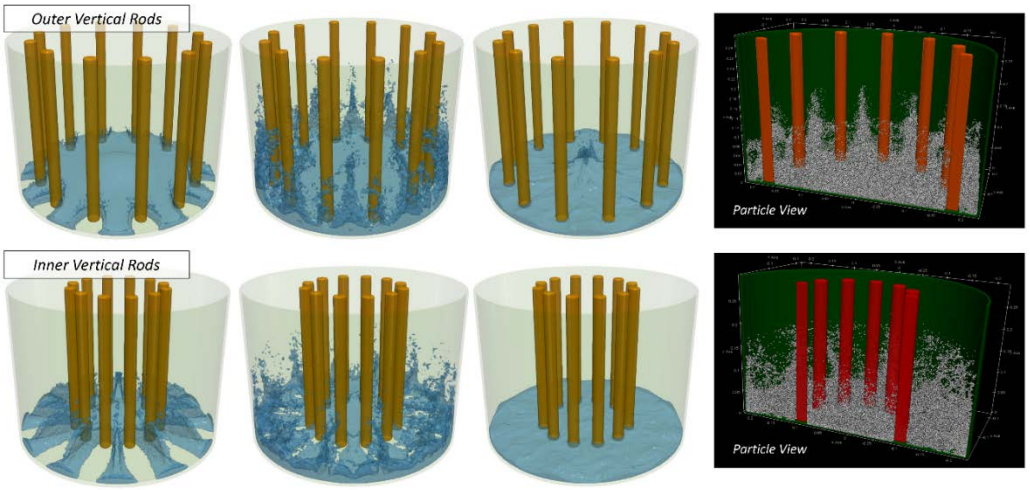


Figure 2.17. 3D Simulation Results of Developed SPH Code for 12 Vertical Rods Sloshing

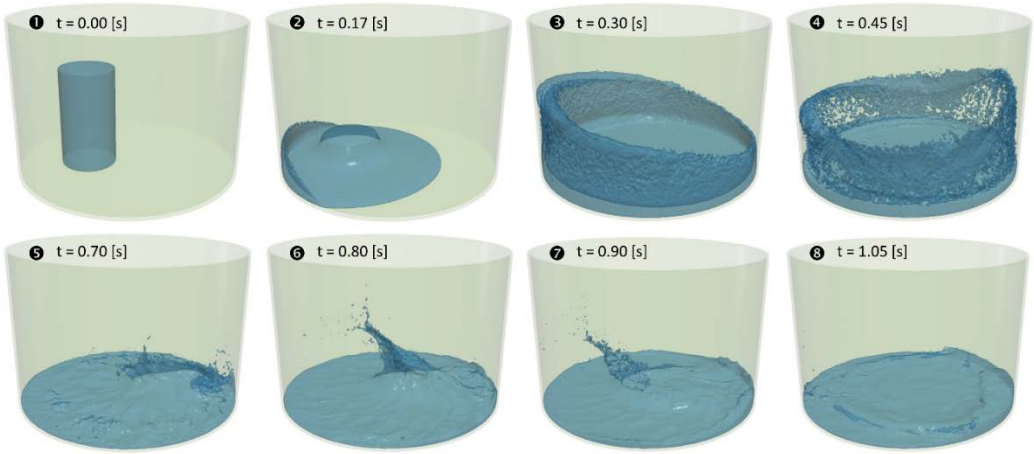


Figure 2.18. 3D Simulation Results of Developed SPH Code for Asymmetric Sloshing Condition

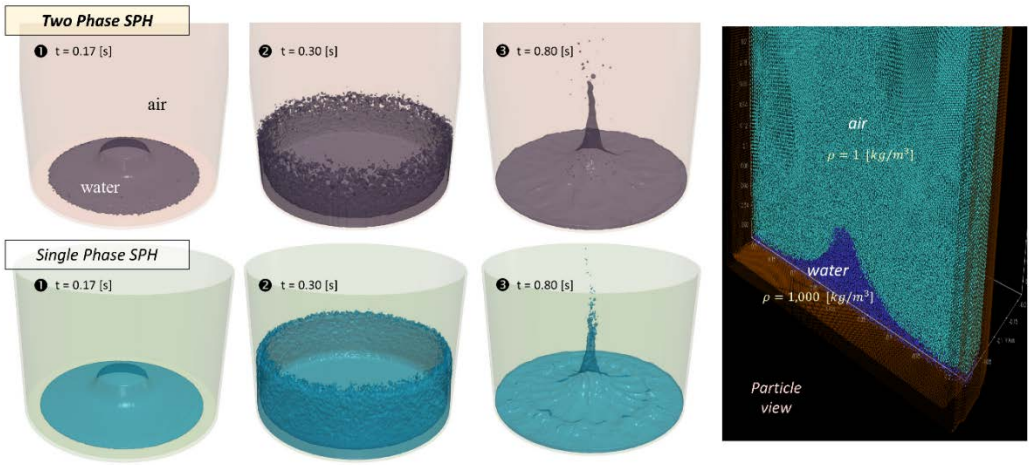


Figure 2.19. 3D Comparison Results for Two-Phase Centralized Sloshing Simulation

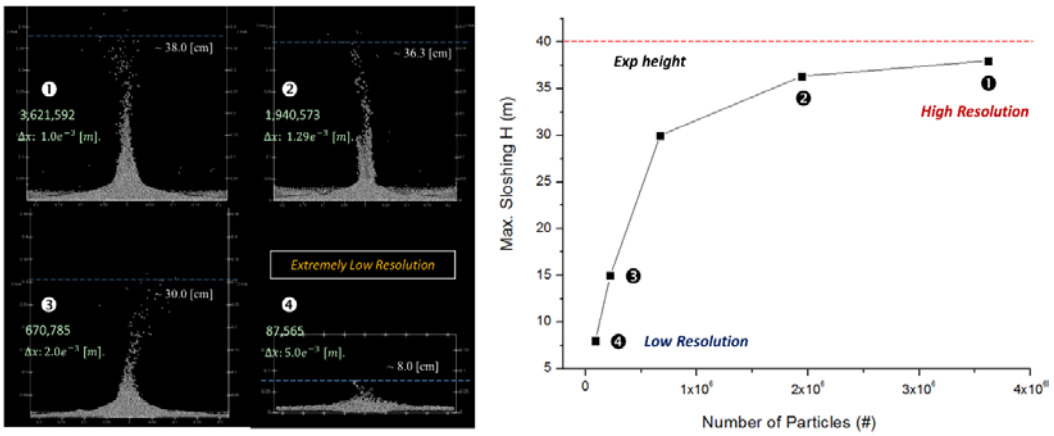


Figure 2.20. Effect of Particle Resolution in SPH Sloshing Simulation

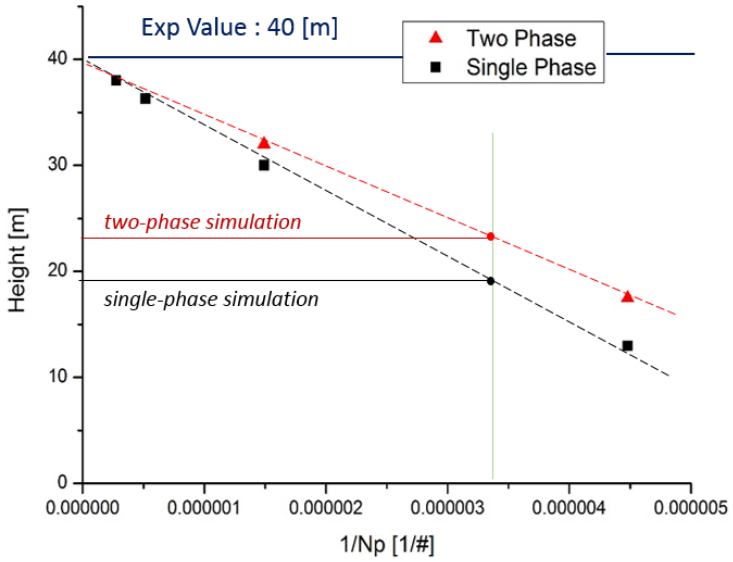


Figure 2.21. Convergence of Results for Particle Resolution (Single/Multi Phase)

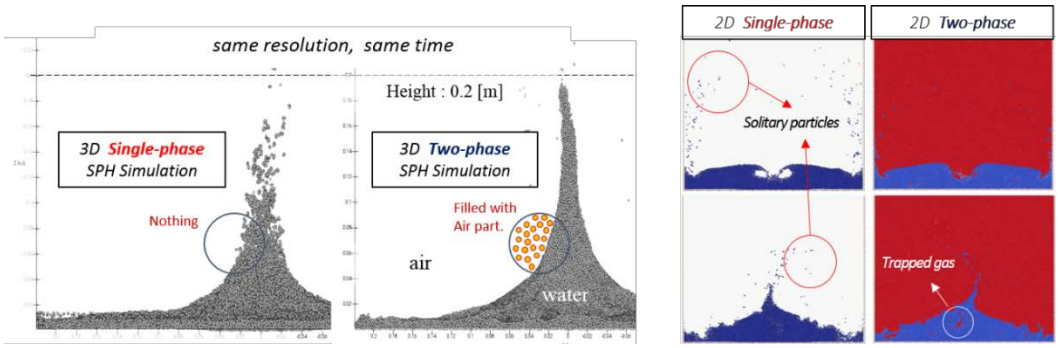


Figure 2.22. Difference between Single and Two Phase Simulation

# Chapter 3

# Solid Phase: Discrete Element Method

The numerical study of solid particle phase can be divided into the traditional continuum approach and discrete model based on the direct simulation method. The continuum approach treats the solid phase also as a continuous substance and ignores the specific behavior of each individual particle. The conservation of mass, momentum, and energy are solved in small regions of the solid material, while the interaction between solid particles depends on the empirical correlation. This continuum approach is effective when the average size of solid particles is much smaller than the characteristic length scale of the simulation.

However, in the case of the behavior of debris particles in this study, detailed interaction between solid particles should be considered since its own relocation behavior is an important parameter. Hence, in phenomena such as sedimentation and leveling of the solid debris bed, a numerical method based on a direct simulation that directly analyzes each collision between solid particles is suitable. A numerical model for the behavior of solid debris particles is constructed using the Discrete Element Method (DEM), which is the most mature and widely used direct simulation method. In this chapter, the DEM contact force model formulation, versatile wall boundary conditions, implementation algorithm, and simulation results including V&V cases are presented in order.

## 3.1 Discrete Element Method (DEM)

Discrete Element Method (DEM), which is firstly proposed by Cundall (1979), is the most widely used numerical method for describing the mechanical behavior of discrete rigid particles. DEM has been applied for the behavior of granular material such as material packing, heaping, hopper flow, and so on. In the DEM technique, the translation and rotation behavior of the particulate rigid body is analyzed by calculating the force and torque due to collision based on Newton's second law of motion. The simplified governing equations for the translational and rotational motion of each solid particle can be written as,

$$m_a \frac{d^2 \boldsymbol{r_a}}{dt^2} = \sum_b \boldsymbol{F_{ab}} + m_a \boldsymbol{g_a} \tag{3.1}$$

$$I_a \frac{d^2 \boldsymbol{\theta_a}}{dt^2} = \sum_b \left( \boldsymbol{r_{ac}} \times \boldsymbol{F_{ab}^t} \right) \tag{3.2}$$

where $m_a$ and $I_a$ are the mass and the moment of inertia of the particle a, $\boldsymbol{r_a}$ and $\boldsymbol{\theta_a}$ are the position vector and angular position vector of the particle a, respectively, and $\boldsymbol{r_{ac}}$ is the vector from the center of mass of particle a to contact point. Only the tangential component of the contact force $\boldsymbol{F_{ab}^t}$ is involved in rotational behavior.

The general DEM simulation sequence is as follows where a detailed DEM algorithm implemented in this study is summarized in section 3.4.

(1) Contact detection between particles

(2) Calculation of contact force ($F_{ab}$) and torque ($\tau_{ab}$)

(3) Calculation of wall condition (detection, collision, sliding, rolling)

(4) Calculation of new position

## 3.2 DEM Contact Force

### 3.2.1 Soft-sphere Contact Model

The DEM contact model can be classified into a hard-sphere model and a soft sphere model depending on the analytic perspective of inter-particle collision. In the hard sphere model, the momentum exchange between particles is solved just in a single collision. Hence, there is a difficulty in solving the collision matrix and there is a limitation that it can be only discussed for smooth spherical particles [Luding, 2008]. For this reason, the hard-sphere model is used within a limited range, while a soft-sphere based collision model is generally used to simulate the behavior of granular material including debris particles in this study.

In the soft sphere model, the collision between granular particles is solved in a spring-dashpot system which allows a thin overlap of contact particles (Figure. 3.1). As shown in Figure 3.1, the spring-dashpot system consists of a spring which provides the elasticity and a damper that corresponds to the energy dissipation in the collision. In the tangential direction, there is also the slider that analyzes rotation and energy dissipation due to the friction. Various contact force models for each of these components are known, which are summarized in the following sub-sections.

### 3.2.2 Contact Force Model

In the soft-sphere based spring-dashpot system, the collision between two particles is a continuous process in a short time period with a slight overlap between particles. It is inherently difficult to accurately describe the inter-particle contact physics over the contact area, as it is related to many geometrical and physical factors such as the shape, material properties, and also movement state of particles [Zhu, 2007]. Hence, the DEM generally adopts simplified equations to determine the contact forces and torques in order to be computationally efficient.

The contact force model can be classified on the basis of how the elastic force for the spring in Figure 3.1 is described. The simplest form of contact force is a linear model, which is proposed by Cundall (1979), where the linear spring is used for the elastic deformation. In addition, there is a nonlinear contact force model in which a nonlinear restoring force (proportional to $3/2$ power of overlap) acts according to Hertz's theory for elastic contact of spheres. Mindlin and Deresiewicz (1953) proposed a general tangential force model, and in combination with Hertz's theory, the most widely used Hertz-Mindlin contact force model was derived. There is also JKR model based on physical elastic collisions [Johnson, 1971], and the normal component formulation of each contact force is briefly summarized in Table 3.1.

In the DEM model implemented in this study, the Hertz-Mindlin contact force model is applied due to its accuracy and simplicity, which is described in detail in the following sub-section.

### 3.2.3 Hertz-Mindlin Contact Force Model

This sub-section describes the Hertz-Mindlin contact force model in detail, which is applied in the DEM model of this study. As described in the previous sub-sections and also shown in Figure 3.1, the collision force between particles is divided into the normal component and the tangential component first, and each is divided into the elastic spring term corresponding to the conservative force and damping term corresponding to dissipation term again. This can be expressed as the following equations.

$$\boldsymbol{F_{ab}} = f_{ab}^{n}\,\hat{\boldsymbol{n}} + f_{ab}^{t}\,\hat{\boldsymbol{t}} \tag{3.3}$$

$$f_{ab}^{n} = f_{spring}^{n} + f_{damper}^{n} \tag{3.4}$$

$$f_{ab}^{t} = f_{spring}^{t} + f_{damper}^{t} \tag{3.5}$$

The unit vector $\hat{\boldsymbol{n}}$ and $\hat{\boldsymbol{t}}$ respectively denote the normal and tangential component between particle a and particle b. $f_{ab}^{n}$ and $f_{ab}^{t}$ represent the magnitude of normal and tangential component of contact force, and each is divided into the elastic term($f_{spring}$) and damping term($f_{damper}$) again.

In the collision situation (Figure. 3.2) of particle a and b, the equivalent properties are defined as follows where $M$, $R$, $E$, $G$, and $\nu$ are mass, radius, Young's modulus, shear modulus, and Poisson's ratio of each particle, respectively.

$$M_{ab}{}^{*} = \left(\frac{1}{M_a} + \frac{1}{M_b}\right)^{-1} \tag{3.6}$$

$$R_{ab}{}^{*} = \left(\frac{1}{R_a} + \frac{1}{R_b}\right)^{-1} \tag{3.7}$$

$$E_{ab}{}^{*} = \left(\frac{1 - \nu_a{}^2}{E_a} + \frac{1 - \nu_b{}^2}{E_b}\right)^{-1} \tag{3.8}$$

$$G_{ab}{}^{*} = \left(\frac{2 - \nu_a}{G_a} + \frac{2 - \nu_b}{G_b}\right)^{-1} \tag{3.9}$$

According to the Hertz's theory of inter-particle elastic normal contact force, the maximum pressure ($P_{max}$) and elastic normal contact force ($f_{spring}^{n}$) in the collision between two spheres are written as follows where $\delta_c$ is contact radius in Figure 3.2.

$$P_{max} = \frac{3\, f_{spring}^{n}}{2\pi {\delta_c}^2} \tag{3.10}$$

$$f_{spring}^{n} = \frac{4E_{ab}{}^{*}}{3R_{ab}{}^{*}}{\delta_c}^3 = \frac{4E_{ab}{}^{*}}{3R_{ab}{}^{*}}\sqrt{R_{ab}{}^{*}\delta_n}^3 = \frac{4}{3}E_{ab}{}^{*}\sqrt{R_{ab}{}^{*}}\ {\delta_n}^{3/2} \tag{3.11}$$

The damping term ($f_{damper}^{n}$) in normal direction also can be derived in a nonlinear form as below:

$$f_{damper}^{n} = -\sqrt{\frac{10}{3}}\frac{\ln(e)}{\sqrt{ln(e)^2 + \pi^2}}\sqrt{M_{ab}{}^{*}K'_n}\, v_n \tag{3.12}$$

$$K'_n = 2E_{ab}{}^*\sqrt{R_{ab}{}^*\delta_n} \tag{3.13}$$

where $e$ is the restitution coefficient between two particles.

Similar to the normal force, the tangential force term, $f_{spring}^t$ and $f_{damper}^t$ are expressed as below.

$$f_{spring}^t = 8G_{ab}{}^*\sqrt{R_{ab}{}^*\delta_n}\,\delta_t = k_t\delta_t \tag{3.14}$$

$$f_{damper}^t = \sqrt{\frac{10}{3}}\frac{ln(e)}{\sqrt{ln(e)^2+\pi^2}}\sqrt{M_{ab}{}^*k_t} \tag{3.15}$$

Here, the overlap in the tangential direction $\delta_t$ is not a geometrically determined variable. $\delta_t$ can be obtained by accumulating the relative velocity between particles at the contact point during the collision period as follows where $v_t$ and $\mathrm{t}'$ are the relative velocity between particles and time, respectively.

$$\Delta\delta_t = v_t\Delta t' \tag{3.16}$$

On the other hand, the contact force in the tangential direction cannot be larger than the friction force acting on the contact surface. When the contact force exceeds the maximum friction force, sliding motion occurs between two contact particles. Therefore the contact force in the tangential direction can be written as below where $\mu_t$ is a friction coefficient between two contact particles.

$$f_{ab}^{t} = min\left(f_{spring}^{t} + f_{damper}^{t}, -\mu_t |f_{ab}^{n}\, \hat{\boldsymbol{n}}|\right) \tag{3.17}$$

The Hertz-Mindlin contact force in each direction corresponding to equations from (3.11) to (3.17) are summarized in Table 3.2.

## 3.3 Wall Boundary Conditions

### 3.3.1 Versatile Wall Boundary Model

The interaction between the solid particles and the wall boundary can be classified into two types. One is the collision with a sufficient normal velocity component, and the other is particle sliding (or rolling) on the boundary surface. In general, when the solid particle collides with a wall boundary, the particle velocity and its angular velocity are balanced within several collisions due to the friction of the wall surface, resulting in a quasi-rolling state. However, the collision behavior and sliding (or rolling) behavior are fundamentally different in physics. Hence, when the solid particle is initially placed on the wall boundary like billiard simulation, solving the solid particle behavior only based on a collision dynamics may cause abnormally large friction force, which can underestimate the particle motion. In addition, there is a limit to control this problem through the empirical modeling of the restitution coefficient, since the results can be influenced by the step size of time integration.

In the case of the self-leveling behavior of solid debris in the ex-vessel cooling,

granular debris particles are packed on the bottom concrete boundary as shown in Figure 1.2. When two-phase natural convection of the fluid occurs due to the decay heat generated from debris particles, solid particles move by drag force. Considering the velocity of the flow and the load due to the upper debris particles, the bottom particles may slide or roll on the boundary in continuous contact with the wall boundary. Therefore, the debris particle behavior can be estimated incorrectly if the interaction with the wall is considered only by the collision. Since the debris particle spreading and relocation behavior greatly affects the coolability of decay heat, a suitable model for the surface behavior of solid particles is required.

In order to overcome these limitations, a new versatile wall boundary model that considers both collision and sliding (or rolling) motion of solid particles is proposed as shown in Figure 3.3. In this boundary model, the collision equations are solved if the magnitude of the normal velocity component is sufficient while sliding and rolling behavior are solved if the magnitude is below a certain threshold. The implementation sequence of this wall boundary model is as follows.

(1) Determine if the solid particle contacts with the wall based on the primitive object function as shown in Figure 3.4.
(2) Calculate the surface normal vector at the contact point
(3) Calculate the surface tangential vector considering both transitional and rotational velocity of the particle
(4) Calculate the normal velocity component $\boldsymbol{v_n}$
(5) Solve the equations for collision dynamics if $|\boldsymbol{v_n}|$ is above the criteria

(6) Solve the physics for sliding & rolling if $|\boldsymbol{v_n}|$ is below the criteria

(7) Update particle position, velocity, angular velocity

The governing equations for each physics are described in the following sections as well as V&V simulations for this wall boundary model.

### 3.3.2 Particle Collision with the Wall

The collision dynamics are solved when a solid particle collides with a wall with sufficient normal velocity as shown in Figure 3.5. If the solid particle approaches the wall with velocity of $v_0$, and angular velocity of $\omega_0$, the velocity vectors at the contact point before and after the collision are calculated as follows,

$$\boldsymbol{v_{c0}} = \boldsymbol{v_0} - \boldsymbol{\omega_0} \times r\,\hat{\boldsymbol{n}} \tag{3.18}$$

$$\boldsymbol{v_{c1}} = \boldsymbol{v_1} - \boldsymbol{\omega_1} \times r\,\hat{\boldsymbol{n}} \tag{3.19}$$

where $\hat{\boldsymbol{n}}$ is the unit normal vector at the contact point $C$, and $\boldsymbol{v_1}$, $\boldsymbol{\omega_1}$ are the velocity and angular velocity vector after the collision, respectively. The unit tangential vector is also obtained by dot product of $\boldsymbol{v_{c0}}$ (Equation 3.18) with normal unit vector $\hat{\boldsymbol{n}}$.

$$\hat{\boldsymbol{t}} = \frac{\boldsymbol{v_{c0}} - (\boldsymbol{v_{c0}} \cdot \hat{\boldsymbol{n}})\hat{n}}{|\boldsymbol{v_{c0}} - (\boldsymbol{v_{c0}} \cdot \hat{\boldsymbol{n}})\hat{n}|} \tag{3.20}$$

In this case, the change of the momentum and angular momentum vector between the collisions are satisfy the equations below.

$$m\,(\boldsymbol{v_1} - \boldsymbol{v_0}) = \boldsymbol{J} \tag{3.21}$$

$$I\,(\boldsymbol{\omega_1} - \boldsymbol{\omega_0}) = -r\,\hat{\boldsymbol{n}} \times \boldsymbol{J} \tag{3.22}$$

Defining the restitution coefficient of the normal direction ($e_n$) and the tangential direction ($e_t$), the dot products of momentum vector in each direction are summarized as follows.

$$\boldsymbol{J} \cdot \hat{\boldsymbol{n}} = -m\,(1 + e_n)\,(\boldsymbol{v_{c0}} \cdot \hat{\boldsymbol{n}}) \tag{3.23}$$

$$\boldsymbol{J} \cdot \hat{\boldsymbol{t}} = -\left(\frac{1}{m} + \frac{r^2}{I}\right)^{-1} (1 + e_t)\,(\boldsymbol{v_{c0}} \cdot \hat{\boldsymbol{t}}) \tag{3.24}$$

Substituting these equations into the above equation (3.21) and (3.22), the final expressions for velocity and angular velocity after the collision are derived as below.

$$\boldsymbol{v_1} = \boldsymbol{v_0} - (1 + e_n)\,(\boldsymbol{v_{c0}} \cdot \hat{\boldsymbol{n}})\,\hat{\boldsymbol{n}} - \frac{1}{m}\left(\frac{1}{m} + \frac{r^2}{I}\right)^{-1} (1 + e_t)\,(\boldsymbol{v_{c0}} \cdot \hat{\boldsymbol{t}})\;\hat{\boldsymbol{t}} \tag{3.25}$$

$$\boldsymbol{\omega_1} = \boldsymbol{\omega_0} + \frac{r}{I}\left(\frac{1}{m} + \frac{r^2}{I}\right)^{-1} (1 + e_t)(\boldsymbol{v_{c0}} \cdot \hat{\boldsymbol{t}})\,(\hat{\boldsymbol{n}} \times \hat{\boldsymbol{t}}) \qquad (3.26)$$

### 3.3.3 Sliding and Rolling on the Wall Boundary

If the solid particle is in constant contact with the wall without sufficient normal velocity component, sliding and rolling occurs on the surface for the particle with curvature. In this situation, the velocity and angular velocity of particle over time ($t'$) are expressed in relation to the sliding friction coefficient ($\mu_s$) as follows,

$$\boldsymbol{v} = \boldsymbol{v_0} - \left(\mu_s g cos\alpha\, \hat{\boldsymbol{t}}\right) t' \qquad (3.27)$$

$$\boldsymbol{\omega} = \boldsymbol{\omega_0} - \left(\frac{\mu_s m g cos\alpha}{I}\, \boldsymbol{r} \times \hat{\boldsymbol{t}}\right) t' \qquad (3.28)$$

where $m$, $I$, and α are the mass, rotational inertia and surface slope, respectively. When solid particles roll (one-to-one contact between the particle surface and the boundary surface) over the wall boundary, the magnitude of velocity $|\boldsymbol{v}|$ is balanced with the magnitude of the cross product of $\boldsymbol{r}$ and $\boldsymbol{\omega}$. From this condition, the speed of rolling ($v_{roll}$) and the time taken to roll ($t_{roll}$) to be used for V&V simulation of wall boundary model, can be derived as follows.

$$v_{roll} = v_0 - (v_0 - r\omega_0)\left[1 + \frac{m\,r^{\,2}}{I}\right]^{-1} \tag{3.29}$$

$$t_{roll} = \frac{v_0 - r\omega_0}{\mu_s g cos\alpha}\left[1 + \frac{m\,r^{\,2}}{I}\right]^{-1} \tag{3.30}$$

When the spherical solid starts rolling, the relative velocity at the contact point is zero, so even if a non-conservative force acts, it does not work. In other words, a rolling rigid body can theoretically roll infinitely without any energy dissipation. However, in reality, there is resistive rolling friction ($\mu_r$) in the physical relationship between the wall boundary and the solid material that damping the rolling behavior such as the surface roughness. The velocity and acceleration considering rolling friction can be summarized as follows.

$$\boldsymbol{v} = \boldsymbol{v_0} - \left(\mu_s g cos\alpha\, \hat{\boldsymbol{t}}\right) t' \tag{3.31}$$

$$\boldsymbol{\omega} = \boldsymbol{\omega_0} - \left(\frac{(\mu_s + \mu_r) m g cos\alpha}{I}\, \boldsymbol{r} \times \hat{\boldsymbol{t}}\right) t' \tag{3.32}$$

## 3.4 DEM Implementation Algorithm

The detailed calculation sequence of the implemented DEM model is described in this section while the overall algorithm for DEM calculation is also summarized in Figure 3.6.

### 3.4.1 Contact Detection

Contact Detection with neighboring DEM particles is performed first in each time step. For the numerical efficiency, the entire computational domain is divided into grids as shown in Figure 3.7, and the contact detection is performed based on these girds rather than comparing the distance to all the other DEM particles. Each DEM particle is assigned to a specific grid according to the location, and the contact detection for each particle is conducted by comparing the distance with the particles within the neighboring grids. Since most simulation cases in this study require a uniform size of solid particles, the size of the grid is determined to be similar to the particle diameter. The contact detection equation for the particle a and the neighboring particle b can be written as below.

$$d_{ab} \leq r_a + r_b \tag{3.33}$$

$d_{ab}$ and r are the distance between particle a and particle b, and the radius of each particle, respectively. Then, the normal overlap ($\delta_n$), unit normal vector ($\hat{\boldsymbol{n}}$), and the position vector ($\boldsymbol{x_c}$) of the contact point are also determined as follows.

$$\delta_n = r_a + r_b - d_{ab} \tag{3.34}$$

$$\hat{\boldsymbol{n}} = (\boldsymbol{x_b} - \boldsymbol{x_a})/d_{ab} \tag{3.35}$$

$$\boldsymbol{x_c} = \boldsymbol{x_a} + \left(r_a - 0.5\,\delta_n\right) \cdot \hat{\boldsymbol{n}} \tag{3.36}$$

### 3.4.2 Estimation of Relative Velocity

The contact forces between the collision particles acting on the contact point are generally determined by the relative velocity between two particles as written in the above equations from (3.11) to (3.17). The relative velocity of the particle a and the particle b on the contact point is defined as,

$$\boldsymbol{v_{rel}} = \left(\boldsymbol{v_b} + \boldsymbol{\omega_b} \times (\boldsymbol{x_c} - \boldsymbol{x_b})\right) - \left(\boldsymbol{v_a} + \boldsymbol{\omega_a} \times (\boldsymbol{x_c} - \boldsymbol{x_a})\right) \tag{3.37}$$

where $\boldsymbol{v}$ and $\boldsymbol{\omega}$ are the velocity and angular velocity vector of each particle, respectively. This relative velocity can be divided into each direction (normal and tangential) by taking the dot product with a unit normal vector $\hat{\boldsymbol{n}}$.

$$\boldsymbol{v_n} = |\boldsymbol{v_{rel}} \cdot \hat{n}|\, \hat{\boldsymbol{n}} \tag{3.38}$$

$$\boldsymbol{v_t} = \boldsymbol{v_{rel}} - \boldsymbol{v_n} \tag{3.39}$$

The tangential overlap ($\delta_t$) is obtained from the above equation (3.16), and the unit tangential vector is also determined as follows, from the above equation

(3.24).

$$\hat{\boldsymbol{t}} = \boldsymbol{v_t} \,/\, |\boldsymbol{v_t}| \tag{3.40}$$

### 3.4.3 Calculation of Contact Force

When the relative velocity vector and the overlap in each direction are determined, the contact force based on the Hertz-Mindlin model is calculated. The detailed equations for the contact force model are summarized in the above equations from (3.11) to (3.17). From the calculated contact force, the particle acceleration ($\dot{\boldsymbol{v}}_{\boldsymbol{a}}$) and also the angular acceleration ($\dot{\boldsymbol{\omega}}_{\boldsymbol{b}}$) of the current time step are determined as follows,

$$\dot{\boldsymbol{v}}_{\boldsymbol{a}} = \boldsymbol{F_{ab}}/m_a \tag{3.41}$$

$$\dot{\boldsymbol{\omega}}_{\boldsymbol{a}} = (\boldsymbol{r_{ac}} \times \boldsymbol{F_{ab}^t})/I_a \tag{3.42}$$

Where $\boldsymbol{F_{ab}^t}$ is the tangential contact force, and $\boldsymbol{r_{ac}}$ is a position vector from the center of particle a to the contact point C.

### 3.4.4 Wall Boundary Conditions and Time Integration

From the particle acceleration calculated in the above equation (3.41) and

(3.42), the velocity, angular velocity, and the position of the next time step can be calculated as follows where $\Delta t'$ is a step size of time integration.

$$\boldsymbol{v_a} = \boldsymbol{v_a} + \frac{\boldsymbol{F_{ab}}}{m_a}\Delta t' \tag{3.43}$$

$$\boldsymbol{\omega_a} = \boldsymbol{\omega_a} + \frac{\boldsymbol{\tau_{ab}}}{I_a}\Delta t' \tag{3.44}$$

$$\boldsymbol{x_a} = \boldsymbol{x_a} + \boldsymbol{v_a}\Delta t' \tag{3.45}$$

Also, the interaction with the wall boundary is estimated according to the equations outlined in section 3.3 if the particle contacts with the wall. The time integration takes place after this step.

## 3.5 V&V and Simulations

Several collision simulations for the basic conservation laws (momentum, angular momentum, energy) are performed to verify the implemented DEM collision model. Also, some simulations for qualitative and quantitative V&V of the proposed particle-boundary interaction model were carried out. The simulation cases are listed in Table 3.3 and the main results are summarized in this section.

### 3.5.1 Conservation of Momentum and Angular Momentum

The momentum of solid particles in all collisions is conserved since all contact forces (including friction force and damping force) are internal forces acting between the colliding particles. If particle 1 and particle 2 collide with the velocity of $\boldsymbol{v_{10}}$ and $\boldsymbol{v_{20}}$ as shown in Figure 3.8, the conservation of momentum can be written as follow.

$$m_1\boldsymbol{v_{10}} + m_2\boldsymbol{v_{20}} = m_1\boldsymbol{v_1} + m_2\boldsymbol{v_2} \tag{3.46}$$

The angular momentum is also conserved in all collisions since the torque due to the tangential contact force is also the internal torque. However, since the angular momentum is defined based on a specific axis, a reference axis is required in order to compare it before and after the collision. Based on the axis on the contact point C, the conservation of angular momentum can be expressed as follows (Figure 3.9).

$$\begin{aligned} &m_1\boldsymbol{r_{c1}} \times \boldsymbol{v_{10}} + m_2\boldsymbol{r_{c2}} \times \boldsymbol{v_{20}} \\ &= I_1\boldsymbol{\omega_1} + m_1\boldsymbol{r_{c1}} \times \boldsymbol{v_1} + I_2\boldsymbol{\omega_2} + m_2\boldsymbol{r_{c2}} \times \boldsymbol{v_2} \end{aligned} \tag{3.47}$$

The momentum and angular momentum were calculated for various collision situations, and it was confirmed that both momentums are well conserved in all collisions.

### 3.5.2 Conservation of Energy in Elastic Collision

The kinetic energy, including both rotation and translation, is conserved in a situation where only the conservative force acts or the non-conservative force acts without any displacement (not work). In the general collision between the solid particles, the energy dissipation occurs since the friction or damping force acting on the contact point works for the specific displacement defined as overlap ($\delta_n$, $\delta_t$). Therefore, in order to confirm the conservation of kinetic energy, it is necessary to assume a hypothetical situation in which only an elastic force (which is the conservative force) acts on the contact point. In this situation, the kinetic energy before the collision is divided into the translational kinetic energy and the rotational kinetic energy after the collision, while the summation is conserved as follows (Figure 3.10).

$$\frac{1}{2}m_1{v_{10}}^2+\frac{1}{2}m_1{v_2}^2=\left(\frac{1}{2}m_1{v_1}^2+\frac{1}{2}m_2{v_2}^2\right)+\left(\frac{1}{2}I_1{\omega_1}^2+\frac{1}{2}I_2{\omega_2}^2\right) \quad (3.48)$$

When the collisions were simulated only with the elastic term of applied Hertz-Mindlin contact force model, it was confirmed that the kinetic energy is well conserved in an elastic collision.

### 3.5.3 V&V Simulations for Wall Boundary Model

The following simulations were performed for quantitative and qualitative

V&V of the wall boundary model proposed in this study. Quantitative results are also included in the figures corresponding to each simulation case.

a. Wall collision of rotating sphere (Figure 3.11)
b. Sliding and rolling of the spherical particles on the wall boundary (Figure 3.12)
c. Descending behavior of the sphere on a slope (Figure 3.13)
d. 3D hopper flow simulation (Figure 3.14)

Through the simulation a above, it can be confirmed that the restitution coefficients in the normal and tangential directions are well reflected in the rotation and translation behavior of the colliding particles. Simulation b was performed to verify the sliding and rolling motion on the boundary with the real physics represented by the above equation (3.29) and (3.30). Simulation c is a case to confirm if the newly proposed boundary model works well according to the established criteria. It has been found that a series of interaction behavior from collision to sliding and rolling is well simulated in accordance with real physics as shown in Figure 3.13. In addition, 3D hopper flow simulation (simulation d, Figure 3.14) was also carried out for qualitative validation of collisions between particles and also the interaction between DEM particles and wall boundary.

### 3.5.4 Granular Collapse of Spherical Particles

The granular collapse behavior of spherical particles was analyzed for validation of the overall DEM model including wall boundary conditions. The

falling test setup of the benchmark experiment is shown in Figure 3.15 [Chou, 2012]. The experimental system consisted of a rectangular cute ($60\text{cm} \times 40\text{cm} \times 5\text{cm}$) and a high-speed camera. The rectangular chute was made of transparent acrylic plates while the polystyrene beads are used for granular particles. In the benchmark experiment, the final static length and deposit angle (Figure 3.15) were analyzed, and it has been shown that the final granular surface has a linear slope. As shown in Figure 3.16, the DEM model in this study well simulates the time-variant granular flow and surface slope, where $t_c$ and $t_f$ are characteristic time ($\sqrt{h/g}$) and final state time, respectively.

Table 3.1. DEM Contact Force Model

| | | |
|---|---|---|
| Linear Contact Force Model | | |
| $f_{spring}^{n} = k_n \delta_n$ | $k_n = 0.094 {E_{ab}}^{*} {R_{ab}}^{*}$ | Misra (1999) |
| Hertz Mindlin Contact Force Model | | |
| $f_{spring}^{n} = k_n {\delta_n}^{3/2}$ | $k_n = \frac{4}{3} {E_{ab}}^{*} \sqrt{{R_{ab}}^{*}}$ | Zhu (2007) |
| JKR Contact Force Model | | |
| $f_{spring}^{n} = k_1 {\delta_n}^{3} - k_2 \sqrt{{\delta_n}^{3}}$ | $k_1 = 4 {E_{ab}}^{*} / (3 {R_{ab}}^{*})$ | Feng (2014) |

Table 3.2. Hertz-Mindlin Contact Force Model

| | |
|---|---|
| Normal Contact Force | |
| $f_{ab}^{n} = f_{spring}^{n} + f_{damper}^{n} = k_n \delta_n - c_n v_n$ | |
| $k_n = \frac{4}{3} E^{*} \sqrt{R^{*} \delta_n}$ | $c_n = \sqrt{\frac{10}{3}} \frac{\ln(e)}{\sqrt{ln(e)^2 + \pi^2}} \sqrt{M^{*} {K'}_n}$ |
| Tangential Contact Force | |
| $f_{ab}^{n} = f_{spring}^{n} + f_{damper}^{n} = k_n \delta_n - c_n v_n$<br>$f_{ab}^{t} = min\left(f_{spring}^{t} + f_{damper}^{t}, -\mu_t \lvert f_{ab}^{n} \hat{n} \rvert\right)$ | |
| $k_t = 8 G^{*} \sqrt{R^{*} \delta_n}$ | $c_s = \sqrt{\frac{10}{3}} \frac{ln(e)}{\sqrt{ln(e)^2 + \pi^2}} \sqrt{M^{*} k_s}$ |

Table 3.3. V&V Simulation Cases for Implemented DEM Model

| **V&V Cases for developed DEM Model** | **Notes** |
|---|---|
| **Single DEM Particle** | |
| Momentum Conservation<br>*Without damping*<br>*Without rotation*<br>*All physics included* | Figure 3.8 |
| Energy Conservation (elastic)<br>*Normal elastic force only*<br>*Tangential elastic force included*<br>*( with rotational energy)* | Figure 3.10 |
| Angular Momentum Conservation<br>*All physics included* | Figure 3.9 |
| **Wall Boundary Treatment** | |
| Wall Collision<br>*Without rotation*<br>*Rotation of DEM particle included* | Figure 3.10 |
| Sliding & Rolling on the Surface<br>*on the flat surface*<br>*on the inclined surface* | Figure 3.11<br>Figure 3.12 |
| 3D Hopper Flow | Figure 3.13 |
| **Granular Flow** | |
| Granular Collapse of Spherical Particles | Figure 3.16 |

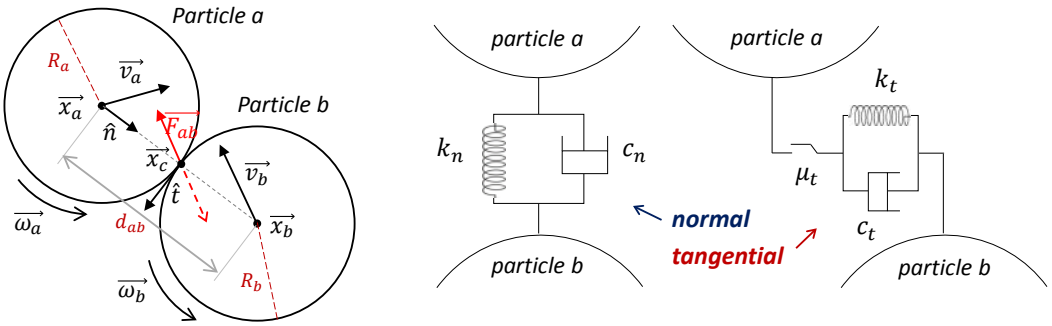


Figure 3.1. Spring-Dashpot System of Soft-Sphere Collision Model

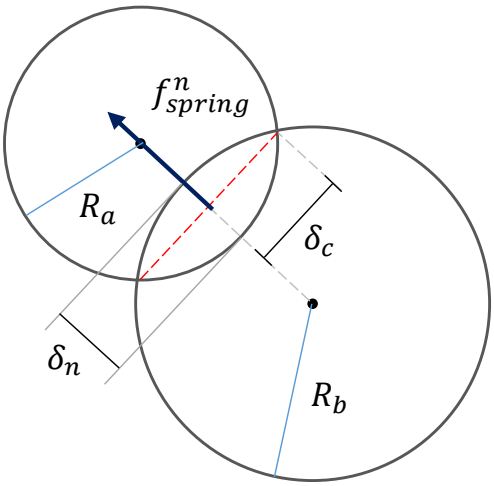


Figure 3.2. Inter-particle Collision in Soft-Sphere Model

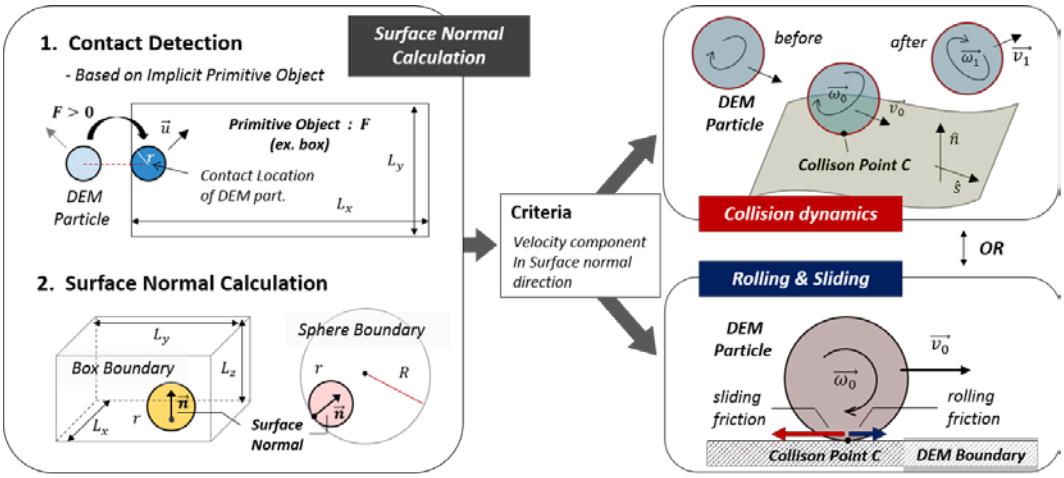


Figure 3.3. Versatile Wall Boundary Treatment Model in This Study

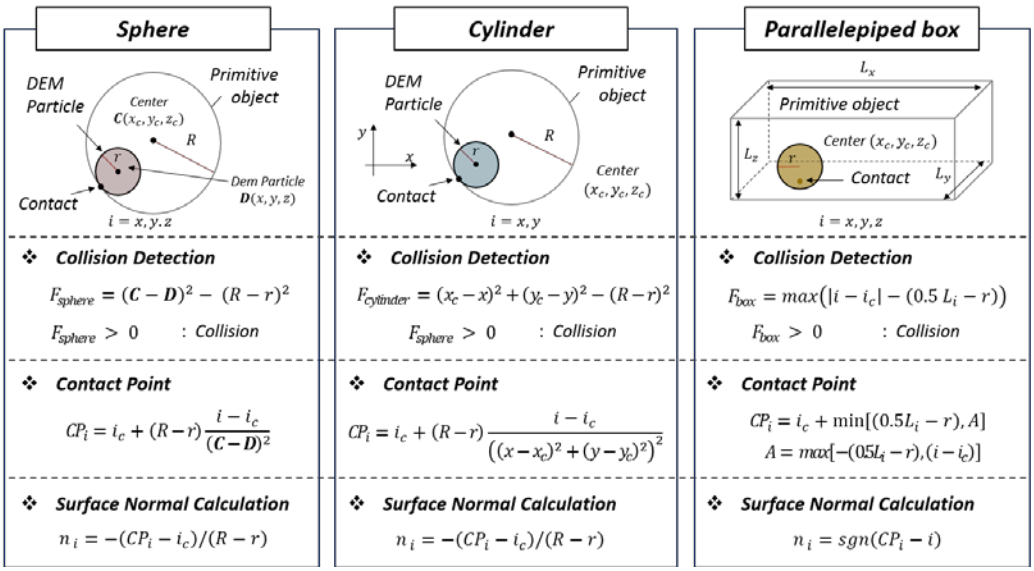


Figure 3.4. Implicit Primitive Object for DEM Wall Boundary Condition

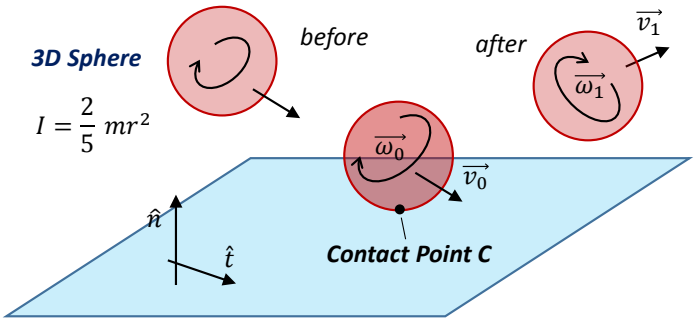


Figure 3.5. Particle Collision with Wall Boundary

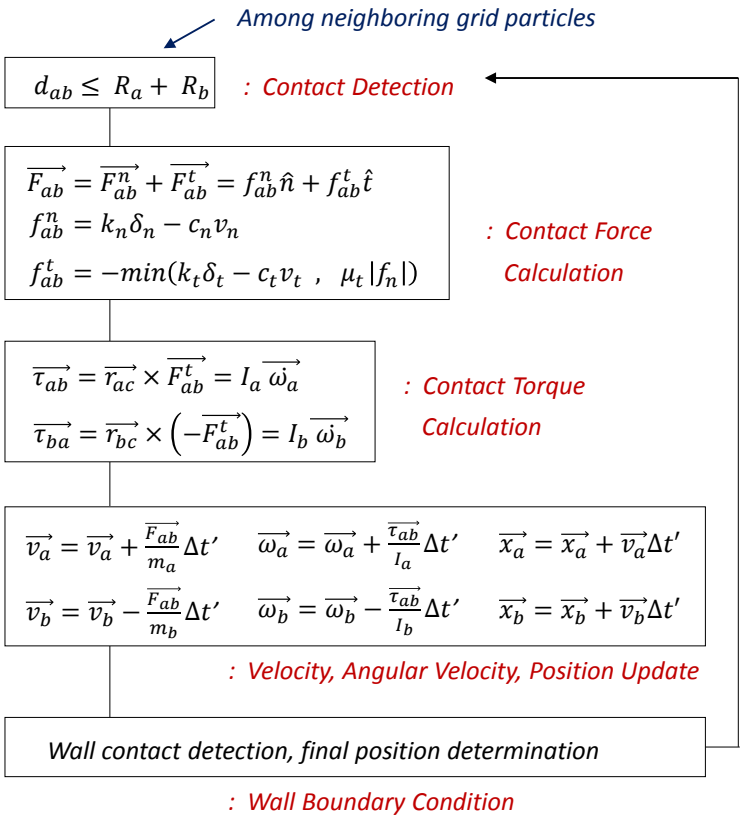


Figure 3.6. Algorithm of Implemented DEM Model

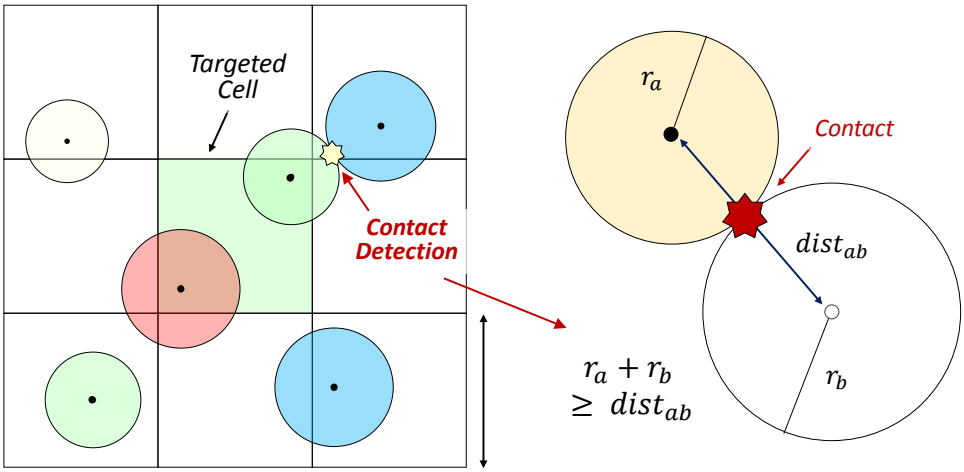


Figure 3.7. Grid-Based Contact Detection

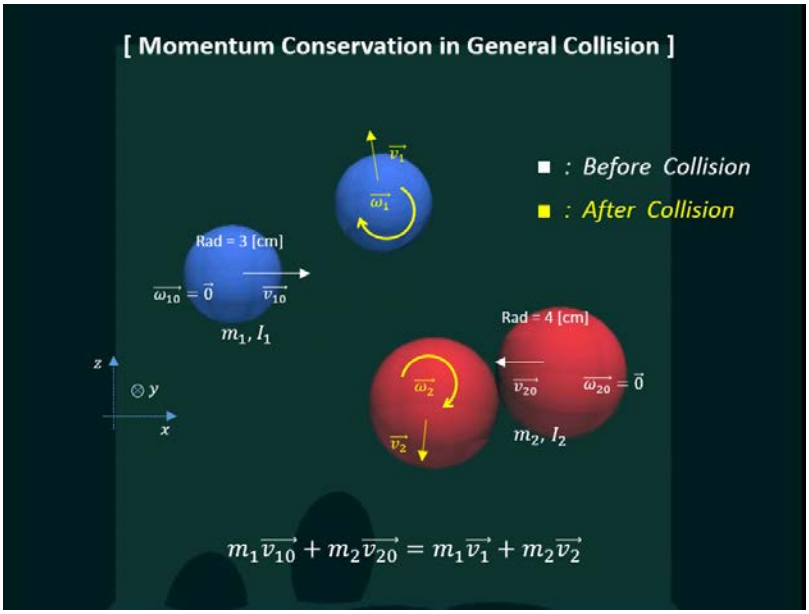


Figure 3.8. Conservation of Linear Momentum in Collision

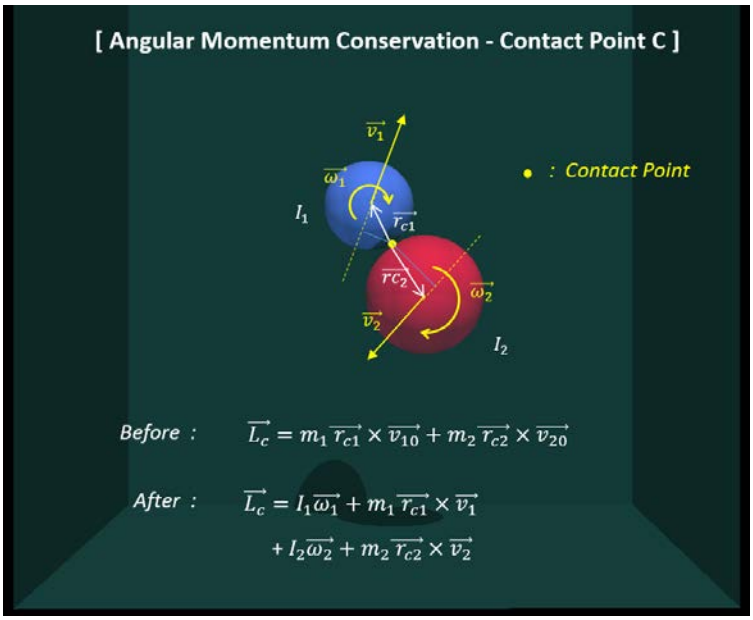


Figure 3.9. Conservation of Angular Momentum in Collision

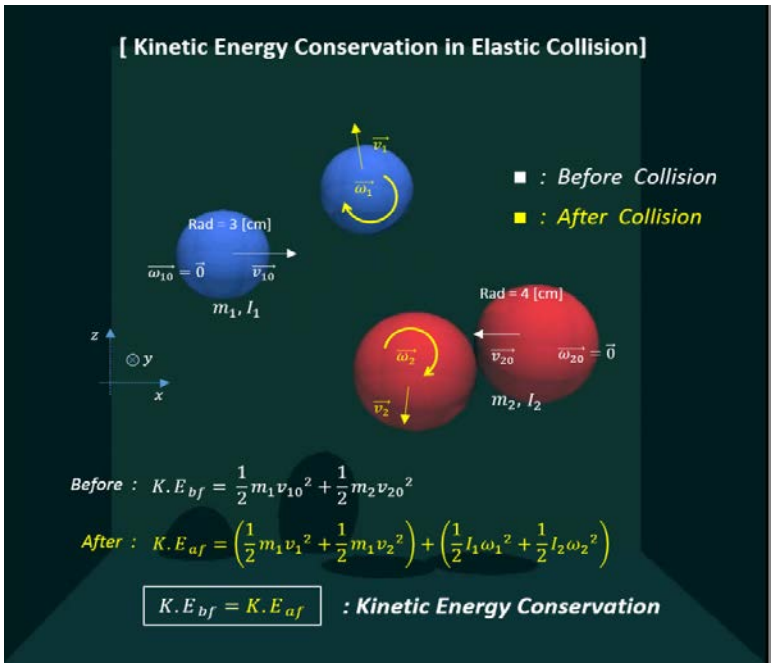


Figure 3.101. Conservation of Kinetic Energy in Elastic Collision

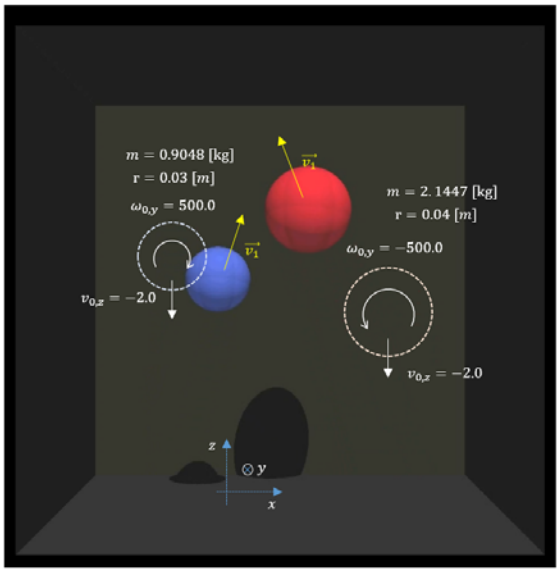


*Conservation of linear momentum, and angular momentum*

$$m\,(\vec{v_1} - \vec{v_0}) = \vec{J} \quad \cdots\cdots\ a$$

$$I\,(\vec{\omega_1} - \vec{\omega_0}) = -r\,\hat{n} \times \vec{J} \quad \cdots\cdots\ b$$

***[ Particle 1 ]*** *– first collision*

$\vec{v_0} = (0, 0, -2.0)$ $\quad \vec{v_1} = (0.4286, 0, 1.8)$

$\vec{\omega_0} = (0, 500.0, 0)$ $\quad \boxed{\vec{\omega_1} = (\mathbf{0, 464.586, 0})}$

*From eqn a,* $\vec{J} = m(\vec{v_1} - \vec{v_0}) = (0.3878, 0, 3.438)$

$\therefore\ \hat{n} \times \vec{J} = (0, 0.3878, 0)$

*Substitute to eqn b,*

$$\vec{\omega_1} = \vec{\omega_0} - \frac{r}{I}(\hat{n} \times \vec{J}) = \boxed{(\mathbf{0, 464.583, 0})}$$

Figure 3.11. Wall Collision of Rotating Sphere

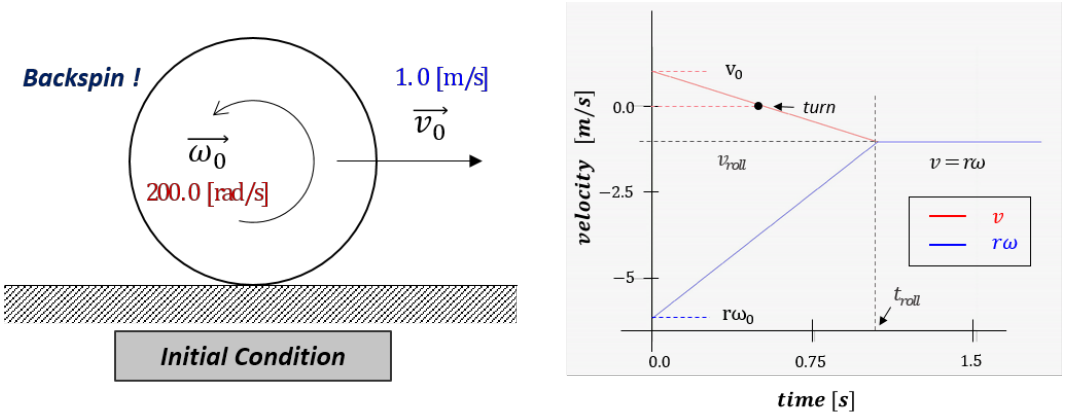


Figure 3.12. Sliding and Rolling of Spherical Particle on the Wall boundary

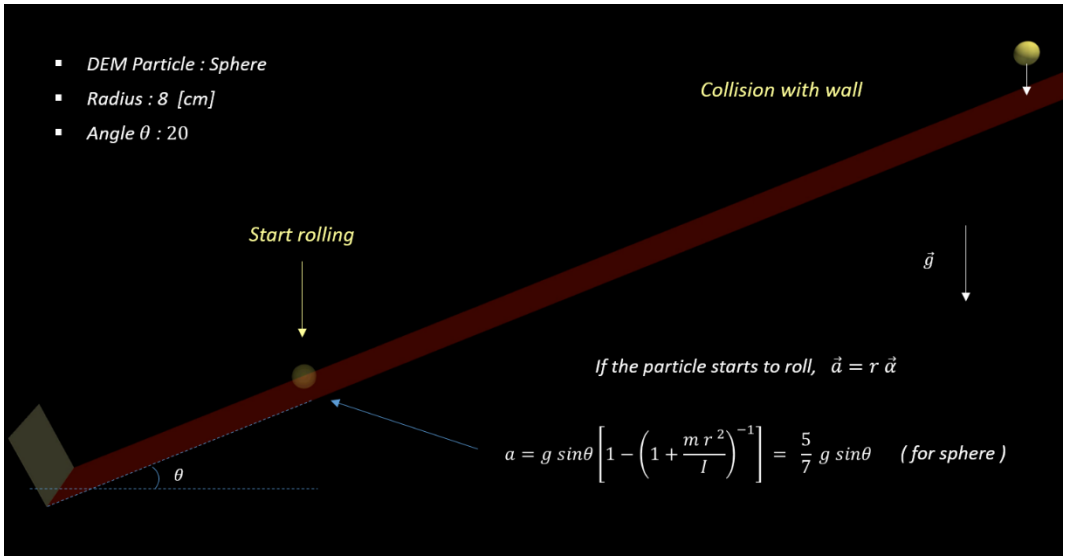


Figure 3.13. Descending Behavior of the Sphere on Slope

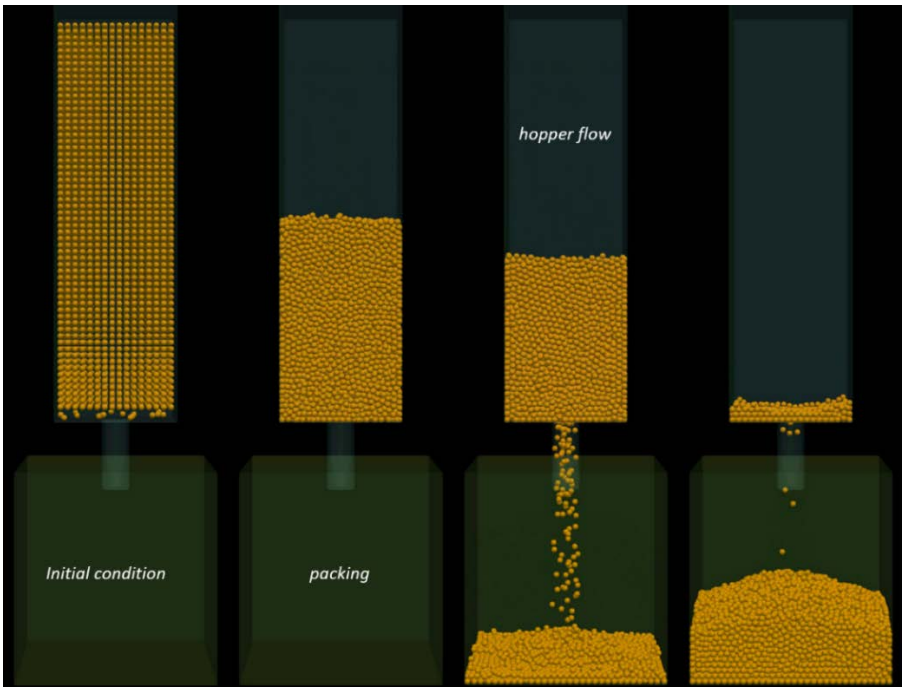


Figure 3.14. 3D Hopper Flow Simulation

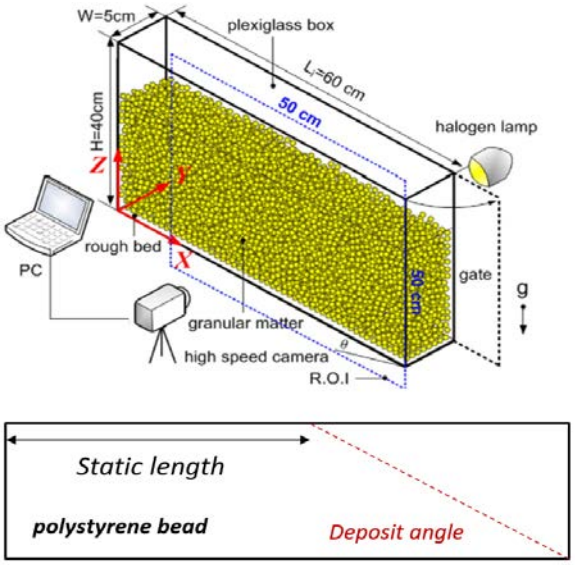


Figure 3.15. Benchmark Experimental Setup for Granular Collapse Behavior [Chou, 2012]

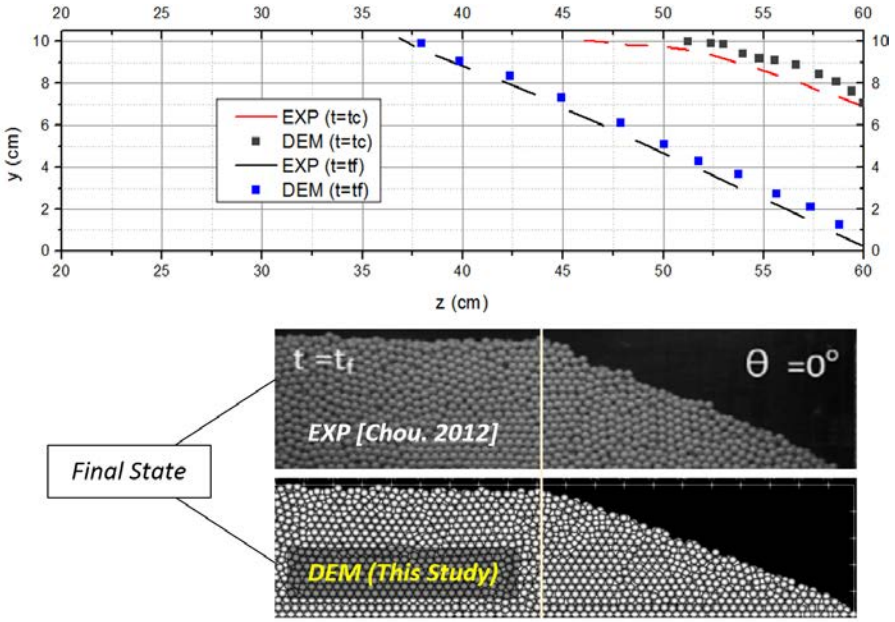


Figure 3.16. DEM Validation Results for Granular Collapse Behavior

# Chapter 4

# Two-Way Phase Coupling of SPH and DEM

In this study, the developed Lagrangian SPH model (Chapter 2) and DEM model (Chapter 3) were coupled in order to deal with the vapor-driven 3-phase behavior of particulate debris particles in the late phase of LWR severe accident. This chapter covers the coupling mechanism between SPH and DEM with the governing equations, the algorithm of the two-way coupled model, and several V&V simulation results as well.

## 4.1 Unresolved Coupling of SPH and DEM

Since the SPH and DEM are both fully Lagrangian-based numerical methods, there are many similarities in solving the governing equations. Thus, the potential in coupling two methods is higher than the coupling of DEM with Eulerian-based CFD methods.

Generally, the approaches for coupling the SPH and DEM can be classified into two groups. One is the resolved method that simulates the behavior of each phase by completely separating the computational domain, and the other is the unresolved method. In the resolved method, the SPH particles are significantly

smaller than the solid particles in order to analyze the flow (streamline) around the solid particles. Since SPH and DEM are based on the same methodology, the feasibility of resolved coupling is potentially high. However, this method is suitable when the behavior of each solid particle or the flow disturbance by a single solid particle is the main focus of simulation. In other words, there are limitations for the resolved coupling method in solving particulate flow, since it requires an extremely high-resolution for SPH particles.

In this respect, the unresolved coupling method of SPH and DEM is effective for particulate debris behavior (sedimentation, sloshing, self-leveling, etc.) where the overall behavior of debris particles is important. The SPH particles are of comparable size of the DEM solid particles, and the locally averaged Navier Stokes equation is solved for the fluid phase since the solid phase and fluid phase overlap the computational domain as shown in Figure 4.1. In addition, the empirical closure correlations (drag coefficient, lift coefficient, etc.) are used to capture the momentum transport between liquid and solid phase, since it is no longer a first principle numerical scheme. The main features of the unresolved coupling method of SPH and DEM are outlined below.

- Overlap b/w SPH and DEM Particles
- Locally Averaged N-S Equation (Two-Fluid Model)
- Empirical Closure Equations (ex. Drag Force)
- SPH Particle Size ~ DEM Particle Size
- Large Number of DEM Particles
- Efficient for Particulate Flow (Granular Flow)

## 4.2 Governing Equations

As described in the previous section, the locally averaged Navier-Stokes equation is solved for the fluid phase (SPH), which is slightly different from the SPH governing equations in Chapter 2. Considering this, the unresolved coupling sequence of SPH and DEM can be divided into the following three steps.

a. Solving locally averaged N-S equation
b. Solving coupling force acting on DEM particles
c. Solving the reaction force for SPH particles (Two-way Coupling)

The following sub-sections describe the governing equations for the above three steps.

### 4.2.1 SPH Particles: Locally Averaged N-S Equations

The fluid phase (SPH) is governed by a locally averaged Navier Stokes equation for an incompressible fluid. The corresponding momentum equation can be written in the Lagrangian description as below,

$$\rho_f \frac{\partial(\varepsilon \boldsymbol{u_f})}{\partial t} = -\varepsilon \nabla \mathrm{P} + \mu_f \nabla \cdot (\varepsilon \nabla \boldsymbol{u_f}) + \varepsilon \rho_f \boldsymbol{g} + \boldsymbol{S_f} \qquad (4.1)$$

where ε is the volume fraction of fluid f, $\rho_f$ and $\mu_f$ are the density and dynamic viscosity of a fluid, respectively. Also, the momentum exchange term $S_f$ is the reaction force by adjacent DEM particles, which is discussed in detail in a later section (Chapter 4.2.3).

Before discretization of the above equation (4.1) into the SPH form, the definition of the local porosity of SPH particles is required. The local porosity of fluid SPH particle $i$ is calculated by summation over neighboring DEM particles within a coupling length $h_c$. The detailed expression is as follow,

$$\varepsilon_i = 1 - \left( \sum_b W_{ib}(h_c) V_b \Big/ \sum_j W_{ij}(h_c) V_j \right) \tag{4.2}$$

where subscript i, j denote targeted SPH particle and neighboring SPH particles, respectively, while subscript b refers to the neighboring DEM particles. $W$ is the kernel weighting function between particles, and V is the volume of the particles. Taking the local porosity into account, the discretized summation form of the above governing equation (4.1) can be written as below,

$$\left(\frac{d\boldsymbol{u}}{dt}\right)_i = -\sum_j \overline{m_j} \left[ \frac{P_i}{\bar{\rho}_i^{\,2}} + \frac{P_j}{\bar{\rho}_j^{\,2}} \right] \nabla_i W_{ij} + \bar{\rho}_i \boldsymbol{g} + \boldsymbol{S_i} \tag{4.3}$$

where $\bar{\rho}$ denotes for the superficial fluid density, which is defined as $\bar{\rho} = \varepsilon\rho$, and $\overline{m}$ refers to the corresponding mass of the fluid particle. In the above equation (4.3), the volume of SPH particles is constant during simulation, since

the mass used in equation (4.3) is also changes as a function of local porosity. This approach is suitable when heavier DEM particles are submerged in the fluid throughout the simulation. However, if the DEM particles enter or exit the fluid area during the simulation, the above governing equation (4.3) should be modified as follow,

$$\left(\frac{d\boldsymbol{u}}{dt}\right)_i = -\sum_j m_j \left[\frac{P_i}{\bar{\rho}_i^{\,2}} + \frac{P_j}{\bar{\rho}_j^{\,2}}\right] \nabla_i W_{ij} + \bar{\rho}_i \boldsymbol{g} + \boldsymbol{S_i} \qquad (4.4)$$

Where constant mass is used instead of $\overline{m_j}$. In this case, SPH particles near DEM particles expand in volume according to their local porosity, and as a result, the total volume of the fluid region is increased by the volume of the submerged DEM particles. Since the volume of SPH particles is variable in this case, a conservative setting for coupling length ($h_c$), or an advanced model for adaptive smoothing length is required.

### 4.2.2 DEM Particles: Coupling Forces Acting on Solid Particles

There are various interaction forces acting on the solid phase including drag force, lift force, virtual mass force, and also non-contact force such as the Van der Waals force. However, in external flow without additional acceleration of the solid particle, the effects of lift force or added mass force are negligible. Thus, only drag force and pressure gradient force (buoyancy force) are taken into account in coupling interaction as dominant driving forces of solid particles.

The force acting on each solid particle by the fluid can be written as below,

$$\boldsymbol{F_a = F_a^P + F_a^D} \tag{4.5}$$

where superscript P and D denote for pressure-gradient and drag, respectively. The first term of the above equation models pressure gradient force, which reduces to the buoyancy force in hydrostatic equilibrium, while the second term in RHS refers to the drag force. The pressure gradient force is the interaction force that the solid particles receive from the pressure field developed by the fluid. Therefore, the pressure gradient force of the DEM particle is calculated by weight averaging the pressure gradient of the neighboring SPH particles ($\boldsymbol{\vartheta}$) as follows [He, 2018] [Robinson, 2013],

$$\boldsymbol{F_a^P} = V_i \sum_j \frac{m_j}{\rho_j} \boldsymbol{\vartheta_j} W_{aj} / \sum_j \frac{m_j}{\rho_j} W_{aj} \tag{4.6}$$

$$\boldsymbol{\vartheta_i} = -\bar{\rho}_i \sum_j \overline{m_J} \left[ \frac{P_i}{\bar{\rho}_i^{\,2}} + \frac{P_j}{\bar{\rho}_J^{\,2}} \right] \nabla_i W_{ij} \tag{4.7}$$

The drag force $\boldsymbol{F_a^D}$ in the above equation (4.5) depends on the local porosity and relative velocity between fluid and particle. Since the behavior of particulate solid debris (ex. Self-leveling) is a granular flow with low porosity, a suitable drag force model should be used for this kind of dense particulate flow. For the dense particulate flow with multiple particles, the drag law can be generalized to,

$$F_a^D = \frac{1}{8} C_d \rho_f \pi d^2 |\boldsymbol{u_{ja}}| \boldsymbol{u_{ja}} f(\varepsilon) \tag{4.8}$$

Where $C_d$ and $\boldsymbol{u_{ja}}$ denote for the general drag coefficient and relative velocity of solid particles, respectively, and $f(\varepsilon)$ is the correction factor taken from Di Felice (1994) which is used to account for the behavior of packed particles. The correction factor in the packed spheres can be written as follows [Di Felice, 1994] [Epstein, 2005],

$$f(\varepsilon) = \varepsilon^{2-\xi} \tag{4.9}$$

$$\xi = 4.7 - 0.65\ exp\left[-\frac{\left(1.5 - \log_{10} Re_p\right)^2}{2}\right] \tag{4.10}$$

where $Re_p$ is Reynolds number for the fluid flow through a bed where the superficial velocity $\varepsilon|\boldsymbol{u_{ja}}|$ is used for the calculation.

$$Re_p = \frac{\rho_f d_p \left(\varepsilon |\boldsymbol{u_{ja}}|\right)}{\mu_f} \tag{4.11}$$

### 4.2.3 SPH Particles: Reaction Force from Momentum Exchange

In a dense particulate flow with a sufficiently large number of solid particles, the reaction force should not be neglected since the presence of solid particles also greatly affects the fluid flow. The rate of momentum exchange ($\boldsymbol{S_i}$) in the

above equation (4.1) and (4.3) can be calculated by a weighted average of coupling force acting on the surrounding DEM particles, as shown in Figure 4.2. Specifically, the coupling force of DEM particle b is given to the SPH particles within the coupling length, and for each SPH particle, these interaction forces received from the DEM particles within the coupling length is added as follow,

$$\boldsymbol{S_i} = -\frac{1}{\bar{\rho}_i}\sum_b \frac{1}{\sum_{j'}\frac{m_{j'}}{\rho_{j'}}W_{bj'}}\boldsymbol{F_b}\,W_{ib} \tag{4.12}$$

where subscript $i, b,$ and $j'$ refer to targeted SPH particle, neighboring DEM particles, and neighboring SPH particles for DEM particle b, respectively. By applying the above equation to equations (4.1) and (4.3), Newton's third law of motion is satisfied. The importance of momentum exchange term is highlighted in the validation section of SPH-DEM phase coupled model (Chapter 4.4).

## 4.3 Algorithm of SPH-DEM Coupled Model

In general CFD-DEM coupling, the step size of time integration required in the DEM model is an order of $10^{-6}$, which is much smaller than that of the CFD model. Thus, the algorithms of CFD and DEM are separate, and the coupling of two models is performed based on the time step size of CFD calculation. However, since the SPH model implemented for the fluid phase in this study is a fully explicit Lagrangian-based CFD method, there is a limit on the step size of time integration. Besides, if the vapor phase is considered in coupled simulation, the required time step size in SPH calculation becomes similar to that of the DEM

model. For this reason, the SPH-DEM phase coupled model implemented in this study performs SPH calculation and DEM calculation within the same algorithm as shown in Figure 4.3. In addition, nearest neighboring particles searching (NNPS) in SPH and contact detection in DEM model are both performed in cell-based, and mutual search in the coupling step (within coupling length) is also conducted based on the grid, as shown in Figure 4.4. The simplified algorithm of theSPH-DEM coupled model is as follows, and also shown in Figure 4.3.

(1) Start & Initialization
(2) Nearest Neighboring Particles Searching (NNPS) – SPH
(3) Contact Detection – DEM
(4) Density, Pressure Estimation – SPH
(5) Momentum Equation – SPH
(6) Inter-particle Collision – DEM
(7) SPH-DEM Coupling Force 1 – DEM
(8) SPH-DEM Coupling Force 2 – SPH (reaction to (7))
(9) DEM Wall Boundary Condition
(10) Time Integration

## 4.4 V&V Simulations for SPH-DEM Coupled Model

The V&V of the implemented SPH-DEM coupled model has been conducted in the following three steps.

a. Single DEM particle behavior in liquid
b. Granular particle flow behavior in liquid
c. Granular particle flow behavior in multi-phase fluid (i.e. 3-phase)

This chapter only covers the simulations of liquid-solid two-phase (a and b above), and the validation for 3-phase flow including vapor phase (c) is described in detail in Chapter 6 (vapor-driven self-leveling behavior of particulate solid debris).

### 4.4.1 Single DEM Particle Behavior

The behavior of a single DEM particle was analyzed in order to verify the coupling forces acting on a DEM particle (above equation 4.6 and 4.8). First, for the verification of the pressure gradient force term (equation 4.6), the behavior of a single solid particle was simulated by assuming a hypothetical situation without drag force (Figure 4.5). The lighter DEM particle float under buoyancy force in the liquid region, and fall off again in the outer region by gravity force. Since both gravity force and pressure gradient force (buoyancy force) are conservative forces, the mechanical energy of the system is conserved, resulting in an oscillating behavior of the DEM particle. As shown in Figure 4.6, the physical properties of oscillation (gradient, amplitude, etc.) were quantitatively well verified.

When a DEM particle with the same physical properties is dropped on a liquid with a drag (Figure 4.7), the damped oscillation of DEM particle was observed due to the energy dissipation by drag force (Figure 4.8). In this case, the

penetration depth of the DEM particle well matched with the results calculated from the analytic equation below, as shown in Figure 4.8.

$$m_p\ddot{\boldsymbol{z}} = -m_p\boldsymbol{g} + m_p\frac{\rho_f}{\rho_p}\boldsymbol{g} - \frac{\rho_f|\dot{\boldsymbol{z}}|}{2}C_d\left(\frac{\pi {d_p}^2}{4}\right)\dot{\boldsymbol{z}} \tag{4.13}$$

In addition, the terminal velocity behavior of a single DEM particle was simulated for overall verification of the coupling force including pressure gradient force and drag force. The time variation of the velocity of the DEM particle was in good agreement with the results calculated from the theoretically derived equations (equation 4.13), as shown in Figure 4.9. In this case, the one-way phase coupling was applied, in which only a solid DEM particle receives the forces from neighboring SPH particles without momentum exchange.

However, the practical drag coefficient correlation is derived from the experimental results which essentially involves the momentum exchange, and the SPH-DEM phase coupling in this study should be also done in two-way in order to satisfy the momentum conservation law. Since the relative velocity between solid and fluid is determined from the velocity distribution of SPH particles within the coupling domain (equation (4.8)), it is necessary to evaluate the validity of the drag coefficient correlations depending on the coupling length($\Delta x_c$). In SPH-DEM two-way coupling in this study, coupling length $\Delta x_c$ is at least 6 times larger than the DEM particle diameter. In other words, the relative velocity between solid and fluid is calculated through the interaction with approximately 12 neighboring SPH particles in each dimension. According to the sensitivity study on coupling resolution for the single-particle terminal velocity

behavior (Figure 4.10), it was found that there was little difference in the simulation results between one-way coupling and two-way coupling when sufficient coupling length was guaranteed. On the other hand, if the coupling length is insufficient as shown in the right case in Figure 4.10, the application of the drag coefficient correlation is inappropriate, and a more fundamental coupling algorithm (resolved method) between SPH and DEM is required.

### 4.4.2 Pressure Drop through Packed Bed

In the late phase of PWR severe accident, the massive corium might release out of the reactor pressure vessel (RPV) and falls down to the ex-vessel coolant forming the melt jet if the In-Vessel Retention (IVR) strategy fails. Based on the assumption that the ex-vessel pool is sufficiently deep, the melt jet can be fragmented into debris particles and sediment on the concrete to form a debris bed. In order to demonstrate the feasibility of the SPH-DEM coupled model on debris bed cooling behavior, the basic pressure drop simulation the packed bed was performed as a validation case. In the SPH-DEM coupled model in this study, the flow resistance through the packed bed is estimated in two steps as follows.

a. DEM Particles: Calculate the drag force acting on each solid particle as a function of local porosity (voidage function, equation (4.8))
b. SPH Particles: Calculate the reaction force received by the neighboring solid particles (equation (4.12)).

Assuming that there are $N_{DEM}$ solid particles in the control volume of $V_{SPH}$,

the relationship between $N_{DEM}$ and $V_{SPH}$ can be described as follows,

$$N_{DEM} = \frac{V_{SPH}(1-\varepsilon)}{V_{DEM}} \tag{4.14}$$

where ε is the averaged local porosity in the packed bed region. In this case, total drag force acting on the DEM particles can be expressed as follows,

$$\overrightarrow{F_{Dp}} N_{DEM} = \frac{3}{4d} C_d \rho \left|\overrightarrow{u_{fp}}\right| \overrightarrow{u_{fp}} (1-\varepsilon)\varepsilon^{1-\chi} V_{SPH} \tag{4.15}$$

The above equation (4.15) can be summarized in pressure drop form as follows, where the vector $\boldsymbol{J}$ denotes the relative superficial velocity.

$$-\frac{dP}{dz} = \frac{3}{4d} C_d \rho |\boldsymbol{J}| \boldsymbol{J} (1-\varepsilon)\varepsilon^{-1-\chi} \tag{4.16}$$

Meanwhile, a great number of empirical models were developed for the prediction of single-phase pressure drop in a packed bed. The Ergun equation below is the most widely used semi-empirical model on the frictional pressure drop in porous media, which has been validated through the various type of flow experiments [Ergun, 1952].

$$-\frac{dP}{dz} = \frac{150(1-\varepsilon)^2 \mu}{d^2 \varepsilon^3} \boldsymbol{J} + \frac{1.75(1-\varepsilon)\rho}{d\varepsilon^3} |\boldsymbol{J}| \boldsymbol{J} \tag{4.17}$$

As shown in Figure 4.11, the above two equations (4.16 and 4.17) show similar trends for various solid particle diameters. In short, the drag force model in SPH-DEM coupled model in this study can be applied to various porosity ranges from the single solid particle to porous media, which shows the same tendency with the well-known Ergun equation for the case of paced bed.

Figure 4.12 shows the additional flow resistance in the packed bed region estimated in SPH-DEM coupled simulation, while the Figure 4.11 shows the comparison between the SPH-DEM simulation results and the analytic results of the above two equations (4.16 and 4.17). It can be seen that the pressure drops are increasing with the flowrates, while the pressure drops of 1.5 [mm] solids are higher than that of 6.0 [mm] spheres. The estimated pressure drops in SPH-DEM coupled simulation are well predicted by the analytic results of the Ergun equation.

### 4.4.3 Granular Flow in Liquid: 3D Dam-Break

To validate the SPH-DEM coupled model for granular particulate flow, a solid-liquid two-phase dam break simulation was conducted and compared with the experimental results reported by Sun (2013). This dam-break simulation is a general test case used for validation of CFD-DEM coupled code. The experiment was conducted by filling the water on one side of a rectangular shaped water tank, and removing the gate with a specific velocity, as shown in Figure 4.13. The conditions for the benchmark experiment are summarized below and also shown

in Figure 4.13.

- Tank overall dimensions: $200[\mathrm{mm}] \times 150[\mathrm{mm}] \times 150[\mathrm{mm}]$
- Size of water column: $50[\mathrm{mm}] \times 100[\mathrm{mm}] \times 100[\mathrm{mm}]$
- Moving gate velocity: $0.68\ [\mathrm{m/s}]$

For the solid particle phase, spherical particles are initially packed behind the moving gate. The physical properties and conditions for the particle phase are listed below.

- Density: $2{,}500\ [\mathrm{kg}/m^3]$
- Total mass of solid particles: $200$ [g]
- Young's modulus: $1.0 \times 10^8$ [Pa]
- Restitution coefficient: 0.9
- Friction coefficient: 0.2

In the SPH-DEM coupled simulation, a water column collapse was also triggered by removing the moving plate as in the benchmark experiment. The simulation conditions are summarized below.

- Time step size: $2 \times 10^{-6}$ [s]
- Number of DEM Particles: 7,762
- Number of SPH Particles (including moving gate): 182,716

The qualitative validation results with the experimental snapshots are shown

in Figure 4.14. The SPH-DEM coupled simulation results and experimental snapshots are compared at a time interval of 0.5[s]. The behaviors of both fluid and solid phase in the benchmark experiment are well reproduced in the SPH-DEM coupled simulation in this study.

In addition, for the quantitative validation of the simulation results, the extent of propagation of the leading front of both the fluid phase and solid particle phase is compared with the experimental data. The following non-dimension parameters are defined for the quantitative comparison.

$$x^* = \mathrm{x}/\mathrm{a} \tag{4.14}$$

$$t^* = t'(2g/a)^{0.5} \tag{4.15}$$

where a is the width of the initial water column as shown in Figure 4.10. It can be seen that the simulation results in this study match well with the benchmark experiment as shown in Figure 4.15.

Also, decoupled simulation and one-way coupled simulation were also performed in order to evaluate the effect of two-way coupling between SPH and DEM method. Here, the one-way coupling means that only the DEM particles move under the influence of fluid, while the SPH particles do not get any reaction forces. As shown in Figure 4.16, only the two-way phase coupled model well simulated the real physics, while the one-way coupled simulation over-estimated both the fluid and solid phases. The results of the decoupled simulation and one-way phase coupled simulation were in good agreement with the experimental results of the single fluid dam-breaking motion, as shown in Figure 4.17.

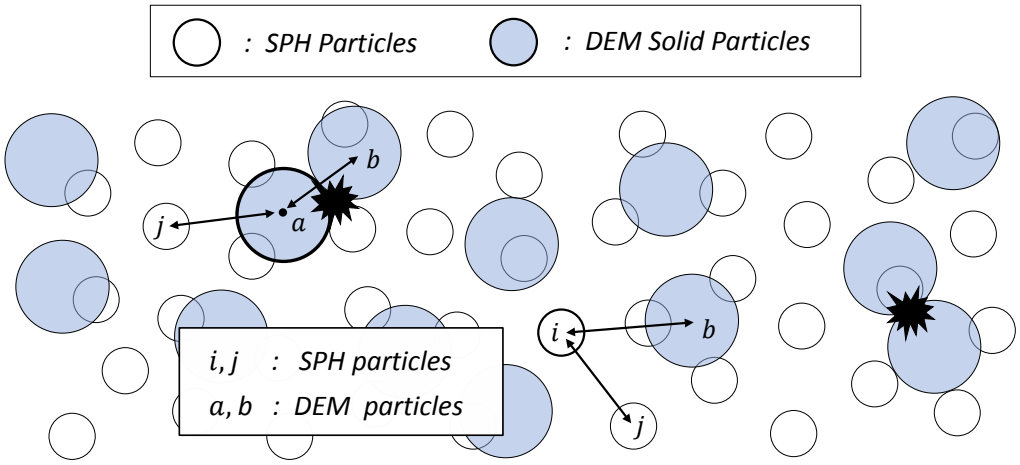


Figure 4.1. Concept of SPH-DEM Unresolved Coupling

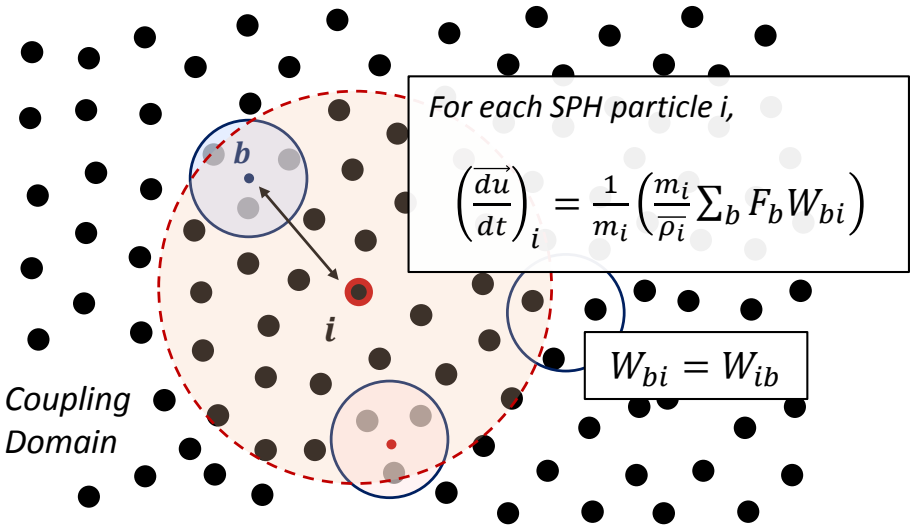


Figure 4.2. Momentum Exchange b/w SPH and DEM Particles

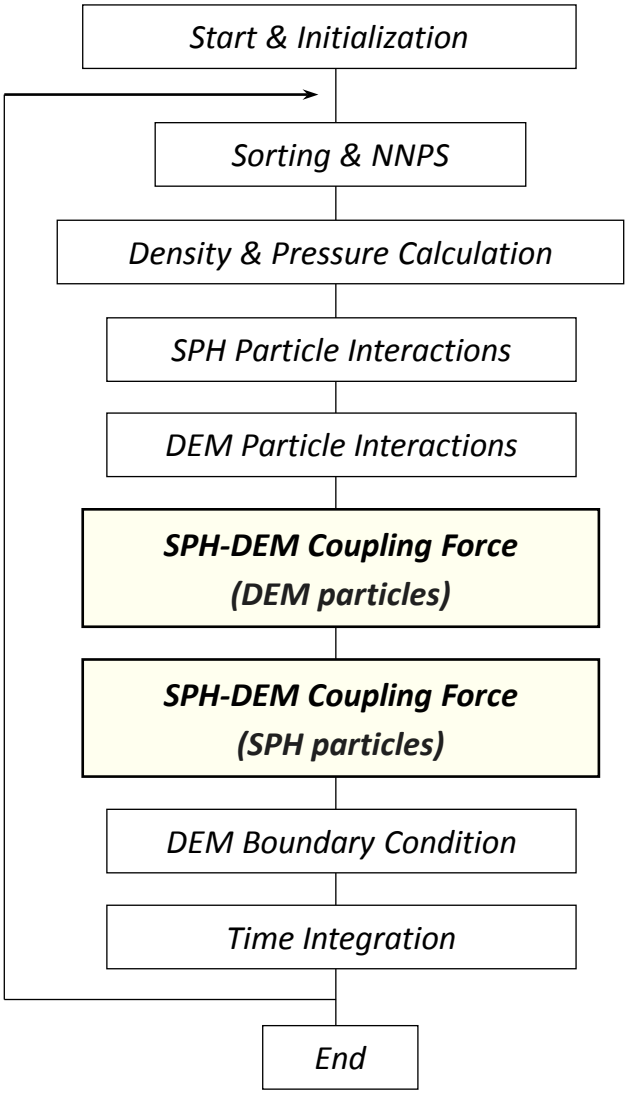


Figure 4.3. Algorithm of SPH-DEM Two-Way Coupled Model

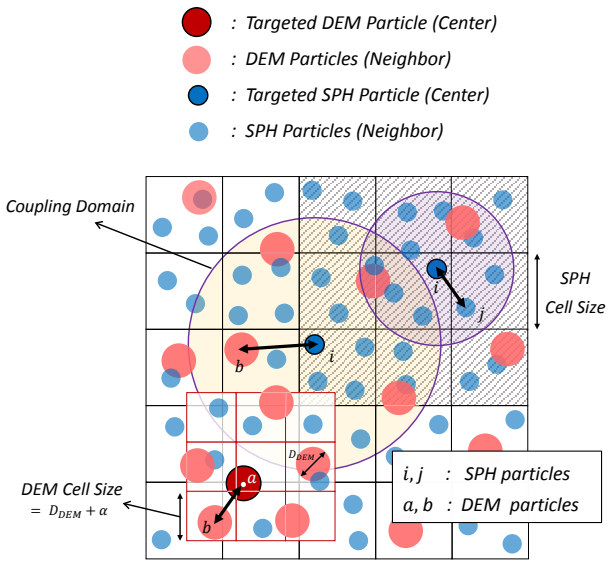


Figure 4.4. NNPS and Contact Detection in SPH-DEM Coupled Model

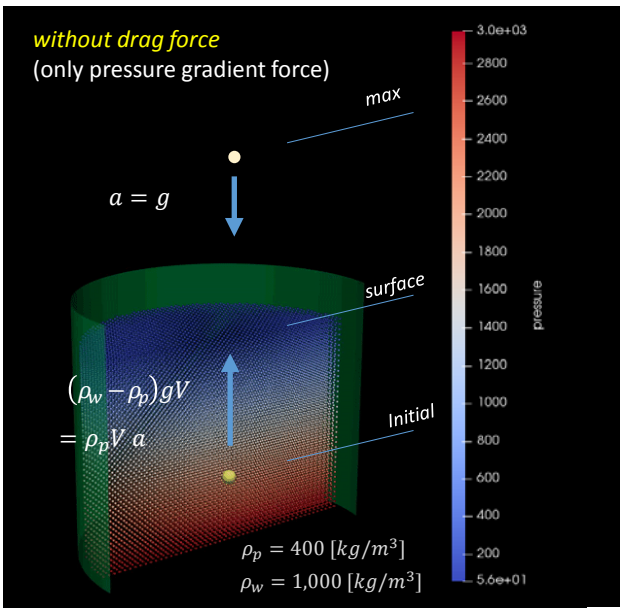


Figure 4.5. Single DEM Particle Behavior without Drag Force

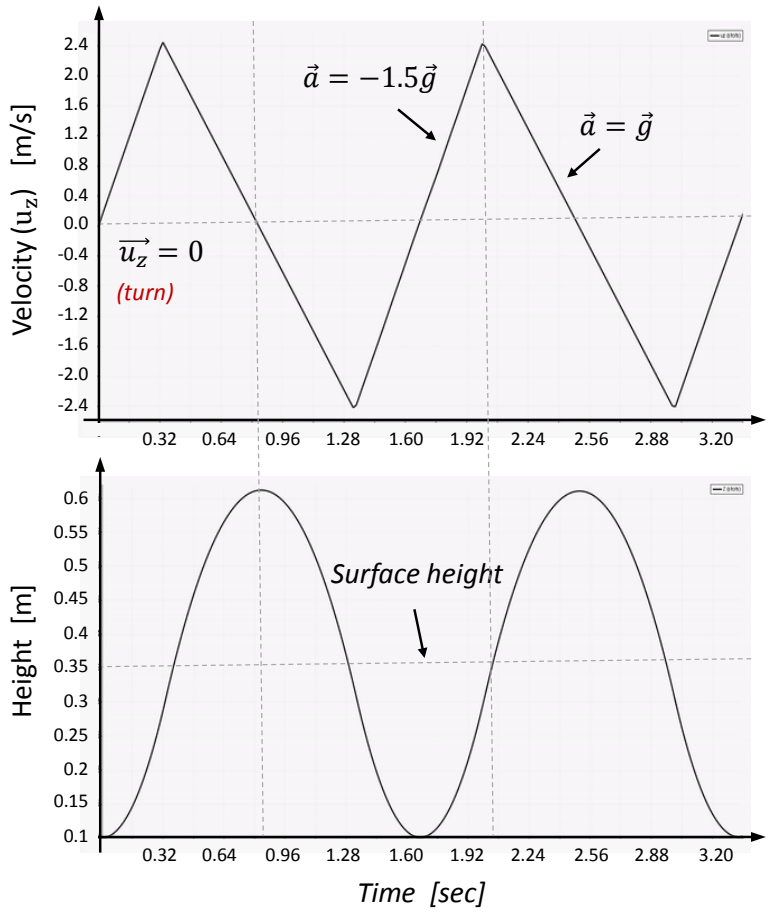


Figure 4.6. DEM Particle Oscillation Due to Gravity and Buoyancy Force

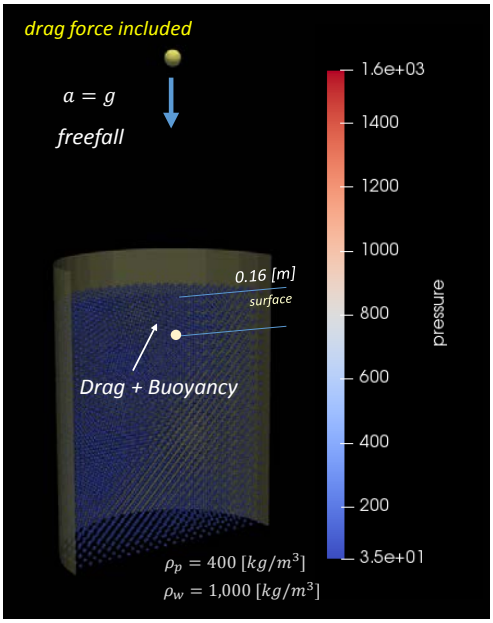


Figure 4.7. Single DEM Particle Freefall (Drag, Buoyancy Force)

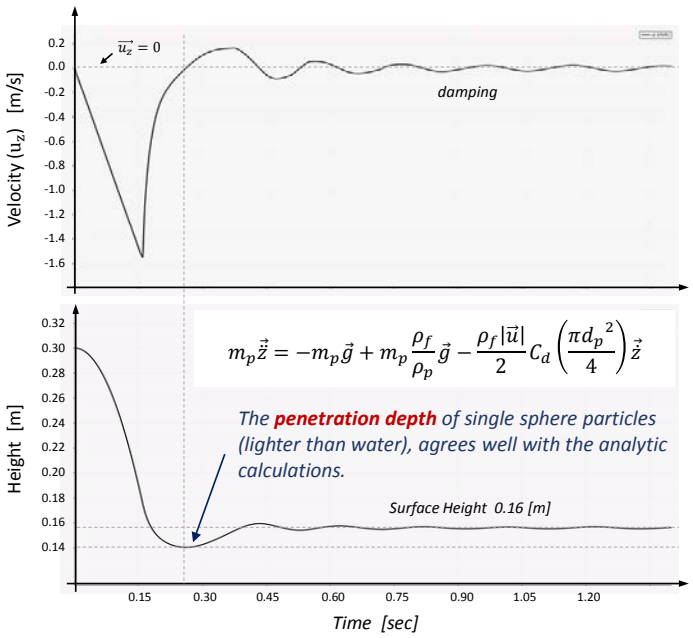


Figure 4.8. Damped Oscillation Due to Energy Dissipation

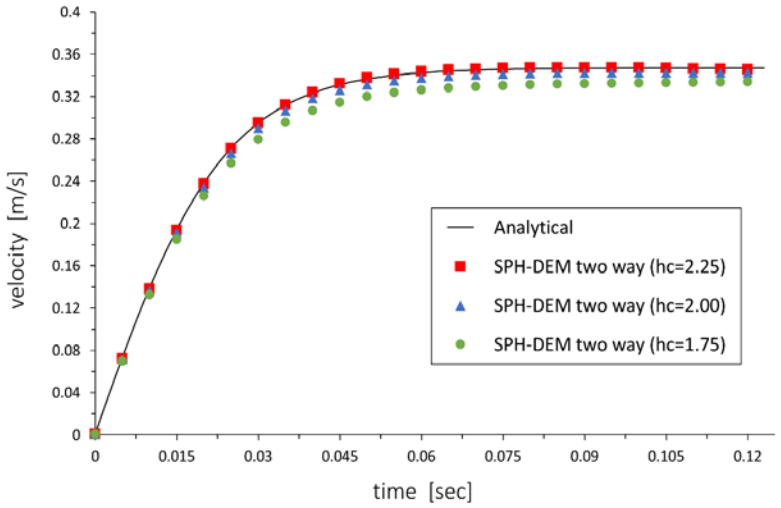


Figure 4.9. Terminal Velocity Behavior of Single DEM Particle

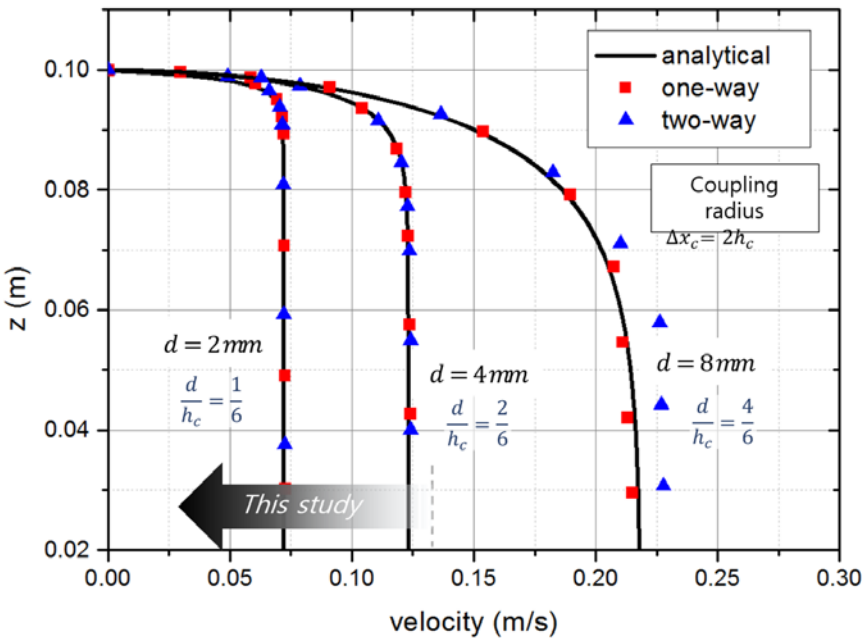


Figure 4.10. Sensitive Study on Coupling Length for Terminal Velocity Behavior

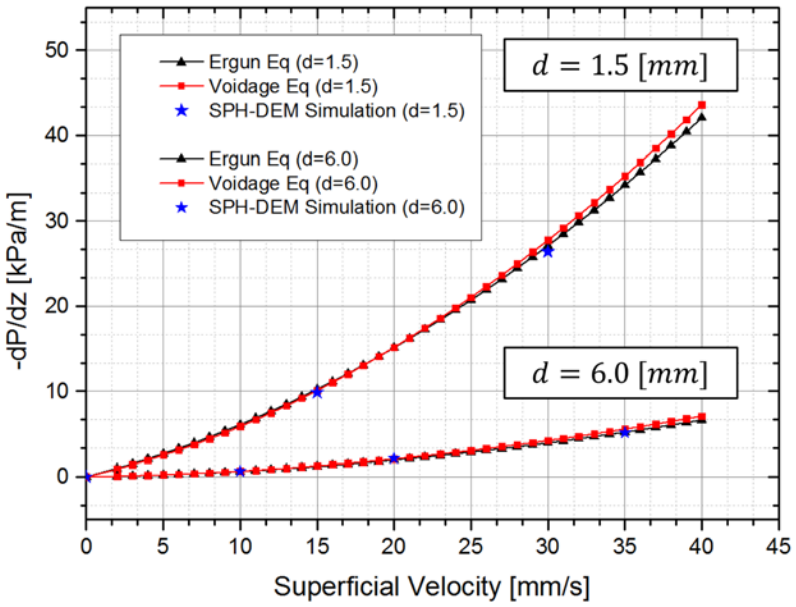


Figure 4.11. Single Phase Pressure Drop through Packed Bed

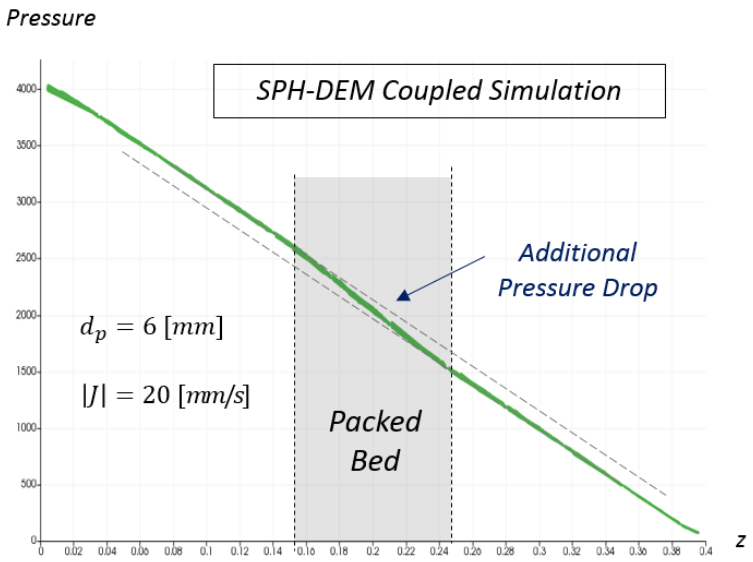


Figure 4.12. Pressure Data of SPH-DEM Phase Coupled Simulation

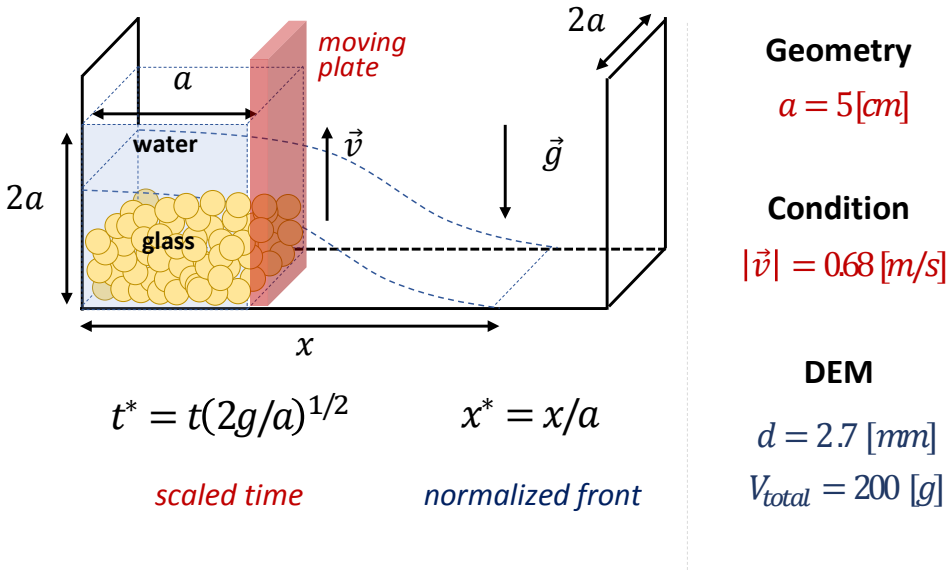


Figure 4.13. Conditions for Solid-Liquid Dam-Break Experiment [Sun, 2013

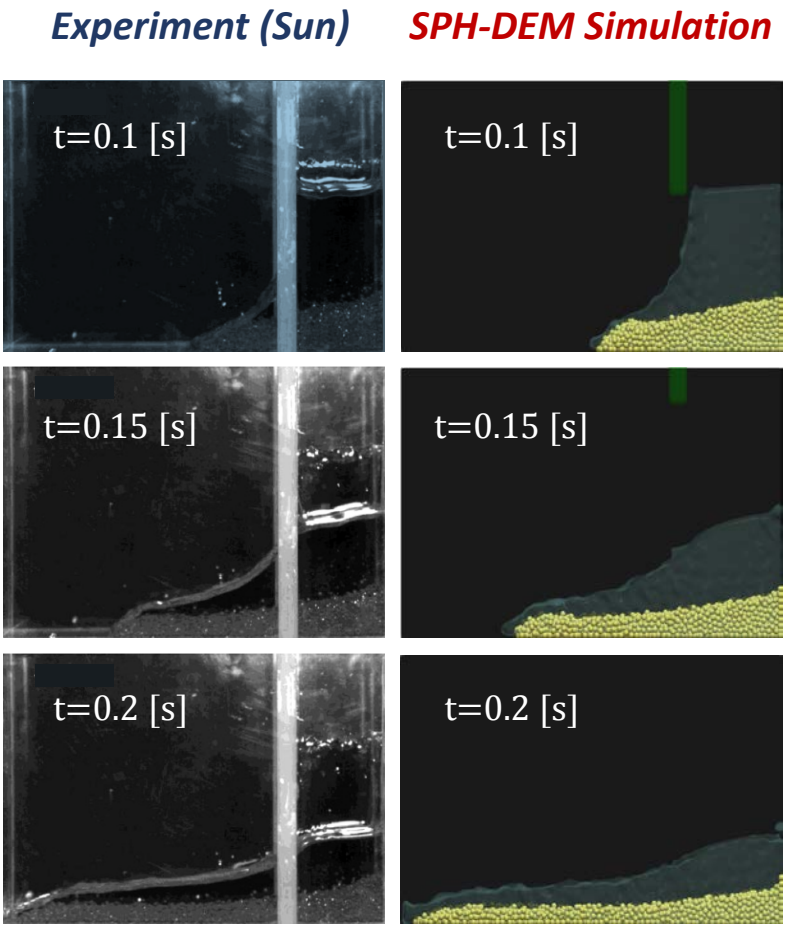


Figure 4.14. Qualitative Results of Solid-Liquid Dam-Break Simulation

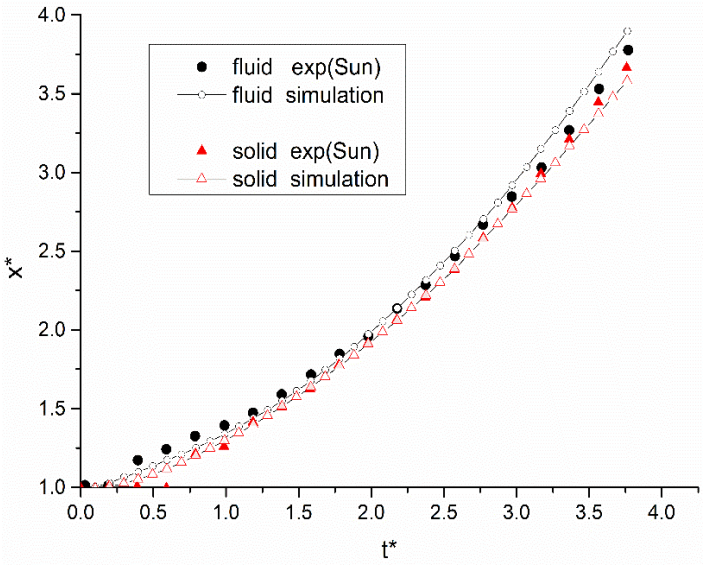


Figure 4.15. Quantitative Validation Result of SPH-DEM Coupled Code

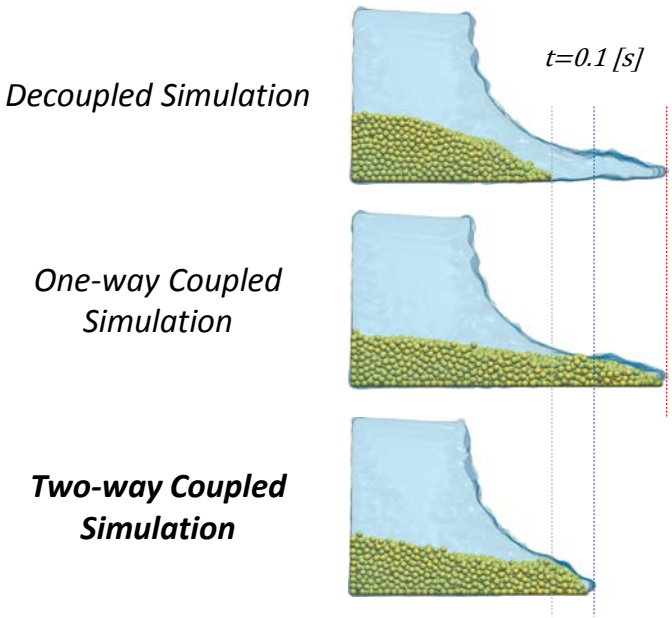


Figure 4.16. Qualitative Comparison Results (decoupled, one-way, two-way)

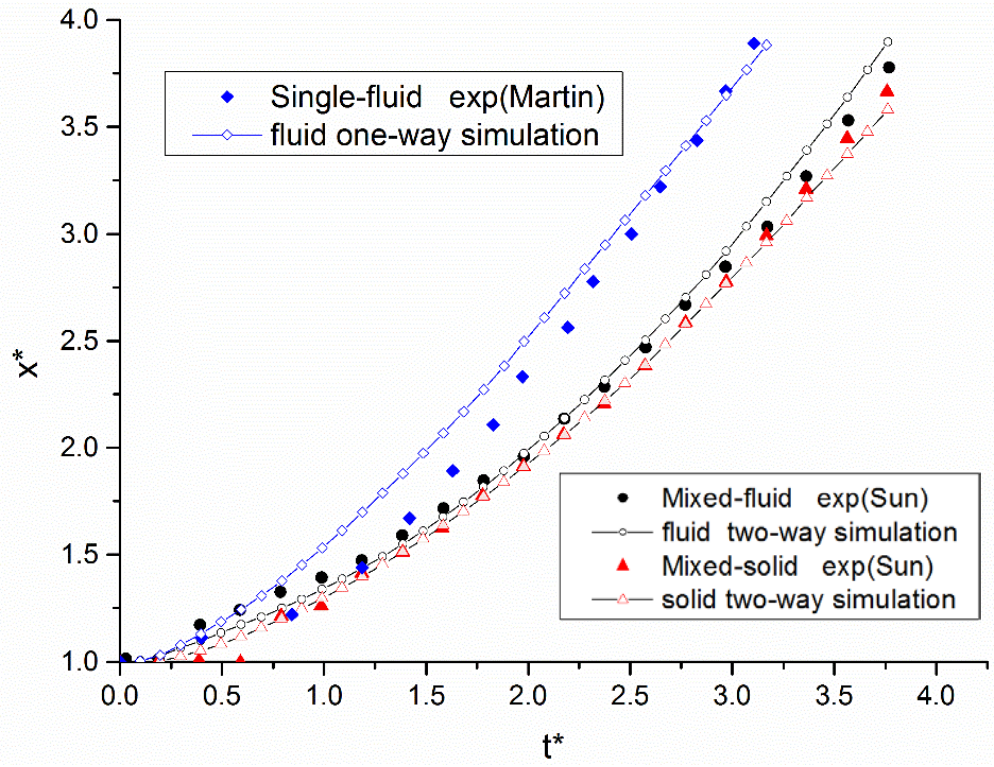


Figure 4.17. Quantitative Comparison Results in Time Variation of Normalized Leading Front (one-way, two-way coupled)

# Chapter 5

# GPU Parallelization of Coupled SPH-DEM Code

The developed SPH-DEM phase coupled model has an essential time step limitation since the SPH and DEM model in this study are both fully explicit numerical methods. Since the accuracy of the simulation in Lagrangian-based numerical methods can be highly affected by the particle resolution, some strategies are required to improve the efficiency of code calculation. Fortunately, solving the governing equations for each SPH particle and DEM particle is relatively easy to parallelize, and can thereby significantly improve the code efficiency through parallelization. (The weakly compressible approach in SPH and the Lagrangian-based governing equations makes parallelization relatively easy by not solving the complex matrix in the model calculation)

The acceleration of the SPH-DEM coupled model was achieved by Graphical Process Unit (GPU) to solve the governing equations of SPH and DEM in parallel for each SPH and DEM particle, rather than to divide the computational area (domain decomposition). The parallelization mechanism of SPH-DEM coupled code and the results of acceleration are described in the sections below.

## 5.1 Parallelization of Governing Equations

### 5.1.1 GPU-based Parallelization

The GPU is a graphic controller developed for large-scale data processing in the computer graphics field. Many commercial architectures, such as OpenCL, ATI Stream, and CUDA C, have been developed. The SPH-DEM coupled code in this study has been parallelized through NVDIA's CUDA architecture, which is the most widely used general-purpose GPU (GPGPU) programing language. Figure 5.1 is a simplified representation of the CUDA memory structure. A block is a unit that acts as a streaming multiprocessor in the GPU memory, and it is composed of shared memory, register, and threads. The shared memory is a space shared by threads in a block, and it is frequently used in data processing in which cooperation among threads is required

### 5.1.2 Parallelization of SPH-DEM Governing Equations

In the calculation of SPH and DEM physical models, one block in Figure 5.1 is mapped to each targeted particle $i$ (SPH) and particle $a$ (DEM), and the threads are assigned to each neighboring particles (SPH) and contact particles (DEM), respectively as shown in Figure 5.2. Similarly, in the calculation of the coupling force between SPH and DEM particles, the neighboring DEM particles for targeted SPH particles and the neighboring SPH particles for targeted DEM particles both are assigned to the treads of each block. Then, each thread stores

the calculated value associated with each neighboring particle (SPH) or contact particle (DEM) in the shared memory, and the summation of each term is performed in the shared memory. In this step, a parallel reduction is carried out, in which the values of the shared memory are summed in parallel while reducing the size of the data by half at every reduction step, as shown in Figure 5.3. Figure 5.4 shows the simplified algorithm of the SPH-DEM coupled code in this study. As shown in the figure, the parallel mapping is applied for most of the particle functions, and the parallel reduction using shared memory is performed in the part for solving the interaction equations with neighboring particles (SPH) or contact particles (DEM).

## 5.2 Parallelization of NNPS and Contact Detection

The SPH method solves the physical models as a form of discretized summation for each neighboring particle, and the DEM method solves the contact forces; therefore, the nearest-neighboring particles search (NNPS hereafter) procedure and contact detection for each SPH and DEM particle must be performed before solving the governing equations for physical models. Generally, the NNPS step and contact detection are the most time-consuming part of the SPH and DEM calculation, respectively, because these procedures should be carried out for each neighboring particle and each contact particle for the targeted center particle. Thus, the performance of the code algorithm highly depends on the efficiency of the NNPS and contact detection procedure.

The NNPS and contact detection of the SPH-DEM coupled code are carried

out based on the rectangular grids as described in Chapter 2 (SPH) and Chapter 3 (DEM). In the SPH-DEM coupled code in this study, a counting sort algorithm is implemented in which particles are rearranged based on the order of each grid index, as described in the previous chapter (Chapter 2). Various GPU parallelization algorithms, including inclusive scanning and atomic add, are applied to all the detailed process of particle sorting. The detailed sequences of the counting sort are as follows.

(1) SPH and DEM particles are assigned to each grid, and the grid index of each particle is determined based on the position, as shown in Figure 5.5(a) and Figure 5.5(b), respectively.
(2) The number of particles belonging to each grid is counted in parallel, using the atomic add function in the CUDA C architecture (Figure 5.5(c)).
(3) The cumulative number summation is carried out with the use of the parallel inclusive scanning method, as shown in Figure 5.5(d).
(4) The starting index at which the particle of each grid stars is obtained.
(5) All of the particles are sorted in grid order based on the starting index and the cell index of each particle, as shown in Figure 5.5(e).

After the above particle sorting is completed, the grid-based NNPS and contact detection are performed also in parallel. The targeted particle is assigned to a block of the CUDA memory, and the adjacent grids of the targeted particle are allocated to the threads of each block, as shown in Figure 5.5. Each thread follows the starting index of grid particles and compares the distance between the grid particles and the targeted particle. Then, each thread determines the neighboring

particles (SPH) or contact particles (DEM) of the targeted particle and saves the index of the particle into the list of neighboring particles of the targeted particle.

## 5.3 Results of GPU Parallelization

### 5.3.1 Speedup in Computation Time

The computation time in the simulation of 3D single-phase dam-break flow was compared before and after the parallelization of developed code. As shown in Figure 5.6, the calculation speed increases by up to 2 orders of magnitude compared to the previous CPU-based code. It can be seen that the effect of code parallelization increases as the number of total particles increases.

### 5.3.2 Parallelization Factors

The degree and efficiency of GPU parallelization were quantified by calculating reference factors such as speedup factor, relative efficiency, and parallelization factor. The speedup factor ($T_1/P_1$) is the ratio of an execution time before parallelization to the execution time after parallelization, which is also written in Figure 5.6 on each number of particles. Since the speedup factor is the function of particle numbers, other factors including relative efficiency, parallelization factor are also the function of particle numbers as summarized in Table 5.1. According to the table, the speedup factor is 157.9 in the case of a

million particles, which means it has been more than 150 times faster than single CPU calculations. In this case, the parallelization factor is also over 0.99, which is enough to expect sufficient performance improvement by parallelization. Also, it can be said that the GPU parallelization is efficient enough since the speedup factor for 3,854 GPU cores reaches 96.3% of the convergence value for the corresponding parallelization factor.

Table 53.1. Parallelization Factors for the Code

| Number of Particles | | $10^3$ | $10^4$ | $10^5$ | $10^6$ |
|---|---|---|---|---|---|
| Speedup Factor ($SF_p$) | $T_1/T_p$ | 36.85 | 77.18 | 117.5 | 157.9 |
| Relative Efficiency | $SF_p/p$ | 0.0103 | 0.0215 | 0.0328 | 0.0440 |
| Parallelization Factor (Amdahl's Law) | $\left(1-\frac{1}{SF_p}\right) * p/(p-1)$ | 0.9731 | 0.9873 | 0.9918 | 0.9939 |

- $T_1$: number of processors (3,584 CUDA cores for GeForce GTX 1080 Ti)
- $T_1$: execution time for one processor (one single CPU in this case)
- $T_p$: execution time for p processors (multi-core GPU)

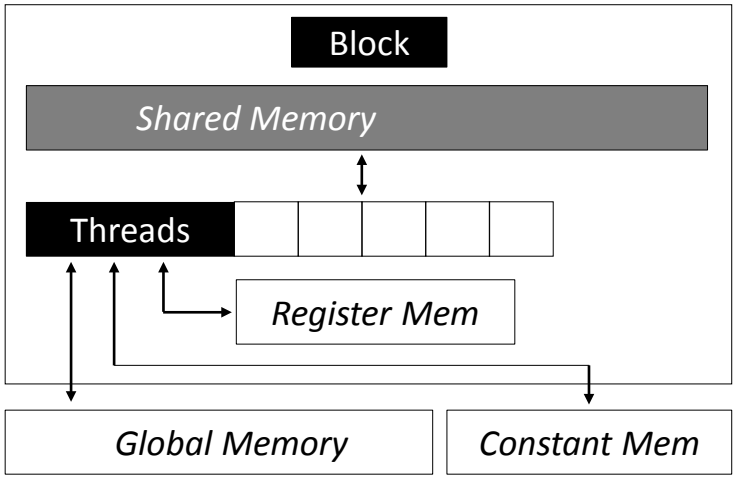


Figure 5.1. Memory Structure of CUDA

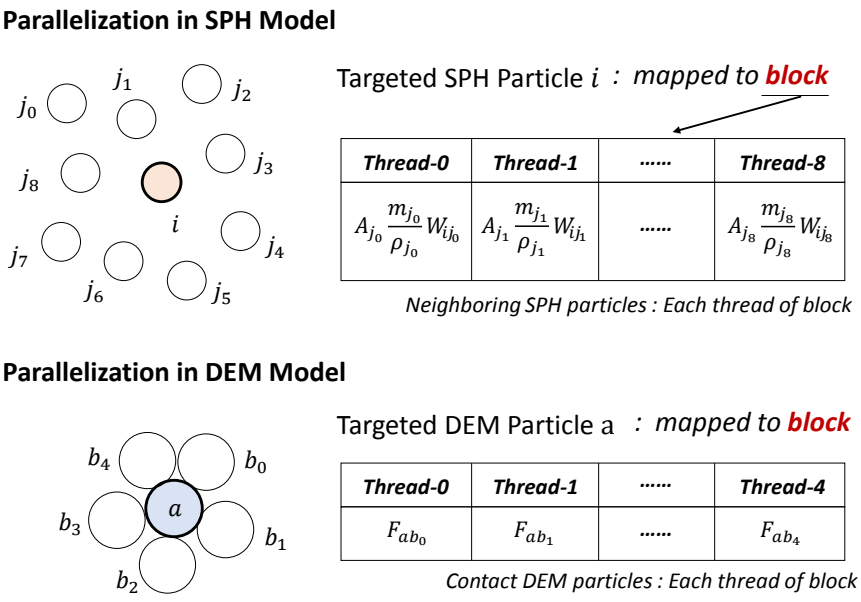


Figure 5.2. Conceptual Description of GPU-based Parallelization of Code

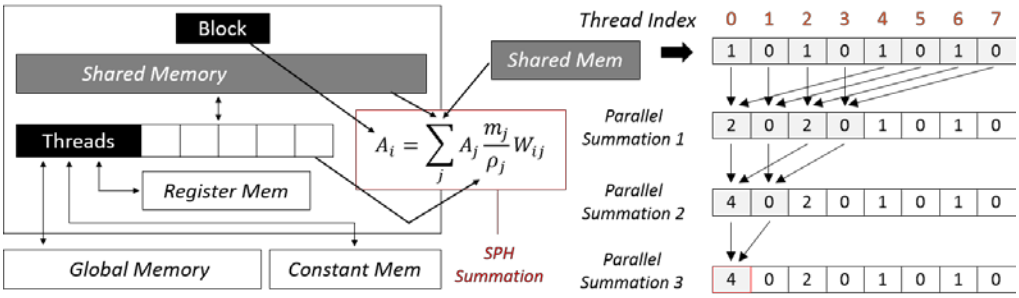


Figure 5.3. Parallel Reduction for Solving Governing Equations of SPH

| | |
|---|---|
| 1. Start Simulation<br>2. Input & Initialization | **Parallelization scheme used in SPH-DEM model** |
| 3. NNPS (SPH)<br>Contact Detection | Counting,<br>Cum sum, sorting |
| 4. Density Calculation | Mapping, Reduction |
| 5. Pressure Calculation | Mapping |
| 6. MTM Conservation | Mapping, Reduction |
| 7. Contact Force (DEM) | Mapping, Reduction |
| 8. MTM Exchange<br>(SPH-DEM Coupling) | Mapping, Reduction |
| 9. Update Properties | Mapping |

Figure 5.4. Simplified Algorithm of Code in Terms of GPU Parallelization

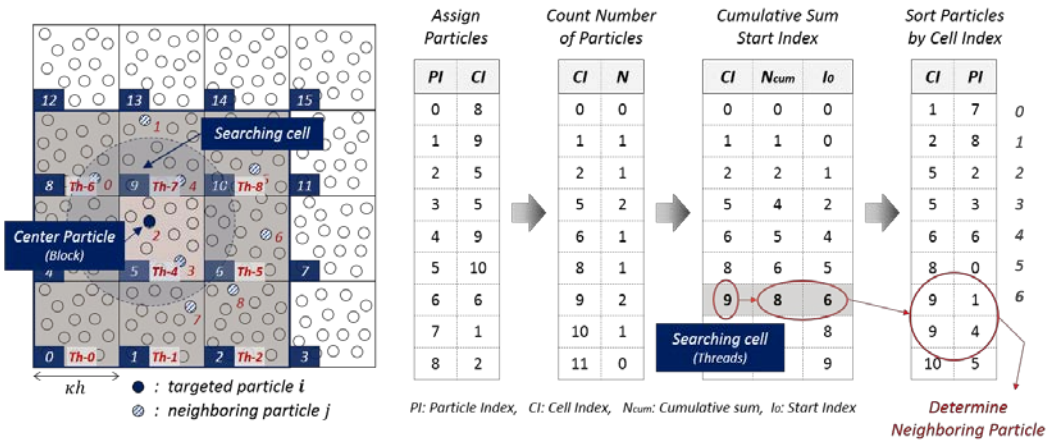


Figure 5.5. Simplified Sorting and Parallelization Algorithm for SPH-DEM Coupled Code

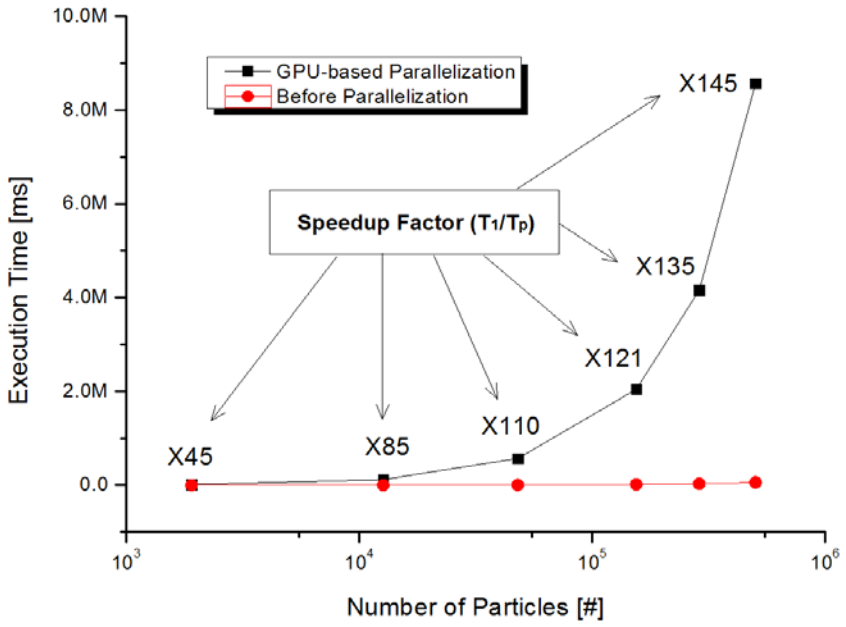


Figure 5.6. Speedup for GPU Parallelization of SPH-DEM Coupled Code

# Chapter 6

# Code Application to Vapor-Driven Leveling Behavior of Spherical Debris

In the late phase of the severe accident of reactor, there are many safety issues related to the 3-phase flow such as melt jet breakup, melt spreading, agglomeration of solid debris, sloshing, self-leveling, and so on. Among them, the vapor-driven self-leveling behavior of particulate solid debris is selected as an application case for demonstration of developed 3-phase flow analysis code in this study. There are some reasons for this.

a. It is suitable to demonstrating the hydrodynamic behavior of each phase.
b. Unresolved coupling of SPH and DEM is suitable for particulate flow.
c. Validation of the newly proposed boundary model is possible since the debris particles are packed on the bottom concrete surface.
d. There are enough benchmarking experiment data for comparison.

The following sections cover benchmarking experiments on self-leveling behavior and also the results of 3D SPH-DEM simulation as well as validation results.

## 6.1 Self-Leveling Behavior of Debris Bed

### 6.1.1 Self-Leveling Issue in LWR

In the late phase of PWR severe accident, failure of In-Vessel Retention strategy may lead to the release of core melt out of the vessel. In the wet cavity strategy with ex-vessel cooling, the core melt may be quenched and fragmented into the solid particles depending on the depth of the wet cavity. These particulate debris particles may spread by coolant drag and finally sediment into a mound shape. Two-phase natural convection occurs due to the decay heat generated from debris particles, which is the main heat removal mechanism of decay heat. In this situation, the steam flow escaping from the porous bed can be a source of mechanical energy, which can move the solid debris particles. Then, the conical shape of the particulate debris bed can change the geometry and be leveled due to the two-phase natural convection (Figure 6.1). This so-called self-leveling phenomenon of debris bed is an important issue in terms of mitigation of severe accident.

### 6.1.2 Self-Leveling Behavior in Terms of Debris Coolability

The wet cavity strategy (ex-vessel reactor cooling) succeeds only if the decay heat from debris particles is removed by two-phase natural convection of coolant (water). Otherwise, the debris bed can be re-melted due to dry out on the debris

particle surface, eventually attacking the containment (MCCI). Therefore, the coolability of the debris bed is a very important safety parameter in the late phase of a severe accident.

Generally, the coolability of the debris bed depends mainly on the properties of the bed including particle size, porosity, and also the overall shape of the debris bed. Especially, the maximum height of the bed is an important factor for debris bed coolability. According to the previous study, the same mass of debris bed can be cooled much easier if it is distributed uniformly over the basemat, rather than if it forms a tall mound-shaped debris bed [Basso, 2016]. A tall bed is hardly coolable since it is most prone to dry-out. Thus, the physical phenomena that can reduce the maximum height of the debris bed are of safety importance in a coolability analysis. In this respect, the self-leveling behavior is an important phenomenon since it may change the non-coolable shape to coolable geometry.

In order to be effective in establishing a coolable geometrical configuration of the bed, the characteristic time scale of the self-leveling should be smaller than the characteristic time scale for reaching dryout and re-melting of debris. If the former time scale (reaching coolable configuration) is shorter than the latter time scale (onset of re-melting), initially non-coolable debris bed becomes coolable due to self-leveling behavior. Therefore, it is necessary to analyze the leveling behavior over time in various conditions (particle size, steam flow rate, porosity, sphericity, etc.).

## 6.2 Benchmark Experiment

Several series of experiments were elaborately designed and conducted in Kyushu University to clarify the mechanisms underlying the self-leveling behavior of debris bed [Cheng, 2012]. The tendency of leveling behavior was analyzed from various experiment cases, and an empirical model was also developed to describe the transient variation in the bed inclination angle during the self-leveling process based on the experimental data. Besides, a parametric study was performed on various experiment factors including particle size, particle density, gas flow rate, and so on.

In these experiments, solid particles and water are contained in a tank, and various methods including gas injection, depressurized boiling, and bottom-heated boiling were employed o simulate the vapor-driven leveling behavior. The gas injection experiment in the rectangular viewing tank was selected as a benchmark experiment for code validation in this study.

A schematic diagram of the experimental setup is shown in Figure 6.2. A rectangular tank with $500mm$ height, $250mm$ width, $55mm$ gap thickness is filled with solid particles with a total volume of $2.5L$. Water and nitrogen gas were employed to simulate the coolant and steam, respectively. The depth of water was maintained at around $400\mathrm{mm}$, and the nitrogen gas was released into the tank from the bottom with a constant flow rate. Over the bottom of the viewing tank, a porous medium called airsotne served as a gas distributor ensuring a uniform percolation of gas. The main experimental conditions for the cases used in validation simulation are as below, and are also summarized in Figure 6.3.

- Particle Size : $6\ [mm]$
- Particle Sphericity : ~1.0 (Sphere)
- Porosity : ~0.42
- Total Volume of Particle : $2.5\ [L]$
- Particle Material : Glass (Glass bead)
- Liquid Material : Purified Water
- Gas Material : Nitrogen Gas ($100\ [kPa]$)
- Nitrogen Gas Flow Rate : $1.53,\ 3.43,\ 4.16\ [L/min]$
- Initial Inclined Angle : $20^{\circ}$~$27^{\circ}$

In this benchmark experiment, the ratio of the inclination angle at time $t'$ to initial angle ($t' = 0$) is defined as $R(t')$, and used to further quantify and anlyze the transient behavior of self-leveling. The simple expression of $R(t')$ is as below,

$$R(t') = \frac{Inclined\ Angle\ at\ t'\ \theta(t')}{Initial\ Inclined\ Angle\ \theta_0} \tag{6.1}$$

where $\theta$ *i*s an inclined angle of particle slope as shown in Figure 6.3, and the tangent of inclined angle is calculated as the ratio of the measured height of apex to the half-width of the rectangular tank in the experiment. In each experiment case, $R(t')$ was measured over time, and the experiment data are plotted as shown in Figure 6.4.

## 6.3 SPH-DEM Simulation Setup

For 3-phase flow validation of the developed SPH-DEM coupled code, the simulation was performed under the same conditions as the benchmarking experiment in the above section [Cheng, 2012]. The simulation was performed in exactly the same geometry and conditions with the benchmark experiment, as shown in Figure 6.5. The simulation conditions including the physical properties of DEM particles, the sequence of the SPH-DEM coupled simulation, and the determination method of inclined angle are covered in the following sub-sections.

### 6.3.1 Properties and Simulation Conditions

The physical properties of the fluid and solid used in this simulation were mostly referred to the real properties of purified water, nitrogen gas, and glass bead used in the benchmark experiment. For the properties that are not described in the benchmark experiment such as restitution coefficient and friction coefficient, the physical properties were obtained from the numerical analysis conducted in the same institution [Guo, 2013]. The physical properties of SPH and DEM particles used in the simulation are as follows.

1. Purified Water (SPH)

- Density: 1,000 [$kg/m^3$]
- Dynamic Viscosity: 0.001 [Pa · s]

2. Nitrogen Gas (SPH)

- Density: 1.126 [$kg/m^3$]

- Dynamic Viscosity: $1.789 \times 10^{-5}$ [Pa · s]

3. Glass Bead (DEM)

- Density: 2,590 [$kg/m^3$]
- Elasticity Modulus: $1.0 \times 10^{10}$ [Pa]
- Poisson's Ratio: 0.25
- Particle Diameter: 6 [mm]
- Restitution coefficient: 0.9
- Friction Coefficient: 0.3

As described in the previous chapter (Chapter 4), the unresolved coupling of SPH-DEM is effective when the SPH particle resolution is similar to the characteristic size (Diameter) of the DEM particle. Since the diameter of the DEM particles is fixed (6 mm) in this simulation, the applicable SPH resolution range is pre-determined. In the case of the time-step of the simulation, the step size required for the vapor phase SPH simulation is similar to that of DEM calculation ($\sim 10^{-6}$). Therefore, time integration was performed in the same algorithm. In addition, SPH particles corresponding to nitrogen gas are generated and injected at a constant rate that satisfies the volumetric gas flow rate given in the benchmark experiment. The conditions for SPH-DEM coupled leveling simulation are as follows.

- SPH Particle Spacing: 3.6 [mm]
- Coupling Length: 14.4 [mm]
- Time Step Size : $2.0 \times 10^{-6}$

- Nitrogen SPH Particles Velocity: $1.85, 4.16, 5.04\ [\mathrm{mm/s}]$
- Number of SPH Particles: $231{,}664$
- Number of DEM Particles: $12{,}480$

### 6.3.2 Sequence of SPH-DEM Leveling Simulation

The sequence for performing SPH-DEM simulation under the benchmark experiment conditions can be summarized as follows.

(1) SPH, DEM particle generation. In the case of DEM particles, the total volume of particles should be same as experiment condition ($2.5\mathrm{L}$) considering the packed porosity ($\sim 0.52$)
(2) DEM particle packing using DEM wall boundary condition. DEM particles should be packed in a mound shape by applying a wall boundary model inclined to around $25^{\circ}$ degree (Figure 6.5).
(3) Particles initialization. The DEM wall boundary that packed the DEM particles is removed and the particles are initialized to have a stable shape. The SPH particles are also coupled with DEM particles in this step.
(4) Nitrogen SPH particle injection. The nitrogen SPH particles are generated in a checkerboard shape in order to simulate the airstone (porous medium) in the benchmark experiment, as shown in Figure 6.6.
(5) Upper SPH boundary moving. The upper SPH boundary is raised in a constant velocity satisfy the incompressible condition in the computational domain.

### 6.3.3 Determination of Inclined Angle

In the benchmark experiment, the inclined angle of solid particles slope is defined based on the maximum height of solid particles. Specifically, the tangent of the inclined angle is calculated as the ratio of the measured height of apex to the half-width of the rectangular tank. The following definition of inclined angle is also applied in the simulation of this study,

$$\theta(t') = tan^{-1}\left(\frac{Height\ of\ Apex,\ H_{apex}(t')}{Half\ Width\ of\ Tank,\ W_{tank}}\right) \tag{6.2}$$

where $H_{apex}$ and $W_{tank}$ are the maximum height of apex and half-width of the rectangular tank, respectively. The maximum height of DEM particles was determined only for the particles within a specific area in order to exclude the effect of particles leaning on the sidewall, as shown in Figure 6.7.

## 6.4 Validation Results and Discussions

### 6.4.1 SPH-DEM Simulation Results

The SPH-DEM phase coupled simulation for self-leveling behavior was performed for three different gas inlet flow rate ($1.53,\ 3.43,\ 4.16\ [L/min]$). The simulation results for the case with a gas flow rate of $4.16\ [L/min]$ are

compared with the snapshots of the experimental result in Figure 6.8. From Figure 6.8, the self-leveling behavior of solid particle bed is clearly visible. The inclined angle, which was initially $20.5^{\circ}$, dropped to $15.1^{\circ}$ after 20 seconds under the influence of nitrogen gas-driven self-leveling behavior.

### 6.4.2 Validation Result

Figure 6.9 shows the comparison of $R(t')$ values, which is the ratio of the inclination angle at time $t'$ to initial angle, versus time $t'$ between experimental data and simulation results for the case with gas flow rate of $4.16\ [L/min]$. The data labeled SIMMER on Figure 6.9 are the results for the Eulerian-DEM coupled analysis performed in the same institution with the benchmark experiment [Guo, 2013], where SIMMER code is an Eulerian-based multiphase, multicomponent, multi-velocity field fluid dynamics code developed for the safety analysis of fast reactor.

As shown in Figure 6.9, the SPH-DEM coupled simulation results in this study well predict the long-term leveling behavior of solid particles in the benchmark experiment, showing better agreement than the results of Eulerian-DEM coupled simulation.

### 6.4.3 Effect of Gas Flow Rate

According to the previous experiments on self-leveling behavior, the equivalent power density appeared as a driving factor of leveling motion. Namely, the larger the equivalent power density, the faster the self-leveling proceeds

[Zhang, 2011]. In the gas injection experiment (benchmark experiment in this study), the gas flow rate can play an analogous role as shown in Figure 6.4. In this study, the self-leveling simulation was performed on three different gas velocities in order to analyze the effect of the gas flow rate. As shown in Figure 6.10, the inverse relation between $R(t')$ and gas inlet velocity can be clearly observed in simulation, which agrees well in the tendency with the results of experiments.

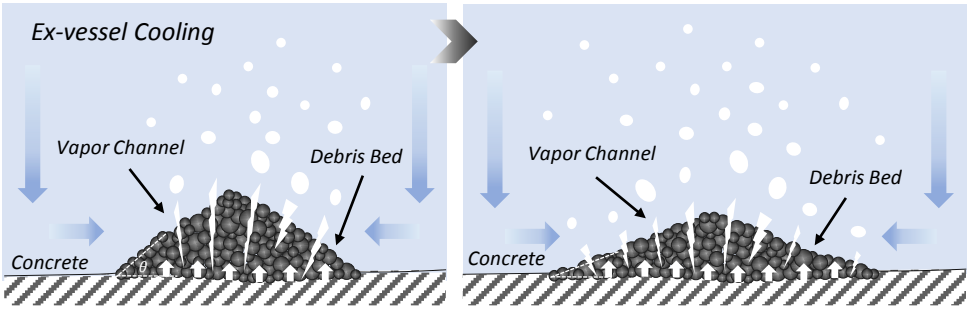


Figure 6.1. Mechanism of Debris Bed Self-Leveling

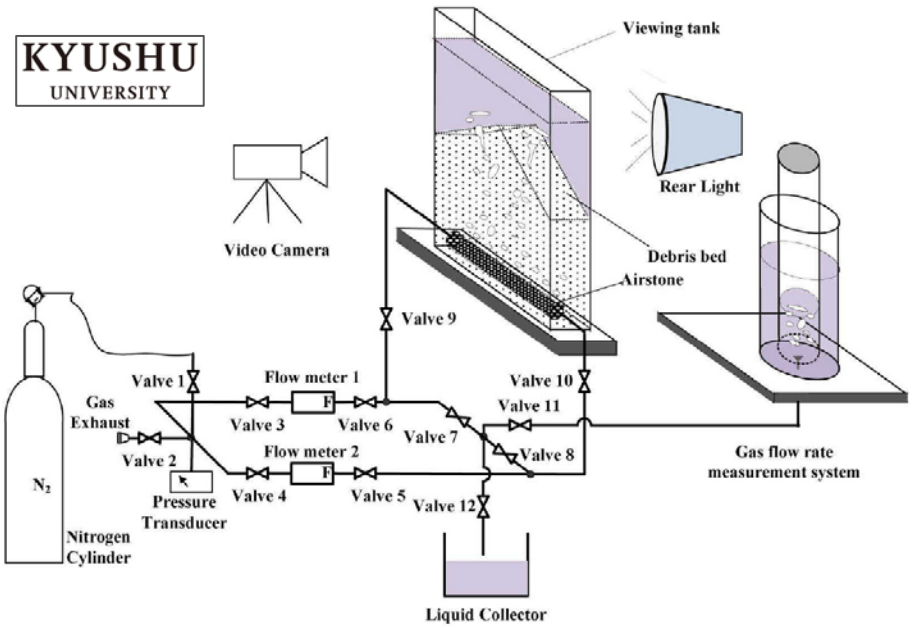


Figure 6.2. Schematic View of Experimental Apparatus [Cheng, 2012]

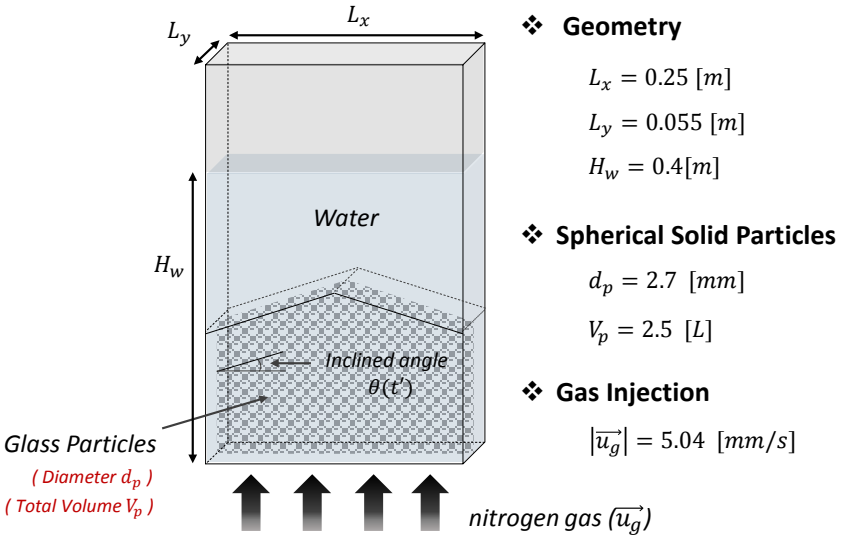


Figure 6.3. Conditions for Benchmark Leveling Experiment

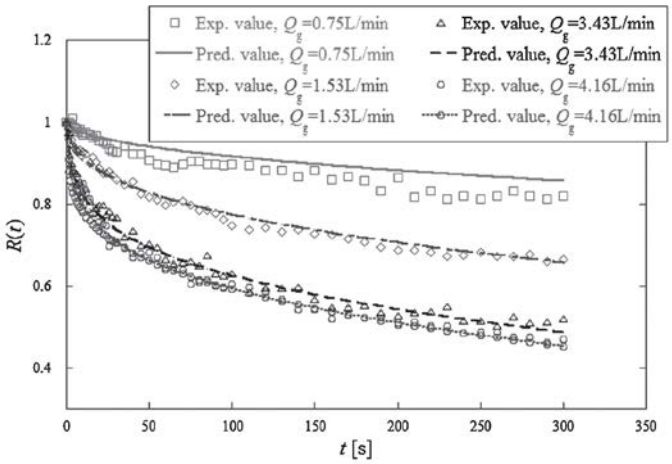


Figure 6.4. Time Variation of Inclined Angle in Benchmark Experiment [Cheng, 2012]

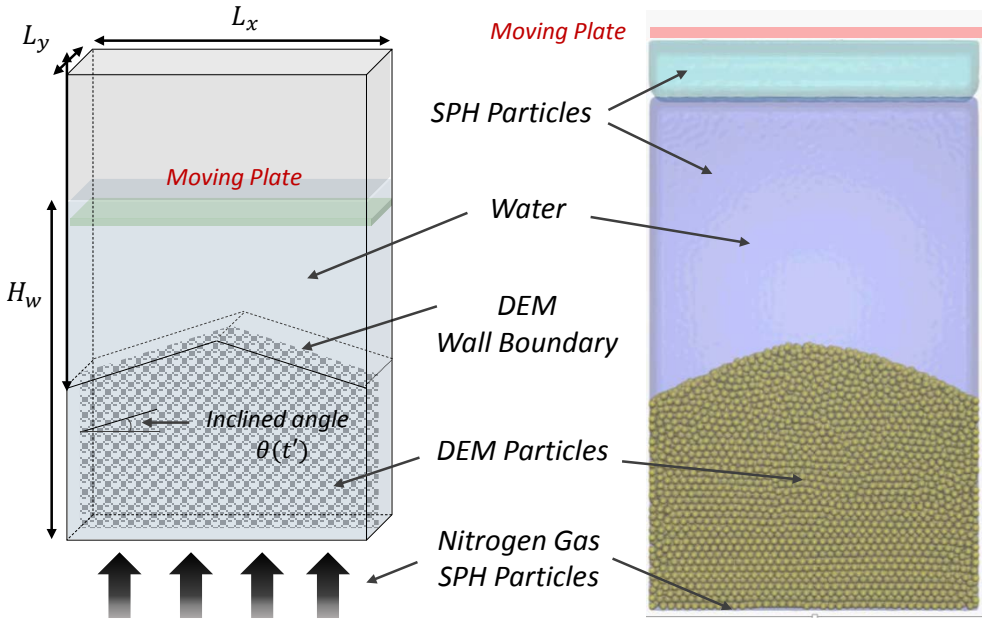


Figure 6.5. Geometry of SPH-DEM Coupled Leveling Simulation

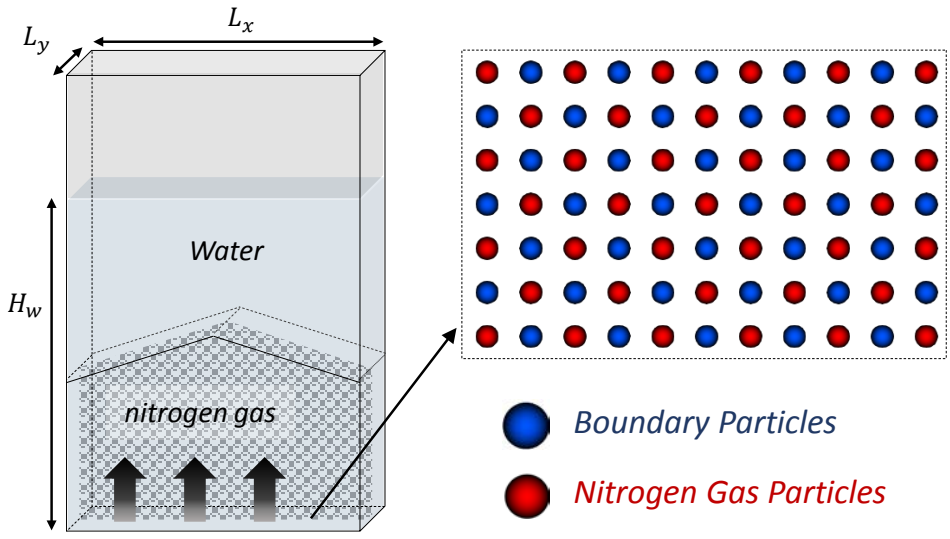


Figure 6.6. Gas Injection in SPH-DEM Coupled Simulation

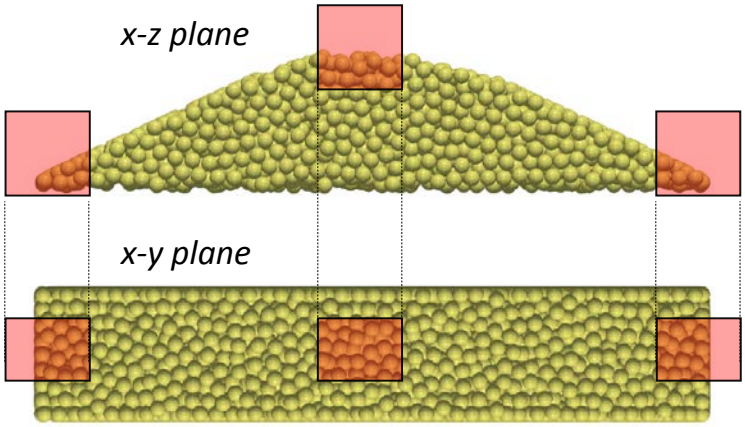


Figure 6.7. DEM Particles Used for Data (Height) Analysis

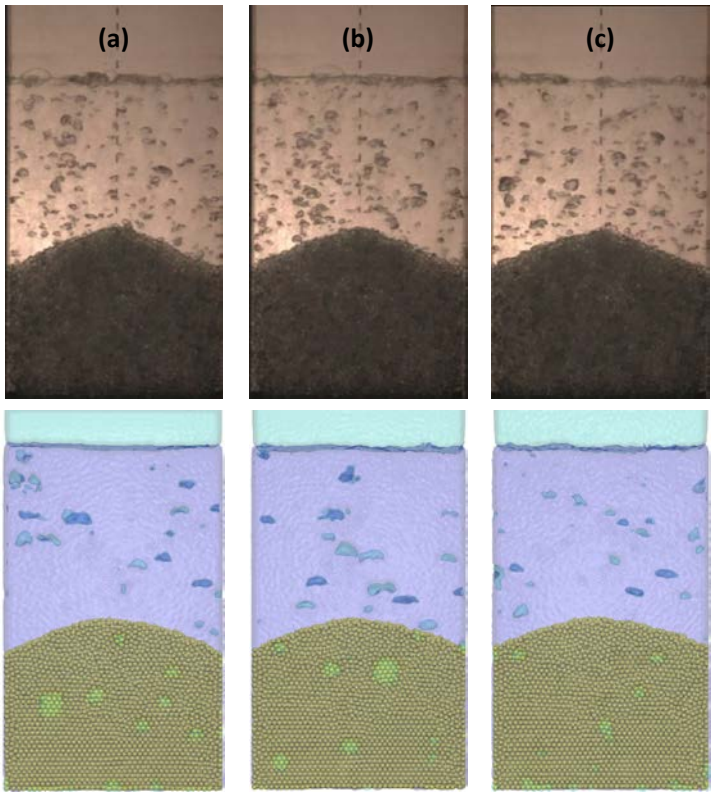


Figure 6.8. Snapshots Comparison b/w Experiment and SPH-DEM Simulation
(a) $t' = 5s$, (b) $t' = 10s$, (c) $t' = 15s$

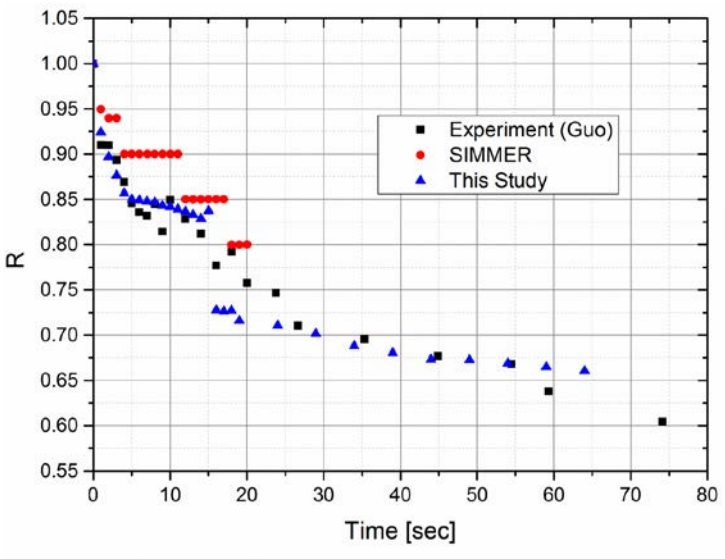


Figure 6.9. Validation Results for Time Variation of $R$ Value

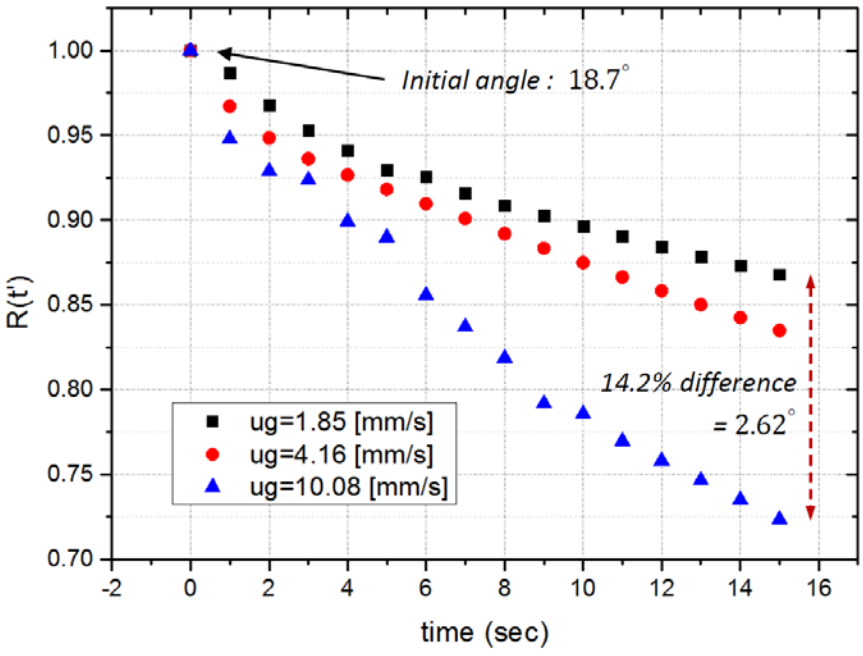


Figure 6.10. Effect of Gas Flow Rate on Self-Leveling Behavior

# Chapter 7

# Summary

## 7.1 Summary

In this study, the GPU-parallelized SPH-DEM phase coupled code was developed for the simulation of 3-phase hydrodynamic phenomena involving solid particles related to fuel debris in a reactor severe accident. The results, achievement, and findings of the study are summarized as follows.

1. Development of Multi-Phase SPH Code
    A. Lagrangian-based in-house SPH code has been developed for the analysis of incompressible multi-phase flow.
    B. An improved density estimation model and surface tension model was newly proposed for accurate tracking of the liquid-vapor interface.
    C. Qualitative and quantitative validations were carried out through various V&V cases including bubble terminal velocity behavior, multi-phase dam break, and multi-phase sloshing simulation. The results were well agreed with the benchmark data.
    D. It has been identified that the implemented two-phase SPH model well simulates the interface without any linearization of density, and also

better predicts the real free surface flow compared to the single-phase SPH.

2. Development of DEM Code
   A. A DEM code for solid particles was developed based on the soft-sphere collision model using Hertz-Mindlin contact force equations.
   B. A versatile wall boundary model incorporating both collision and sliding & rolling behavior was newly proposed in order to cover the wall interaction of packed solid particles.
   C. The momentum and angular moment were well conserved in all type of inter-particle collisions.
   D. A series of particle-boundary interaction behaviors including collision and also sliding and rolling were well proven in several V&V simulations.

3. Two-Way Phase Coupling of SPH-DEM
   A. The numerical code system for incompressible 3-phase flow is newly developed by a two-way phase coupling of SPH-DEM.
   B. An unresolved coupling approach between SPH and DEM was adopted for the analysis of particulate debris behavior.
   C. Validation of SPH-DEM coupled code was performed for solid-fluid pressure drop and dam-breaking behavior. The simulation results matched well with the result of the benchmark experiment.

4. GPU Parallelization of Coupled SPH-DEM Code

A. The SPH-DEM coupled code was parallelized based on Graphical Process Unit (GPU).
B. Various parallelization schemes were used for both solving governing equations of each SPH and DEM particle and finding the neighbor particles in SPH or contact particles in DEM.
C. Based on the benchmark calculation, the calculation speed increases by up to 2 orders of magnitude after code parallelization.
D. GPU parallelization in this study was efficient enough since the speedup factor reached 96.3% of the convergence value for the corresponding parallelization factor.

5. Code Application to Self-Leveling Simulation of Spherical Debris
   A. The simulation on vapor-driven debris bed self-leveling behavior was performed as a case study for the demonstration of developed SPH-DEM coupled code for 3-phase flow.
   B. The simulation results showed good agreement with the results of benchmark experiments both in qualitative and quantitative manners.
   C. The leveling behavior of solid particles in the simulation was suppressed in a lower gas flow rate, as also observed in the benchmark experiment.

## 7.2 Recommendations

The result of this research suggests following further studies.

1. The simulation and validation of the self-leveling behavior of solid particles in this study were carried out in a thin rectangular tank with cm scale. Since the benchmark experiments on self-leveling behavior were also carried out in relatively larger cylinder shaped tanks at Kyushu University and KTH, it is recommended to conduct the numerical simulations in cylindrical geometry based on a larger number of particles and higher particle resolution.
2. This study is focused on the hydrodynamic behavior of particulate solid within the incompressible multi-phase flow. However, in order to simulate the behavior of solid debris in actual reactor conditions, various advanced physics should be incorporated especially with regard to heat transfer and phase change, as shown in Figure 1.2. It is recommended to expand the scope of developed code through implementation and V&V of each physics listed in Figure 1.2.
3. If the validations of advanced physical models including turbulence, phase change, and non-spherical DEM particles are made, it is recommended to apply the code for actual reactor conditions. It is expected that the numerical experiments can be performed on the actual reactor conditions using developed SPH-DEM coupled code, which is hard to be conducted in laboratory-scale experiments.
4. The newly developed SPH-DEM coupled code used the unresolved coupling strategies between two methods. Thus it is suitable for particulate granular flow rather than single rigid body behavior. In this respect, the following numerical studies are recommended associated with the behavior of fragmented solid debris in addition to self-leveling phenomena.

A. Vapor-driven sloshing behavior of particulate debris (LMR)

B. Vapor entrainment in sedimentation behavior of solid particles (LWR)

# References

Adami, S., X. Y. Hu, and Nikolaus A. Adams. "A new surface-tension formulation for multi-phase SPH using a reproducing divergence approximation." *Journal of Computational Physics* 229.13 (2010): 5011-5021.

Basso, Simone, Alexander Konovalenko, and Pavel Kudinov. "Effectiveness of the debris bed self-leveling under severe accident conditions." *Annals of Nuclear Energy* 95 (2016): 75-85.

Brackbill, Jeremiah U., Douglas B. Kothe, and Charles Zemach. "A continuum method for modeling surface tension." Journal of computational physics 100.2 (1992): 335-354.

Breinlinger, Thomas, et al. "Surface tension and wetting effects with smoothed particle hydrodynamics." *Journal of Computational Physics* 243 (2013): 14-27.

Buck, Michael. "Modelling of the late phase of core degradation in light water reactors." (2007).

Buruchenko, Sergei K., and Alejandro JC Crespo. "Validation DualSPHysics Code for Liquid Sloshing Phenomena." 2014 22nd International Conference on Nuclear Engineering. American Society of Mechanical Engineers, 2014.

Cheng, Songbai, et al. "A two-dimensional experimental investigation on the sloshing behavior in a water pool." Annals of nuclear energy 114 (2018): 66-73.

Cheng, Songbai, et al. "An experimental study on pool sloshing behavior with

solid particles." *Nuclear Engineering and Technology* 51.1 (2019): 73-83.

Cheng, Songbai, et al. "Experimental studies and empirical models for the transient self-leveling behavior in debris bed." *Journal of nuclear science and technology* 48.10 (2011): 1327-1336.

Chou, H. T., et al. "Discrete element modelling and experimental validation for the falling process of dry granular steps." *Powder technology* 231 (2012): 122-134.

Cleary, Paul W. "Modelling confined multi-material heat and mass flows using SPH." *Applied Mathematical Modelling* 22.12 (1998): 981-993.

Clift, Roland, John R. Grace, and Martin E. Weber. *Bubbles, drops, and particles*. Courier Corporation, 2005.

Cossins, Peter J. *The Gravitational Instability and its Role in the Evolution of Protostellar and Protoplanetary Discs. Chapter 3: Smoothed Particle Hydrodynamics-Or: How I Learned to Stop Worrying and Love the Lagrangian*. Diss. PhD thesis, University of Leicester, 2010.

Cundall, Peter A., and Otto DL Strack. "A discrete numerical model for granular assemblies." *Geotechnique* 29.1 (1979): 47-65.

DEM Solutions Ltd. 2016. EDEM 2.6 Theory Reference Guide. Edinburgh: DEM Solutions Ltd.

Di Felice, Rosa. "The voidage function for fluid-particle interaction systems." *International journal of multiphase flow* 20.1 (1994): 153-159.

Gingold, Robert A., and Joseph J. Monaghan. "Smoothed particle hydrodynamics: theory and application to non-spherical stars." *Monthly notices of the royal astronomical society* 181.3 (1977): 375-389.

Gomez-Gesteira, Moncho, et al. "SPHysics–development of a free-surface fluid solver–Part 1: Theory and formulations." Computers & Geosciences 48 (2012): 289-299.

Grenier, Nicolas, et al. "An Hamiltonian interface SPH formulation for multi-fluid and free surface flows." Journal of Computational Physics 228.22 (2009): 8380-8393.

Guo, L., and Koji Morita. "Numerical simulation of 3D sloshing in a liquid–solid mixture using particle methods." *International journal for numerical methods in engineering* 95.9 (2013): 771-790.

Guo, Liancheng, et al. "Numerical simulation of self-leveling behavior in debris bed by a hybrid method." *2013 21st International Conference on Nuclear Engineering*. American Society of Mechanical Engineers Digital Collection, 2013.

Guo, Liancheng, Koji Morita, and Yoshiharu Tobita. "Numerical simulations on self-leveling behaviors with cylindrical debris bed." *Nuclear Engineering and Design* 315 (2017): 61-68.

Harada, Takahiro, Seiichi Koshizuka, and Yoichiro Kawaguchi. "Smoothed particle hydrodynamics on GPUs." Computer Graphics International. Petropolis: SBC, 2007.

He, Yi, et al. "A GPU-based coupled SPH-DEM method for particle-fluid flow with free surfaces." *Powder technology* 338 (2018): 548-562.

Hegeman, Kyle, Nathan A. Carr, and Gavin SP Miller. "Particle-based fluid simulation on the GPU."*International Conference on Computational Science*. Springer, Berlin, Heidelberg, 2006.

Hirt, Cyril W., and Billy D. Nichols. "Volume of fluid (VOF) method for the dynamics of free boundaries." *Journal of computational physics* 39.1 (1981): 201-225.

Hwang, Byoungcheol, et al. "Numerical validation and investigation for the sedimentation of solid particles in liquid pool using the CFD-DEM coupling algorithm." *Nuclear Engineering and Design* 355 (2019): 110364.

Kelager, Micky. "Lagrangian fluid dynamics using smoothed particle hydrodynamics." *University of Copenhagen: Department of Computer Science* 2 (2006).

Koshizuka, Seiichi, and Yoshiaki Oka. "Moving-particle semi-implicit method for fragmentation of incompressible fluid." *Nuclear science and engineering* 123.3 (1996): 421-434.

Li, Liangxing, et al. "Pressure losses and interfacial drag for two-phase flow in porous beds with coarse particles." *Annals of Nuclear Energy* 101 (2017): 481-488.

Liu, Gui-Rong, and Moubin B. Liu. *Smoothed particle hydrodynamics: a meshfree particle method*. World scientific, 2003.

Luebke, David, and M. Harris. "General-purpose computation on graphics hardware." Workshop, SIGGRAPH. 2004.

Markauskas, D., et al. "Comparative study on mesh-based and mesh-less coupled CFD-DEM methods to model particle-laden flow." *Powder Technology* 305 (2017): 78-88.

Markauskas, Darius, and Harald Kruggel-Emden. "Coupled DEM-SPH simulations of wet continuous screening." *Advanced Powder Technology* 30.12 (2019): 2997-3009.

Maschek, Werner, Claus Dieter Munz, and Leonhard Meyer. "Investigations of sloshing fluid motions in pools related to recriticalities in liquid-metal fast breeder reactor core meltdown accidents." *Nuclear technology* 98.1 (1992): 27-43.

Maschek, Werner, et al. "Investigation on upper bounds of recriticality energetics of hypothetical core disruptive accidents in sodium cooled fast reactors." Nuclear Engineering and Design326 (2018): 392-402.

Maschek, Werner, et al. "Simulation experiments for centralized liquid sloshing motions." KERNFORSCHUNGSZENTRUM KARLSRUHE-PUBLICATIONS-KFK (1992).

Mayrhofer, Arno, et al. "Combining Blender with SPHysics, an Introduction." (2010).

Monaghan, Joe J. "Simulating free surface flows with SPH." *Journal of computational physics* 110.2 (1994): 399-406.

Monaghan, Joe J. "Smoothed particle hydrodynamics." *Annual review of astronomy and astrophysics* 30.1 (1992): 543-574.

Monaghan, Joe J. "Smoothed particle hydrodynamics." *Reports on progress in physics* 68.8 (2005): 1703.

Monaghan, Joseph John, and Ashkan Rafiee. "A simple SPH algorithm for multi-fluid flow with high density ratios." *International Journal for Numerical Methods in Fluids* 71.5 (2013): 537-561.

Morris, Joseph P. "Simulating surface tension with smoothed particle hydrodynamics." International journal for numerical methods in fluids 33.3 (2000): 333-353.

Morrison, Faith A. *An introduction to fluid mechanics*. Cambridge University Press, 2013.

Nickolls, John, et al. "Scalable parallel programming with CUDA." Queue 6.2 (2008): 40-53.

Peng, Bo. *Discrete element method (DEM) contact models applied to pavement simulation*. Diss. Virginia Tech, 2014.

Pigny, Sylvain L. "Academic validation of multi-phase flow codes." Nuclear Engineering and Design 240.11 (2010): 3819-3829.

Raji, Abdulganiy Olayinka. "Discrete element modelling of the deformation of bulk agricultural particulates." (1999).

Roache, Patrick J. Verification and validation in computational science and

engineering. Vol. 895. Albuquerque, NM: Hermosa, 1998.

Robinson, Martin, Marco Ramaioli, and Stefan Luding. "Fluid-particle flow modelling and validation using two-way-coupled mesoscale SPH-DEM." *arXiv preprint arXiv:1301.0752* (2013).

Sanders, Jason, and Edward Kandrot. CUDA by Example: An Introduction to General-Purpose GPU Programming, Portable Documents. Addison-Wesley Professional, 2010.

Siegel, Jakob, Juergen Ributzka, and Xiaoming Li. "CUDA memory optimizations for large data-structures in the gravit simulator." *Journal of Algorithms & Computational Technology* 5.2 (2011): 341-362.

Suzuki, Tohru, et al. "A scenario of core disruptive accident for Japan sodium-cooled fast reactor to achieve in-vessel retention." Journal of Nuclear Science and Technology 51.4 (2014): 493-513.D.E.

Vorobyev, Alexander. *A Smoothed particle hydrodynamics method for the simulation of centralized sloshing experiments*. KIT Scientific Publishing, 2012.

Xia, Xilin, and Qiuhua Liang. "A GPU-accelerated smoothed particle hydrodynamics (SPH) model for the shallow water equations." Environmental Modelling & Software 75 (2016): 28-43.

Xu, Wen-Jie, Xue-Yang Dong, and Wen-Tao Ding. "Analysis of fluid-particle interaction in granular materials using coupled SPH-DEM method." *Powder Technology* 353 (2019): 459-472.

Yakush, Sergey, and Pavel Kudinov. "Effects of water pool subcooling on the debris bed spreading by coolant flow." *Proceedings of ICAPP 2011, Paper* 11416 (2011): 2-5.

Yamano H., Hosono S., Sugaya M Analysis of sloshing experiments // Proc. of 14th JAEA-FZK/CEA/IRSN/ENEA SIMMER-III/IV Review Meeting, Karlsruhe, Germany, September 9–12, 2008.

Zhang, Aman, Pengnan Sun, and Furen Ming. "An SPH modeling of bubble rising and coalescing in three dimensions." *Computer Methods in Applied Mechanics and Engineering* 294 (2015): 189-209.

Zhu, H. P., et al. "Discrete particle simulation of particulate systems: theoretical developments." *Chemical Engineering Science* 62.13 (2007): 3378-3396.

Ergun, Sabri. "Fluid flow through packed columns." *Chem. Eng. Prog.* 48 (1952): 89-94.

# 국문 초록

가압경수로 중대사고 후기 과정에서 핵연료 용융물 노내 억류 전략의 실패로 용융 핵연료가 용기 바깥쪽 침수 공동으로 재배치되면, 공동의 깊이나 제트의 속도 등의 조건에 따라 핵연료 파편화가 발생할 수 있다. 이러한 핵연료 파편물에서 발생하는 붕괴열에 의해 냉각재의 상변화가 이루어지면, 이상유동 자연대류와 고체 파편물이 공존하는 3상유동 시스템이 된다. 핵연료 용융물의 제트 파쇄, 하강 및 퇴적, 평탄화 등 일련의 과정에서 다양한 형태의 파편물 3상 냉각 거동이 발생할 수 있으며, 핵연료 파편물의 붕괴열이 충분히 제거되지 못하면 파편물의 응집 및 재용융이 발생할 수 있다. 중대사고 완화의 관점에서 이러한 3상 냉각 거동에 대한 상세한 이해가 필요하지만, 이상유동 자연대류, 이상유동 열전달, 고화, 용융, 비등, 유동-입자 상호작용 등을 포함하는 거동 자체의 복잡성으로 인해 관련 현상들의 예측 및 평가는 큰 불확실성을 내포하고 있다.

전통적인 핵연료 파편물을 포함한 3상 거동 해석은 다른 중대사고 해석과 마찬가지로 경험적 방법론에 의존한 보수적인 접근 방법이나 고체 입자와 이상 유체를 모두 연속체로 가정하는 다유체 모델을 기반으로 이루어졌다. 최근에는 이러한 방법론들이 가지는 본질적인 한계를 극복하고자 고체 입자들 사이의 충돌이나 회전을 별개로 다루는 이산요소법(Discrete Element Method, DEM)과 격자 기반의

오일러리안 전산유체해석(CFD) 기법을 연계하는 형태로 서로 간의 상호작용을 해석하는 연구들이 많이 이루어지고 있다.

한편, 최근에는 하드웨어 및 소프트웨어의 성능이 비약적으로 좋아지면서 격자(Grid)에 기반하지 않고 질점 하나하나의 움직임을 따라가면서 유동에 대한 지배방정식을 해석하는 라그랑지안 유체해석기법의 응용이 늘어나고 있다. 라그랑지안 해석 기법에서는 다상유동 해석 시에 액체와 기체 두 상을 완전히 별개의 영역으로 해상하여 지배방정식을 풀기 때문에 계면 마찰력이나 항력, 양력 등에 대한 별도의 상관식 없이 제 1 원리 기반으로 유동을 해석할 수 있어, 이상유동에 대한 보다 근본적인 해석이 가능하다.

핵연료 파편물의 생성 및 3상 냉각 거동과 관련된 현상들은 대부분 기체 상의 생성이나 이상유동 자연대류에 영향을 받는 현상들로 액체 기체 사이의 인터페이스가 복잡하고 역동적인 경향이 있기 때문에, 액체-기체 다상유동에 효과적인 라그랑지안 기반의 유체해석 기법과 강체 이산요소법(DEM)을 연계하면 효과적인 3상 유동 해석 체계를 구축할 수 있다. 하지만, 핵연료 파편물을 포함한 3상 냉각 거동과 관련하여 라그랑지안 입자 기반 유체해석 기법을 활용한 연구는 세계적으로도 아직 수행된 바가 없다.

이러한 필요성에 따라, 본 연구에서는 대표적인 입자 기반의

유체해석 방법론 중 하나인 완화입자유체동역학(Smoothed Particle Hydrodynamics, SPH) 기법과 강체의 충돌, 병진, 회전 운동을 직접적으로 다루는 이산요소법(DEM)의 연계를 통해 고체 입자를 포함한 3상 유동 해석을 위한 라그랑지안 해석 체계를 구축하였다. 고체 입자와 유체 사이의 연계는 mm 이하의 스케일을 가지는 핵연료 파편물의 형상적 특성을 고려하여 두 상 사이의 겹침을 허용하여 운동량 교환을 모델링하는 비해상(unresolved) 방식으로 이루어졌다. 또한, SPH 유체 모델, DEM 강체 모델, SPH-DEM 연계 모델 각각에 대한 검증을 다양한 스케일에서 다양한 실험 연구들과의 비교를 통해 수행하였다.

한편, 완화입자유체동역학(SPH) 기법과 이산요소법(DEM) 모델은 라그랑지안 해석 기법의 특성상 컴퓨터 성능의 비약적인 발전에도 불구하고 오일러리안 해석 기법에 비해 계산 효율 및 시간에 대한 상대적인 제약이 존재한다. 특히 액체-기체의 이상유동 해석을 다룰 경우 기체 상의 밀도가 작기 때문에 라그랑지안 유체해석 기법에서는 더 작은 시간 간격이 요구된다. 이에 본 연구에서는 그래픽 처리 장치 (Graphics Processing Unit, GPU)를 활용하여 SPH 해석, DEM 해석, SPH-DEM 연계 해석이 모두 각 라그랑지안 질점에 대해 동시에 수행될 수 있도록 GPU 기반의 연계코드 병렬화 및 가속화를 수행하였다.

마지막으로 개발한 라그랑지안 기반의 3상유동 해석 체계의 유용성 입증을 위해 원자로 중대사고 후기 과정에서 발생할 수 있는 핵연료 파편물 층(debris bed)의 평탄화(self-leveling) 거동에 대한 검증 해석을 수행하였다. 시간에 따른 파편물 층 표면의 형상 변화를 타 기관에서 수행된 기체주입 실험과 비교하는 형태로 검증이 이루어졌다. 분석 결과, 본 연구에서 개발한 SPH-DEM 연계해석 코드가 고체 입자 상을 포함한 수력학적 3상 거동을 정량적으로, 정성적으로 잘 해석하는 것을 확인하였다.

본 연구에서 개발한 라그랑지안 기반의 SPH-DEM 3상유동 해석 체계는 원자로 중대사고의 해석적 관점에서 기존의 수치해석 기법들이 다루기 어려웠던 현상들에 대한 대안 또는 상호 보완의 역할을 할 수 있다. 또한, 본 연구에서 개발한 코드는 제 1원리 기반의 물리 법칙을 기반으로 유동 및 강체의 거동을 해석하기 때문에 실험으로 구현하기 어려운 조건이나 스케일에 대한 수치적 재현이 가능하고, 이를 바탕으로 기존의 스케일링 법칙을 검증하거나 실험 결과가 없는 영역에서 수치 데이터를 생성하여 기존의 상관식을 개선하는데 활용할 수 있다. 이러한 점에서 본 연구는 원자로 중대사고의 해석이나 안전성 평가와 관련하여 불확실성을 저감하는데 기여한다.

**주요어**

완화입자유체동역학, 이산요소법, 양방향 연계, GPU 병렬화, 원자로 중대사고, 파편물 층, 파편층 평탄화

학번: 2014-21417